January 2015

SYNTHESIS, CHARACTERIZATION, AND KINETIC EVALUATION OF PLANAR AND SUPPORTED HETEROGENEOUS CATALYSTS

Michael D. Detwiler
Purdue University

Recommended Citation

Detwiler, Michael D., "SYNTHESIS, CHARACTERIZATION, AND KINETIC EVALUATION OF PLANAR AND SUPPORTED HETEROGENEOUS CATALYSTS" (2015). *Open Access Dissertations*. 1349.
https://docs.lib.purdue.edu/open_access_dissertations/1349

Graduate School Form 30
Updated 1/15/2015

PURDUE UNIVERSITY
GRADUATE SCHOOL
Thesis/Dissertation Acceptance

This is to certify that the thesis/dissertation prepared

By Michael D. Detwiler

Entitled

SYNTHESIS, CHARACTERIZATION, AND KINETIC EVALUATION OF PLANAR AND SUPPORTED HETEROGENEOUS CATALYSTS.

For the degree of Doctor of Philosophy

Is approved by the final examining committee:

Fabio Ribeiro Chair	
Jeffrey Greeley Co-chair	
W. Nicholas Delgass Co-chair	
Dmitry Zemlyanov	

To the best of my knowledge and as understood by the student in the Thesis/Dissertation Agreement, Publication Delay, and Certification Disclaimer (Graduate School Form 32), this thesis/dissertation adheres to the provisions of Purdue University's "Policy of Integrity in Research" and the use of copyright material.

Approved by Major Professor(s): Fabio Ribeiro

Approved by: John A. Morgan 5/1/2015

Head of the Departmental Graduate Program Date

SYNTHESIS, CHARACTERIZATION, AND KINETIC EVALUATION OF PLANAR AND SUPPORTED HETEROGENEOUS CATALYSTS

A Dissertation

Submitted to the Faculty

of

Purdue University

by

Michael D. Detwiler

In Partial Fulfillment of the

Requirements for the Degree

of

Doctor of Philosophy

August 2015

Purdue University

West Lafayette, Indiana

For my family.

ACKNOWLEDGMENTS

The successes in my Ph. D. would not have been possible without the support and guidance of others. I have very sincere gratitude for all of the efforts of my advisors, Profs. Fabio Ribeiro and Nick Delgass. Both have instilled in me a sense of scientific rigor and curiosity that have enabled me to contribute to solving scientific problems. I am certainly not the only person to recognize their talents: because of their decades of hard work and achievement, never during my Ph. D. did I have to worry about funding for research.

I was very fortunate to collaborate with a large number of extremely competent researchers. From Dmitry Zemlyanov and Anna Nartova I learned the art and science of developing and performing UHV experiments and meticulously analyzing the results. Jeffrey Greeley and his students, especially Xiang-Kui Gu and Paulami Majumdar, helped me better understand my experimental results with theory, and helped me to learn how to communicate effectively with theorists. Ron Reifenberger was an excellent voice of reason in our meetings, often bringing back conversations to planet earth. Expert technical guidance from Yury Zvinevich and David Taylor saved me a number of times.

I was also very lucky to have great peers along the way in the surface science subgroup. Amir, thank you for being at Purdue and tacking many of the same challenges as me. I could not have asked for a better coworker and friend. Lukas, I wish you could have stayed in the United States longer, but I understand the allure of skiing in your backyard. To Cory and Ian, the future of UHV group looks bright, best of luck, and thank you for your help, especially at the end.

What I will miss most about my time at Purdue are my friends. I have been very lucky to live with some great people at Purdue: Steve Smith, Vince Kispersky, Shane Bates, Greg Honda, Erik Sheets, Kevin Brew, Matt Louvier, and Jamie Harris. I will always remember other members of the catalysis group and am grateful for your excellent technical discussions and friendship: John Degenstein, Paul Dietrich, Sara Yohe, Yanran Cui, Harsh Choudhari, Dhairya Mehta, Fred Sollberger, Atish Parekh, and others. Plenty of other folks not mentioned anywhere above also allowed me to maintain a positive mental state during graduate school, and I am honored to be your friend–but there are too many to list here. I must give gig thank-you's to Deb Bowman and Katie Field for keeping things running smoothly in the background, and a huge thank you to Linda for keeping my office clean. I also could not have completed my Ph. D. without the support and love of my family and friends back home.

Finally, I must acknowledge my funding source: This material is based upon work supported as part of the Institute for Atom-efficient Chemical Transformations (IACT), an Energy Frontier Research Center funded by the U. S. Department of Energy, Office of Science, Office of Basic Energy Sciences. The U. S. Department of Energy is the reason that I am financially solvent after 5 years of graduate school (and two lucrative summer internships before that!), so a huge thanks to them and, by extension, American taxpayers.

TABLE OF CONTENTS

APPENDICES

LIST OF TABLES

LIST OF FIGURES

Figure Page

ABSTRACT

Detwiler, Michael D. PhD, Purdue University, August 2015. Synthesis, Characterization, and Kinetic Evaluation of Planar and Supported Heterogeneous Catalysts. Major Professors: Fabio H. Ribeiro and W. Nicholas Delgass.

An integrated approach for biomass upgrading to fuels requires catalyst synthesis, characterization, and kinetic evaluation. The work was divided in three areas, 1–preparation and characterization of model catalysts containing metal oxide overcoats and metal nanoparticles synthesized by atomic layer deposition (ALD), a gas-phase material deposition technique, 2–the study of structure sensitivity for formic acid decomposition on planar Pt catalysts, and 3–characterization of bimetallic Pt-M (M = Re, Mo) catalysts using surface sensitive techniques and theory.

In the first project, metal oxide overcoats, which have been found to prevent metal nanoparticle deactivation via sintering and coking in biomass upgrading reactions, were prepared by ALD. In this work, model alumina-overcoated catalysts were synthesized by exposing Pd(111), Pt(111), and Cu(111) surfaces to trimethylaluminum at ca. 10^{-6} mbar and a co-reactant (H_2O or O_2) at ca. 10^{-6} or 0.1 mbar. Nominal Al coverages differed on each surface after saturation trimethylaluminum exposure ($\geq$ 500 L) at 200°C in the order Pd(111) (1.4 ML) > Pt(111) (1.0 ML) > Cu(111) (no Al), and Al alloyed only with Pd(111). Trimethylaluminum adsorbed on Cu_2O-covered Cu(111), consuming adsorbed oxygen. Overlayer morphologies and adsorbed carbon species were found to be different on each surface, indicating that the interaction of trimethylaluminum with transition metal surfaces is substrate-dependent. Details of each reaction mechanism are discussed. Atomic layer deposition was also used for the synthesis of metallic nanoparticles. Dissociative adsorption sites for M(II) (M = Pd or Cu) hexafluoroacetylacetonates (hfac) on rutile $TiO_2(110)$ to form adsorbed (hfac) and M(hfac) were determined, and annealing this surface resulted in the formation of M nanoparticles.

In the second project, formic acid decomposition kinetics were evaluated on planar Pt catalysts. Hydrogen is necessary for oxygen removal from biomass, and formic acid, a byproduct of biomass upgrading, catalytically decomposes to produce H_2 and CO_2 or H_2O and CO. Batch reactor kinetics were found to be structure-insensitive on Pt(111), (100), and a polycrystalline foil under standard reaction conditions (1% HCOOH, 1.875% H_2, 1.875% CO, $P_{\text{Total}} = 800$ Torr, 220°C), within measurement precision. Approximate CO_2 formation turnover rates were 2.6 ± 0.6, 3.7 ± 1.0, and 3 ± 2 s^{-1} at 220°C on Pt(111), (100), and Pt foil, respectively, while CO selectivity remained < 1% for conversions < 10%.

Finally, bimetallic Pt-M (M = Re, Mo) catalysts were characterized in the third project. Exposing Re/Pt(111) surfaces synthesized by ultra-high vacuum chemical vapor deposition to oxygen formed ReO_x ($0.5 < x < 1$). Oxygen desorbed above 973 K, and a Pt skin formed over Re, which bound O and CO more weakly than either monometallic surface. Adsorbate frequencies were calculated by density functional theory and compared to experiment, which confirmed that rhenium oxide clusters were present on the O-exposed, Pt skin surface. Theoretical calculations showed that the binding energy trends observed by XPS and HREELS experiments can be explained on the basis of d-band centers of Pt-Re systems. Pt-Mo catalysts supported on multiwall carbon nanotubes were also characterized by x-ray photoelectron spectroscopy which revealed the presence of Pt_xMo ($2 < x < 3$) alloy, Mo carbide-like, Mo^{4+}, and Mo^{6+} phases, confirming x-ray absorption results. Catalysts with more Mo relative to Pt contained fewer Pt monometallic and more Pt_xMo bimetallic nanoparticles, and at the highest Mo loadings Mo oxide and carbide-like phases dominated, indicating that Mo phase distribution is a function of Mo loading.

1. INTRODUCTION

Due to long-term supply uncertainties and concern about greenhouse gas emissions, the search for renewable, sustainable sources of energy has taken center stage in multiple research areas. [1] This is true especially for the transportation sector, which relies almost completely on petroleum. [2] Some technologies that show promise as alternatives to petroleum are electric vehicles, hydrogen fuel cell vehicles, and liquid fuels derived from biomass. None of the above technologies are mature. Electric vehicles suffer from battery cost and performance issues and will necessitate the development of infrastructure related to vehicle charging. Hydrogen fuel cells require advances in hydrogen storage technology and the related refueling infrastructure. [3] If electricity or hydrogen for these technologies are produced from conventional fossil fuels, these alternatives will continue contributing to the atmospheric concentration of CO_2.

One promising renewable fuel source is biomass, and, as a result, a variety of different pathways for upgrading biomass feedstocks to liquid fuels and other high value chemicals have been under development. [4] Common forms of lignocellulosic biomass have 75-80% of the energy density of gasoline a per-carbon basis. [5] Biomass is already used for production of gasoline blending agents. The largest scale production of biomass-derived fuel in the United States currently is ethanol from corn, however, this process relies heavily on government subsidies and uses a food crop for fuel, which has ignited ethical debate. [6]

Using less expensive lignocellulose feedstocks for biomass conversion to liquid fuel is “viewed as the end-goal feedstock.” [3] A multitude of conversion technologies are being studied for upgrading these feedstocks including gasification, pyrolysis followed by hydrodeoxygenation, biological methods, and liquefaction. [5] One proposed reaction network that relies heavily on aqueous phase catalytic reforming to to carry out these chemical transformations focuses on upgrading the simple biomass-derived sugars xylose and glucose to fuels in the Diesel, gasoline, or jet fuel range. It is outlined in Figure 1.1. In short, this reaction network relies on a variety of chemical processes to upgrade biomass-derived C5 and C6 sugars to furfural and levulinic acid (LA), respectively. Through subsequent upgrading steps involving reduction, these two products are further upgraded to γ-valerolactone, a platform molecule for production of fuels in the gasoline, Diesel, or jet fuel range. [7] The entire reaction network relies heavily on H_2 input for both reduction of furfural and LA as well as for C-C coupling of mono-functional oxygenates. As a result, H_2 generation was also included in this pathway.

Many of the reactions in the reaction network, including those used for H_2 generation (formic acid decomposition and aqueous phase reforming) occur on heterogeneous catalysts. Heterogeneous catalysts are materials that alter the kinetics of a chemical reaction. They exist in a phase other than that of the reactants. By altering reaction kinetics, catalysts can increase the yield of valuable products per unit time and decrease the amounts of undesirable byproducts over the same time frame. The global catalyst market, of which heterogeneous catalysts make up the largest portion, is approximately \$15 billion per year. [8] Many heterogeneous catalysts take the form of dispersed metal nanoparticles on an oxide support. Heterogeneous catalysts are often preferred to homogeneous catalysts (where the catalyst is the same phase as the reactants) for several reasons. First, expensive separation of the catalyst from products and unreacted reactants is not necessary. Second, heterogeneous catalysts can be recovered and recycled (or when their production cost is low as in the case of zeolites, disposed of safely). From a reaction engineering standpoint, heterogeneous catalysts are better for most continuous processes. Heterogeneous reactions also do not necessitate the use of a solvent.

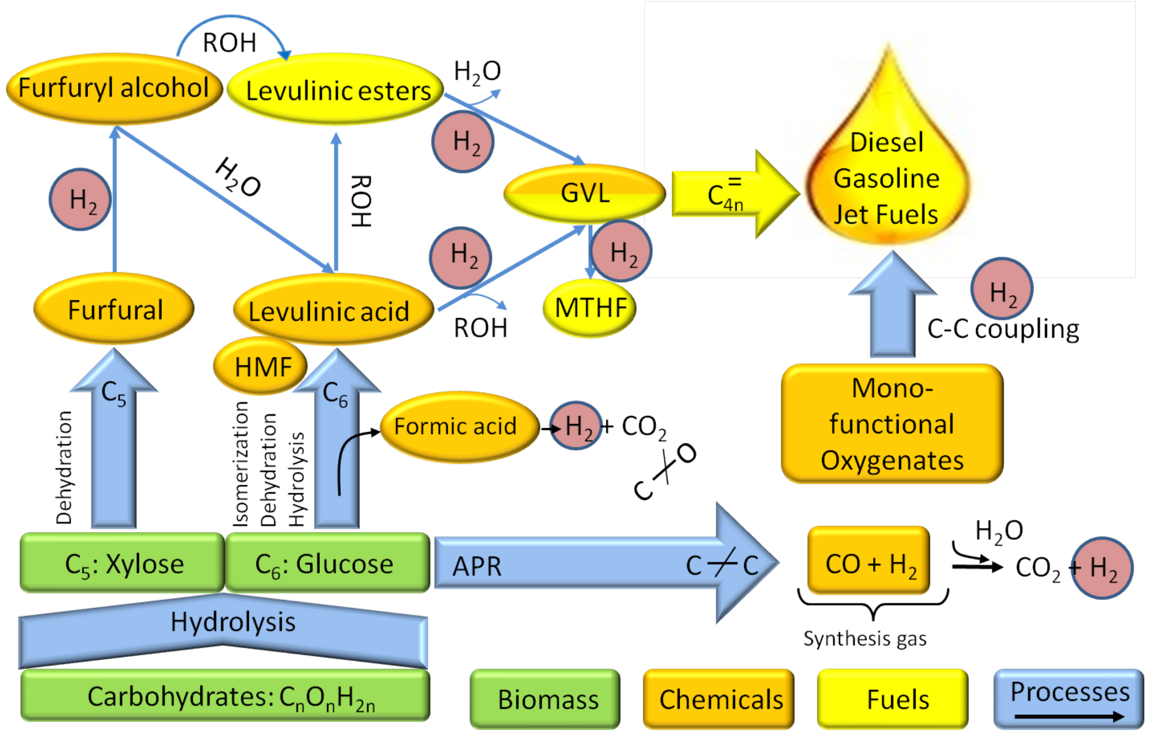

Figure 1.1. Chemical reaction network for the upgrading of biomass-derived carbohydrates to liquid fuels. This network is the focus of the Institute for Atom Efficient Chemical Transformations, a United States Department of Energy Frontier Research Center.

However, heterogeneous catalysts are difficult to develop and use. Catalyst stability (the ability of the catalyst to maintain the maximum reaction rate and desired product selectivity over time) may deteriorate during reactions under harsh conditions, including many biomass upgrading reactions in the above reaction network. It is often difficult to identify the active site(s) (the part of a catalyst that does the work) for a reaction, as heterogeneous catalysts are usually non-uniform. Extensive pore structures of supported heterogeneous catalysts often present difficulties in understanding catalyst structure, the reaction mechanism, and measurement of reaction kinetics due to diffusion or heat transfer issues. All of the above challenges are present for biomass upgrading reactions, as the reactions are often performed at high temperature in aqueous phase on multifunctional catalysts.

Model catalysts, used to approximate real catalytic systems, are simpler versions of catalysts used industrially. Often, solid model catalysts have simplified geometries and contain only some components of a real catalyst, e. g., the metal(s), support, etc. These simplified systems may take the form of metal nanoparticles supported on nonporous supports such as multi-walled carbon nanotubes (MWCNTs), or, simpler still, the effect of the active metal may be modeled by a flat single crystal. Single crystals are models of just one face of a metal nanoparticle, which has a variety of exposed surface faces. Unsupported systems like metal single crystals also eliminate the effect of the catalyst support.

These systems allow one to study adsorption/desorption processes, changes in the catalyst structure as a result of adsorption or other treatments, and the interactions of adsorbates, often in an ultra-high vacuum (UHV) environment. UHV is necessary to study these simple systems for several reasons. Defined as a vacuum of pressure $< 1 \times 10^{-9}$ Torr or less, UHV enables the use of various spectroscopic techniques like electron spectroscopies. The level of contamination is also easier to control in UHV.

More complex forms of model catalysts exist. A metal-on-oxide system may be approximated by the deposition of one or more metals on an oxide single crystal surface. An inverse catalyst may be synthesized by the deposition of an oxide on a metal surface, which can provide additional information about the role of the support in a reaction. An excellent discussion of modeling supported catalysts is given in Reference [9].

For complicated reactions on complicated catalyst systems such as those shown in Figure 1.1, studying reactions on model catalysts can increase understanding of the reaction mechanism and kinetics. This can, in turn, result in better design of real catalysts. Fundamental information gained from such studies not only aids in development of new catalysts for biomass reactions, but also provides information on several fundamental catalytic processes including hydrogenation/dehydrogenation, C-C and C-O bond cleavage, etc. These reactions have wide ranging impact.

1.1 Reactions of Interest

Work in this dissertation involves two reactions in the network shown in Figure 1.1: formic acid decomposition and aqueous phase reforming. Both generate hydrogen for subsequent upgrading steps.

1.1.1 Formic Acid Decomposition

A common byproduct of many biomass upgrading reactions is formic acid. As it relates specifically to the reaction network shown in Figure 1.1, formic acid is produced from the conversion of C5 and C6 sugars to furfural and levulinic acid (LA); it comprises as much as 20% of the reaction products by weight. [7,10] In subsequent reaction steps, LA is hydrogenated to produce γ-valerolactone, a platform chemical for further upgrading to fuels. The requirement for external hydrogen may be partially alleviated by the decomposition of formic acid. [11, 12] Formic acid decomposes catalytically to form hydrogen and carbon dioxide. It may also dehydrate, forming water and carbon monoxide. On Pt, for example, the catalytic decomposition of formic acid produces nearly CO-free H_2. [13, 14] If this decomposition step is performed *in situ*, the need for a LA purification step is also eliminated. Formic acid also holds potential as a hydrogen carrier for direct formic acid fuel cells. [15]

As mentioned above, knowledge gained from studying reactions of simple molecules on metal surfaces has broad impact. In addition to its potential for hydrogen production and storage, formic acid has long been used as a probe of catalytic activity on various surfaces. [16, 17] It is the simplest carboxylic acid, and can act as a model compound for deoxygenation of larger carboxylic acids. Historically, formic acid decomposition on transition metals was used to develop one of the early volcano plots of reaction rate versus a descriptor, in this case, the heat of formation of the bulk metal formate. [17] In this plot, metals to the left of the peak (with lower ΔH_f) exhibit reaction rates lower than those measured on metals at the peak because the adsorption of formic acid is rate-limiting. Metals to the right of the peak (with higher ΔH_f) are slower than the peak rates because the formation or desorption of products is slow. Metals at the top of the volcano have an optimum balance between dissociating reactants and forming products, which was first discussed by Sabatier. [18] This, and similar volcano plots, have been used for the development of bimetallic catalysts for several decades in which two metals are combined to make one catalyst in an attempt to use less expensive metals and maximize catalyst rate and selectivity. [19]

Due to the increasing costs of common catalytic metals like Pt, improvements in experimental techniques, and the ability to study complex catalytic reactions from first principles using computers, some are revisiting the results of Sachtler's classic study, [20, 21] and extending the ideas to new catalytic systems. Formic acid decomposition, then, is being revisited by studies using modern kinetic and spectroscopic techniques and first principles calculations in order to understand the fundamentals of this reaction. Recently, microkinetic models based on density functional theory calculations predict catalyst TORs, selectivities, and reaction mechanisms without the need for experiments. [22, 23] These results are used along with scaling relationships involving energetic descriptors to predict optimum catalyst configurations. Due to limited computational power, these studies often employ single crystal model catalysts. Ideally, kinetic experiments on single crystal surfaces should be used to validate these models. In addition to varying the active metal, changing the exposed single crystal face can predict which structures have the highest rate for a particular reaction. Shape-selective synthesis with an emphasis on controlling the geometry of exposed planes is an emerging area in catalyst synthesis. [24, 25] Chapter 2 of this dissertation focuses on the kinetic measurement of formic acid decomposition on Pt single crystals and polycrystalline foils.

1.1.2 Aqueous Phase Reforming

The catalytic reforming of oxygenated hydrocarbons in liquid water, referred to as aqueous phase reforming (APR), relies on C-C bond scission of C2-C6 oxygenated hydrocarbons and the water-gas shift reaction to produce low-CO streams of H_2. [26–28] APR saves energy by eliminating the vaporization of the hydrocarbon and water, and can be done in a single catalytic step at about 500 K. C-O bond cleavage is an undesired competing pathway which forms light alkanes, unsuitable for use in liquid fuels. Bimetallic Pt-metal catalysts have been shown to improve the H_2 generation rates of APR and alter the product selectivity. [29,30] The search for bimetallic Pt-M (M = transition metal) catalysts that maximize C-C bond scission and H_2 generation rate while simultaneously minimizing unwanted side reactions is ongoing. Chapter 7 of this dissertation outlines the novel synthesis of a model Re/Pt(111) system and its behavior toward probe molecules, and Chapter 8 details the characterization of a Pt-Mo/MWCNT bimetallic catalyst used for APR and hydrodeoxygenation reactions.

1.2 Atomic Layer Deposition for Catalyst Synthesis

Given the ongoing efforts to develop new catalysts for biomass upgrading reactions, focus has turned to how to synthesize these new catalysts. One gas phase technique under investigation for catalyst synthesis is atomic layer deposition (ALD).

1.2.1 Introduction to Atomic Layer Deposition

Atomic layer deposition is a special type of chemical vapor deposition (CVD) process that relies on self-limiting reactions of gas phase precursors with a solid surface. Due to its self-limiting nature, ALD gives superior control over film thickness and excellent conformity, even on irregular geometries. The simplest type of ALD, AB-type, relies on two coreactants: coreactant A, a precursor containing the metal of interest, and coreactant B, which replenishes the functional group necessary for the next ALD cycle. Reactants are dosed sequentially, and the ALD reactor is purged with an inert or vacuum between cycles. Precursor exposure times are on the order of seconds. ALD is typically performed in flow reactors with reactant dosing pressures of < 10 Torr. The technique is used for deposition of a wide range of materials including metal oxides, nitrides, etc; for a complete list, refer to the detailed review by Puurunen. [31]

ALD was developed by two groups independently: the Finnish group led by Suntola applied for the first ALD patent in 1974, and Profs. Aleskovskii and Koltsov in the Soviet Union used an ALD technique to deposit metal oxides in the early 1960s. [32] For more information about the history and development of ALD, refer to References [31] and [33] and references therein. The primary application of ALD has historically been and continues to be microelectronic fabrication. Recently, the semiconducting gate oxide material in metal oxide semiconductor field effect transistors have been synthesized by ALD, which have enabled continued scaling down of device size. [34]. Emerging areas of interest include corrosion prevention [35] and heterogeneous catalyst synthesis, discussed below.

1.2.2 Atomic Layer Deposition in Catalysis

The catalysis community at large has long focused on improving the stability of heterogeneous catalysts, and tuning catalytic function by better controlling catalyst structure during synthesis. Both of these challenges are relevant for biomass upgrading reactions: many upgrading reactions proceed under harsh aqueous phase environments at high temperatures, and fine-tuning catalyst behavior for multiple functions or selectively for one function are appealing, given the complexity of biomass-derived molecules.

For improved catalyst stability, much work has been done on protecting metal nanoparticles from deactivation by sintering and coking using porous ALD-deposited metal-oxide overcoats (see, for instance, References [36–38]). This porous overlayer allows reactants to reach and react with metal nanoparticles on the surface, but prevents sintering of nanoparticles by preventing their diffusion. For some reactions the overcoat has been found to prevent coking, or carbonaceous buildup, by preferentially blocking the most active catalytic sites and/or modifying ensemble size. Superior stability with overcoated catalysts has been demonstrated specifically for biomass conversion reactions. [39]

Gaining better control of the catalyst structure and thus its performance is also an area to which ALD can contribute. Multi-functional catalysts, for instance, often contain more than one active metal. For bimetallic systems, current methods of catalyst synthesis such as successive or co-impregnation form mixtures of particle types. Electroless deposition offers more control than other aqueous-phase preparation techniques, however, suffers from a submonolayer coverage limitation and is unable to easily form well-mixed alloy nanoparticles. [40] ALD offers better control than aqueous phase techniques for a variety of bimetallic systems for synthesis of both core-shell and well-mixed alloy nanoparticles. Through careful choice of ALD co-reactants, processing conditions, and initial functional group coverage (which controls ALD nucleation sites), several ALD cycles can be performed to make dispersed monometallic nanoparticles, then the metal precursor can be changed to grow shells on these nanoparticles, avoiding deposition on the support. Alternatively, the metal ALD precursor can be varied cycle to cycle to form well-mixed alloy nanoparticles. [41, 42]

Understanding how ALD precursors interact with metal and oxide surfaces is one of the top technical challenges of ALD catalyst synthesis currently. As the number of ALD cycles used for catalyst synthesis is often low (< 10), the substrate itself can be thought of as one of the ALD reactants. Learning about ALD surface chemistry in an ALD flow reactor is difficult, as the pressure (few mTorr to 10 Torr) and precursor exposure times (few seconds) limits the number of applicable surface sensitive techniques. Knowledge of the substrate-precursor interaction can be gained by using surface sensitive characterization techniques in UHV. Zaera has advocated for the use of UHV experiments to learn more about the surface chemistry of ALD. [43]

Several chapters of this dissertation are devoted to the use of surface sensitive experiments in UHV and *in situ* environments to learn more about the interaction of ALD reactants with different surfaces. Chapters 4 and 5 detail the interactions of TMA and water with Pd(111) and Pd(111). Chapter 6 looks at the interaction of TMA with Cu(111) and Cu_2O/Cu(111). Chapter 3 details work on using Pd and Cu ALD precursors followed by annealing to form Pd and Cu nanoparticles on $TiO_2(110)$.

2. KINETICS OF GAS PHASE FORMIC ACID DECOMPOSITION ON PLATINUM SINGLE CRYSTAL AND POLYCRYSTALLINE SURFACES

2.1 Abstract

Formic acid dehydrogenation turnover rates (TORs) were measured on Pt(111), Pt(100), and polycrystalline Pt foil surfaces at 800 Torr between 413–513 K in a batch reactor connected to an ultra-high vacuum (UHV) system. The TORs, apparent activation energies, and reaction orders are not sensitive to the structure of the Pt surface, within the precision of the measurements. CO introduced into the batch reactor depressed the formic acid dehydrogenation TOR and increased the reactions apparent activation energies on Pt(111) and Pt(100), consistent with behavior predicted by the Temkin equation. Two reaction mechanisms were explored which explain the formic acid decomposition mechanism on Pt, both of which include dissociative formic acid adsorption, rate limiting formate decomposition, and quasi-equilibrated hydrogen recombination and CO adsorption. No evidence was found that catalytic supports used in previous studies altered the reaction kinetics or mechanism.

2.2 Introduction

Conversion of biomass to liquid fuels and valuable chemicals requires a large hydrogen input. Formic acid, produced as a byproduct of many of these upgrading reactions, can catalytically decompose to produce H_2 and CO_2 or H_2O and CO. On Pt, reported dehydrogenation selectivity is near 100%. [13,14] In this study, the kinetics of formic acid dehydrogenation on Pt(111), Pt(100), and a Pt foil were measured at a total pressure of 800 Torr with formic acid concentration of approximately 1% and temperatures between 413–513 K. TORs did not vary on the surfaces tested within the precision of the measurements. In this work, results obtained here are compared to other formic acid decomposition studies on Pt in the literature and discuss simple reaction mechanisms for formic acid dehydrogenation.

2.2.1 Kinetics of Formic Acid Decomposition on Platinum

Several kinetic studies have been carried out for formic acid decomposition on various Pt catalysts; a review follows. A discussion of extrapolated TORs from these works is given in the discussion section in which they are compared to those measured in this study.

Ojeda and Iglesia reported an activation energy of 72 ± 4 kJ mol^{-1} for Pt/Al_2O_3 in the temperature range 343–383 K. [13] They found that the reaction is zero order with respect to formic acid above formic acid partial pressures of 15 Torr (about 2%) at 353 K; and below 15 Torr the reaction is fractional positive order. They found the dehydrogenation selectivity is near 100%, forming < 10 ppm CO. They observed decreasing HCOOH dehydrogenation TORs on Pt/Al_2O_3 as Pt particle size increased, as observed by TEM. Solymosi et al. [14] studied formic acid decomposition on Pt/C. On 2% Pt/Norit the measured apparent activation energy was 70.7 ± 3 kJ mol^{-1} between 380–425 K. Decomposition was zero order with respect to formic acid at formic acid concentrations of 5–6%. Selectivity to hydrogenation was between 98–99%.

Chun et al. [44] measured rates on Pt_4-cluster/SiO_2 and conventional Pt/SiO_2 catalysts. They measured an apparent activation energy of 69 kJ mol^{-1} on the Pt_4-cluster catalyst at 100% dehydrogenation selectivity in the temperature range 273–288 K (the freezing point of formic acid is 281.6 K). On the conventional Pt/SiO_2 catalyst, decomposition proceeded through both pathways, with measured activation energies of 41 kJ mol^{-1} for dehydrogenation and 73 kJ mol^{-1} for dehydration between 363–443 K. Activation energies on the Pt_4 cluster catalyst for deuterium labeled formic acid compounds were measured to be 54, 49, and 24 kJ mol^{-1} for HCOOD, DCOOH, and DCOOD, respectively. Block and Vogl measured an activation energy of 66 kJ mol^{-1} on a Pt catalyst. [45] A transition from fractional positive formic acid order to a zero order regime was also observed.

2.2.2 Mechanistic Insights into Formic Acid Decomposition on Platinum

Insights into the decomposition mechanisms of formic acid on Pt have been gained through studies on technical catalysts, single crystals studied in UHV, and first principles calculations. These works are reviewed here.

For technical catalysts work, on Pt/Al_2O_3, Ojeda and Iglesia observed a normal kinetic isotope effect with DCOOH and DCOOD, but not HCOOD; that is, ${}^{r_H}/{}_{r_D} > 1$ for DCOOH and DCOOD, but was close to unity for HCOOD. [13] This suggests that formate C-H (or C-D) bond activation is rate determining.

Many studies have been performed on Pt single crystals in UHV. Avery studied formic acid on clean Pt(111) with combined TP and HREELS experiments. [46] Formic acid adsorbs as a multilayer at 130 K with coverage of 3-5 Monolayers (ML). At 170 K, the multilayers desorb, leaving behind bidentate bridging formates, observed by HREELS. The only products from decomposition on clean Pt(111) were H_2 (T_p = 370 K) and CO_2 (T_p = 260 K). CO was observed in the TP experiment, but was attributed to the back or sides of the crystal or the Pt support, as no CO was observed on the crystal surface in HREELS. The existence of bridging formates on Pt(111) following desorption of multilayer formic acid was confirmed by Columbia and coworkers. [47] Columbia and Thiel also studied formic acid decomposition on clean Pt(111). [48] For formic acid exposures at 100 K of less than 0.3 L, only CO_2 (T_p = 260 K) and H_2 (T_p = 350-400 K) were observed. From HREELS, the formic acid multilayers that adsorbed at 130 K had a molecular orientation parallel to the crystal surface. At 150 K, the loss assigned to out of plane OH bending of the molecular acid was attenuated, and new losses appeared which were attributed to the bridging formate. By 170 K the molecular acid losses disappeared completely. Abbas and Madix also studied formic acid decomposition on Pt(111). [49] After saturation dosing of DCOOH at 195 K and heating, they observed H_2, HD, and D_2 (T_p = 321, 309, and 313 K, respectively), CO_2 (T_p = 265, 361, and 426 K; main peak is 265 K), H_2O and D_2O (265 and 295 K), and CO (473 and 531 K). CO and water species were attributed to defect sites (discussed below). No adsorbed C or O was observed by AES after heating to 600 K. The bidentate bridging formates observed in the above studies that incorporated HREELS formed a $(\sqrt{3} \times \sqrt{3})$R30° LEED pattern on Pt(111) between 170–260 K after exposure to formic acid at 100 K, as observed by Jensen. [50]

Hofmann et al. [51] observed bridging formates in HREELS on Pt(110)-(1×2) after adsorption at 155 K. DCOOH was adsorbed on Pt(110) at 200 K. [52] Products observed were D_2O (260 K), H_2O, CO_2 (260 K), H_2, D_2, and CO. No reaction products were observed from formic acid decomposition on Pt(100)-hex. [53] Following 0.3 mPa·s exposure at 100 K, only multilayer and monolayer desorption were observed at 155 and 200 K, respectively. No evidence of CO, CO_2, or H_2 evolution was observed up to 700 K. The hex reconstruction was still observed by LEED following the TP experiment.

Several UHV studies probed the effect of coadsorbates on the formic acid decomposition mechanism. Avery also studied formic acid with coadsorbed atomic oxygen on Pt(111). [46] In addition to H_2 and CO_2 at the same T_p as observed on clean Pt(111), H_2O (T_p = 180 K) was also generated. Avery also identified formates on Pt(111)-O_{ads}. [54] HREELS features were the same for pre-adsorbed O surfaces as they were for the clean surface, but more intense, indicating 6 to 7 times more adsorption on the O-predosed surface. Similarly, Columbia et al. observed CO_2, H_2O, and CO_2 desorption from Pt(111)-O_{ads}, and found that higher formic acid exposures were required in order to generate H_2 in the presence of O_{ads} compared to clean Pt(111). [55]

Following their work on the clean Pt(111) surface, Abbas and Madix studied formic acid decomposition on (2×2) and $(\sqrt{3} \times \sqrt{3})$R30° structured overlayers of S on Pt(111). [49] On both surfaces, the only products after dosing DCOOH at 200 K and heating to 600 K were CO_2 and the hydrogenic species H_2, D_2, and HD, whereas CO and water containing species were also observed from the clean Pt(111) surface. This was attributed to preferential S adsorption on defect sites.

Columbia and Thiel studied formic acid decomposition on CO-dosed Pt(111). [48] Adsorbed CO was found to inhibit the ability of Pt(111) to decompose the formate intermediate, as H_2 and CO_2 yields decreased as CO adsorption increased, and desorption of molecular acid increased. H_2 and CO_2 yields did not track each other as a function of CO coverage, however, so the presence of CO likely introduces a new decomposition pathway. HREELS indicated a broad low frequency feature at high CO coverages, indicative of a carbonaceous residue which may be liked to this alternate pathway.

On Pt(100), which was unreactive as clean Pt(100)-hex, Kizhakevariam and Stuve studied co-adsorption of ^{18}O. [53] ^{18}O was adsorbed at 500 K, and the sample was cooled to 100 K for HCOOH adsorption. Reaction-limited CO_2, H_2O, and $H_2{}^{18}O$ desorbed at T_p = 310 K. All CO_2 desorbed as mass 44 (no ^{18}O-containing CO_2 species), implying that the O-C-O linkage was unbroken. No CO or H_2 was observed. ^{18}O was left in excess on the surface following desorption of reaction products and desorbed as $^{18}O_2$ at approximately 750 K.

First principles calculations have also been used to probe this reaction. Gao et al. [56] studied the gas phase decomposition on clean and H_2O covered Pt(111). They found that, in agreement with the UHV literature, the reaction pathway involving decomposition of a bridging formate intermediate and hydrogen recombination is the most likely reaction pathway. Coadsorbed water does not alter the pathway but promotes O-H and C-H bond scission. Yoo et al. [22] determined reaction energetics on a variety of flat and stepped single crystal transition metal surfaces using DFT. These parameters were used to develop a microkinetic model, and calculated turnover rates were plotted as functions of CO and OH adsorption energies to form a 3-dimensional volcano plot. They predicted a HCOOH decomposition TOR of approximately 10 s^{-1} on Pt(111) at 400 K and P = 1 bar with near 100% selectivity to H_2.

The objectives of this project were to determine structure sensitivity of formic acid decomposition reaction on low-index Pt single crystals. This required a kinetic study of formic acid decomposition on low-index Pt single crystals. The kinetic study included measurement of CO_2 turnover rates (TOR), determination of activation energies, reaction orders for reactants and products, and rate constants under a variety of conditions. Briefly, it was found that formic acid decomposition TOR is not sensitive to the structure of the catalyst for Pt(111), Pt(100), and a polycrystalline foil sample.

2.3 Methods and Materials

Kinetic experiments were performed in a 1.4 L gas phase stainless steel batch reactor connected to a UHV chamber via a welded metal bellows transfer arm allowing for sample transfer between the two chambers without air exposure. This apparatus has been described previously. [57, 58] The batch reactor was pumped with a turbomolecular pump in order to reach pressures $< 1 \times 10^{-6}$ Torr for sample transfer to the UHV chamber. The UHV chamber was equipped with an ion gun (PHI 04-161) and resistive heating for sample preparation, and a PHI 15-255G double pass cylindrical mirror electron energy analyzer equipped with an electron gun for X-ray photoelectron spectroscopy (XPS) and Auger electron spectroscopy (AES), and low energy electron diffraction (LEED) (OCI Vacuum Microengineering BDL800IR-ISH-FIX) for sample characterization before and after reaction. The UHV chamber was also equipped with a UTI-100C quadrupole mass spectrometer. The base pressure of the UHV chamber was ca. 5×10^{-10} Torr.

2.3.1 Pt Single Crystal and Foil Samples

Pt(100) and Pt(111) single crystals (Princeton Scientific) with orientation accuracy $< 0.1°$ were mounted to the sample holder via spot welded stainless steel pins on each side of the crystal. Current was passed directly through the pins for resistive heating. A Eurotherm 2408 temperature controller controlled the temperature. Crystal temperature was measured by a K-type thermocouple spot welded to either the side of the single crystal or the back of the foil. Each sample was remounted and the thermocouple leads re-welded several times during a campaign of kinetic experiments.

Samples were prepared before each series of experiments by repeated cycles of Ar^+ sputtering (5×10^{-5} Torr Ar, 1–2 keV electrons), O_2 treatment (1×10^{-6} to 2×10^{-5} Torr, 773–1073 K), and annealing in vacuum at 1073 K. Samples were checked for contaminants by AES or XPS after cleaning to confirm that no contaminants other than C or O were present on the sample surface. C and O contaminants from residual formic acid vapor were unavoidable. A detailed discussion is given in the results section. Single crystal samples were checked by LEED to ensure that the expected surface construction was present. Hexagonal (111)-(1×1) and square (100)-(1×1) diffraction patterns were observed on the Pt(111) and (100) crystals after the standard cleaning procedure, respectively. For Pt(100), as noted above, residual contamination lifted the hex reconstruction. [59]

2.3.2 Kinetic Experiments and Data Analysis

Reaction gases and formic acid vapor were introduced to the batch reactor one at a time via stop valves on the gas manifold. The manifold was pumped by a scroll pump after dosing each gas. An MKS Baratron pressure transducer with ± 0.1 Torr accuracy was used to monitor the amount of gas introduced to the reactor. Formic acid (Thermo Scientific, 99+%) and water (Millipore, 18.2 MΩ resistivity) were introduced from the vapor space in sealed glass containers containing 1-2 mL of the liquid. Each liquid was degassed before reaction by several cycles of freeze-pump-thaw. Other gases used were CO (Research purity, Matheson, 99.998%), H_2 (Praxair, UHP, 99.999%), and N_2 (Research grade, Airgas, 99.9997%). Gas dosing order was typically formic acid, water (if dosed), H_2, CO, and balance N_2 for a total pressure of 800 Torr. For some runs CO was dosed before H_2, but this did not have a measurable impact on the CO_2 TOR. After dosing, gases were circulated in two loops by two bellows pumps (Metal Bellows, MB-21). One circulation loop included a Nicolet Nexus 670 Fourier transform infrared (FTIR) spectrometer with gas cell for analysis. Gases were permitted to mix for approximately 5 minutes before data collection began to ensure a well-mixed system.

2.3.3 Kinetic Experiments

CO_2 turnover rates (TORs) were calculated by measuring the CO_2 evolution monitored by the gas phase asymmetric stretching mode IR peak at 2349 cm^{-1}. A data point from 25 averaged spectra was collected approximately every 10 s using Omnic version 7.2a data acquisition software. CO_2 concentration was related to absorbance using a calibration curve prepared by measuring the CO_2 absorbance peak area for several dilutions of a $500 \pm 2\%$ ppm CO_2 in N_2 gas mixture. Batch reactor walls were kept at room temperature during all experiments. The change in bulk reaction gas temperature due to heating of the sample was negligible, as the formic acid dimer to monomer ratio remained constant during reaction. This was possible because the recirculation flow kept the volume of heated gas near the sample small and the heat added to the gas by the sample was lost through the walls of the reactor and recirculation system.

CO_2 TORs were calculated by numerically differentiating batch reactor data and were normalized to the calculated geometric Pt atom density of the front face of each single crystal: 1.5×10^{15} and 1.3×10^{15} Pt atoms cm^{-2} for Pt(111) and (100), respectively. Pt atom density on the Pt foil surface was assumed to be 1.5×10^{15} cm^{-2}. The backsides of each sample were assumed to be inactive because they were neither polished nor sputter cleaned. Reported TORs were collected following cleaning of the sample and then after at least one run of half an hour or more. The TOR usually drops considerably after this first run then remains roughly constant for subsequent runs. A detailed discussion is given in the results section.

Activation energy and reaction order runs were performed multiple times on different days in the stable kinetic regime. For activation energy measurements, temperature was varied over the relevant temperature range dwelling at each point for 2 to 5 minutes. Temperatures were varied randomly, and at least the final point was collected at the same temperature as the first point in order to account for catalyst deactivation and hysteresis. Because reactions were run in batch mode, gases were recharged for each point for an order collection experiment. Concentrations for reaction order experiments were varied randomly and the first point was always repeated at the end of the series to account for catalyst deactivation and hysteresis. Formic acid reaction orders are plotted against the natural log of the effective formic acid monomer concentration which takes into account the presence of dimer in the gas phase. The partial pressures of the formic acid monomer, P_m, and dimer, P_d, fractions are expressed in Equation 2.1:

$$K = \frac{P_m^2}{P_d} = 10^{10.755 - \frac{3090}{T}} \tag{2.1}$$

where K is the equilibrium constant in Torr and T is the temperature in Kelvin. [60,61] Equation 2.1 was used to calculate the partial pressures of monomer and dimer present in the gas phase.

2.3.4 *Ex situ* Characterization

AES spectra were collected using 3 keV incident electrons in differential mode using a PHI lock-in amplifier. XPS spectra were collected using a non-monochromated Mg source (hν = 1253.6 eV) with constant pass energy = 50 eV. The binding energy scale was calibrated using Au 4f$_{7/2}$ and Cu 2p$_{3/2}$ peaks at 83.8 eV and 932.4 eV, respectively, taken from a sputter cleaned sample containing Au and Cu foils. The fwhm of the Au $4f_{7/2}$ line was 1.36 eV. Spectra were analyzed using CasaXPS version 2.3.16 PR 1.6 (Casa Software Ltd.). To calculate coverage from XPS results, Fadleys approach was followed, [62] which assumes a non-attenuating adlayer at fractional coverage. Details are given in Appendix A.

2.4 Results

2.4.1 Analysis of Gas Phase IR Spectra

Figure 2.1 shows FTIR spectra before and after 52 minutes of reaction on Pt(100) at 473 K. The only observed product of formic acid decomposition is CO_2 as seen by the increase in absorbance of the asymmetric CO_2 stretching peak at 2349 cm^{-1}. Quantification of CO and H_2O, products of dehydration, was not successful. CO could not be quantified in any kinetic experiments for which CO was co-fed. For experiments where CO was not co-fed, no intensity change was observed in the C=O stretching region at 2143 cm^{-1}. The limit of detection for CO was about 0.5 ppm. For all experiments, dehydrogenation selectivity was $> 99\%$. Asymmetric stretching features of water between 1400–1700 cm^{-1} were present in background spectra barely above the noise level due to impurity of the formic acid (99+% pure), these were not quantified, and did not change during reaction. A typical FTIR spectrum of the contents of the gas cell before and after reaction are given in Figure 2.1 and IR assignments are given in Table 2.1.

2.4.2 System Validation

To ensure that measured rates resulted from formic acid decomposition on the Pt surface, two blank experiments were performed. In the first blank experiment the CO_2 TOR was measured on a piece of 316 stainless steel (SS) foil spot welded between the two heating leads. The areal rate at 493 K on the 316 SS blank was approximately 5×10^{-10} moles CO_2 cm^{-2} s^{-1}, while the measured areal rates on Pt(111) and Pt(100)

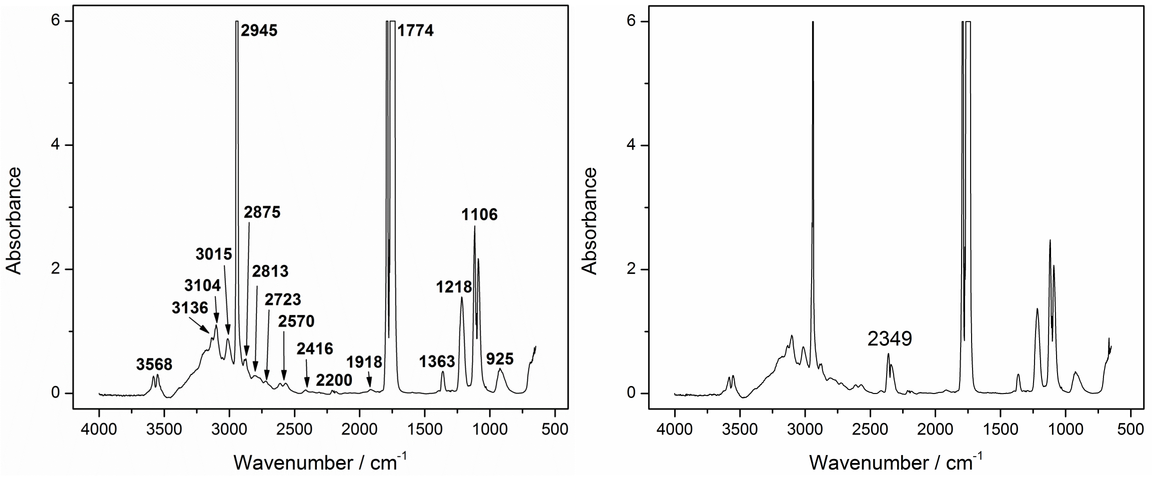

(a) 0 min.

(b) 52 min.

Figure 2.1. FTIR spectra of reactor charged with 1 Torr HCOOH, 800 Torr total pressure (balance N_2) at start of reaction on Pt(100) and after 52 min. at 473 K.

under the same conditions were greater than 6×10^{-9} and 8×10^{-9} moles CO_2 cm^{-2} s^{-1}, respectively. The areal rate of 5×10^{-10} moles CO_2 cm^{-2} s^{-1} represents a maximum rate on surfaces other than the active Pt for a reaction with catalyst present, as the blank is replaced with the actual catalyst, so only decomposition on the SS heating pins would lead to an error in the rate measurement on SS surfaces.

In the second validation experiment the background activity of the batch reactor was measured with a Pt catalyst present. With Pt(111) loaded, the reactor was charged with gases used under standard conditions except for formic acid (15 Torr H_2, 15 Torr CO, 800 Torr total, balance N_2). At 493 K, the measured CO_2 formation TOR on Pt(111) was approximately 0.05 molecules CO_2 (Pt atom)$^{-1}$ s^{-1}. Under the same conditions with 5 Torr formic acid present, the average TOR on Pt(111) was 2.6 ± 0.6 (Pt atom)$^{-1}$ s^{-1}.

The rate reported throughout this work is the rate of formation of CO_2. Direct calibration and measurement of CO_2 peak area instead of using formic acid peaks (both monomer and dimer contributions) is a more straightforward route for calculation of the decomposition TOR. The formic acid decomposition TOR was measured for comparison to the CO_2 TOR for an experiment with 1 Torr initial pressure of formic acid ($P_{H_2} = 15$ Torr, Total Pressure 800 Torr, balance N_2). The CO_2 TOR calculated for this run at 473 K was 1.80 molecules CO_2 (Pt atom)$^{-1}$ s^{-1}. The decomposition TOR of formic acid was measured to be 1.77 molecules formic acid (Pt atom)$^{-1}$ s^{-1}, calculated by the decrease in the ν(C-O) peaks for monomer and dimer at 1106 and 1218 cm^{-1}, respectively, where concentrations of monomer and dimer were calculated using Equation 2.1, indicating that generation of CO_2 can be fully attributed to formic acid decomposition. Additionally, the dehydrogenation rate of the formic acid monomer and one half the rate of the dimer for this experiment were both equal to ca. 0.6 s^{-1} (resulting in the total overall rate of 1.8 s^{-1} reported above by adding 2 times the dimer TOR to the monomer TOR), indicating that formic acid dimers readily decomposed forming two monomers near or on the hot catalytic surface.

Internal heat and mass transfer limitations were not present, as the single crystals and Pt foil were non-porous. Based on the data shown below in Figure 2.5 and data gathered previously on this system, it is unlikely that external heat and mass transfer limitations are affecting the rate. Smeltz et al. [58] measured a TOR of 0.34 ± 0.02 s^{-1} for NO oxidation on Pt(111) using the same reactor system at 573 K, and verified that the rate of mass transfer to the surface was at least one order of magnitude higher than the rate of reaction using reaction gas mixtures of < 100 ppm for NO and NO_2. Not only are the gas concentrations in this study much higher (with the exception of CO_2), but similar TORs were observed at 413 K under the conditions used in Figure 2.5b on Pt(100)(red line, TOR = 0.37 s^{-1}). In the same activation energy run, TORs as high as 3.45 s^{-1} were measured, and all points fell on the same line.

The variability in TOR due to thermocouple mounting position on the Pt single crystals was found to be much less than the day-to-day variability in measured TOR, as the TOR at standard conditions and other kinetic parameters (activation energy, reaction orders) were collected several times over the course of several months during which time the sample was remounted many times.

2.4.3 Rate Stabilization

Supported catalysts in flow reactors are typically subjected to long stabilization periods under reaction conditions before kinetic measurements begin. This is not possible for batch reactors. Therefore, the TOR was permitted to stabilize during several consecutive runs before collecting TORs reported for kinetic parameters. For kinetic experiments on low surface area metal single crystals, the factor most affecting TOR variability is likely contamination of the surface by species left after reaction from either the decomposition mechanism itself or transport of external contaminants in the reaction chamber to the crystal surface. These external contaminants may arise from chamber or sample holder contamination, contamination of the reaction gases, or diffusion of contaminants from the bulk of the single crystal to the surface.

Contamination was monitored before and after experiments using XPS and/or AES. Prior to reaction, C and O were already present on the Pt surfaces. Transfer to the reactor introduced both C and O on the surface of the single crystal. Due to poor control of C and O contamination before a reaction, TORs collected on a completely C- and O-free surface (according to AES) were not reproducible. C and O coverages increased on all catalysts after the first 30 minutes of reaction following cleaning, and then remained constant for subsequent reactions. From XPS, stabilized coverages of C and O ranged between 1–3 ML and 0.4–0.6 ML, respectively, on Pt(111) and Pt(100) surfaces. Typical C and O coverages during several consecutive reactions are plotted in Figure 2.2.

Other contaminants detected after some reactions were Cu and S. Cu is most likely associated with migration of Cu from the sides of the single crystal from spot welding with Cu electrodes, as the amount of Cu present after several runs qualitatively tracked with the number of times a single crystal had been spot welded to the sample

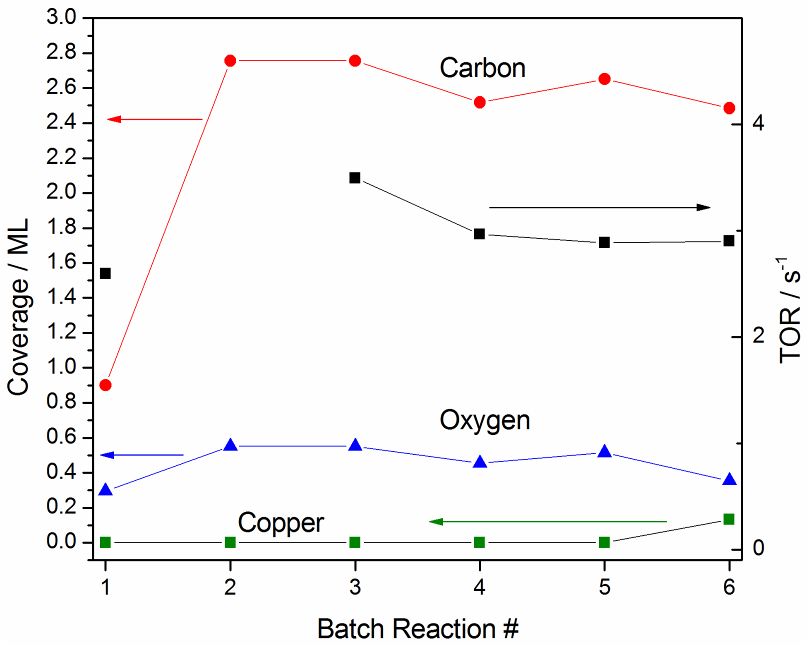

Figure 2.2. Carbon (red circle), oxygen (blue triangle), and copper (green square) contaminant coverages from XPS plotted against reaction number for a series of consecutive reactions on Pt(111). Plotted on the right y-axis is the CO_2 TOR (black square). Reaction conditions were 5 Torr HCOOH, 15 Torr H_2, 15 Torr CO, 800 Torr total (balance N_2), T = 493 K.

holder. Above the limit of detection for both AES and XPS, Cu does not affect the TOR more than the run-to-run variability. From XPS, Cu coverage did not exceed 0.2 ML. However, it should be noted that if the Cu were affecting the rate, it might not need to migrate to the front side of the crystal. In fact, trace Cu was detected on the stainless steel blank sample, which may explain at least some of the background activity of this sample.

S contamination was sometimes observed by AES, but was detected by XPS only once after a reaction with contaminated water. From the high resolution XPS region scan following this reactions, the S coverage was approximately 0.2 ML. From this core level scan, the limit of detection was calculated to be approximately 0.07 ML using standard procedures in the CasaXPS software. S coverage estimation for small amounts of sulfur is difficult from AES alone due to overlap of Pt NNN and S LMM peaks at a kinetic energy of ca. 150 eV, so from this calibration method typical S contamination coverages were estimated to be ≤ 0.07 ML.

In general, the TOR qualitatively tracks most closely to the coverages of carbon and oxygen. For runs occurring within the first 30 minutes of cleaning, the rate is usually higher than subsequent runs for which carbon and oxygen coverages have stabilized. The rate decreases by about 2 times between the first run and subsequent runs when the rate has stabilized. This type of deactivation is not unprecedented in this system. [58] Uncorrected peak-to-peak intensity ratios from AES support this assertion. In Figure 2.3, TORs are plotted for several consecutive batch reactions on Pt(100), and AES peak intensity ratios for the labeled points are given in Table 2.2. Qualitatively, the rate does not track with S or Cu for the points labeled, as the difference in S_{152}/Pt_{168} and Cu_{920}/Pt_{168} intensity ratios are large before and a few runs after cleaning, yet the rate is nearly the same.

Within a run, the initial rate is stable as evidenced by a plot of CO_2 concentration versus time, shown in Figure 2.4. Numerically differentiating the data and converting to a TOR yields a slope standard error that is approximately 3 orders of magnitude smaller than the TOR, a typical slope standard error for a plot of CO_2 concentration versus time within a run. This error, usually on the order of 0.005 s^{-1}, is negligible compared to the day-to-day and run-to-run variability in TOR (± 0.6 and ± 1.0 s^{-1} for Pt(111) and Pt(100), respectively). Conversion of formic acid was kept below 10%, usually between 1-5%, for each run to ensure that the change in concentration of each gas phase species is much smaller than that species total concentration.

2.4.4 Kinetics

Turnover rates (TORs) for Pt(111) and Pt(100) are normalized to the calculated number of Pt atoms on ideal Pt(111)-(1×1) and (100)-(1×1) surfaces, equal to 1.5×10^{15} and 1.3×10^{15} atoms cm^{-2}, respectively. Normalized TORs, apparent activation

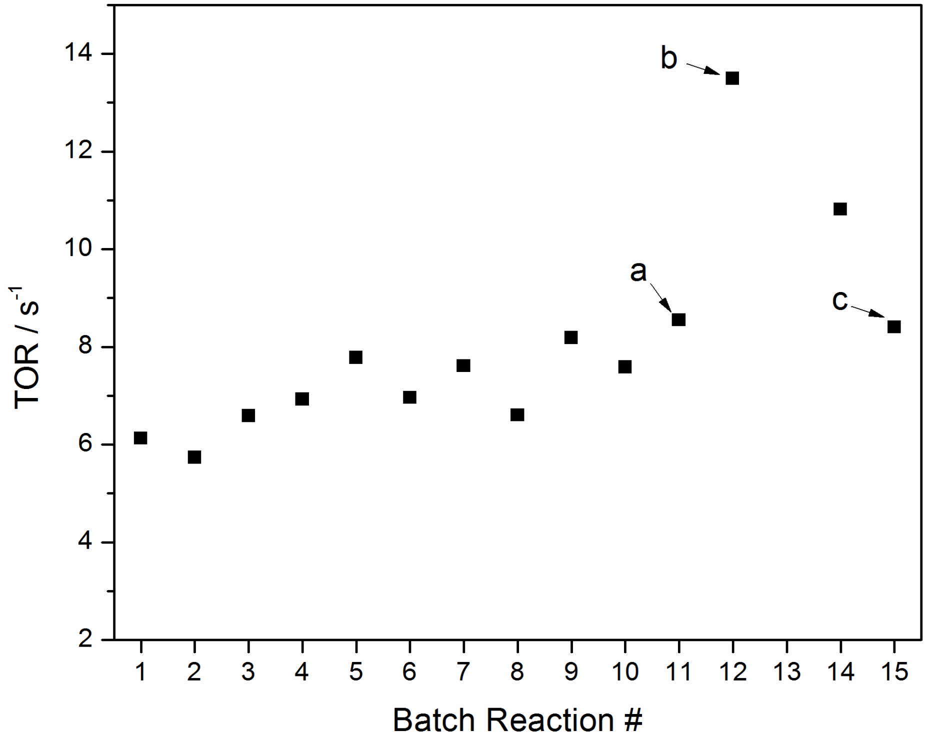

Figure 2.3. CO_2 TOR for a series of consecutive batch reactions on Pt(100). The sample was cleaned by Ar^+ sputtering and annealing at 1073 K at the point labeled (b). Reaction conditions were 5 Torr HCOOH, 15 Torr H_2, 15 Torr CO, 800 Torr total (balance N_2), T = 503 K.

energies, and reaction orders for experiments carried out at standard conditions (5 Torr FA, 15 Torr H_2, 15 Torr CO, 800 Torr total, balance N_2, T = 493 K) are summarized in Table 2.3. The error in TOR on all catalysts was large on a day-to-day basis: average TORs for Pt(111) and Pt(100) were 2.6 ± 0.6 and 3.7 ± 1.0 molecules CO_2 (Pt atom)$^{-1}$ s^{-1}, respectively. The areal rate on Pt foil was measured to be $(7.5 \pm 5.0) \times 10^{-9}$ moles CO_2 cm^{-2} s^{-1}, compared to $(6.4 \pm 1.5) \times 10^{-9}$ and $(8.1 \pm 2.2) \times 10^{-9}$ for Pt(111) and (100), respectively.

Average apparent activation energies, E_{app}, at standard conditions were 86 ± 11, 102 ± 14, and 94 ± 12 kJ mol^{-1} for Pt(100), (111), and foil, respectively, where the error is one standard deviation of E_{app} values calculated between runs. Runs used to

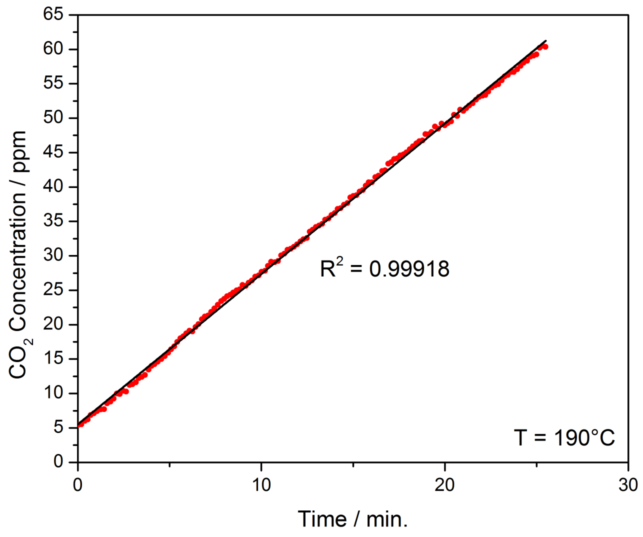

Figure 2.4. Plot of CO$_2$ concentration versus time for a typical batch reaction.

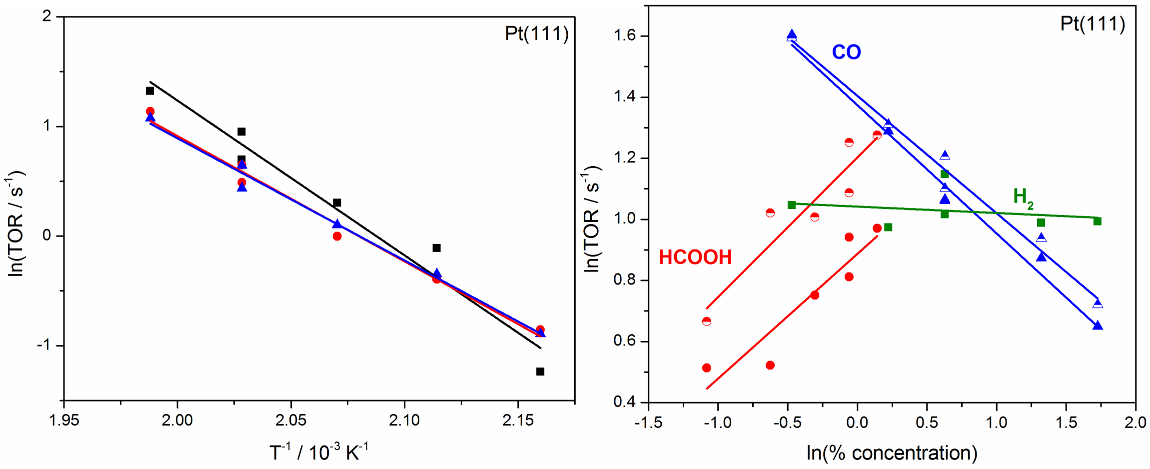

(a) Arrhenius Plots

(b) Reaction Orders

Figure 2.5. (a) Arrhenius plots for formic acid decomposition on Pt(111). Conditions: 5 Torr HCOOH, 15 Torr H$_2$, 15 Torr CO, 800 Torr total (balance N$_2$). (b) HCOOH, CO, and H$_2$ reaction order plots on Pt(111) at T = 493 K.

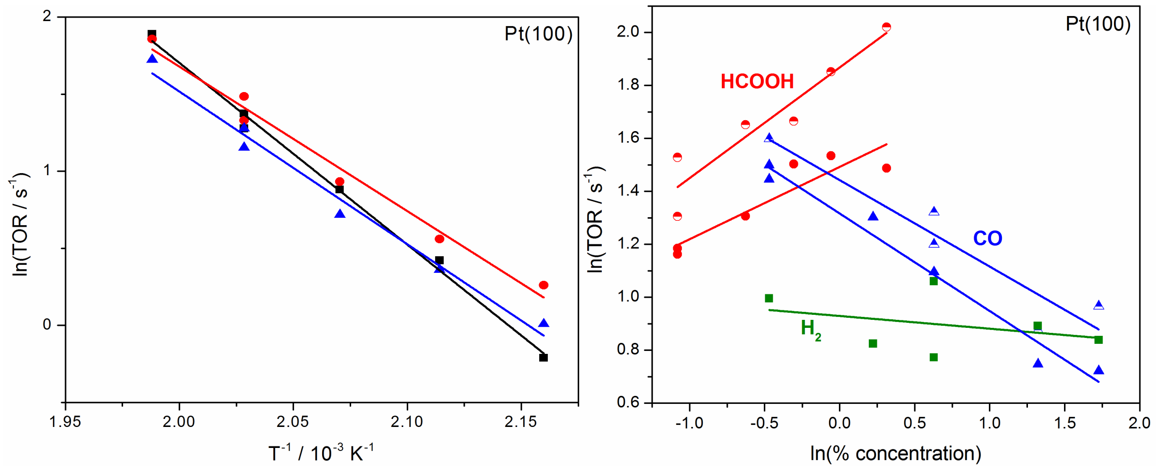

(a) Arrhenius Plots

(b) Reaction Orders

Figure 2.6. (a) Arrhenius plots for formic acid decomposition on Pt(100). Conditions: 5 Torr HCOOH, 15 Torr H_2, 15 Torr CO, 800 Torr total (balance N_2). (b) HCOOH, CO, and H_2 reaction order plots on Pt(100) at T = 493 K

calculate the average values of E_{app} at standard conditions are shown in Figures 2.5 and 2.6 for Pt(111) and Pt(100), respectively.

The average formic acid reaction orders were 0.35±0.10, 0.43±0.03, and 0.35±0.15 for Pt(100), Pt(111), and Pt foil, respectively. These orders are reported with respect to the effective formic acid monomer concentration, which is calculated by addition of the monomer concentration predicted by Equation 2.1 to two times the dimer concentration predicted by Equation 2.1. Errors reported for reaction orders represent one standard deviation between runs. Measured CO orders were -0.35 ± 0.03, -0.40 ± 0.03, and -0.43 ± 0.05 on the same surfaces, and H_2 was approximately zero order on all surfaces. H_2O was found to be zero order on Pt(100) and Pt(111), and CO_2 was zero order on Pt(100) using initial CO_2 concentrations less than 200 ppm. Typical reaction order plots for HCOOH, CO, and H_2 on Pt(111) and Pt(100) are given in Figures 2.5 and 2.6, respectively.

Experiments to measure kinetics were also performed on Pt(111) and Pt(100) using lower initial CO partial pressures (standard pressure of 2 Torr). Kinetic pa-

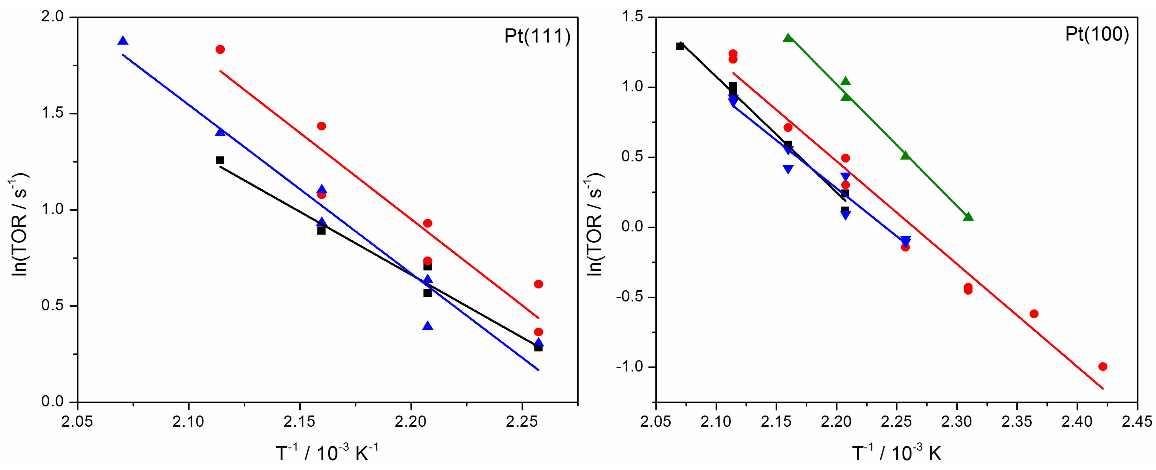

(a) Arrhenius Plots, Pt(111)

(b) Arrhenius Plots, Pt(100)

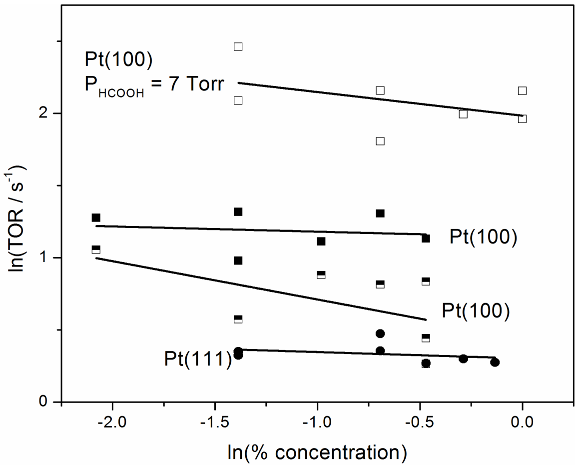

(c) Reaction Orders, Pt(111) and (100)

Figure 2.7. Apparent activation energies and CO reaction orders collected on Pt(111) and Pt(100) for low initial CO concentrations. (a) Arrhenius plots for formic acid decomposition on Pt(111). Conditions: 5 Torr HCOOH, 2 Torr H_2, 2 Torr CO, 800 Torr total (balance N_2). (b) Arrhenius plots for formic acid decomposition on Pt(100). Conditions: 5 Torr HCOOH, 2-15 Torr H_2, 2 Torr CO, 800 Torr total (balance N_2). (c) CO Orders collected on both Pt(111) and Pt(100). Conditions were 5 Torr HCOOH, 2 Torr H_2, 800 Torr total, T = 463 K unless otherwise noted.

rameters at these reaction conditions are summarized in Table 2.4. Average apparent activation energies on Pt(111) and Pt(100) at these conditions, plotted in Figure 2.7, were 67 ± 11 and 65 ± 7 kJ mol^{-1}, respectively. Under these conditions, the CO reaction order was approximately 0, as shown in Figure 2.7.

2.4.5 Characterization with XPS

UHV-XPS was used in an attempt to identify surface species left after a reaction and to check the oxidation state of the Pt substrate. The spectra showed that only C and O species were left after a reaction, in addition to the Cu and S contaminants described above. The Pt $4f_{7/2}$ line had a BE of 70.9 eV before and after reaction, assigned to metallic Pt, [68] indicating that the Pt oxidation state was unchanged during reaction. In the C 1s region, it was not possible to differentiate C from formic acid contamination in the background and C left from the reaction. On all surfaces, a peak at about 284.3 eV was observed before and after reaction, assigned to isolated C, chain carbon, or graphitic carbon, which have been reported to produce C 1s BEs of 283.8, 284.1, and 284.8 eV, respectively. [69] After some runs, another peak at around 286 eV was observed, but it was unclear if this peak, assigned to CO-containing species, was left from a true reaction intermediate or re-adsorption of residual gases during transfer of the single crystal. Other than observing accumulation of C and O during the first reaction after cleaning, *ex situ* XPS did not provide additional clues regarding the formic acid decomposition pathway.

2.5 Discussion

Measured apparent activation energies for HCOOH:CO concentration ratios < 1 (CO partial pressure = 15 Torr) on the Pt surfaces tested range from 86 ± 11 kJ mol^{-1} for Pt(100) to 102 ± 14 kJ mol^{-1} on Pt(111), with Pt foil having an intermediate activation energy of 94 ± 12 kJ mol^{-1} under the standard conditions used in this study. In all cases, these activation energies are higher than those reported in the literature for other kinetic studies on Pt-containing catalysts for formic acid decomposition. Reported values range between 41–72 kJ mol^{-1}. [13,14,44,45] However, when the initial CO partial pressure was decreased to 2 Torr from 15 Torr, the measured apparent activation energies on Pt(111) and Pt(100) dropped to 67 ± 11 and 65 ± 7 kJ mol^{-1}, respectively, which fall within the range of reported literature values. Furthermore, fractional positive formic acid order values measured in this study are in agreement with a fractional positive order reported for formic acid partial pressures of less than ca. 15 Torr on Pt/Al_2O_3. [13]

Direct comparison of TORs measured in this study to those published for supported Pt catalysts is not possible due to differences in reaction conditions. Nevertheless, some comparisons can be made. Ojeda et al.
citeOjeda:2009 found that for Pt/Al_2O_3, the TOR decreases with increasing particle size. The turnover rate at their largest particle size, 8 nm, is approximately 1.2×10^{-2} molecules HCOOH decomposed per surface metal atom per second at 353 K (30 Torr HCOOH). Extrapolating to 463 K using their measured E_{app} of 72 kJ mol^{-1} measured over the range 343–383 K yields a TOR of 4.1 s^{-1}. Extrapolating the TOR measured by Solymosi at 423 K on Pt/C to 463 K yields a TOR of 2.1 s^{-1} using their reported E_{app} of 70.7 kJ mol^{-1}, measured in the range 380–425 K in ca. 38–46 Torr formic acid. For comparison, the average TORs on Pt(111) and Pt(100) for 2 Torr initial CO partial pressure in 800 Torr total pressure at 463 K are 2.3 ± 0.8 and 2.4 ± 1.0 s^{-1}, respectively, but these TORs were collected in the fractional formic acid order regime whereas the studies above measured kinetics in the zero order regime. Extrapolation to the zero-order regime was not performed.

The goal of this work is not to present a comprehensive review of possible mechanistic routes for formic acid decomposition on Pt. Nevertheless, simple mechanisms were examined to determine the consistency of our data and that in the literature with reasonable assumptions regarding the kinetics of the reaction. Elementary steps include dissociative adsorption of formic acid as formate ($HCOO \cdot S$; $S =$ site) and a hydrogen atom ($H \cdot S$), as observed in UHV experiments on Pt(111) [46, 48] and

Pt(110), [51] formate dissociation to gaseous CO_2 and another bound hydrogen atom, and finally hydrogen recombination. The literature supports this mechanism by showing that C-H cleavage of the formate hydrogen is kinetically relevant and hydrogen recombination is semi-equilibrated on Pt/Al_2O_3. [13] A CO adsorption-desorption step was also added. The elementary steps for a single-site formate dissociation step are shown in Equations 2.2–2.5.

$$HCOOH + 2 \cdot S \overset{K_1}{\rightleftarrows} HCOO \cdot S + H \cdot S \tag{2.2}$$

$$HCOO \cdot S \overset{k_2}{\rightarrow} CO_2 + H \cdot S \tag{2.3}$$

$$2H \cdot S \overset{K_3}{\rightleftarrows} H_2 + 2S \tag{2.4}$$

$$CO + S \overset{K_4}{\rightleftarrows} CO \cdot S \tag{2.5}$$

This mechanism yields the rate equation found in Equation 2.6, where L is the total number of sites, and its derivation can be found in Appendix B.

$$r = \frac{LK_1 k_2 K_3^{1/2}[HCOOH]}{[H_2]^{1/2}\left(1 + \frac{K_1 K_3^{1/2}[HCOOH]}{[H_2]^{1/2}} + \frac{[H_2]^{1/2}}{K_3^{1/2}} + K_4[CO]\right)} \tag{2.6}$$

This mechanism explains the various reaction order regimes. First, the fractional to zero-order regime transition for formic acid is satisfied, as this mechanism predicts that the formic acid order, n_{HCOOH}, is a function of formate coverage ($n_{HCOOH} = 1 - \theta_{HCOO}$), assuming that higher formate coverages are present at higher formic acid gas phase concentrations. Second, it requires CO order, n_{CO}, to be negative and that $\theta_{CO} = |n_{CO}|$. Finally, the H_2 order (n_{H2}) must be fractional negative. While the hydrogen coverage was not conclusively observed in our experiments, it was found to be close to zero, with the slope of the hydrogen order plots being generally negative but with large standard errors (error = approximately ± 100–200% of the slope).

Given that the greatest possible value of n_{H2} is -0.2 at $\theta_{H2} = 0$, we cannot rule out a fractional negative H_2 order from our experiments. Based on the measured formic acid and CO orders, this mechanism predicts steady state coverages of the two species equal to 0.6 and 0.4 ML, respectively.

A similar mechanism includes an extra site in the second elementary step for formate dissociation, with all other steps the same:

$$HCOO \cdot S + S \overset{k_2}{\rightarrow} CO_2 + H \cdot S + S \tag{2.7}$$

This mechanism yields the rate equation given in Equation 2.8 where z is the coordination number. Its derivation can be found in Appendix B.

$$r = \frac{zLK_1k_2K_3^{1/2}[HCOOH]}{[H_2]^{1/2}\left(1 + \frac{K_1K_3^{1/2}[HCOOH]}{[H_2]^{1/2}} + \frac{[H_2]^{1/2}}{K_3^{1/2}} + K_4[CO]\right)^2} \tag{2.8}$$

This mechanism also explains the phenomena described above for the single site decomposition mechanism including $n_{H2} = -0.2$ at $\theta_{H2} = 0$. Predicted θ_{HCOO} and θ_{CO} are 0.3 and 0.2 ML, respectively. Since the total coverage of surface adsorbates ≥ 0.5 ML in this case, and this range is much less than for the single site mechanism, for which $\theta_{Total} = 1$ (assuming $\theta_{H2} = 0$), the dual site mechanism seems more likely, since the dehydrogenation TOR did not become zero-order in formic acid as the formic acid concentration was increased.

CO was the only possible reaction product observed to affect the rate of reaction and kinetic parameters. The drop in apparent activation energy with lower CO concentrations was observed alongside an increase in the CO order from fractional negative to zero. This behavior is explained at least qualitatively by the Temkin equation, [70] which relates the apparent and real activation energies to surface species reaction orders and heats of adsorption in cases where adsorption equilibrium is reached quickly relative to the rate of surface reaction:

$$E_{app} = E_a - \sum_i n_i q_i \tag{2.9}$$

In Equation 2.9, E_{app} and E_a are the apparent and real activation energies, n_i is the reaction order with respect to species i, and q_i is the heat of adsorption of species i. The heat of adsorption of CO on Pt(111) with $\theta_{CO} = 0.4$ ML, the calculated CO coverage for HCOOH:CO < 1, is approximately 113 kJ mol^{-1}. [71] In this case, the Temkin equation predicts a real activation energy of about 57 kJ mol^{-1} given the measured apparent value of 102 kJ mol^{-1} and CO order of -0.4. This is within the error of the measured $\mathrm{E_{app}}$ in the FA:CO $>$ 1 regime of 67 ± 11 kJ mol^{-1}. On Pt(100)-(1 × 1), using a similar approach and assuming a heat of adsorption of 140 kJ mol^{-1} (measured at 0.5 ML), [72] the Temkin equation predicts a real activation energy of 37 kJ mol^{-1}, lower than the measured value of 65 ± 7 kJ mol^{-1}. In both cases, the calculated activation energy in the fractional negative CO order regime is lower than the measured value in the zero-order CO regime, but this may be the result of the other species present on each surface, which could lower the CO adsorption energy. While the change in n_{HCOOH} from the measured 0.4 here to zero order should also produce a change in apparent activation energy as stated above, the measured value is close to those reported in literature for the zero-order regime. There is no simple, reversible formic acid adsorption step in our proposed mechanisms (i. e. $HCOOH + S \rightleftarrows HCOOH \cdot S$). If, instead, the enthalpy of reaction of the first elementary step is used in place of the heat of adsorption of formic acid on Pt(111), calculated to be -38.8 kJ mol^{-1} for a formate coverage of 0.375 ML and H coverage of 0 ML, [73] then the change in apparent activation energy between the two regimes is expected to be 15.5 kJ mol^{-1} or less, within the error of experiment.

Comparison of the kinetic parameters measured on metal single crystals to those measured on highly dispersed nanoparticles on porous supports is critical, as differences in the parameters may reveal the effect of the catalyst support, or the effect of small metal particle size. For the case of a catalyst support effect, the reaction may proceed directly on the support or at the interface between the support and active metal. In this study, measured apparent activation energies and reaction orders for runs with low initial CO concentrations are in good agreement with literature values from studies on supported catalysts where CO was not co-fed, supporting the conclusion that the previous supports used with Pt for formic acid decomposition (Al_2O_3, [13] C (Norit) [14]) did not substantially alter the reaction mechanism. In the case of small metal nanoparticles, under-coordinated corner or perimeter atoms on nanoparticles could be responsible for the majority of catalytic activity. [74] Ojeda et al. demonstrated that smaller Pt nanoparticles have a higher TOR than larger nanoparticles. [13] Abbas and Madix, on the other hand, have previously attributed defect sites on Pt(111) to dehydration activity using temperature programmed experiments. [49] Given that selectivity toward dehydrogenation is $> 98\%$ [13, 14] ($>$ 99% in this work for when CO was not co-fed), consistency with the work of Abbas and Madix would suggest that the smaller Pt nanoparticles used by Ojeda et al. demonstrate superior TORs due to intrinsic electronic effects of smaller nanoparticles, not necessarily because of their most under-coordinated sites (corners, edges). The most under-coordinated sites are likely blocked by CO, either co-fed or produced in the reaction at defect sites but slow to desorb, since CO adsorbs more strongly on under-coordinated Pt atoms. [75] At high CO concentrations, CO can block more terrace sites, resulting in the reduction of the dehydrogenation TOR, but at low CO concentrations the effect is negligible, hence the near-zero CO order at CO partial pressures of 2 Torr. In this work, defect sites are also likely to be covered by other contaminants discussed above.

2.6 Conclusions

Formic acid dehydrogenation is not sensitive to the structure of Pt single crystal or foil catalysts tested within the precision of the measurements based on the TORs on Pt(111), Pt(100), and Pt foil at the reaction conditions used. Apparent activation energies for formic acid dehydrogenation measured on Pt(111) and Pt(100) in an initial CO partial pressure of 2 Torr at 800 Torr total pressure around 493 K are in agreement with those obtained from the literature on other Pt catalysts. CO, when included at partial pressures > 2 Torr in the initial reaction gas mixture, was shown to decrease the formic acid TOR on all surfaces, behavior explained qualitatively by the Temkin equation. The results suggest that supports used previously for Pt catalysts (Al_2O_3, [13] C (Norit) [14]) do not affect the reaction mechanism, and that under-coordinated sites, which strongly bind CO, could be poisoned by CO.

Table 2.1.
Observed FTIR peaks, references, and vibrational mode assignments for batch reactor charged with 1 Torr HCOOH, 800 Torr total pressure (balance N_2) and held at room temperature. *Assignments without references are unanimous for that mode in the Reference(s) column.

Frequency / cm^{-1}	Reference(s)	Assignment*
	HCOOH	
1033	1033, [63] 1033.4 [64]	δ(CH)
1106	1103.8, [65] 1105, [63] 1105.4 [64]	ν(C-O), [63,65] COH-CO def. [64]
1393	1380.6, [65] 1387, [63] 1387.0 [64]	δ(CH), [63,64] δ(H-C=O) [65]
1774	1776.6, [65] 1770, [63] 1776.2 [64]	ν(C=O)
2945	2942.0, [65] 2943, [63] 2943.8 [64]	ν(CH)
3568	3568.9, [65] 3570, [63] 3570.0 [64]	ν(OH)
	$(HCOOH)_2$	
925	917 [66]	δ(OH)
1218	1214.0, [65] 1218 [66]	ν(C-O)
1308	1283 [66]	n.a.
1363	1365 [66]	δ(CH)
1918	1923 [66]	n.a.
2200	2222 [66]	n.a.
2416	2427, [66] 2415 [67]	ν(C=O)+ δ(OCO) or 2ν(C-O) [67]
2570	2582, [66] 2570 [67]	δ(OH) + ν(C-O) [67]
2613	2623, [66] 2610 [67]	δ(OH) + ν(C-O) [67]
2723	2735, [66] 2722 [67]	2δ(OH) [67]
2813	2815, [66] 2810 [67]	ν(C=O)+ ν(C-O) [67]
2875	2856 [67]	ν(C=O)+ ν(C-O)
2887	2886 [66]	n/a
3015	3028, [66] 2990 [67]	ν(C=O)+ δ(OH) [67]
3055	3040 [67]	ν(C=O)+ δ(OH)
3104	3110 [66,67]	ν(C=O)+ δ(OH), [67] ν(OH) [66]
3136	3150 [66]	n.a.
3389	3385, [66] 3362 [67]	ν(C=O)+ ν(C=O) [67]

Table 2.2.
Uncorrected AES peak intensity ratios from spectra corresponding to the labeled points in Figure 2.3.

Point	C_{272}/Pt_{168}	O_{510}/Pt_{168}	S_{152}/Pt_{168}	Cu_{920}/Pt_{168}
a	2.3	0.6	3.5	0.4
b	0.1	0.1	0.0	0.0
c	2.1	0.5	1.3	0.1

Table 2.3.

Kinetic parameters for formic acid decomposition at standard reaction conditions (5 Torr HCOOH, 15 Torr H_2, 15 Torr CO, 800 Torr total, balance N_2, T = 493 K). *The TOR on Pt foil assumes an atomic surface density of 1.5×10^{15} atoms cm^{-2}.

			Reaction Orders				
Catalyst	TOR at 493 K/ s^{-1}	E_{app} / kJ mol^{-1}	HCOOH	CO	H_2	H_2O	CO_2
Pt(111)	2.6 ± 0.6	102 ± 14	0.43 ± 0.03	-0.40 ± 0.03	0	0	0
Pt(100)	3.7 ± 1.0	86 ± 11	0.35 ± 0.10	-0.35 ± 0.03	0	0	-
Pt Foil	3 ± 2*	94 ± 12	0.35 ± 0.15	-0.43 ± 0.05	0	-	-

Table 2.4.
Kinetic parameters for formic acid decomposition with low initial CO concentrations. Standard conditions were 5 Torr HCOOH, 2-15 Torr H_2, 2 Torr CO, 800 Torr total (balance N_2), T = 463 K. * Error is the standard error of the slope for a single order experiment.

Catalyst	TOR at 463 K/ s^{-1}	E_{app} / kJ mol^{-1}	HCOOH Order	CO Order	H_2 Order
Pt(111)	2.3 ± 0.8	67 ± 11	0.55 ± 0.9*	0	0
Pt(100)	2.4 ± 1.0	65 ± 7	-	0	0

3. PALLADIUM AND COPPER NANOPARTICLE FORMATION ON TITANIA (110) BY THERMAL DECOMPOSITION OF PALLADIUM(II) AND COPPER(II) HEXAFLUOROACETYLACETONATE

3.1 Abstract

Palladium nanoparticles were synthesized by thermal decomposition of palladium(II) hexafluoroacetylacetonate ($Pd(hfac)_2$), an atomic layer deposition (ALD) precursor, on a $TiO_2(110)$ surface. According to X-ray photoelectron spectroscopy (XPS), $Pd(hfac)_2$ adsorbs on $TiO_2(110)$ dissociatively yielding $Pd(hfac)_{ads}$, $hfac_{ads}$, and adsorbed fragments of the hfac ligand at 300 K. A (2×1) surface overlayer was observed by scanning tunneling microscopy (STM), indicating that hfac adsorbs in a bidentate bridging fashion across two Ti 5-fold atoms and Pd(hfac) adsorbs between two bridging oxygen atoms on the surface. Annealing of the $Pd(hfac)_{ads}$ and $hfac_{ads}$ species at 525 K decomposed the adsorbed hfac ligands, leaving PdO-like species and/or Pd atoms or clusters. Above 575 K, the XPS Pd 3d peaks shift toward lower binding energies and Pd nanoparticles are observed by STM. These observations point to the sintering of Pd atoms and clusters to Pd nanoparticles. The average height of the Pd nanoparticles was 1.2 ± 0.6 nm at 575 K and increased to 1.7 ± 0.5 nm following annealing at 875 K. The Pd coverage was estimated from XPS and STM data to be 0.05 and 0.03 monolayers (ML), respectively, after the first adsorption/decomposition cycle. The amount of palladium deposited on the $TiO_2(110)$ surface increased linearly with the number of adsorption/decomposition cycles with a growth rate of 0.05 ML or 0.6 Å per cycle. We suggest that the removal of the hfac ligand and fragments eliminates the nucleation inhibition of Pd nanoparticles previously observed for the $Pd(hfac)_2$ precursor on TiO_2.

3.2 Introduction

Palladium is used for numerous catalytic applications including carbon-carbon coupling, [76] hydrocarbon hydrogenation and dehydrogenation, [77, 78] hydrocarbon oxidation and combustion, [79, 80] and the purification of automotive exhaust gases. [81] Recently, atomic layer deposition (ALD) has emerged as a technique promising greater control for synthesis of nanometer and subnanometer transition metal particles including Pd on oxide supports for heterogeneous catalysis. [36,82–87] Primarily used to grow thin films, ALD is based on self-limiting surface reactions in which a surface is alternately exposed to different precursors separated by purging inert gas or vacuum, providing atomically controlled growth. [88] Nanoparticles can be grown on oxide supports during early stages of ALD processes for heterogeneous catalysis applications. Palladium nanoparticles synthesized by ALD using palladium(II) hexafluoroacetylacetonate $Pd(hfac)_2$ as a Pd precursor demonstrated higher selectivity toward desired products and particle stability compared to traditionally prepared catalysts in reactions such as methanol decomposition, [84] ethanol and isopropyl alcohol oxidation, [87] and oxidative dehydrogenation of alkanes. [36]

Formation of nanoparticles from (hfac)-based organometallic precursors has exhibited a nucleation delay and requires a high number of ALD cycles ($>$ 100 cycles) that limits its large scale application. Different characterization techniques have been used to isolate the surface intermediates and identify the surface active sites during the initial precursor exposure. Fourier transform infrared (FTIR) measurements suggested that $Pd(hfac)_2$ decomposes to $Pd(hfac)_{ads}$ and $Al(hfac)_{ads}$ upon adsorption on Al_2O_3 and the resulting nucleation delay period was assigned to possible surface poisoning with $Al(hfac)_{ads}$ species. [83, 89, 90] Using gas-phase infrared spectroscopy, Weber et al. [91] suggested that H_2 and O_2 plasmas are required to remove the hfac ligands and other carbon moieties left from $Pd(hfac)_2$ adsorption on Al_2O_3. Adsorbed hfac ligands were also suggested to block adsorption sites on TiO_2 for Pt particle formation using $Pt(hfac)_2$ as the precursor. [92]

In addition to surface intermediates, the substrate chemistry can also change the growth behavior of the (hfac)-based precursors. Pd nucleation is faster on ZnO than Al_2O_3 at the same conditions. 100 ALD Pd cycles on ZnO yields Pd islands with 10 to 20 nm domains. However, 200 cycles were required to form islands consisting of 10 nm domains on Al_2O_3. [84] X-ray photoelectron spectroscopy (XPS) studies of $Cu(hfac)_2$ adsorption on Pt(111) showed chemical differences compared to the $Cu(hfac)_2$ on copper and TiO_2 systems. The hfac group formed on copper and TiO_2 surfaces remained intact until 373 and 473 K, respectively, whereas hfac species formed on Pt(111) showed significant decomposition by 300 K. [93, 94] Moreover, surface contamination existing prior to deposition has been shown to influence the decomposition pathway and the final structure of nanoparticles. X-ray absorption spectroscopy (XAS) showed, for example, that residual chlorine on the TiO_2 surface can participate in the decomposition pathway of $Pd(hfac)_2$. In the presence of chlorine, $Pd(hfac)_2$ decomposed to form $Pd(hfac)Cl_{2,ads}$ and $Ti(hfac)_{ads}$ species. [95]

All of these studies demonstrate that the initial substrate-$Pd(hfac)_2$ interaction and existing surface species play a major role in tailoring the final properties of the nanoparticles and the Pd growth behavior. As recently highlighted by Zaera, [43] fundamental surface science studies can serve as a tool to understand the intermediates involved in the deposition mechanism, and for elucidating how the overall precursor-substrate interaction process takes place during the initial exposure of the precursor.

In this chapter, $Pd(hfac)_2$ was used for synthesis of Pd nanoparticles on the $TiO_2(110)$ surface. The evolution of the organometallic precursor was monitored by surface sensitive characterization techniques including X-ray photoelectron spectroscopy (XPS) and scanning tunneling microscopy (STM) to better understand the adsorption and thermal decomposition pathways of $Pd(hfac)_2$ on $TiO_2(110)$, as well as to track the formation of Pd nanoparticles (NPs).

3.3 Experimental Methods

3.3.1 Instruments

Experiments were performed in two separate UHV systems. An Omicron Surface Analysis Cluster at Birck Nanotechnology Center (BNC), Purdue University, consisting of an ultrahigh vacuum (UHV) preparation chamber and μ-metal analysis chamber with base pressures of 1×10^{-9} and 5×10^{-11} mbar, respectively, was used for XPS analysis. The preparation chamber was equipped with a mass spectrometer, an Ar^+ sputtering gun, resistive sample heating, and a leak valve for dosing ALD precursors. The analysis chamber was equipped with XPS, low energy electron diffraction (LEED), high resolution electron energy loss spectroscopy (HREELS), and resistive sample heating. The second experimental apparatus at the Center for Nanoscale Materials (CNM), Argonne National Laboratory, was an Omicron VT SPM system equipped with a variable temperature STM/AFM (Omicron VT-SPM XA), a preparation chamber for dosing ALD precursors through a leak valve, an Ar^+ sputtering gun, and resistive sample heating. The base pressure in the STM and preparation chambers was $\leq 5 \times 10^{-11}$ mbar. STM images were obtained using etched W tips. STM images were analyzed using WSxM software. [96] Pymol software (version 1.5.0.4) was used for molecular visualization.

$TiO_2(110)$ single crystals of 9 mm diameter and 1 mm thickness (Princeton Scientific Corp.) were used. In both systems, the sample cleaning procedure consisted of repeated cycles of Ar^+ sputtering and vacuum annealing at 925 K. For the XPS study, sample temperature was measured by a K-type thermocouple spot-welded to the stainless steel back plate, and crystal cleanliness was monitored by XPS and LEED. The appearance of the fresh crystal changed from transparent to light blue following several cleaning cycles, the signature of a slightly reduced crystal. [97]

$TiO_2(110)$ crystals were exposed to Pd(II) hexafluoroacetylacetonate ($Pd(hfac)_2$) (Aldrich, 99.9%) in the preparation chambers of both systems. $Pd(hfac)_2$ powder was loaded into a miniature 50 mL Swagelok stainless steel cylinder and was pumped by a turbo pump several times before each dosing. All gas lines were regularly heated overnight at 423 K. For the XPS experiment, dosing was performed through a leak valve for 10 min. at a pressure of ca. 5×10^{-7} mbar for an exposure of 225 L to ensure saturation. Higher exposures of $Pd(hfac)_2$ did not change surface Pd coverage. Dosing pressure was determined during a test experiment, and the ion gauge was kept off during $Pd(hfac)_2$ exposure to avoid electron-induced decomposition of $Pd(hfac)_2$. For the STM experiment, the maximum achievable $Pd(hfac)_2$ base pressure was much lower (ca. 4×10^{-9} mbar) due to system geometry differences; however, the sample sat approximately 2 in. away from a dosing capillary aimed at the sample. $Pd(hfac)_2$ was dosed at approximately this pressure for 60 min. to ensure saturation.

XPS data were acquired using a nonmonochromatic Mg Kα X-ray source ($h\nu =$ 1253.6 eV) at 150 W. High resolution spectra were recorded at a constant pass energy of 20 eV. The resolution, defined as the full-width at half-maximum (fwhm) of the Ti $2p_{3/2}$ peak, was approximately 1.1 eV. Unfortunately, no energy scale correction was foreseen by the analyzer manufacturer (analyzer, Omicron EAC 125; controller, Omicron EAC 2000), and therefore it was possible only to set the Au $4f_{7/2}$ peak at 84.0 eV by changing the spectrometer work function. Slight sample charging was corrected by fixing the Ti $2p_{3/2}$ peak at 459.3 eV.

XPS data were analyzed with CasaXPS (version 2313Dev64) software. Curve fitting was done assuming a Gaussian/Lorentzian line shape (30% Lorentzian, CasaXPS function: SGL(30)) for symmetric peaks and an asymmetric Lorentzian shape (CasaXPS function: LF(1,1.5,25,70)) for asymmetric peaks. Coverages were calculated from XPS data using the procedures outlined in Appendix A.

3.4 Results

3.4.1 X-ray Photoelectron Spectroscopy for $Pd(hfac)_2/TiO_2$ System

Figure 3.1 shows XPS spectra of the F 1s, O 1s, Pd 3d, and C 1s core-levels obtained after saturation exposure of the $TiO_2(110)$ surface to $Pd(hfac)_2$ at 300 K. The structure of the $Pd(hfac)_2$ molecule is shown inside the F 1s region in Figure 3.1.

The main component of the F 1s peak is at 688.3 eV and represents a CF_3 functional group in hfac ligand. The minor F 1s peak detected at 684.9 eV is assigned to Ti-F. [98] The O 1s spectrum was fitted with two components at 530.6 and 532.1 eV. The former peak is a feature of TiO_2, and the latter represents oxygen atoms in the hfac ligand. Supporting this assignment, heating the sample to 575 K causes hfac ligands to decompose (discussed below), and the peak at 532.1 eV is absent. This same peak was observed following adsorption of $Cu(hfac)_2$ on the TiO_2 surface. [94] Palladium is represented by a single broad Pd $3d_{5/2}$ peak (fwhm = 1.6 eV) at 336.9 eV. The observed binding energy (BE) is slightly higher than 336.6 eV, which is the reference value for PdO (see, for instance, Reference [99] and references therein). Intact $Pd(hfac)_2$ adsorbed in multilayers on a copper substrate is characterized by a Pd $3d_{5/2}$ peak at 339.1 eV. [100] Therefore, the component at 336.9 eV was assigned to a palladium atom in a $Pd(hfac)_{ads}$ species. This assignment is further confirmed by XPS quantification and STM images (discussed later).

Analysis of the C 1s region revealed contributions from several species (Figure 3.1). The first is an hfac species, which is characterized by three components, each representing a distinct chemical state of the carbon atoms in hfac (see Figure 3.1). These components at 285.2, 287.5, and 292.4 eV were assigned to carbon atoms in C-H, C-O, and CF_3 , respectively. Our assignments are based on Hantsche, [101] and these values are in good agreement with those observed for $Cu(hfac)_2$ and $Pd(hfac)_2$. [100,102–105] Characteristic BEs are summarized in Table 3.1.

To identify fragments from hfac cracking, the area ratio between the CF_3, C-O, and C-H components was constrained to 2:2:1 during curve fitting based on the stoichiometry of the hfac group (Figure 3.1). As shown in Figure 3.1, the hfac components alone were not enough for a proper fitting of the C 1s region; therefore, other components were added. The highest BE peak at approximately 297.5 eV was an O 1s ghost peak excited by Al Kα radiation (a dual Mg/Al X-ray gun was used). Inclusion of the O 1s ghost peak in the curve fitting was crucial to ensure correct background subtraction and spectrum deconvolution. The ratio between the O 1s and ghost peak

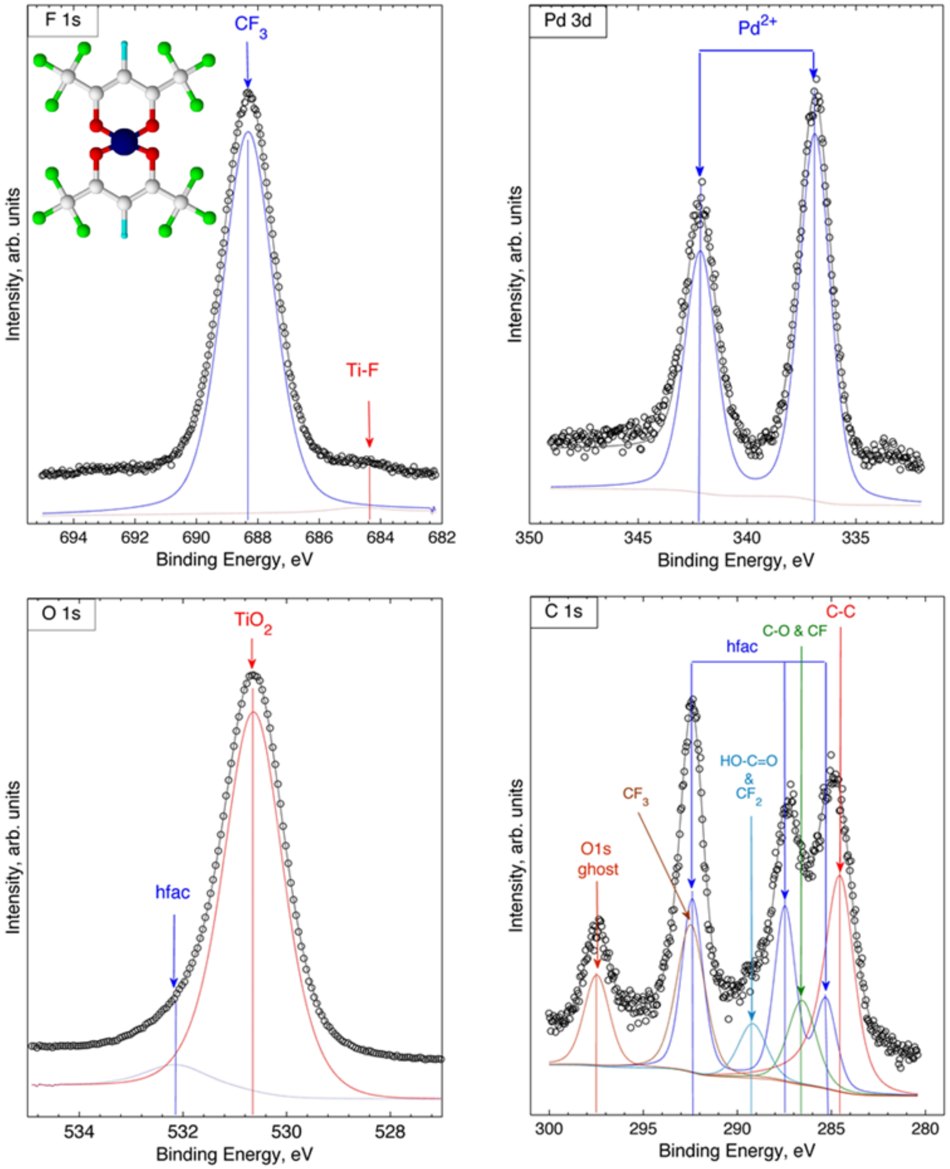

Figure 3.1. The F 1s, O 1s, Pd 3d and C 1s photoemission spectra obtained after exposure of the $TiO_2(110)$ surface to $Pd(hfac)_2$ up to saturation at 300 K. Ball and stick schematic of $Pd(hfac)_2$ molecule is shown inside F 1s region (Pd atom: blue, O atoms: red, C atoms: white, F atoms: lime, H atoms: cyan).

areas was always constant, confirming this assignment. The O 1s ghost peak area was excluded from carbon quantification. The four other components represent de-

Table 3.1.
Binding energies of characteristic XPS features observed after $Pd(hfac)_2$ adsorption at room temperature and subsequent thermal decomposition.

	Binding Energy / eV				
Species	C 1s	F 1s	Pd $3d_{5/2}$	O 1s	Ti $2p_{3/2}$
$Pd(hfac)_{ads}$	285.2 (C-H), 287.5 (C=O), 292.4 (CF_3)	688.3	336.9	532.1	
TiO_2				530.6	459.3
O 1s Ghost (from Al Kα)	297.5				
	Fragments of $Pd(hfac)_2$				
CF_3	292.5	688.3			
CF_2, HO-C=O	289.2				
CF, CO	286.4				
C-H, C-C	284.5				
TiF_x		684.9			
PdO_x and Pd NPs			336.2-335.5		

composition fragments of the hfac group: residual carbon (carbon bonded to carbon and/or hydrogen only) is assigned to the peak at 284.5 eV, the component at 286.4 eV is a feature corresponding to C-F and/or C-O species (carbon bonded to oxygen or fluorine), CF_2 and carboxyl groups are characterized by the peak at 289.2 eV, and the peak at 292.5 eV is due to CF_3 species. Partial dissociation of the hfac species likely occurs during adsorption. Caution was taken to avoid radiation damage by minimizing exposure to the X-ray flux. Characteristic Pd(hfac)$_2$ core levels (F 1s, C 1s, Pd 3d) were collected first followed by Ti 2p and O 1s. Radiation-induced decomposition of the precursor was only observed during prolonged exposure to X-rays by the appearance of the F 1s peak at 684.9 eV, which was a signature of precursor decomposition.

The coverage of adsorbed species was calculated using Equation A.7 in Appendix A. The F 1s, Pd 3d, and C 1s peaks represented the adlayer, and the Ti 2p peaks represented the substrate. At room temperature (Figure 3.1), the adlayer was assumed to consist of Pd(hfac)$_{ads}$ and hfac$_{ads}$ species along with fragments of the hfac ligand. To calculate the coverage of Pd(hfac)$_{ads}$+hfac$_{ads}$, corresponding contributions of these characteristic components were taken from the F 1s, C 1s, and O 1s peaks (hfac components only), which were obtained using the curve fittings shown in Figure 3.1. For Pd, the entire Pd 3d region was used for coverage calculations. The coverages of Pd(hfac)$_{ads}$+hfac$_{ads}$ based on the F 1s, Pd 3d, and C 1s regions were equal to 0.10, 0.10, and 0.08 ML at 300 K, respectively (Table 3.2). The coverages were normalized to the stoichiometric ratio of Pd:C:F in the Pd(hfac)$_2$ molecule (1:10:12). The other quantification parameters, for instance, the ratio between the CF$_3$ carbon component of C 1s and the CF$_3$ fluorine component of F 1s, matched the stoichiometry as well. The equal value between the normalized coverages (ca. 0.1 ML) for the Pd, C, and F showed that the surface species kept the original stoichiometry of the molecule and can consist of Pd(hfac)$_2$ or Pd(hfac)$_{ads}$+hfac$_{ads}$. However, the Pd 3d$_{5/2}$ XPS peak at 336.9 eV eliminates the presence of the Pd(hfac)$_2$ molecule and allows us to conclude that following Pd(hfac)$_2$ exposure at 300 K, the TiO$_2$(110) surface is covered by the Pd(hfac)$_{ads}$+hfac$_{ads}$ species at a coverage of approximately 0.1 ML. Cracked fragments of hfac such as C-H, C-C, CF, CO, CF$_2$, carboxyl groups, and CF$_3$ species were also present on the surface.

The effect of temperature on Pd(hfac)$_2$ adsorption was investigated by exposing the TiO$_2$(110) surface to Pd(hfac)$_2$ at 300, 375, and 450 K. For higher adsorption temperatures, the extent of fragmentation of the hfac$_{ads}$ and Pd(hfac)$_{ads}$ species in-

Table 3.2.
Coverage of hfac species as a function of adsorption temperature, calculated based on Pd 3d, C 1s, and F 1s regions. C 1s and F 1s columns use only hfac components from XPS fitting for the calculation.

	Coverage / ML		
Adsorption Temp. / K	Pd 3d	C 1s	F 1s
300	0.10	0.08	0.10
375	0.11	0.09	0.08
450	0.12	0.09	0.10

creased. At 300 K, the symmetric F 1s peak at 688.3 eV represents the CF_3 functional group in the hfac ligand. With increasing adsorption temperature, a peak at 684.9 eV grows, which is the signature of the TiF bond (spectra not shown). [98] The maximum concentration of TiF occurred at 450 K due to the thermal decomposition of the hfac ligand. At 300 K, a single chemical state of palladium as $Pd(hfac)_{ads}$ was observed at 336.8 eV, but a new Pd $3d_{5/2}$ peak at 336.2 eV appeared following adsorption at 375 and 450 K (not shown). The appearance of this peak could be due to $Pd(hfac)_{ads}$ decomposition and the appearance of a PdO_x ($x < 1$) species and/or Pd clusters. The coverage of the hfac-containing species was calculated using Equation A.7 in Appendix A based on the Pd 3d, C 1s, and F 1s peaks, and the results are summarized in Tables 3.2 and 3.3.

The observed trend in these calculations demonstrated that the hfac coverage does not change with adsorption temperature, the extent of hfac cracking increased, and the amount of palladium increases. The conclusion is that, at elevated adsorption temperatures, some products of $Pd(hfac)_2$ decomposition desorb, leaving palladium atoms on the surface. This assumption is supported by the observation of the Pd $3d_{5/2}$ peak at 336.2 eV assigned to a PdO_x species and/or Pd clusters.

Table 3.3.
Coverage of carbon-containing species as a function of adsorption temperature. HC's = residual hydrocarbons.

	Coverage / ML				
Adsorption Temp. / K	C-F + C-O	HC's	CF_2 + HO-C=O	CF_3	hfac
300	0.28	0.54	0.16	0.37	0.09
375	0.23	0.65	0.15	0.39	0.09
450	0.33	0.78	0.16	0.38	0.09

Thermal decomposition of the adlayer prepared by exposure of $TiO_2(110)$ to $Pd(hfac)_2$ at 300 K was studied by heating in a stepwise manner from 300 to 875 K under UHV. Relevant XPS spectra are shown in Figure 3.2.

Following heating at 575 K, the CF_3 species represented by the F 1s peak at 688.3 eV was replaced by the TiF species, represented by the F 1s peak at 684.9 eV. The TiF species decomposed completely following heating at 875 K. In the Pd 3d region, heating to 375 K resulted in the appearance of a Pd $3d_{5/2}$ peak at 336.2 eV, which was assigned to a PdO_x ($x < 2$) species and/or Pd clusters and/or atoms. The intensity of the $Pd(hfac)_{ads}$ components decreased reaching a plateau at 525 K, indicating decomposition of the $Pd(hfac)_{ads}$ species (Figure 3.2). At 775 K, the Pd $3d_{5/2}$ peak was at 335.8 eV. This BE is too low to be assigned to a PdO_x species; [99] therefore, we assume that the PdO_x species decomposed. However, this BE is too high for bulk metallic Pd, which is characterized by a Pd $3d_{5/2}$ peak at 335.0 eV. [99] Thus, we conclude that this shift to a higher binding energy is caused by the size effect in Pd metal nanoparticles, which give shifts to a higher BE because of incomplete final state relaxation. [106] With increasing temperature, the Pd $3d_{5/2}$ peak at 335.8

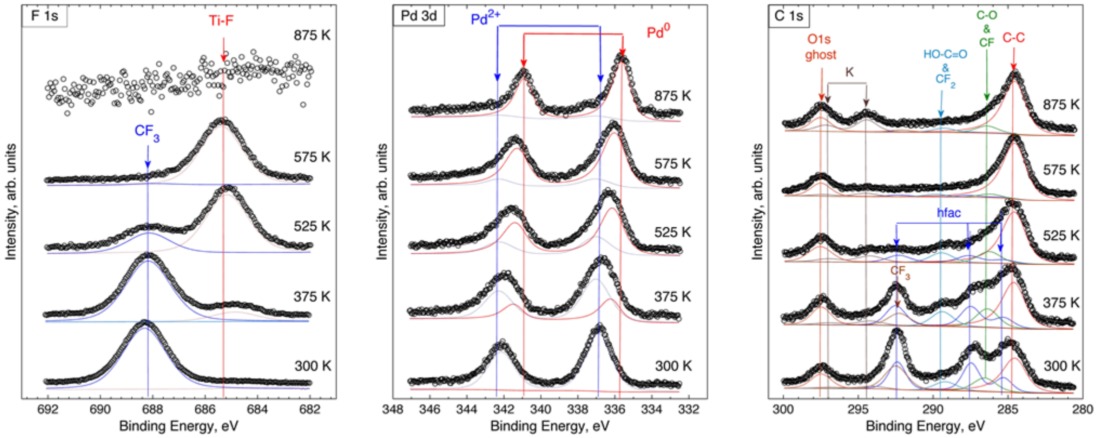

Figure 3.2. The F 1s, Pd 3d and C 1s XPS spectra obtained following $TiO_2(110)$ exposed to $Pd(hfac)_2$ at 300 K and heated at 375, 525, 575, 775, and 875 K. The spectra were collected at the specified temperature.

eV shifted toward a lower BE and reached 335.6 eV following annealing at 875 K. The BE shift toward lower binding energies observed between 775 and 875 K is assigned to a sintering effect that partially removes the final state relaxation limitation.

Thermal decomposition of adsorbed hfac-containing species and the transformation of its dissociation fragments were traced by monitoring the coverages of different carbon species during annealing (Figure 3.2). The $Pd(hfac)_{ads}$ species fully decomposes at 525 K, in agreement with the conclusion reached based on the evolution of the Pd 3d spectra (Figure 3.2). CF_3 fragments associated with the decomposition of the hfac ligand follow the same trend and, therefore, have thermal stability similar to $Pd(hfac)_{ads}$. The CF_2, carboxyl, and CF species are likely intermediates of $Pd(hfac)_{ads}$ and $hfac_{ads}$ decomposition. CF_2 and CF species might form through decomposition of CF_3 by transfer of fluorine atoms to $TiO_2(110)$. Above 575 K, the carbon species related to hfac groups vanish, and only a single asymmetric peak related to graphitic carbon or other carbon species formed by decomposition of the organic moieties could be detected. The carbon remaining following annealing at 875

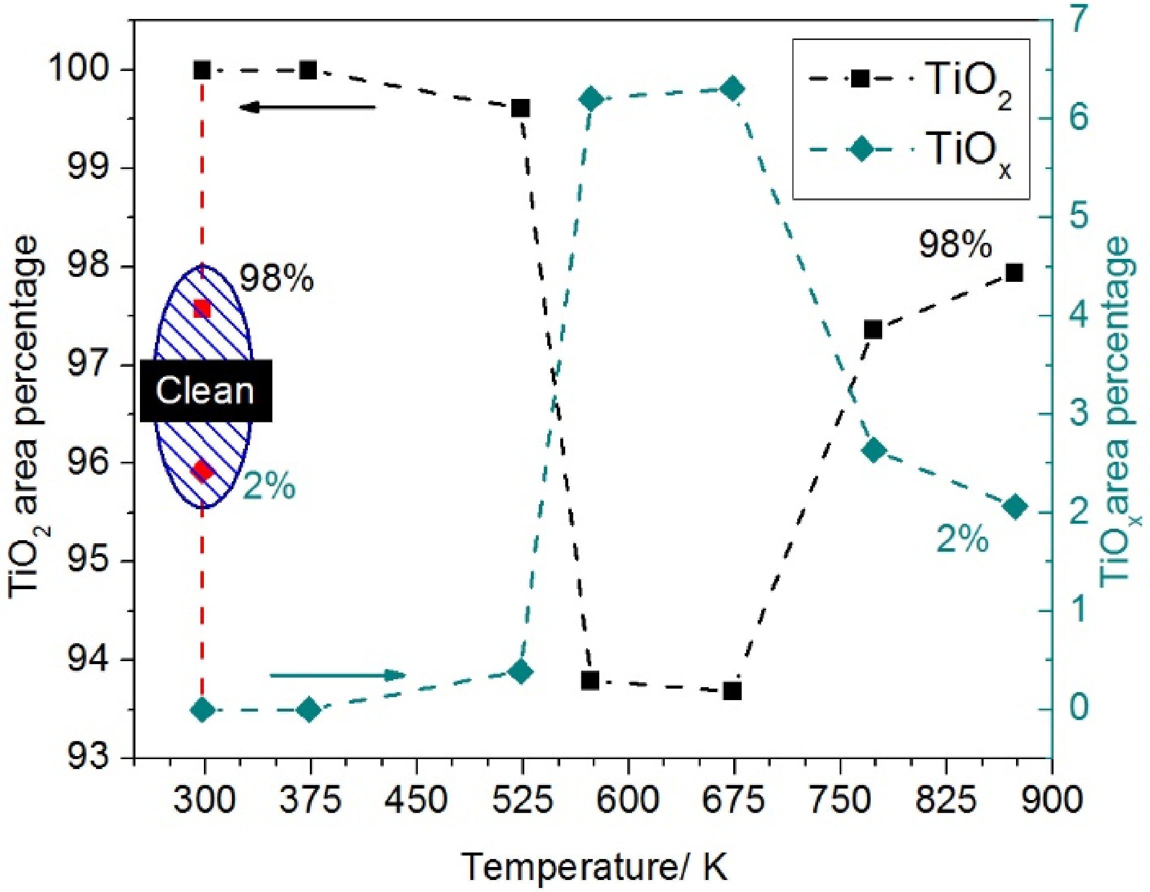

Figure 3.3. Changes in area percentage of TiO_2 and TiO_x components upon heating for clean $TiO_2(110)$, $Pd(hfac)_2$ exposure at 300 K, and during annealing to 875 K. The shaded area shows the fractions of TiO_2 and TiO_x for the clean $TiO_2(110)$ single crystal before $Pd(hfac)_2$ exposure.

K is likely graphitic. Potassium, a bulk crystal contaminant, diffuses from the bulk to the surface during annealing at 875 K.

Detailed XPS analysis of surface chemical states also revealed possible adsorption sites for $Pd(hfac)_{ads}$ and $hfac_{ads}$. The clean $TiO_2(110)$ surface was characterized by the Ti $2p_{3/2}$ peak at 459.3 eV, which is a feature of stoichiometric TiO_2. An additional Ti $2p_{3/2}$ peak at 457.5 eV assigned to reduced titania, TiO_x ($x < 2$), was also observed (spectra not shown).

The evolution of the TiO_x and TiO_2 components is shown in Figure 3.3. The TiO_x component disappears following $Pd(hfac)_2$ adsorption. However, the TiO_x peaks reappeared upon heating to 525 K, the same temperature at which the $Pd(hfac)_{ads}$ and $hfac_{ads}$ species decomposed. This suggests that the reduced titania centers are involved in $Pd(hfac)_2$ adsorption and/or dissociation. The oxygen atoms of the hfac ligand might interact with the reduced TiO_x centers providing oxygen needed for a fully oxidized surface. Following decomposition of the $hfac_{ads}$ ligands at 575 K in UHV, the TiO_x area percentage increases to ca. 6.5% before returning to the original value of ca. 2% following heating at 875 K (Figure 3.3). The increase of the TiO_x contribution at 575 K might be due to the reaction of the surface oxygen from stoichiometric TiO_2 with carbon fragments from the hfac ligands. Heating to 875 K results in the diffusion of the oxygen vacancies to the bulk and return of the surface to its initial state.

The number of $Pd(hfac)_2$ adsorption and decomposition cycles on the $TiO_2(110)$ surface determines the amount of the deposited Pd. Palladium coverages and palladium layer thicknesses are shown in Figure 3.4 for four consecutive cycles of $Pd(hfac)_2$ adsorption at 300 K followed by heating to 875 K in UHV. XPS spectra for consecutive cycles are similar to those for the first deposition cycle. In addition to the Pd coverage, the thicknesses are presented for comparison with the value of growth per cycle (GPC) for $Pd(hfac)_2$ ALD measured by quartz crystal microbalance (QCM), which assumes formation of a uniform overlayer after each cycle. Similarly, we have used a uniform Pd overlayer XPS quantification model. The details of the thickness calculations are provided in the Supporting Information. Growth is linear, with a GPC of 0.6 Å (Figure 3.4). Therefore, the amount of deposited palladium can be controlled by the number of adsorption and decomposition cycles. The linear growth of Pd indicates that the remaining graphite-like carbon does not block adsorption sites for $Pd(hfac)_2$.

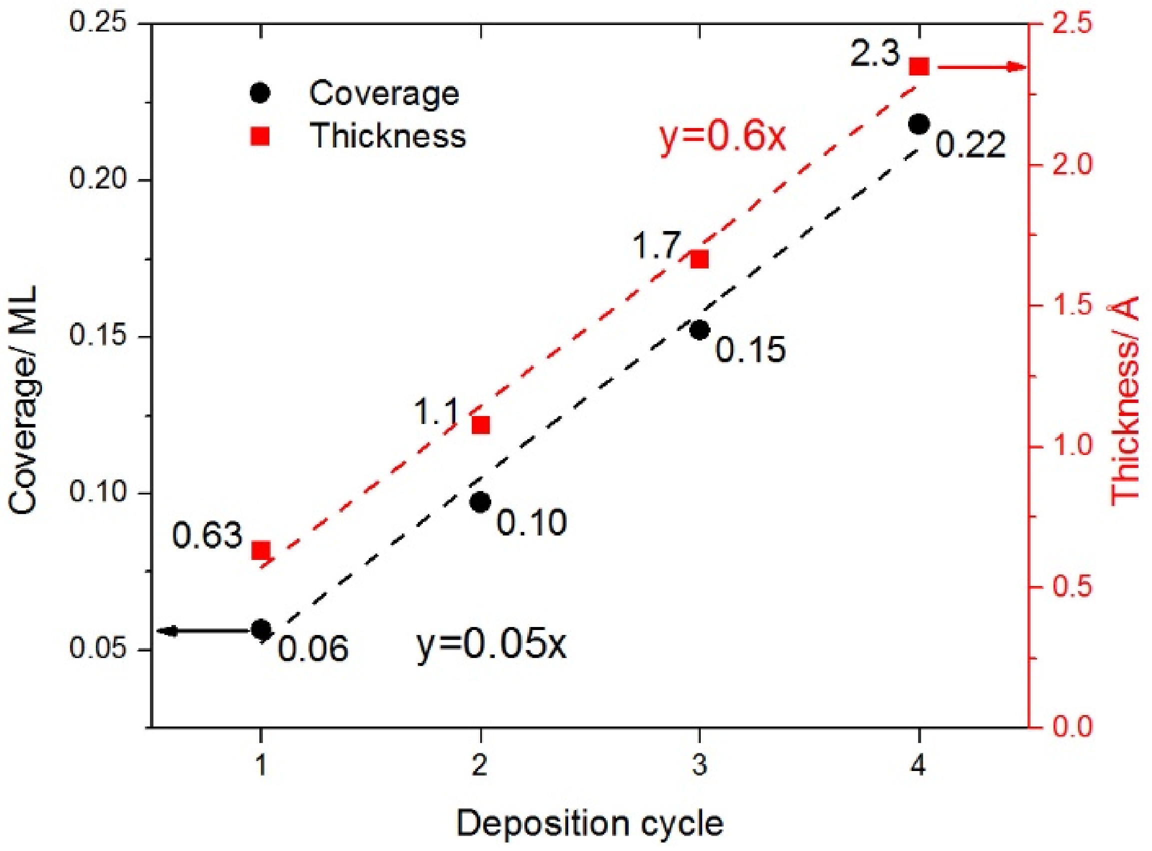

Figure 3.4. Pd growth curve showing the coverage of the Pd in ML versus number of deposition cycles. Each cycle consists of adsorption of Pd(hfac)$_2$ at 300 K followed by annealing in UHV to 875 K.

3.4.2 STM for Pd(hfac)$_2$/TiO$_2$ System

To complement the XPS results with topography data, an STM investigation was performed. A typical 100 × 100 nm STM image of the clean TiO$_2$(110) surface following the preparation procedure, described in the Experimental Methods section, is shown in Figure 3.5 A. Irregularly shaped terraces are present, as are defect sites that show up as bright spots and added rows. The spots might be oxygen vacancies or other defect types, and the added rows act as precursors for the TiO$_2$(110)-(1×2) surface reconstruction. [107] The measured step height was approximately 3.2 ± 0.2 Å, in agreement with the expected value of 3.24 Å for rutile TiO$_2$(110). Alternating bright and dark rows running along the [001] direction are visible. The spacing between bright rows and between dark rows in the [1$\bar{1}$0] direction is approximately 6.5 Å. Within bright rows, the spacing between features was approximately 3 Å. An atomic resolution image after Fourier transform filtering is shown in the inset in Figure 3.5 A with the dimensions labeled. These dimensions correspond to a bulk terminated $TiO_2(110)$-(1×1) surface, where the bright features are attributed to surface 5-fold Ti atoms and the dark features to bridging oxygen atoms. [107]

A 100×100 nm image following saturation dosing of $Pd(hfac)_2$ at RT is shown in Figure 3.5 B. This surface is characterized by bright clusters with similar approximate size and density as the defect sites on the clean TiO_2, and bright, discontinuous rows running along the [001] direction with inter-row spacing of approximately 6.5 Å. Though the discontinuities could not be resolved in all images, a Fourier transform of an area containing discrete features revealed their spacing along a row in the [001] direction to be approximately 6 Å (inset, Figure 3.5 B). The dimensions of these dark and bright spots correspond to a structured (2×1) overlayer, which can be assigned to bidentate bridging hfac ligands bonding through both oxygen atoms to two 5-fold Ti atoms, and $Pd(hfac)_{ads}$ with Pd bonding to two surface bridging oxygen atoms shown schematically in the ball model in Figure 3.6. The contrast in the STM images allows to identify the adsorption species and adsorption sites: Pd(hfac), if bound between two bridging oxygen atoms, would protrude further from the surface than an hfac ligand bound to two 5-fold coordinated Ti atoms, and would therefore appear brighter on the basis of topography. Based solely on topography, then, the adsorbed hfac ligands would appear as the dark spots also in a (2×1) arrangement. The contrast may also be explained by electronic arguments. For example, the appearance of dark and bright areas was reported in the STM images of the Si(111)-(7×7) surface exposed to $Cu(hfac)_2$. [108] On the basis of the bias dependence, dark areas were assigned to hfac ligands and the bright regions to Cu atoms when empty electronic states of the sample were tested at positive bias voltage. The STM images shown in Figure 3.5 were obtained at positive biases. Therefore, hfac ligands might appear as the dark rows.

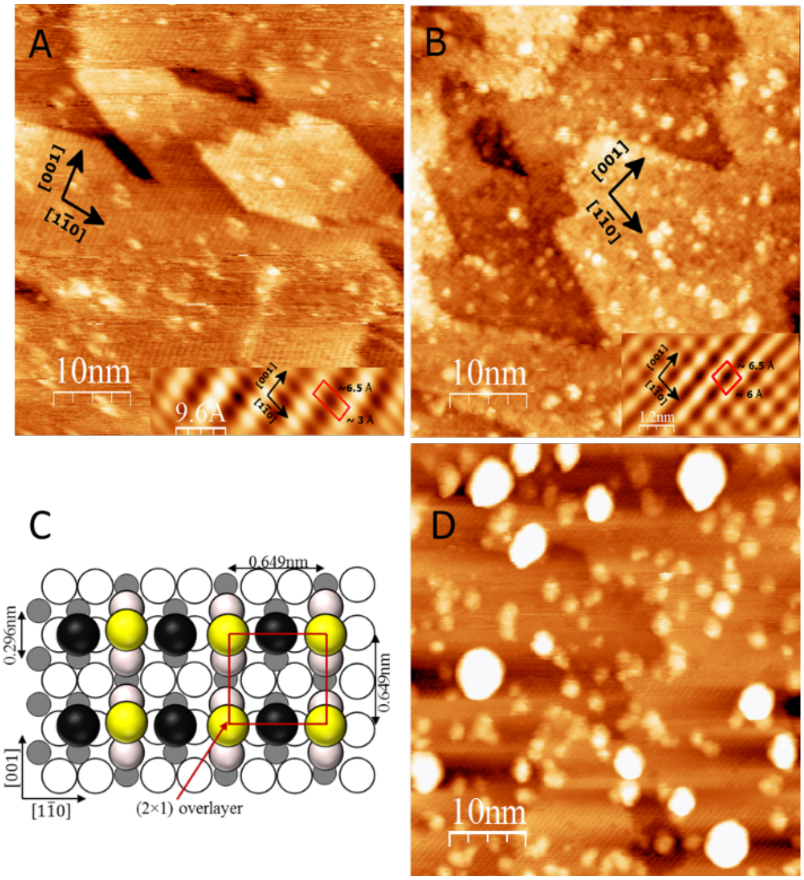

Figure 3.5. STM images of the $TiO_2(110)$ surface. A: Clean $TiO_2(110)$ following sputtering and annealing cycles (V = +2.0 V, I = 70 pA). Inset: Atomic scale image after Fourier transform showing the unreconstructed (1×1) unit cell. B: TiO_2 following dosing of $Pd(hfac)_2$ for 60 min. at room temperature (V = +1.75 V, I = 0.1 nA). Inset: Small scale image after Fourier transform showing structured (2×1) overlayer of adsorbates. The bright spots are assigned to $Pd(hfac)_{ads}$ group. C: Model for $Pd(hfac)_2$ adsorbed on $TiO_2(110)$: The $Pd(hfac)_2$ dissociates. The resulting hfac (hfac: black spheres) binds to two five-fold coordinated Ti atoms (gray spheres) in a bi-dentate fashion and the Pd(hfac) (Pd(hfac): yellow spheres) adsorbs between two bridging oxygen (oxygen: white spheres). The adsorption geometry matches the experimental value reported in image B inset. D: Following annealing of the as-deposited sample to 875 K for 20 min. (V = +0.5 V, I = 2.0 nA).

The $Pd(hfac)_{ads}$ species is expected to have a higher density of states above the Fermi level than those for the $hfac_{ads}$ group, leading to the $Pd(hfac)_{ads}$ species appearing as

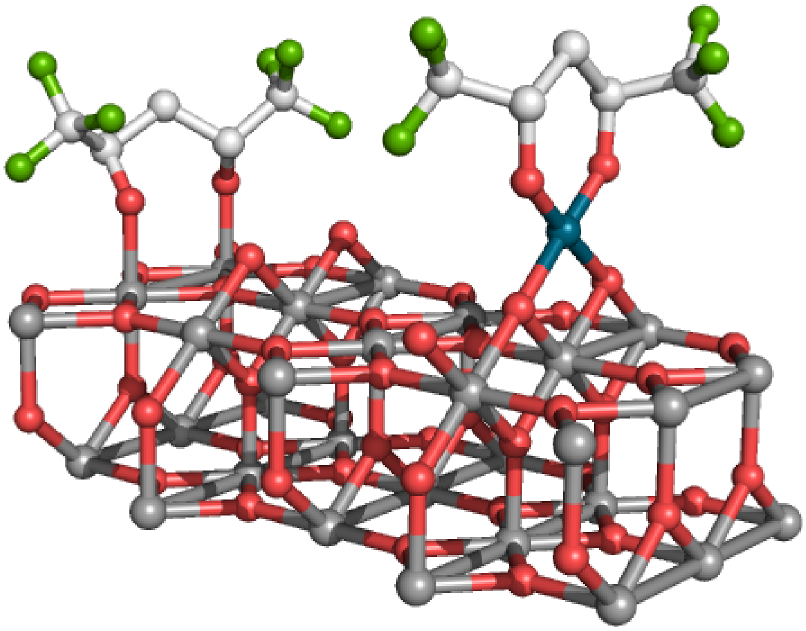

Figure 3.6. $Pd(hfac)_2$ molecule adsorbed on the $TiO_2(110)$ surface at room temperature. $Pd(hfac)_2$ dissociates into an hfac ligand, which bonds across neighboring 5-fold coordinated Ti sites (grey atoms), and a Pd(hfac), which bonds across bridging O atoms (red atoms) on the surface. Adsorbed Pd(hfac) is responsible for the (2×1) structure observed after $Pd(hfac)_2$ adsorption at room temperature. Adjacent Pd(hfac) and hfac groups are not shown for clarity.

the bright spots (Figure 3.5 B). Unfortunately, the $Pd(hfac)_{ads}$+$(hfac)_{ads}$ adlayer was not stable under the LEED electron beam, and therefore the LEED patterns were not collected.

The proposed model for dissociative $Pd(hfac)_2$ adsorption on $TiO_2(110)$ is in agreement with an observed (2×1) overlayer following dosing of $Cu(hfac)_2$ on $TiO_2(110)$. [94,109] The authors of those studies noted that the distance of the two oxygen atoms in the hfac ligand of $Cu(hfac)_2$ is 2.79 Å, close to the distance of 2.96 Å between two 5-fold surface Ti atoms on $TiO_2(110)$, which makes that site suitable for adsorption of hfac. This is close to the value of 2.77 Å between two O atoms in an hfac ligand in $Pd(hfac)_2$. [110]

Following annealing at 575 K, nanoparticles appeared with an average height of 1.2 ± 0.6 nm (not shown), where the error is one standard deviation from the average value. Uncertainty in the height distribution arises from the difficulty in determining which features are Pd nanoparticles, which are agglomerations of ligand fragments, and which are original defects in the TiO_2 surface. The best quality images were obtained at lower bias and higher tunneling current (V = +0.8 V, I = 1.0 nA) than for the previous experiment, indicating that surface conductivity had increased. This might be due to the formation of Pd nanoparticles.

Annealing at 875 K resulted in the agglomeration of the nanoparticles, and the unreconstructed $TiO_2(110)$-(1×1) surface reappeared, as shown in Figure 3.5 D. These results agree with the XPS data, which demonstrated the complete decomposition of the $hfac_{ads}$ species at 575 K and Pd nanoparticle sintering at 875 K. The average height of the nanoparticles was 1.7 ± 0.5 nm at 875 K. Even after annealing to 875 K, the particle size is within the range where a size-dependent BE shift could be observed. Therefore, the +0.6 eV shift of the Pd $3d_{5/2}$ peak from the peak position for the bulk palladium (335.0 eV) could be assigned to a particle size effect. No preferential nucleation of the Pd NPs was observed at step edges. The coverage of Pd particles was estimated from the STM data to be 0.03 ML at 875 K. This value is in good agreement with the 0.05 ML calculated using the XPS data. It must be noted that the apparent lateral dimension of these nanoparticles depends on the STM tip shape and, therefore, is not used. The coverage estimation from STM assumes a hemispherical nanoparticle shape in which the radius is approximately equal to the height.

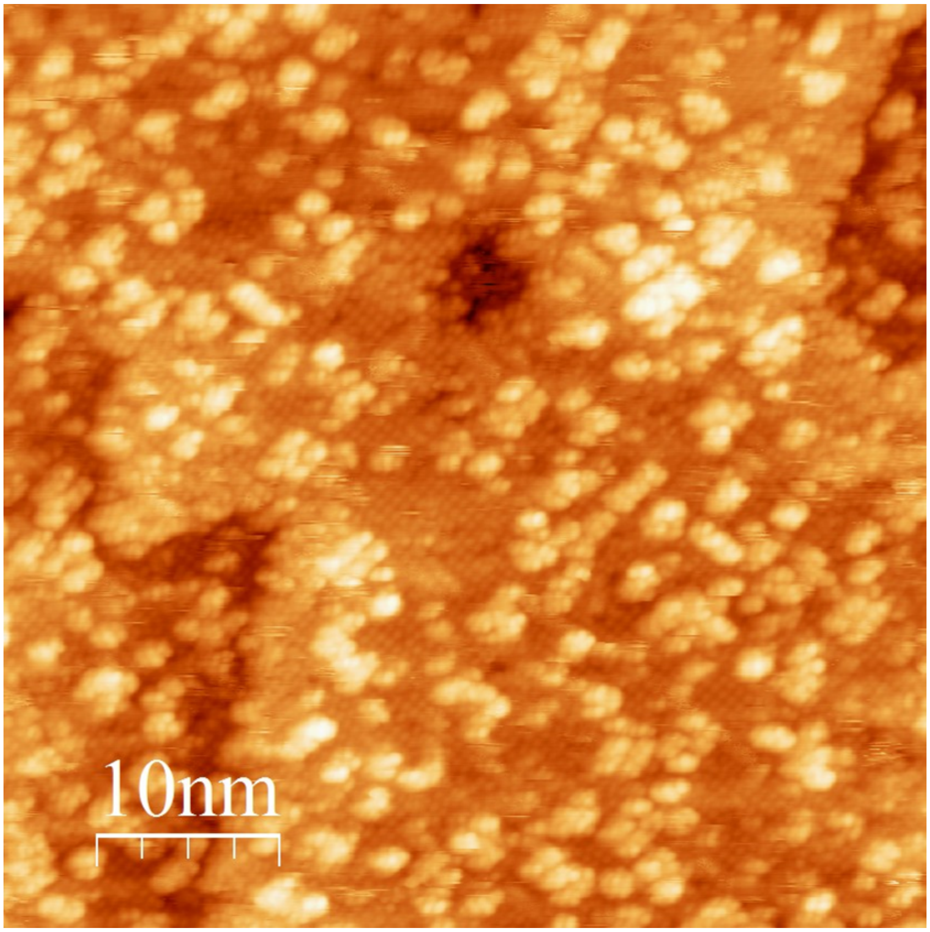

Figure 3.7. 50 nm × 50 nm image of the $TiO_2(110)$ surface following saturation dosing of $Cu(hfac)_2$ at room temperature. $I_t = 80$ pA, V = 1.75 V.

3.4.3 STM for $Cu(hfac)_2/TiO_2$ System and Bimetallic Cu-Pd System

Deposition of $Cu(hfac)_2$ on $TiO_2(110)$ was also studied by STM. Images taken after room temperature adsorption are qualitatively similar to those observed after $Pd(hfac)_2$ adsorption. The adsorption mechanism appears to be the same as for $Pd(hfac)_2$ on $TiO_2(110)$, which is consistent with previous literature reports for the $Cu(hfac)_2/TiO_2(110)$ system. [94,109]. The structured (2×1) overlayer is present, as well as bright clusters on top of the overlayer. An image of the as-dosed $TiO_2(110)$ surface is shown in Figure 3.7.

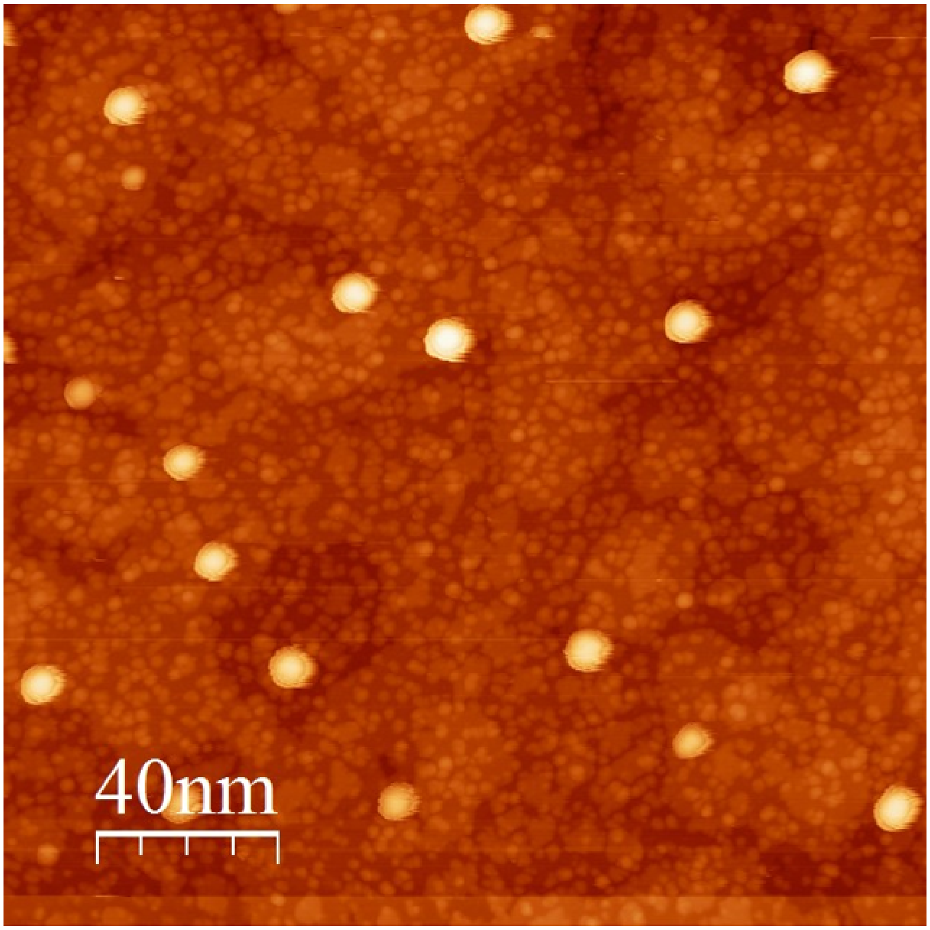

Figure 3.8. 200 nm × 200 nm image of the $TiO_2(110)$ surface following saturation dosing of $Cu(hfac)_2$ at room temperature and subsequent annealing at 500°C. $I_t = 50$ pA, $V = 2.50$ V.

Annealing this surface to 500°C resulted in the formation of Cu nanoparticles with average height of 2.7 ± 0.5 nm. This surface is shown in Figure 3.8.

Following the formation of Cu nanoparticles, the surface was exposed to a saturation dose of $Pd(hfac)_2$ at room temperature in order to study the interaction of the Pd precursor with Cu. Pairs of nanoparticles were observed on this surface (Figure 3.9). Though more work must be done to determine the composition of these nanoparticles, nanoparticle pairs were not observed following annealing the surface exposed to only $Cu(hfac)_2$ at 500°C. These features may be related to the redox trans-

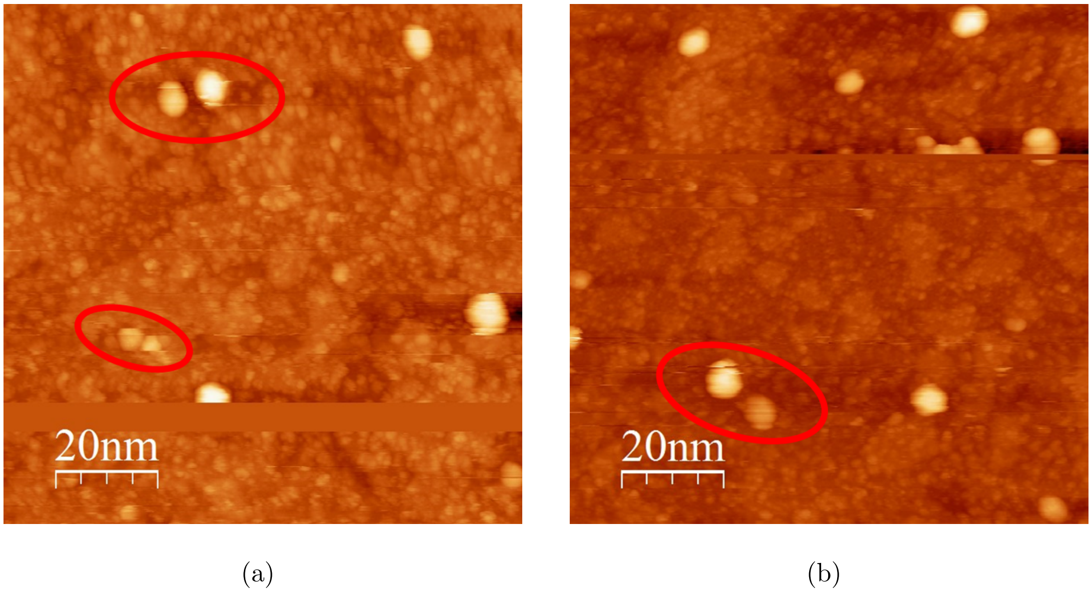

(a) (b)

Figure 3.9. Images of the $TiO_2(110)$ surface following saturation dosing of $Cu(hfac)_2$ at room temperature, subsequent annealing at 500°C, and saturation dosing of $Pd(hfac)_2$ at room temperature. (a) $I_t = 30$ pA, $V = 2.80$ V, 100 nm × 100 nm. (b) $I_t = 50$ pA, $V = 2.50$ V, 100 nm × 100 nm.

metalation reaction that has been observed between $Pd(hfac)_2$ and Cu^0, forming Pd^0 and $Cu(hfac)_2$. [100, 105]

Annealing the sample to 500°C after dosing $Pd(hfac)_2$ resulted in new nanoparticles with an average height of 1.32 ± 0.51 nm, in addition to the existing nanoparticles with average height of 2.7 ± 0.5 nm, which was unchanged (Figure 3.10).

XPS of this surface was inconclusive with regards to the presence of monometallic or bimetallic nanoparticles. More work must be done to determine the identities of these nanoparticles.

3.5 Discussion

On the basis of the experimental data, the mechanism shown in Figure 3.11 is proposed for the interaction of $Pd(hfac)_2$ with $TiO_2(110)$. The cleaning procedure of $TiO_2(110)$ causes thermal desorption of surface oxygen leaving behind a partially

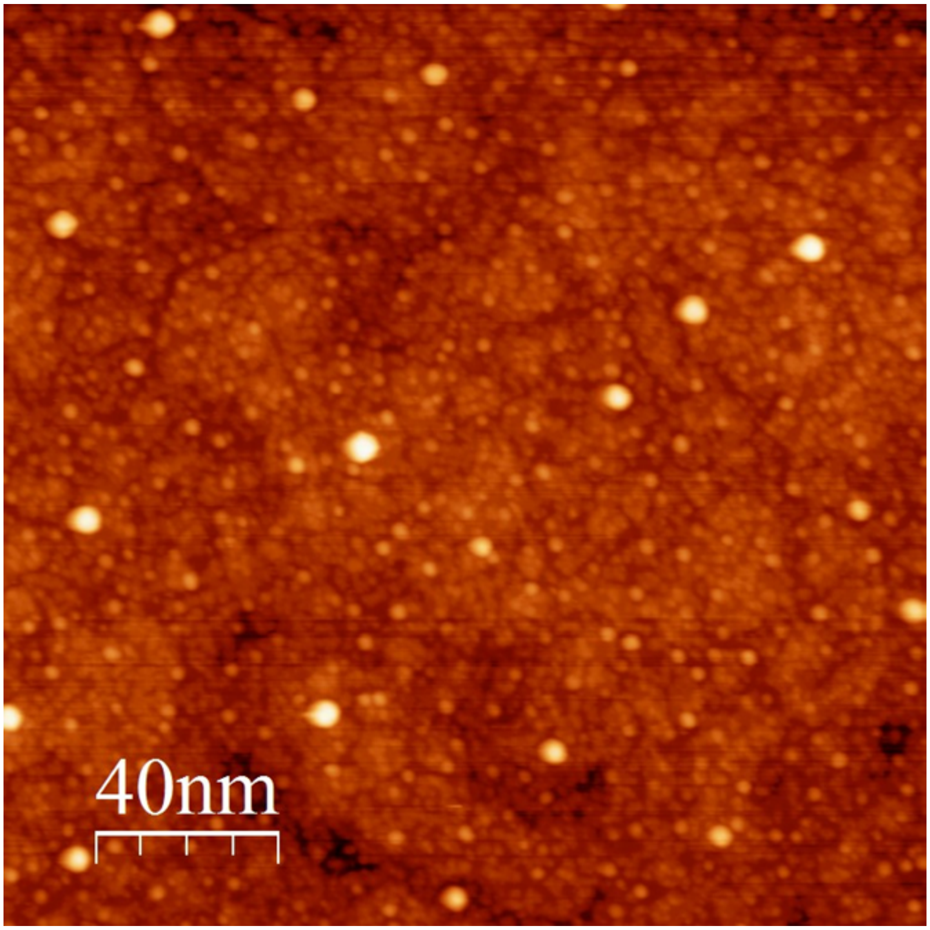

Figure 3.10. STM images of the $TiO_2(110)$ after dosing $Cu(hfac)_2$, annealing to 500C, dosing $Pd(hfac)_2$, and annealing to 500C. $I_t = 80$ pA, V = 2.50 V, 200 nm × 200 nm.

reduced surface with TiO_x species. [107] Upon adsorption at 300–450 K, the $Pd(hfac)_2$ precursor dissociates to $(hfac)_{ads}$ and $Pd(hfac)_{ads}$ species. Further decomposition of the $(hfac)_{ads}$ and $Pd(hfac)_{ads}$ species occurs at 375 and 450 K. The $(hfac)_{ads}$ and $Pd(hfac)_{ads}$ species form a (2×1) surface overlayer. The hfac fragment adsorbs in a bidentate bridging fashion across two Ti 5-fold atoms and Pd(hfac) adsorbs between two bridging oxygen atoms (Figure 3.6). Following $Pd(hfac)_2$ adsorption, the TiO_x species disappeared, showing that $hfac_{ads}$ and its cracked fragments reoxidize the surface (Figure 3.3). This implies that in a parallel path with the adsorption on Ti

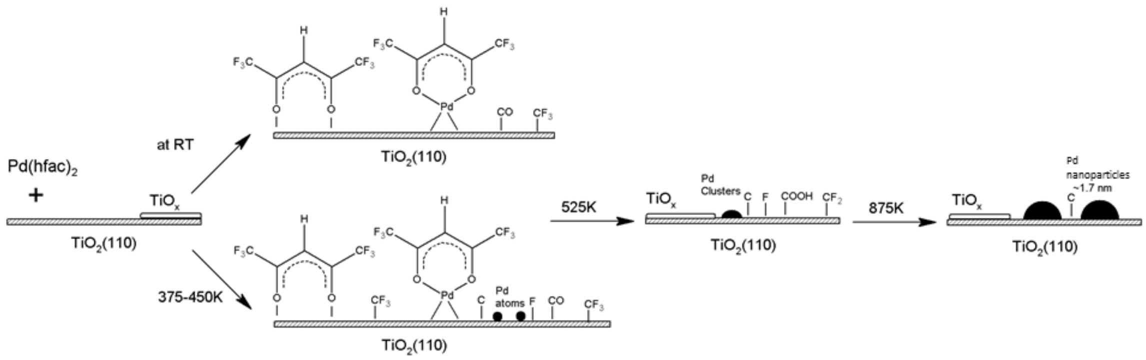

Figure 3.11. Schematic of the reaction of Pd(hfac)$_2$ with a TiO$_2$(110) surface.

5-fold atoms, the hfac$_{\mathrm{ads}}$ species can adsorb on the TiO$_{\mathrm{x}}$ defects and compensate for the lack of oxygen.

Cracked fragments of the hfac ligand were observed at all adsorption temperatures. The degree of hfac decomposition increases with increasing adsorption temperature. Heating the adsorbed layer resulted in decomposition of the Pd(hfac)$_{\mathrm{ads}}$ and(hfac)$_{\mathrm{ads}}$ species, which dissociated at approximately 525 K, leaving cracked hfac fragments and Pd^0 clusters (Figure 3.11). The CF$_3$ species underwent decomposition through sequential loss of fluorine atoms, which then bond to titanium. TiF species were observed on the surface up to 775 K. No fluorine-containing species were detected at 875 K. Carbon atoms segregate to graphitic-like (CC) structures at 575 K. The rest of the carbon-containing species partially desorb: the carbon level decreases upon heating until 675 K and then remains unchanged upon further annealing to 875 K. Once the hfac groups thermally decomposed at 525 K, reduced titania appeared on the surface. At 875 K, the level of reduced titania returned to the original level of the clean TiO$_2$(110) surface due to diffusion of surface oxygen vacancies to the bulk (Figure 3.3).

Following annealing at 775 K, the Pd coverage decreased to 0.07 ML, indicating sintering of the Pd nanoparticles, which is accompanied by the Pd 3d$_{5/2}$ peak shifting toward a lower BE. This BE shift is attributed to the formation of larger Pd nanoparticles. It could also be attributed to the encapsulation of Pd nanoparticles by TiO_x species; however, for Pd particle encapsulation to take place, the TiO_2 support must first be reduced. [111] Here, the TiO_x component decreases continuously upon annealing to 875 K, which indicates absence of encapsulation in our system.

Because $hfac_{ads}$ and its cracked fragments can block $Pd(hfac)_2$ adsorption, their removal is critical for the next deposition cycles. As shown in Figure 3.4, on the surface free of hfac ligands and decomposition fragments, the amount of palladium linearly increases with the number of deposition cycles. The key factor for linear growth was thermal decomposition and removal of the hfac ligands at 875 K prior to each cycle of the $Pd(hfac)_2$ adsorption. On the other hand, for a real $Pd(hfac)_2$ ALD process, the number of typical ALD cycles required to reach steady-state Pd ALD growth was reported to be between 20 to 100 ALD cycles. [83] QCM measurements for $Pd(hfac)_2$ and formalin ALD on TiO_2 showed 0.22 Å growth per cycle. [90] This is about $^1/_3$ of the value of 0.6 Å per cycle calculated from our XPS data. The residual fluorine- and carbon-containing contaminations might cause surface poisoning during the first few cycles (see for instance Elam et al. [83]). The contaminations could be a reason for the lower growth per cycle. Surface blocking by $hfac_{ads}$ and its fragment moieties was assumed to be responsible for Pd nucleation delay on the Al_2O_3 and TiO_2 surfaces. [83, 89, 90]

Following annealing at 875 K, Pd nanoparticles with an average height of 1.7 ± 0.5 nm were obtained. Assuming a hemispherical shape of the particle, the average diameter at the base of the particle is 3.4 ± 1.0 nm. The Pd coverage was estimated to be 0.1 ML after $Pd(hfac)_2$ exposure, and 0.03–0.05 ML after annealing at 875 K, respectively.

3.6 Conclusions

$Pd(hfac)_2$ adsorption is a self-limiting reaction on the $TiO_2(110)$ surface yielding $Pd(hfac)_{ads}$ and/or $hfac_{ads}$ species and partial hfac fragmentation at room temperature. The removal of the hfac ligand and its fragments through thermal decomposition eliminates the initial growth delay period and results in linear growth of Pd on the $TiO_2(110)$ surface. The Pd amount linearly increases with the number of adsorption/dissociation cycles with an average growth per deposition cycle of about 0.05 ML (0.6 Å).

3.7 Acknowledgment

Adapted with permission from Gharachorlou, A.; Detwiler, M. D.; Nartova, A. V.; Lei, Y.; Lu, J.; Elam, J. W.; Delgass, W. N.; Ribeiro, F. H.; Zemlyanov, D. Y. Palladium Nanoparticle Formation on $TiO_2(110)$ by Thermal Decomposition of Palladium(II) Hexafluoroacetylacetonate. *ACS Appl. Mater. Interfaces*, 2014, 6, 14702-14711. Copyright 2014 American Chemical Society.

4. THE SURFACE CHEMISTRY OF TRIMETHYLALUMINIUM ON PD(111) AND PT(111)

4.1 Abstract

The behavior of trimethylaluminium (TMA) was investigated on the surfaces of Pt(111) and Pd(111) single crystals. TMA was found to dissociatively adsorb on both surfaces between 300–473 K. Surfaces species observed by HREELS or XPS after TMA adsorption at 300 K included Al-$(CH_3)_x$ (x = 1, 2, or 3) and $CH_{x,ads}$ (x = 1, 2, or 3) on Pt(111), and ethylidyne (CCH_3), $CH_{x,ads}$ (x = 1, 2, or 3), and metallic Al on Pd(111). DFT calculations predicted methylaluminum (MA, Al-CH_3) to be the most kinetically favorable TMA decomposition product on (111) terraces of both surfaces, however, strong HREELS signatures for Al-$(CH_3)_x$ were detected only on Pt(111). DFT calculations also showed that further dissociation of MA to metallic aluminum and methyl groups to be more kinetically favorable on step sites of both metals. In our proposed reaction mechanism, MA migrates to and dissociates at Pd(111) steps at 300 K forming adsorbed methyl groups and metallic Al. Some methyl groups dehydrogenate and recombine forming ethylidyne. Metallic Al or ejected Pd atoms from steps diffuse across Pd(111) terraces until coalescing into irregularly shaped islands on terraces or steps, as observed by STM. Upon heating above 300 K, the Pd-Al alloy diffuses into the Pd bulk. On Pt(111), a higher coverage of carbon-containing species following TMA adsorption at 300 K prevented MA diffusion and dissociation at steps, as evidenced by isolated clusters of MA in STM images. Heating above 300 K resulted in MA dissociation, but no Pt-Al alloy formation was observed. We conclude that the differing abilities of Pd and Pt to hydrogenate carbonaceous species plays a key role in MA dissociation and alloy formation, and, therefore, the adsorption and

dissociation chemistry of TMA depends on properties of the metal substrate surface and determines thin film morphology and composition.

4.2 Introduction

Palladium and platinum are widely used for heterogeneous catalytic reactions, including carbon-carbon coupling, [112] hydrocarbon oxidation, [79] water-gas shift, [113] and environmental pollution control. [81, 114, 115] Pd and Pt are also the catalysts of choice for hydrogen sensors and fuel cell devices. [116–118] One of the problems for catalytic application of these metals is deactivation due to particle instability (sintering) and carbon deposition (coking). Recently, over-coating Pd and Pt nanoparticles with thin alumina layers synthesized by atomic layer deposition (ALD) using trimethylaluminium (TMA) and water as precursors has been shown to prevent catalyst deactivation. [36,38,85,86,119,120] ALD is a variation of chemical vapor deposition (CVD) based on self-limiting reactions between gaseous precursors and a solid substrate typically covered with functional groups. [121] TMA is one of the most widely used ALD organometallic precursors, and the TMA-water ALD system is one of the most studied (see for instance reference [31] and references therein). Our goal was to study the interaction of TMA with bare transition metal surfaces. There were several attempts in the past to study the TMA reaction pathway on Pd and Pt surfaces. Density functional theory (DFT) predicted that TMA can catalytically dissociate on bare Pd(111) and Pt(111) surfaces, [85, 122] and adsorbed methylaluminum (MA, Al-CH_3,ads) and metallic aluminum were found to be the most thermodynamically favorable TMA decomposition products. TMA adsorption and alumina overlayer growth mechanisms on Pd and Pt have been studied using quadrupole mass spectrometry (QMS) [36, 83, 85, 123] and quartz crystal microbalance (QCM). [36,41,123] On Pd, TMA was hypothesized to form a discontinuous film rather than a continuous overlayer. CO adsorption was observed even after 8 cycles of TMA-water ALD. Lu et al. [85] proposed that on Pd(111) $CH_{3,\mathrm{ads}}$ species block TMA adsorption and can result in non-uniform alumina coverage on Pd. Decomposition of TMA was also suggested to occur preferentially on under-coordinated sites such as steps. [86] Decomposition products block these sites from decomposing additional TMA molecules.

Studying the interaction between an ALD precursor and a substrate by probing surface intermediates during ALD processes is challenging since ALD is typically performed in a flow reactor at millibar pressures with precursor exposure times of a few seconds. Specifically, understanding the chemistry of adsorbed carbon-containing species, which are unavoidable in TMA ALD due to the attached methyl groups, [85] is difficult using only characterization techniques integrated into a conventional ALD reactor. For ultra-thin (< 10 nm) alumina coatings on heterogeneous catalysts, [124] the catalytic substrate itself becomes one of the ALD reactants, and understanding the substrate's role in determining the ALD film chemistry is impossible without using surface sensitive techniques. As highlighted by Zaera, [43] surface characterization techniques in well-controlled environments can improve understanding ALD surface chemistry.

In this publication, we investigate the interaction of TMA with Pd(111) and Pt(111) surfaces using density functional theory (DFT) and surface sensitive characterization techniques, specifically, X-ray photoelectron spectroscopy (XPS), scanning tunneling microscopy (STM), and high resolution electron energy loss spectroscopy (HREELS). This study highlights different hydrocarbon chemistries of Pd and Pt surfaces, which result in different surface morphologies and adlayer compositions during the first TMA ALD half cycle.

4.3 Experimental Methods

Experiments were performed at the Birck Nanotechnology Center (BNC) in an Omicron Surface Analysis Cluster consisting of ultra-high vacuum (UHV) preparation and μ-metal analysis chambers with base pressures of 1×10^{-9} mbar and 5×10^{-11}

mbar, respectively. The preparation chamber was equipped with a residual gas analyzer, Ar^+ sputtering gun, STM tip conditioner, internal bake out system (stab-in quartz IR lamps), and a system of leak valves connected to two separate ALD precursor manifolds. Water and TMA were introduced to the chamber through separate leak valves. The analysis chamber was equipped with XPS, low energy electron diffraction (LEED), HREELS, and STM. The sample could be heated resistively in both chambers. Sample temperature was measured by a K-type thermocouple attached to the sample holder.

STM images were obtained using an Omicron ambient temperature UHV STM/AFM in constant current (topographic) mode. Electrochemically etched W tips were used after conditioning by electron bombardment in UHV. STM images were analyzed using WSxM v3.1 software, [96] and were used to determine the fractal dimension (d_p) based on perimeters and areas of observed islands. The d_p value, which depends on the chosen yardstick length (i.e. size of a pixel), was used to measure perimeter of the fractal islands (P). The yardstick length (δ), which is obtained by dividing total area scanned by the number of pixels in each image, was 0.15 nm. We have considered only islands with an area greater than $200\delta^2$ in our analysis. [125]

HREELS spectra were acquired using an ELS5000 instrument (LK Technologies) in the specular direction with primary beam energy of 5.0 eV. The full width at half maximum (fwhm) of the elastic peak was usually 2.8 meV (23 cm^{-1}), and the intensity of the elastic peak was above 105 cps. All HREELS spectra presented in the paper have been normalized to the elastic peak intensity.

XPS data were acquired using non-monochromatic Mg Kα X-ray radiation ($h\nu =$ 1253.6 eV) with X-ray gun power of 150 W. High resolution spectra were recorded at constant pass energy of 20 eV. The resolution, measured as the FWHMs of the Pd $3d_{5/2}$ and Pt $4f_{7/2}$ peaks, was approximately 1.2 eV. Unfortunately, no energy scale correction was foreseen by the analyzer manufacturer (the electron energy analyzer - Omicron EAC 125 and the analyzer controller - Omicron EAC 2000); therefore, it was possible only to set the Au $4f_{7/2}$ peak to 84.0 eV. Photoelectrons were collected at a photoemission angle of 45° with respect to the surface normal.

XPS data were analyzed with CasaXPS (version 2313Dev64) software. Metallic components of Pt 4f, Pd 3d, Al 2s, Al 2p, and graphitic/carbidic C 1s components, were fitted using an asymmetric Gaussian/Lorentzian line shape with the tail dampening (CasaXPS Line shape=LF(1,1.8,30,90)). Nonmetallic species of C 1s, Al 2s, and Al 2p were fit with symmetric Gaussian/Lorentzian line shapes (CasaXPS Line shape=GL(10) or SGL(10)). Spin-orbit splitting doublets in the Pt 4f ($4f_{7/2}$ and $4f_{5/2}$), Pd 3d ($3d_{5/2}$ and $3d_{3/2}$), and Al 2p ($2p_{3/2}$ and $2p_{1/2}$) spectra were subject to spacing constraints of 3.33, 5.26, and 0.43 eV, respectively. [68] Area ratios for spin-orbit coupling doublets were kept constrained to the expected multiplicity ratios, and FWHMs of these spin-orbit coupling doublets were constrained to be equal. To quantify the XPS result, we followed Fadley's approach [62] which assumes a non-attenuating adlayer at fractional coverage. Coverage (Θ) was measured in monolayers (ML), which is the ratio between the number of adsorbed species and the number of surface atoms (Pt or Pd) on (111) plane. Coverage was calculated using Equation A.7 in Appendix A.

Pd(111) and Pt(111) single crystals with 9.0 mm diameter and 1.0 mm thickness (MaTecK) with orientation accuracy of $< 0.5°$ were used. The single crystals were cleaned by repeated cycles of Ar^+ sputtering and annealing in vacuum at 1000 K and in oxygen at 623 K. Cleanliness was monitored by XPS, LEED, STM, and HREELS.

The single crystals were exposed to TMA (Aldrich, 97%) in the preparation chamber via a leak valve. Prior to dosing TMA, several cycles of freeze-pump-thaw were performed for purification. Dosing lines were heated overnight at 423 K, and the lines were filled with TMA and pumped several times before dosing. In order to passivate the chamber walls for each experiment, the preparation chamber without the sample was exposed to TMA just before dosing to a single crystal. Exposures are reported in Langmuir (L, $1\ \mathrm{L} = 1 \times 10^{-6}$ Torr·s), and were calculated from uncorrected ion gauge measurements. The ionization gauge was left on during TMA dosing, but this did not affect the state of the deposited material as verified by HREELS and XPS. Reported exposure values are estimates because TMA decomposition on chamber walls likely depends on the history of gas exposures, and this might cause errors in reported exposure values especially at low TMA exposures.

DFT calculations were performed by Vienna ab initio simulation package (VASP) [126] using project augmented wave (PAW) [127] potential and PW91 exchange-correlation functional. [126] A plane wave cutoff of 400 eV was used. The optimized lattice constants of bulk Pd and Pt are 3.956 and 3.985 Å, respectively. Four-layer slabs were used to model (111) and (211) surfaces with (2×2) and (1×3) unit cells, respectively. To prevent the artificial interaction between the repeated slabs along z-direction, 12 Å of vacuum was introduced with correction of the dipole moment. A $(4 \times 4 \times 1)$ k-point mesh was used to sample the Brillouin zone. The bottom two layers were fixed, and the remaining atoms and adsorbates were relaxed until the residual forces were less than 0.02 eV/Å. Transition states and reaction barriers were searched by the climbing-image nudged elastic band (CI-NEB) method. [128]

4.4 Results

4.4.1 X-ray Photoelectron Spectroscopy

Figure 4.1 shows nominal Al coverages following exposure of Pd(111) and Pt(111) surfaces to TMA at 473 K. Al coverages were calculated from XPS data using the non-attenuating adlayer model given in Equation A.7 in Appendix A. XPS Al 2s, Al 2p, C 1s, Pd 3d, and Pt 4f core-level regions are shown in Figures 4.2 and 4.3. Al coverage increased with exposure on both surfaces until reaching saturation at about 500 L, demonstrating that TMA acts as an ALD precursor on Pd(111) and Pt(111) under high vacuum conditions. Saturation coverages of aluminum (Θ_{sat}) were 1.40 and 0.96 ML on Pd(111) and Pt(111) surfaces, respectively. The nominal Al coverage of > 1 ML on Pd(111) is a result of Pd-Al alloy formation, discussed below. It should

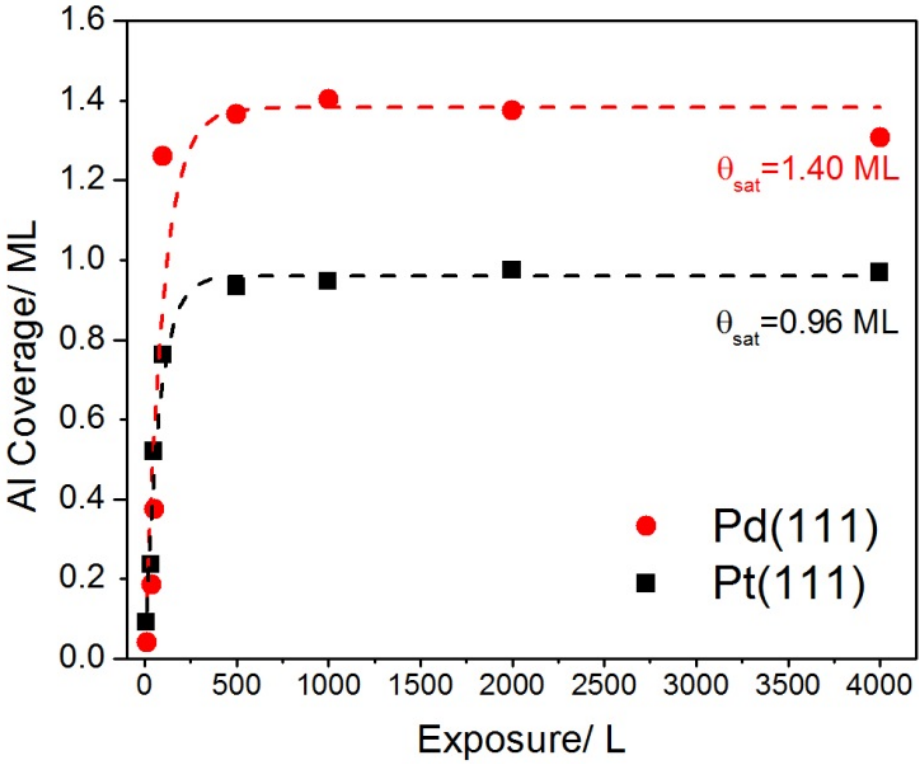

Figure 4.1. Aluminum coverage on Pd(111) and Pt(111) surfaces versus TMA exposure at 473 K. The dashed lines are to guide the eye.

also be noted that the model used to calculate coverages from the XPS data assumes a non-attenuating overlayer, which tends to overestimate coverage.

Figure 4.4 shows typical Al 2s and Al 2p core-level regions obtained from Pt(111) and Pd(111) surfaces exposed to 2000 L TMA at 473 K, and Figure 4.5 shows Pd 3d and Pt 4f core level regions obtained from Pd(111) and Pt(111) surfaces before and after TMA exposure at the same conditions. The Al 2p peak overlaps with Pt 4f; therefore, the Al 2s peak was used for analysis for experiments with Pt(111). On Pt(111), the Al 2s peak was fitted with one component at 118.1 eV, and on Pd(111), the Al 2p region was fitted with one pair of spin orbital components, Al $2p_{3/2}$ and Al $2p_{1/2}$, and the centroid of Al 2p peak was located at 72.9 eV. These BEs are close to reported values for metallic Al of 118.0 eV [129] and 73.0 ± 0.1 eV [130] for Al 2s and Al 2p, respectively. As reported previously for both surfaces, [85, 122] TMA

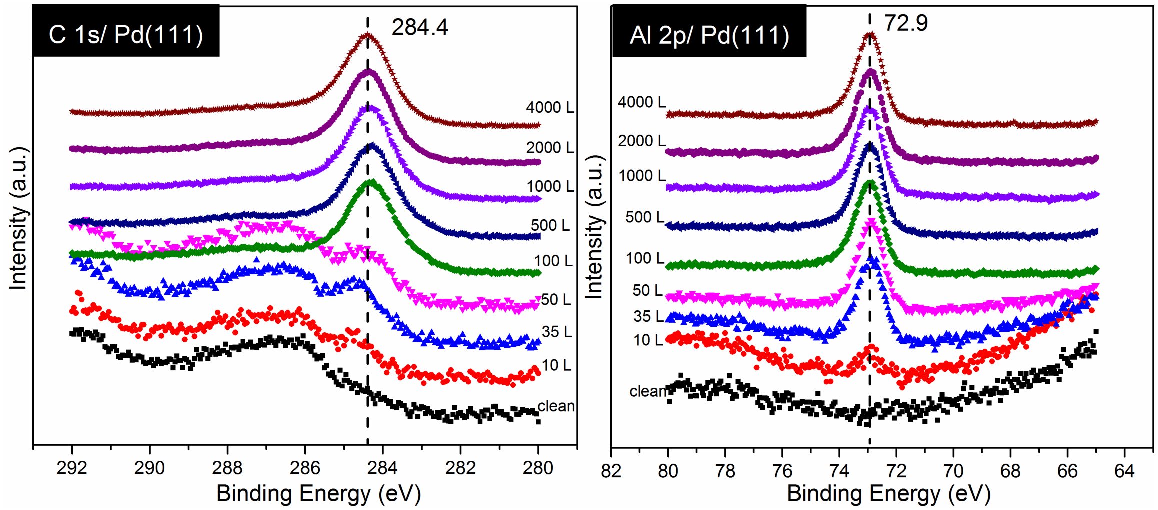

(a) C 1s

(b) Al 2p

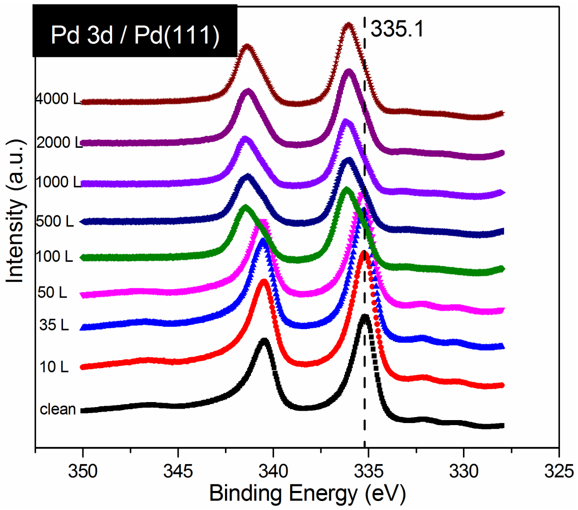

(c) Pd 3d

Figure 4.2. C 1s, Al 2p, and Pd 3d XPS regions for various TMA exposures at 473 K on Pd(111).

was predicted to dissociate to Al-$(CH_3)_x$ species (x = 0, 1, 2), which might have BEs close to those for metallic Al. On the clean surfaces, the Pd $3d_{5/2}$ and Pt $4f_{7/2}$ peaks were located at 335.2 and 71.0 eV, respectively, which are characteristic positions for metallic Pd and Pt, respectively (see for instance references [68, 99] and references

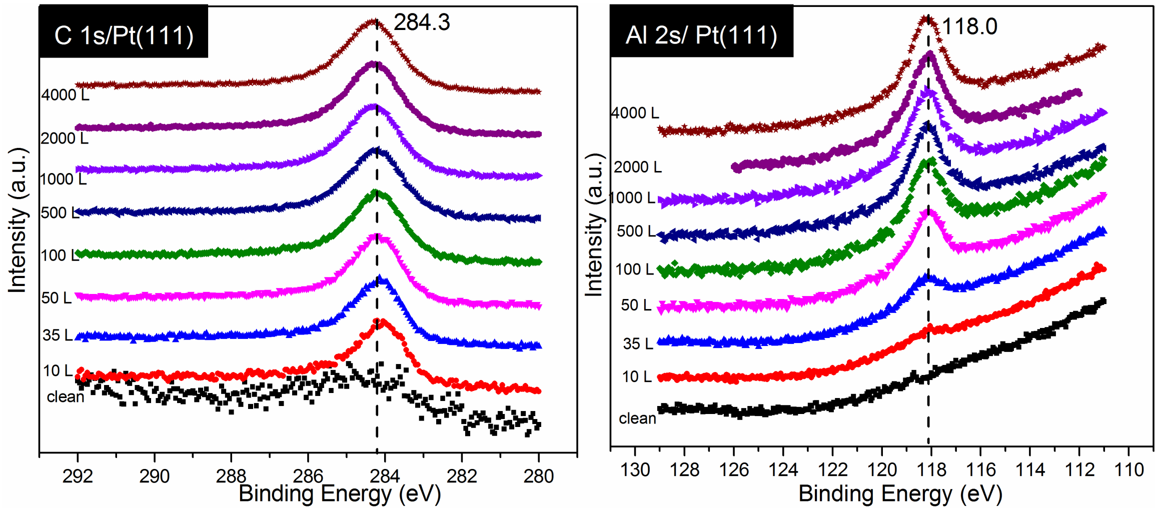

(a) C 1s

(b) Al 2s

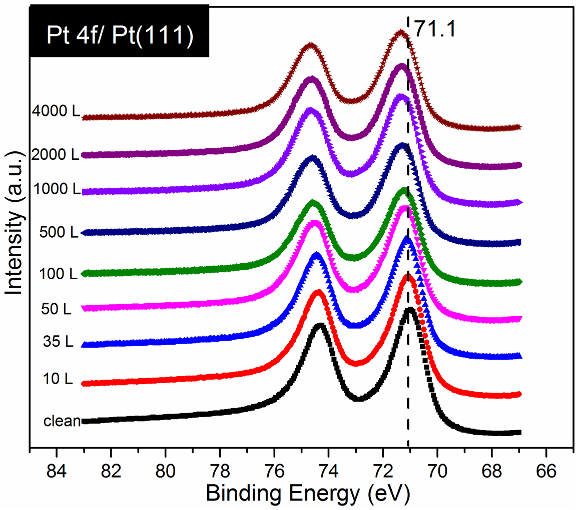

(c) Pt 4f

Figure 4.3. C 1s, Al 2s, and Pt 4f XPS regions for various TMA exposures at 473 K on Pt(111).

therein). Following TMA exposure, the centroid of the Pd $3d_{5/2}$ peak shifted to 336.1 eV (Figure 4.5). The curve-fitting analysis yielded two Pd $3d_{5/2}$ components at 335.2 and 336.2 eV, comprising 36% and 64% of the total Pd 3d peak area, respectively.

The Pt $4f_{7/2}$ peak shifted to 71.2 eV and slightly broadened after TMA adsorption, but was still fitted with one peak (Figure 4.5).

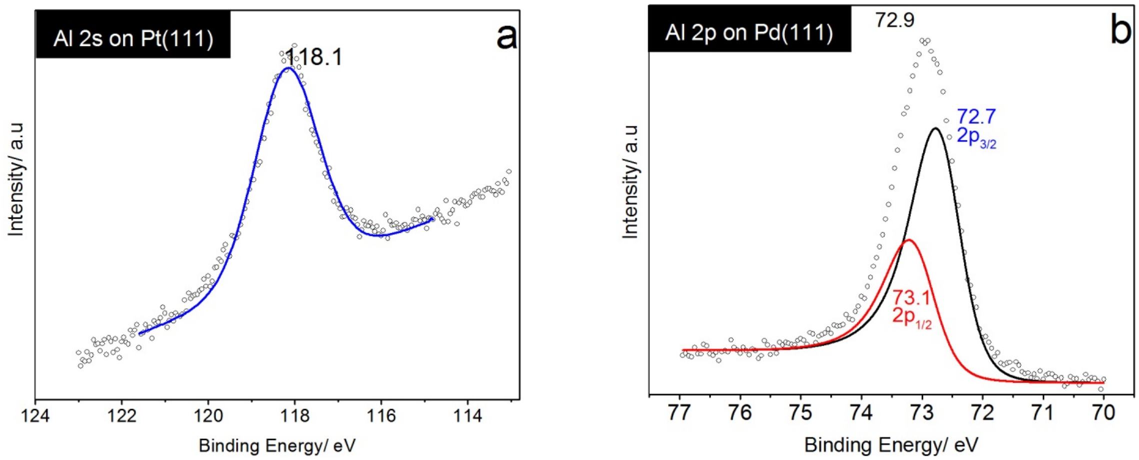

(a) Al 2s on Pt(111)

(b) Al 2p on Pd(111)

Figure 4.4. XPS core-level regions of (a) Al 2s from Pt(111) and (b) Al 2p from Pd(111) following exposure to 2000 L TMA at 473 K.

The changes in the Pt 4f and Pd 3d core-level regions upon TMA adsorption are consistent with reported BE shifts from several phenomena. First, Pd or Pt might alloy with Al. BE shifts of +0.8 to +2.1 eV for Pd 3d and +0.9 to +1.2 eV for Pt 4f have been reported for Pd-Al [131–134] and Pt-Al [135–137] alloys, respectively. Second, adsorbed Al or Al-$(CH_3)_x$ species could cause a BE shift. For example, Pt 4f core-levels have been reported to shift by +1.3 eV upon adsorption of CO on Pt(111). [138] Third, C could diffuse into the Pd bulk, forming a PdC_x phase. Teschner et al. [139] and Gabasch et al. [80] have assigned Pd 3d peaks at 335.7 and 335.34 eV, respectively, to a PdC_x phase. In order to determine the origin of the above BE shifts, Al adlayers prepared at 473 K by exposure of Pd(111) and Pt(111) to 3 L and 10 L TMA, respectively, were heated at 623 K in UHV. The results are shown in Figure 4.6. On Pd(111), Al coverage gradually decreased with time from approximately 0.2 ML to 0.1 ML while the BE of the Al 2p peak remained at 72.9 eV. After exposure of the annealed surface to 4 × 10^4 L oxygen at 623 K, the Al

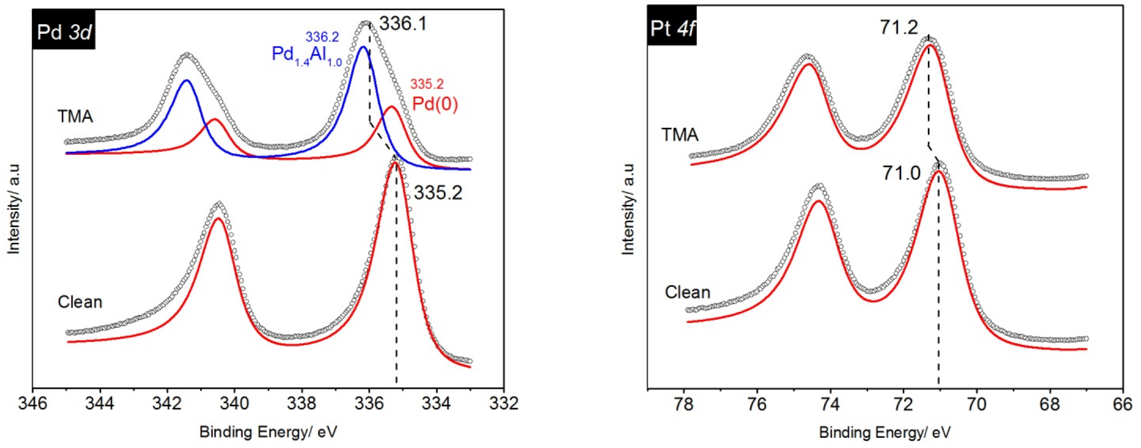

(a) Pd 3d on Pd(111)

(b) Pt 4f on Pt(111)

Figure 4.5. Pd 3d and Pt 4f core-level regions obtained from clean Pd(111) (left) and Pt(111) (right) surfaces (bottom spectra) and following exposure to 2000 L TMA at 473 K (top spectra).

coverage jumped beyond the initial value to approximately 0.25 ML (the blue shaded regions in Figure 4.6). The Al 2p peak shifted to 74.1 eV, a characteristic position for Al_2O_3. [140] This behavior is consistent with Al dissolution into the Pd bulk during heating, then segregation to the surface during O_2 exposure. On Pt(111), Al coverage did not change during annealing at 623 K in UHV as shown in Figure 4.6, which proved that Al did not diffuse into the Pt bulk, and that Al did not evaporate. The Al 2s peak at 118.1 eV did not shift upon heating in UHV. In addition, subsequent O_2 exposure did not change the Al coverage, as shown in the shaded blue region of Figure 4.6. The Al 2s peak broadened and shifted to 118.5 eV, and a shoulder appeared on the higher binding energy side at 118.9 eV.

Based on this analysis, we assigned the Pd $3d_{5/2}$ peaks at 335.2 and 336.2 eV to metallic Pd and a Pd-Al alloy, respectively. Assuming that all Al from XPS quantification of the Al 2p or Al 2s regions is alloyed with Pd, the average Pd-Al alloy composition is $Pd_{1.4}Al_{1.0}$, and the calculated thickness of the alloy was estimated to be 1.2 nm. The corresponding Al 2p peak shift for a +2.1 eV shift in the Pd 3d peak was reported to be approximately +0.1 eV relative to metallic Al, [141] hence,

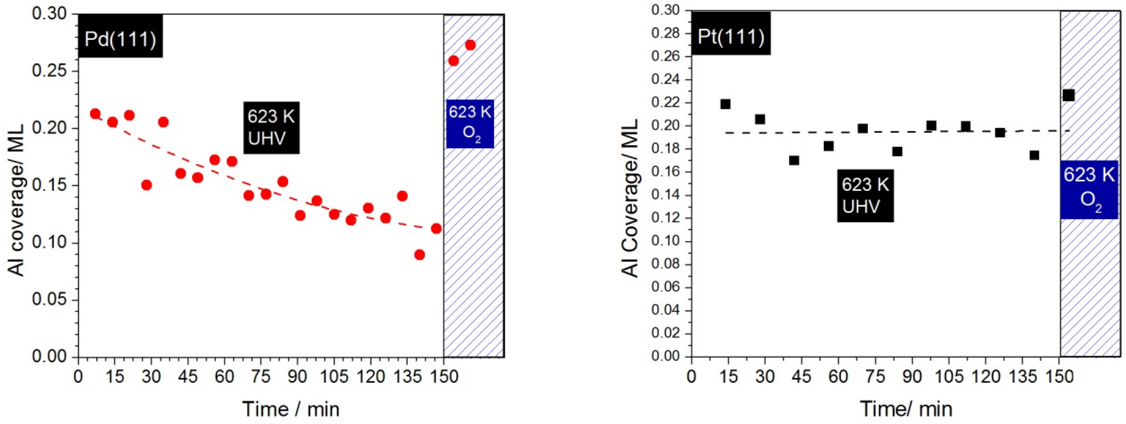

(a) Pd(111) (b) Pt(111)

Figure 4.6. Aluminum coverage on Pd(111) (left panel) and Pt(111) (right panel) as a function of time at 623 K in UHV. The points within the shaded regions were obtained following 4×10^4 L O_2 exposure at 623 K. The initial Al adlayers were prepared by exposing Pd(111) and Pt(111) to 3 L and 10 L of TMA, respectively, at 473 K. The XPS data were obtained at 623 K. The dashed lines serve to guide the eye.

a corresponding Al 2p peak shift for the Pd-Al alloy here was not observed. In the case of Pt(111), the shift of +0.2 eV and slight broadening of the Pt $4f_{7/2}$ peak was assigned to the influence of the surface adsorbates. We observed a +0.2 eV BE shift of the Pt $4f_{7/2}$ peak after exposing Pt(111) to TMA using surface-sensitive synchrotron-based XPS, confirming the surface nature of the phenomenon. [122] For a lab XPS, the EAL of a Pt 4f photoelectron excited by Mg Kα X-ray radiation is approximately 10.5 Å, meaning that bulk layers dominate the signal and that surface changes would result in only a slight peak shift and broadening. Therefore, we conclude that no Pt-Al alloy formed, consistent with our synchrotron-based XPS results. [122]

Plotted in Figure 4.7 are carbon to aluminum ratios versus TMA exposure at 473 K on Pd(111) and Pt(111). C:Al was about 2.5 on Pt(111) and 1.3 on Pd(111) at saturation TMA exposures (> 500 L). As shown in the inset of Figure 4.7, the carbon coverage increased rapidly on Pt(111) at TMA exposures < 50 L. The initial C:Al ratio of 6.5 on the Pt(111) surface at 10 L exposure was higher than the expected value of 3:1 based on TMA stoichiometry. This error might have been introduced by using the Al 2s peak for quantification which had a low relative sensitivity factor and, as a result, a poor signal-to-noise ratio. Additionally, despite our best efforts to avoid TMA decomposition during exposure (see the Experimental section), TMA molecules might decompose on the walls of the chamber, and this could result in a C:Al ratio > 3. TMA and hydrocarbon fragments could adsorb on the surface simultaneously. The decreasing C:Al ratio with increasing TMA exposure suggests that TMA replaced hydrocarbons on the surface until reaching an equilibrium C:Al ratio of 2.5.

The behavior of carbon on Pd(111) was different: carbon coverage at low TMA exposures was negligible, but aluminum coverage increased with TMA exposure (Figure 4.7). This demonstrated that Pd(111) can hydrogenate hydrocarbon species originating from TMA dissociation. At higher Al coverage the Pd(111) surface lost its ability to remove carbon. The C:Al ratio was 1.3 at the saturation Al coverage of 1.4 ML.

4.4.2 High Resolution Electron Energy Loss Spectroscopy

Since a single C 1s peak was observed at ca. 284.3 eV, identification of carbonaceous species following exposure of Pd(111) and Pt(111) to TMA based on XPS alone was not possible. Therefore, TMA adsorption on Pd(111) and Pt(111) was studied using HREELS. Figure 4.9 shows HREELS spectra obtained from the Pt(111) surface exposed to 6 L TMA at 300 K and then annealed at 373 and 473 K in UHV. Table 4.1 summarizes the literature data for TMA and other relevant hydrocarbon species adsorbed on metal surfaces. Table 4.2 lists the assignments of main HREELS peaks observed in each experiment.

HREELS data confirmed dissociative adsorption of TMA on Pt(111) at 300 K. The peak at 2950 cm^{-1} was assigned to asymmetric stretching of CH_3, $\nu_{as}(CH_3)$; 2906 cm^{-1} to symmetric stretching of CH_3, $\nu_s(CH_3)$; 1460 cm^{-1} to asymmetric de-

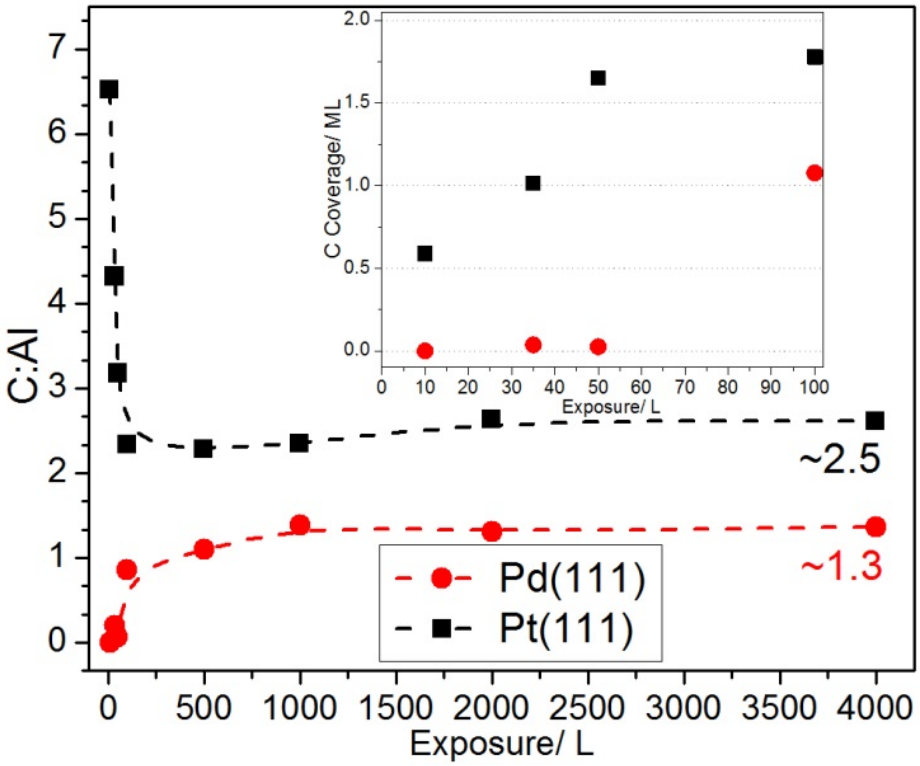

Figure 4.7. Carbon to aluminum coverage ratio plotted against TMA exposure on Pt(111) and Pd(111) surfaces at 473 K. Coverages were calculated using XPS data. Inset: Carbon coverage as a function of TMA exposure for exposures up to 100 L. The dashed lines are to guide the eye.

formation of CH_3, $\delta_{as}(CH_3)$; 1176 cm^{-1} to symmetric deformation of CH_3, $\delta_s(CH_3)$; 750 cm^{-1} to rocking of CH_3, $\rho(CH_3)$; and 540 cm^{-1} to deformation of Al-$(CH_3)_x$, δ(Al-$CH_3)_x$. These spectroscopic signatures unambiguously pointed to the presence of Al-$(CH_3)_{x,ads}$ (x = 1, 2, or 3) species. The resolution of HREELS was not sufficient to discriminate between Al-CH_3, Al-$(CH_3)_2$, and Al-$(CH_3)_3$. The peak at 1210 cm^{-1} was assigned to a symmetric deformation of CH_3 adsorbed on Pt(111), $\delta_s(CH_3)$. Stretching vibrations of $CH_{3,ads}$ species on Pt(111) were expected around 2950 cm^{-1} but likely overlapped with Al-$(CH_3)_x$ stretching bands. The deformation (δ(CH)) and rocking ($\rho(CH_2)$) vibrations of CH_{ads} and $CH_{2,ads}$, respectively, would be located around 700-860 cm^{-1}, however, the region below 1000 cm^{-1} is crowded with peaks, so these species may be present. In summary, TMA adsorption on Pt(111) at 300 K led to the formation of adsorbed species including Al-$(CH_3)_x$ (x = 1, 2, or 3), and $CH_{x,ads}$ (x = 1, 2, or 3).

Heating this adlayer at 373 K resulted in changes to the HREELS spectrum. All vibrations associated with Al-$(CH_3)_{x,ads}$ species decreased in intensity, but the deformation band at 1210 cm^{-1} of the $CH_{3,ads}$/Pt(111) species did not change. A new peak was observed at 1380 cm^{-1} and was assigned to the in-plane bending mode of methylene, $CH_{2,ads}$. A peak at 3030 cm^{-1}, the stretching mode of $CH_{2,ads}$, appeared after heating at 373 K. Methylene has been observed during the thermal decomposition of TMA and trimethylindium (TMIn) on the GaAs(100) surface. [142, 143] In our case, methylene might form through decomposition of Al-$(CH_3)_{x,ads}$ followed by migration of methyl groups to Pt(111) and subsequent dehydrogenation. Further dehydrogenation of $CH_{2,ads}$ to CH_{ads} was not confirmed because the region around 700 cm^{-1} is filled with unresolved features which hindered detection of the δ(CH) peak. Additionally, the stretching frequency of CH_{ads} may overlap with stretching bands of $CH_{3,ads}$ around 2950 cm^{-1}.

No C-H loss peaks were detected following heating at 473 K, indicating complete dehydrogenation of hydrocarbons. XPS data showed the presence of carbon after annealing to 623 K (Figure 4.8). Based on literature data, [144, 145] remaining carbon could be in the form of atoms and/or clusters. No straightforward assignment was made for low frequency features below 1000 cm^{-1}. A weak peak centered at approximately 1980 cm^{-1} was assigned to CO_{ads} originating from residual CO in the vacuum system.

Figure 4.9 displays HREELS spectra obtained after exposure of the Pd(111) surface to 6 L TMA at 300 K and following annealing at 373 and 473 K in UHV. Table 4.3 shows the assignments of the main HREELS peaks observed after TMA adsorption on Pd(111) and heating in UHV. The HREELS peaks at 1012 (ν(C-C)), 1090 ($\rho(CH_3)$), 1328 ($\delta_s(CH_3)$), 1400 ($\delta_{as}(CH_3)$), 2890 ($\nu_s(CH_3)$), and 2964 ($\nu_{as}(CH_3)$) cm^{-1} were

Table 4.1.
Main characteristic vibrations of hydrocarbon species on metal surfaces. [a] t: terminal,[b] x = 1, 2, or 3.

Mode	Al-$(CH_3)_x$[b]	M-CH_3	M=CH_2	M≡CH	Ethylidyne
$\nu_{as}(CH_3)$	2940-2950 [142, 146–149]				2890-2928 [150–153]
$\nu_s(CH_3)$	2900-2907 [146–148]	2955-3044 [154–156]			2890-2928 [150–153]
$\nu_{as}(CH_2)$			2900-2925 [142, 143, 157]		
$\nu_s(CH_2)$			2850 [157]		
ν(CH)				2950-2975 [144, 158]	
$\delta_{as}(CH_3)$	1430-1450 [142, 159, 160]	1420-1435 [154, 156]			1400-1420 [150, 153]
$\delta_s(CH_3)$	1196-1217 [146, 147, 149, 159, 160]	1180-1285 [154–156]			1329-1350 [150–153, 161]
$\delta(CH_2)$			1340 [142, 143]		
ν(C-C)					900-1180 [144, 151–153]
$\rho(CH_3)$	650-742 [142, 146]	882-1040 [154–156]			923 [162]
$\rho(CH_2)$			860-865 [142, 143]		
δ(CH)				770-805 [144, 158, 162]	
δ(Al-CH_3[t])[a]	567 [146]				
ν(M-C)		495-520 [156]			371 [151]

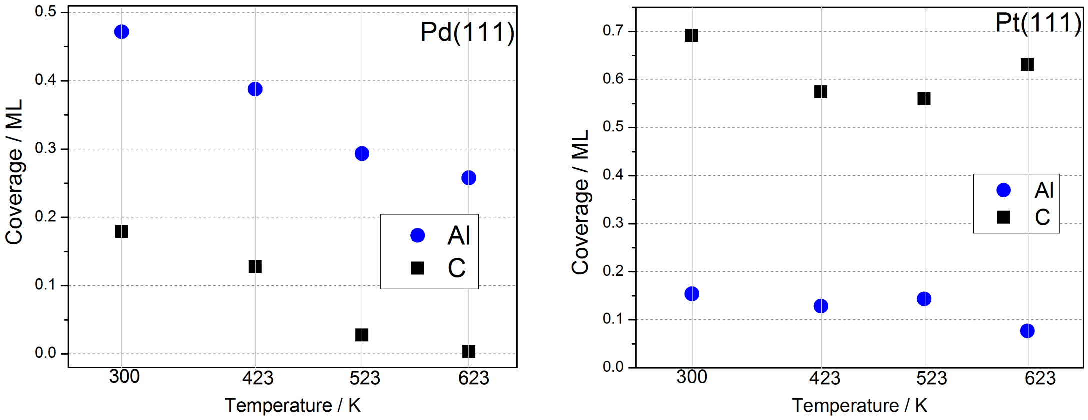

(a) Pd(111)

(b) Pt(111)

Figure 4.8. Al and C coverages after exposure of (a) Pd(111) and (b) Pt(111) surfaces to 2.5 L TMA at room temperature and annealing up to 623 K.

characteristic peaks of ethylidyne ($\equiv CCH_{3,ads}$). The peak at 1210 cm^{-1}, also observed on Pt(111), was assigned to symmetric deformation of CH_3 adsorbed on Pd(111), $\delta_s(CH_3)$. The high frequency region shows a broad, unresolved feature centered at 2940 cm^{-1} which comprises stretching vibrations of all C-H containing species. The individual stretching vibration of CH_3 was not resolved. The presence of $CH_{2,ads}$ was supported by a weak unresolved shoulder at 3035 cm^{-1}. The HREELS region below 1000 cm^{-1} is crowded, and the presence of δ(CH) at about 700 cm^{-1} was not confirmed. Additionally, a weak peak at 1167 cm^{-1} was detected, which is a symmetric deformation $\delta_{as}(CH_3)$ of Al-$(CH_3)_x$. Ethylidyne signatures overlapped with other peaks; however, judging from the peak intensities, the amount of the Al-$(CH_3)_x$ species on Pd(111) was much lower than on Pt(111).

A broad peak centered at about 1780 cm^{-1} was assigned to CO_{ads} which originated from residual CO. The presence of CO_{ads} indicates that the surface had adsorption sites for CO after adsorption/decomposition of 6 L TMA. This was not the case for Pt(111). Also, the CO stretching frequency shifted toward lower energy compared to CO adsorption on a clean Pd(111) surface, where the CO stretching band was at 1928

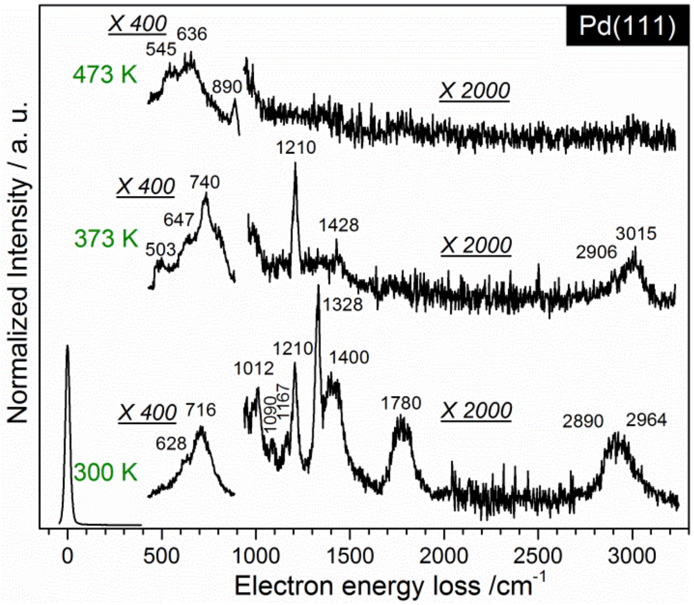

(a) Pd(111)

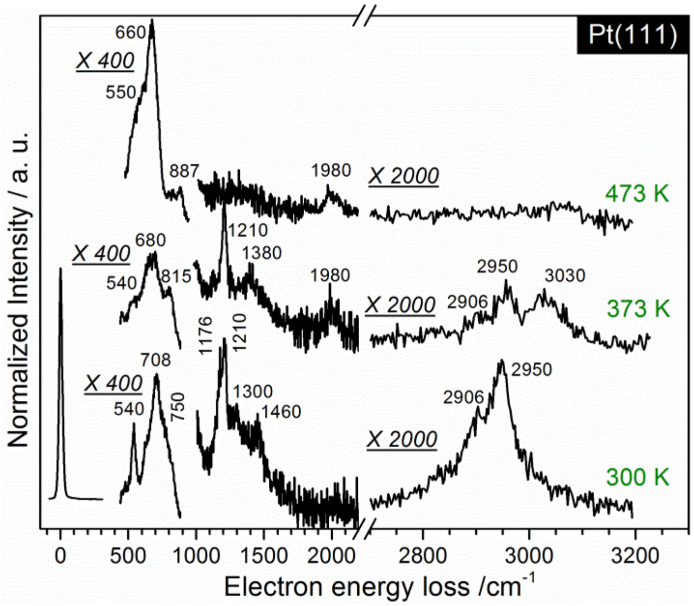

(b) Pt(111)

Figure 4.9. HREELS spectra obtained from (a) Pd(111) and (b) Pt(111) following 6 L TMA exposure at 300 K and subsequent annealing at 373 and 473 K in UHV.

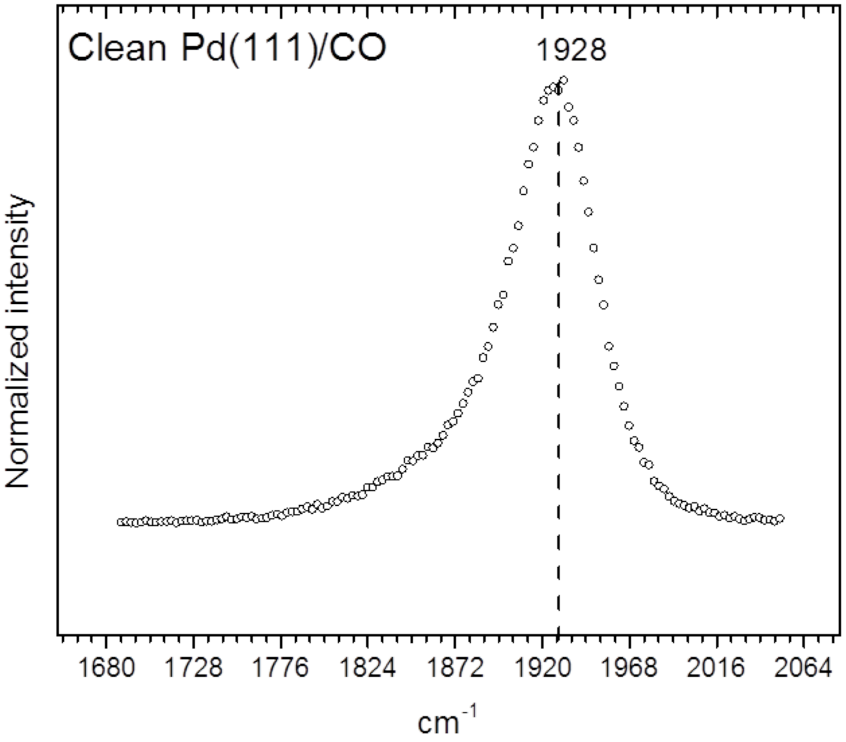

Figure 4.10. HREELS spectrum for room temperature saturation CO adsorption on clean Pd(111).

cm^{-1} for saturation CO coverage at 300 K. This HREELS spectrum is provided in Figure 4.10. The surface hydrocarbon groups may decrease the C-O bonding strength and elongate the CO bond length through the back-donation of metal electrons to $2\pi^*$ orbital of CO. [163] This would result in a shift of CO stretching toward lower frequencies. However, detailed discussion of CO adsorption is beyond the scope of this dissertation.

Heating at 373 K resulted in the disappearance of all ethylidyne peaks. Peaks at 2890 and 2964 cm^{-1}, assigned to $\nu_s(CH_3)$ and $\nu_{as}(CH_3)$ of ethylidyne, were not observed. Ethylidyne is reported to be stable up to 300 K on the Pd(111) surface.

[150, 151, 164] No HREELS peaks of the Al-$(CH_3)_x$ species were detected following heating at 373 K, whereas the symmetric deformation of CH_3 adsorbed on Pd(111) at 1210 cm^{-1} did not change in intensity. The weak peak at 2906 cm^{-1} might be a feature of $\nu_{as}(CH_2)$ for $CH_{2,ads}$ or CH_{ads}; however, δ(CH) at ca. 700 cm^{-1} was not resolved.

No energy loss peaks were observed above 1000 cm^{-1} after heating at 473 K. Based on the XPS data, carbon coverage was ca. 0.1 ML at this temperature (see Figure 4.8). The HREELS region below 1000 cm^{-1} was similar to the spectrum from TMA/Pt(111) at 473 K. No straightforward assignments were possible.

To summarize, HREELS data showed that TMA adsorption on Pt(111) and Pd(111) resulted in different compositions of the adsorbed layers. Al-$(CH_3)_x$ species dominated on Pt(111). Adsorbed CH_x species (x=1, 2, 3) were detected on both Pt(111) and Pd(111). Ethylidyne was only observed on Pd(111). The appearance of ethylidyne proves that Pd(111) can recombine hydrocarbon fragments. Some fraction of the remaining C1 species dehydrogenates completely to atomic carbon, and hydrogen produced is consumed for hydrogenation of other C1 species. CH_3 symmetric bending modes for bridging CH_3 were not observed in HREELS data at ca. 1255 cm^{-1} on either metal at any temperature for spectra collected in the specular direction. [165] Given the instability of the intact TMA monomer on Pd and Pt(111) reported previously, [122] presence of the TMA dimer on either surface is unlikely.

4.4.3 Scanning Tunneling Microscopy

Morphology of the Pd(111) and Pt(111) surfaces was studied by STM after exposure to 2.5 L TMA at 293 K and after subsequent annealing to 423, 523, and 623 K in UHV. Low TMA exposure was chosen for this presentation because higher TMA exposures (> 20 L) resulted in a roughened surface, which impaired STM. STM images of clean Pt(111) and Pd(111) surfaces (shown in Figure 4.11) demonstrated atomically flat terraces separated by monatomic steps with heights of 2.4 and 2.3 Å, respectively. Following exposure of Pd(111) to 2.5 L TMA at 293 K, two additional distinct features were observed: (i) fractal islands that look like Norwegian fjords covering steps that appear to grow out of a step onto the lower plane, and (ii) fractal islands covering terraces. (Figure 4.12a). Terraces and monatomic steps were still distinguishable. The average height of the terrace fractal islands was 2.0 ± 0.3 Å, measured as the bimodal peak histogram of terrace pixel heights (Figure 4.12b). The bimodal distribution confirms the uniform height and flatness of the islands. The fractal features on monatomic steps had a height of 2.0 ± 0.3 Å, the same as the steps. Therefore, the fractal islands and terraces likely had the same composition. According to the XPS and HREELS data, TMA dissociated on Pd(111) to aluminum and hydrocarbon species. The positive Pd 3d BE shift was evidence of Pd-Al alloy formation. We conclude that the fractal islands are composed of a Pd-Al alloy. As reported by Batabyal et al., [166] the shape of the two dimensional fractal islands can be quantified in terms of fractal dimension, d_p, obtained from the relationship between perimeter, P, and area, S, as $\ln P = \frac{d_p}{2} \ln S$. The fractal dimension was $d_p = 1.68 \pm 0.01$ after adsorption of 2.5 L TMA on Pd(111) at 293 K (Figure 4.12c).

Figure 4.13 shows STM images obtained after exposure of Pd(111) to 2.5 L TMA at 293 K and sequential annealing at 423, 523 and 623 K in UHV. The perimeter fractal dimensions and the height distribution histograms were obtained in the same manner as in Figure 4.12 for each temperature; plots are provided in Figure 4.14. Heating at 423 K decreased the fractal dimension to 1.35 ± 0.03. Further heating at 523 K did not alter the d_p value (approximately 1.38 ± 0.02). After annealing at 623 K, d_p decreased to 1.2 ± 0.04. Island height remained constant (ca. 2 Å) after annealing at 300, 423 and 623 K (Figure 4.14). Small pinholes on the surface of Pd-Al islands were noticeable after annealing at 623 K as highlighted by black arrows in Figure 4.13. These pinholes may have formed from the diffusion of Al atoms into the palladium bulk, a hypothesis consistent with the XPS data which show that the aluminum coverage decreased upon annealing (shown in Figures 4.6 and 4.8).

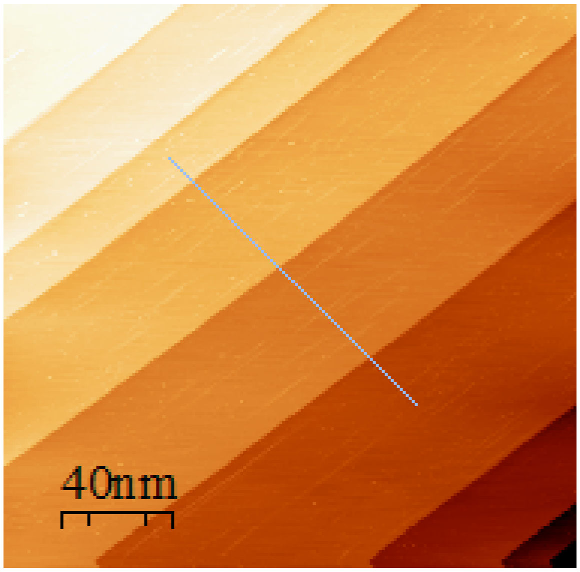

(a) Pd(111)

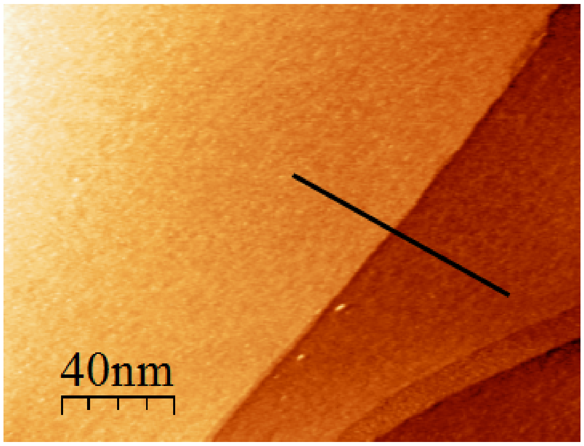

(b) Pt(111)

Figure 4.11. STM images of (a) clean Pd(111) ($I_t = 0.5$ nA, $U_t = 0.5$ V) and (b) Pt(111) ($I_t = 0.3$ nA, $U_t = 0.5$ V) surfaces. Step heights across the profiles are 0.23 nm and 0.24 nm, respectively, for Pd(111) and Pt(111).

Figure 4.15 shows STM images of Pt(111) following 2.5 L TMA exposure at 300 K and consecutive annealing to 423, 523 and 623 K. Unlike for Pd(111), no fractal shaped features were detected on the Pt(111) surface. Bright, elongated spots with

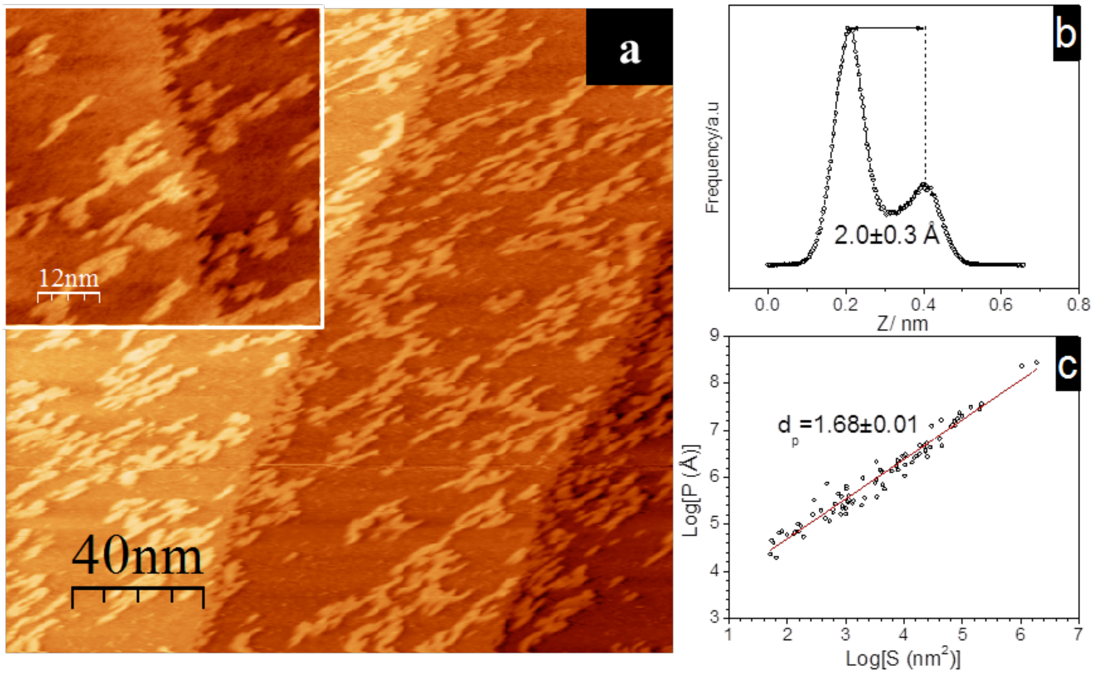

Figure 4.12. (a) STM images of Pd-Al fractal islands on the Pd(111) surface exposed to 2.5 L TMA at 293 K. Imaging conditions: 200 nm × 200 nm, I_t = 0.5 nA, U_t= 0.5 V. (b) Histogram of pixel height on the terraces. (c) Logarithmic plot of the perimeter (P) vs. area (S) relationship of Pd-Al islands.

apparent height of 2.2 ± 0.4 Å were homogeneously distributed on the surface. Based on HREELS data, these bright features were assigned to Al-$(CH_3)_x$ species.

After annealing at 423 K in UHV, bright spots appeared, which can be readily seen in the inset of Figure 4.15. The height distribution had one maximum at about 2.3 Å and a broad tail up to 5 Å (Figure 4.16). According to XPS and HREELS data, at this temperature Al-$(CH_3)_x$ species can dissociate to $CH_{x,ads}$ and aluminum. Likely, these aluminum and/or carbon atoms agglomerated into clusters, which appear in STM images as features of mixed height. Further annealing to 523 K and 623 K narrowed the height distributions of these features to 1.8 ± 0.4 Å and 1.6 ± 0.6 Å, respectively. At these temperatures only aluminum and carbon were observed by

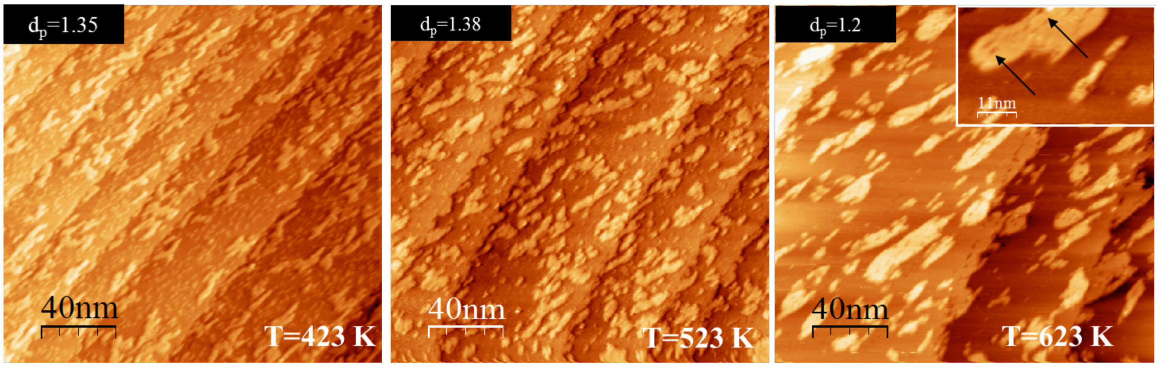

Figure 4.13. STM images of Pd-Al islands after annealing at 423, 523 and 623 K for 15 min. The Pd-Al islands were obtained by exposing Pd(111) to 2.5 L TMA at 293 K. Imaging conditions: 200 nm × 200 nm, I_t= 0.5 nA, U_t = 0.5 V.

XPS. This narrowing of the height distribution and shifting to shorter heights likely corresponds to the flattening of aluminum and/or carbon clusters, consistent with the observation that hydrocarbons on Pt(111) form carbon particles and eventually flat graphite sheets upon heating (see for instance Ref. [167]).

4.4.4 DFT

DFT modeling was performed to better understand the mechanism of TMA interaction with Pd(111) and Pt(111) surfaces. Previous calculations showed that MA is the most favorable TMA decomposition product kinetically and thermodynamically on both Pd(111) and Pt(111); therefore, MA was expected to be the dominant species. [85, 122] Potential energy surfaces for further dissociation of MA on clean Pt(111) and Pd(111) terraces, and clean and CH_3/CCH_3 covered Pd(211) and Pt(211) surfaces are shown in Figure 4.17. The calculated barriers for hollow-site MA dissociation to Al and CH_3 are 1.68 and 1.72 eV on clean Pd(111) and Pt(111), respectively.

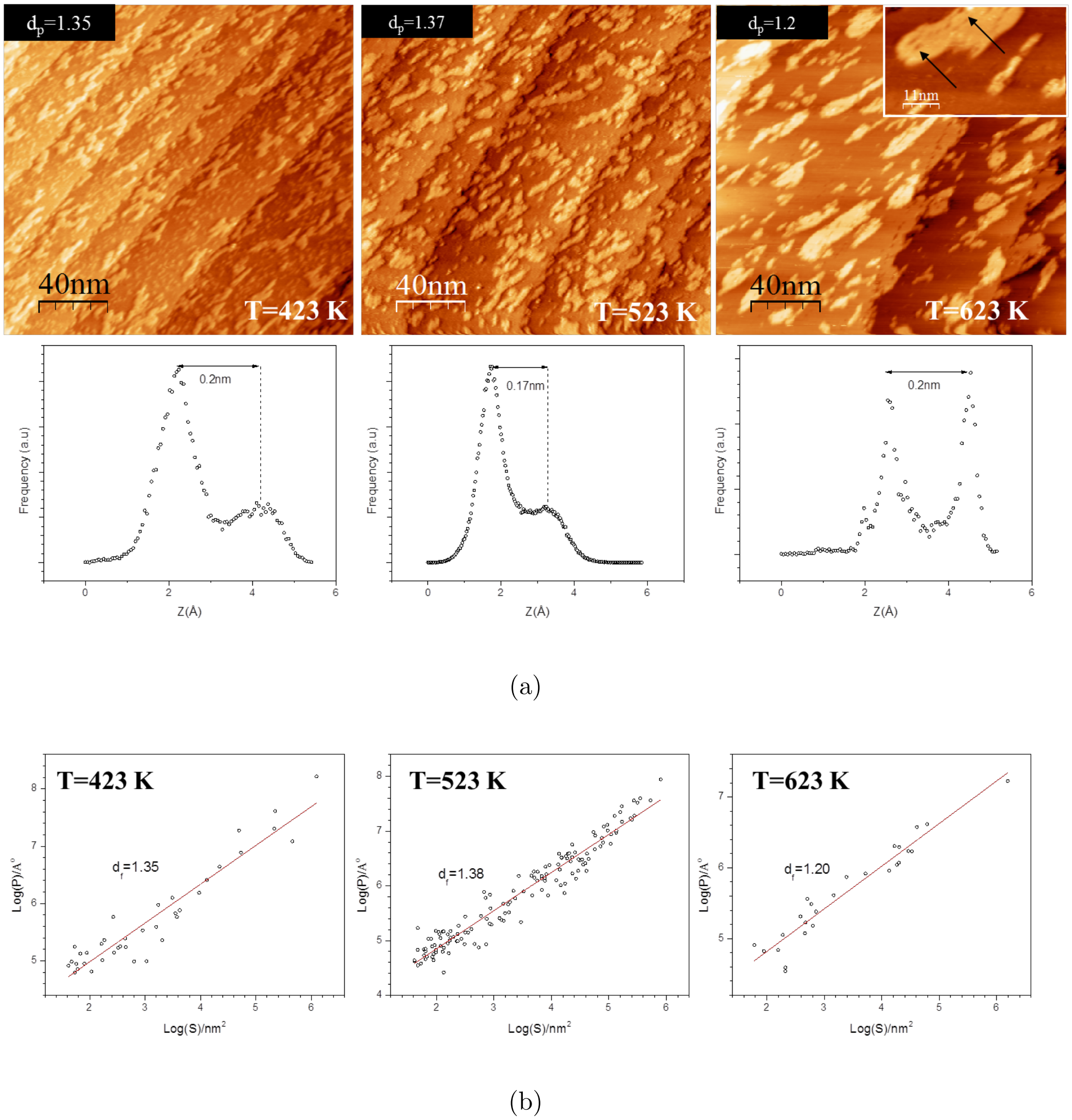

Figure 4.14. (a) Room temperature STM images of 2D Pd-Al islands after annealing the Pd(111) surface to 423, 523, and 623 K for 15 min. Height histogram of pixels in STM images on flat terraces are shown below each image. (b) Plots of the perimeter (P) vs. area (S) at each temperature used for calculating the d_p value.

The ability of defect sites, such as step edges, to dissociate MA was also investigated. On clean Pd(211), the calculated barrier is 0.52 eV for the dissociation of the four-fold-site MA to four-fold-site Al and top-site CH_3 at a step, which is lower by

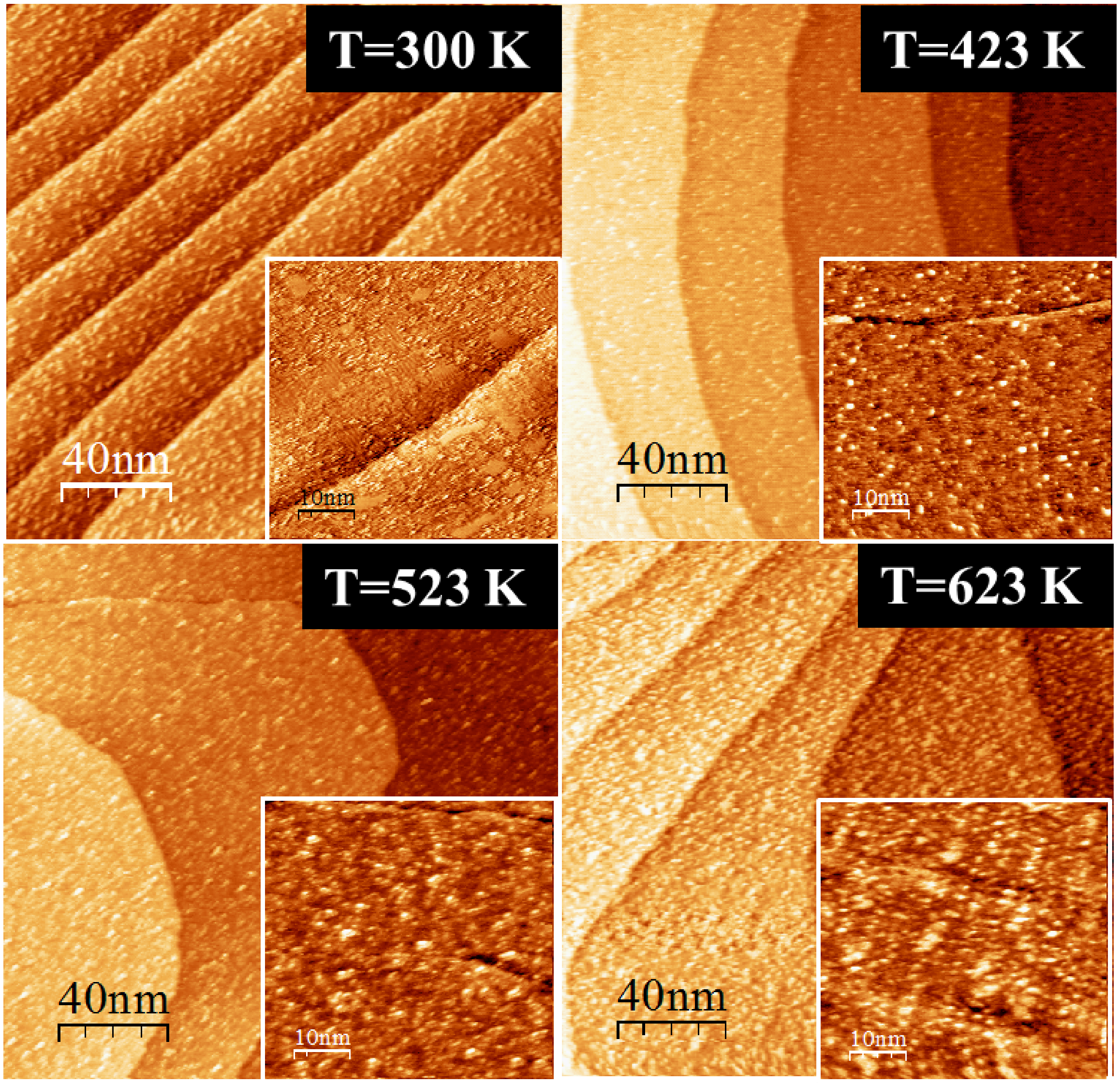

Figure 4.15. STM images (200 nm × 200 nm, insets: 50 nm × 50 nm) obtained after exposing the Pt(111) surface to 2.5 L of TMA at 300 K and subsequent annealing of the sample at 423 K, 523 K and 623 K for 15 min. The tunneling current was 0.3–0.7 nA; the bias was +0.5–+0.8 V.

1.16 eV than the corresponding value on Pd(111) terraces. This lower barrier results from stronger interaction between the abstracted CH_3 and Pd in the transition state (TS) on Pd(211) than on Pd(111). This conclusion is further supported by the shorter

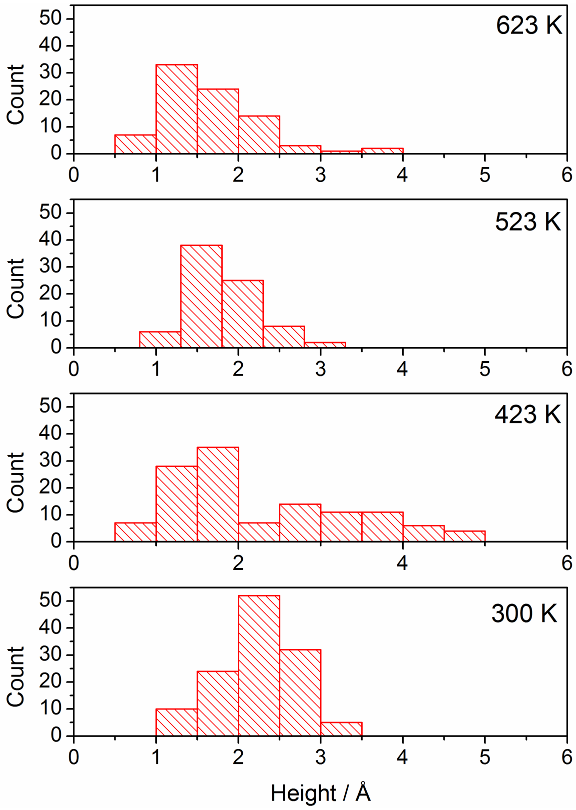

(a)

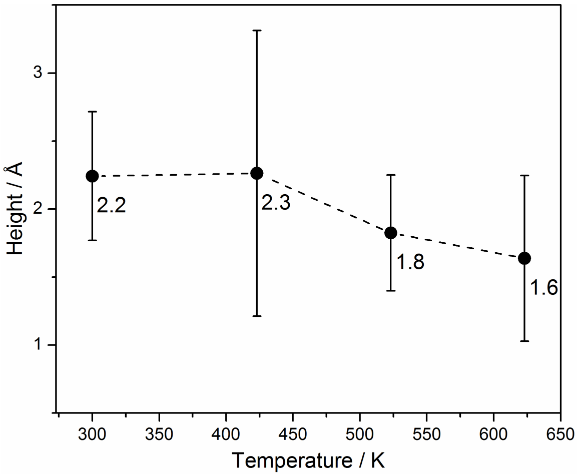

(b)

Figure 4.16. (a) Particle height distributions observed at 300 K and after annealing at the indicated temperatures. (b) Average particle height versus temperature.

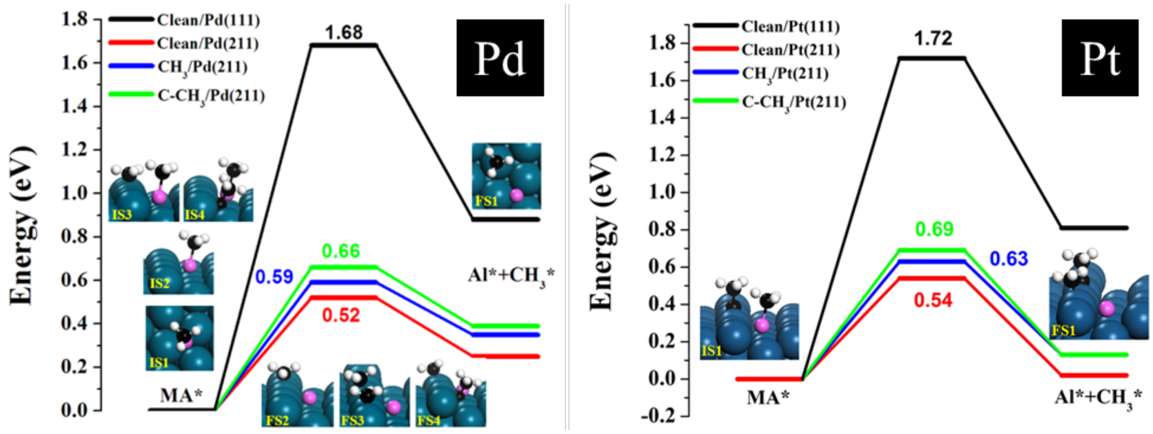

Figure 4.17. Potential energy surfaces of MA dissociation on clean and CH_3/CCH_3 covered (111) terraces and (211) steps for Pd and Pt. Insets are the initial and final states. The blue, pink, black, and white spheres represent Pd, Al, C, and H atoms, respectively.

bond distance of 2.10 Å for C-Pd on Pd(211) compared to 2.16 Å on Pd(111) in its TS. Both of these results point to the conclusion that steps facilitate MA dissociation. Carbon species adsorbed on a Pd step at moderate coverages have only a small influence on MA dissociation. This is because the steric repulsion between existing carbon species and the abstracted CH_3 is relatively small on the unoccupied stepped surface. When the step was covered by $^1/_3$ ML CH_3 or CCH_3, the calculated barriers were 0.59 and 0.66 eV, respectively, which are at most 0.14 eV higher compared to the same values on the clean surface.

Figure 4.17 also shows results for MA dissociation on clean Pt(211) and on the same surface covered with $^1/_3$ ML CH_3 or CCH_3. Although ethylidyne was detected experimentally only on Pd, its impact on MA dissociation on Pt(211) was investigated for comparison. The calculated barrier is 0.54 eV on clean Pt(211), and the barriers are 0.63 and 0.69 eV on Pt(211) covered with CH_3 and CCH_3, respectively, which are close to the values for clean Pt(211) surface.

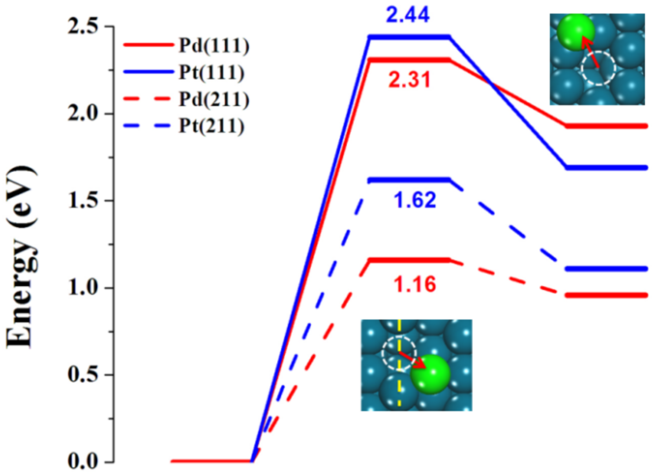

Figure 4.18. Potential energy of vacancy formation on palladium and platinum surfaces. Dashed yellow line is the position of step and the white circle is the vacancy formed. The blue and green spheres represent Pd/Pt atoms and Pd/Pt adatoms, respectively.

The above calculations indicate that the MA dissociation is kinetically more favorable on clean and hydrocarbon covered (up to $^1/_3$ ML CH_3 or CCH_3) Pt and Pd steps than on terraces of either metal.

Alloy formation was modeled as a two-step process: first, a surface metal vacancy is formed, followed by an Al atom filling the vacancy. Figure 4.18 shows that removing an atom from the (111) terrace to form an adatom and a vacancy has barriers of 2.31 and 2.44 eV for Pd and Pt, respectively. However, this process is easier on stepped surfaces. On Pd(211), the calculated barrier is 1.16 eV, lower than on Pd(111) due to the lower coordination number of a Pd atom on a stepped surface. Moreover, the four-fold site Al adatom resulting from MA dissociation can diffuse to a step Pd vacancy with an energy barrier of only 0.02 eV. Therefore, Pd-Al alloying can occur with relatively favorable energetics, at the relatively high temperatures used in our experiments, at the step. Similarly, the calculated barrier of 1.62 eV for Pt vacancy formation on Pt(211) is lower by 0.82 eV than on Pt(111), but higher by 0.46 eV than on Pd(211). Therefore, vacancy formation on steps is more energetically favorable on Pd than on Pt.

4.5 Discussion

Chemical and morphological differences in the resulting surfaces were observed following adsorption of TMA on clean Pd(111) and Pt(111). Proposed reaction mechanisms for each surface are discussed below.

4.5.1 Pd(111)

The TMA adsorption and dissociation mechanism on Pd(111) is presented in Figure 4.19. At 300 K, TMA adsorbs on (111) terraces dissociatively resulting in adsorbed methylaluminum, as predicted by DFT calculations, and methyl groups (Figure 4.19b). $CH_{3,ads}$ was unambiguously identified by HREELS, however, the feature associated with Al-$(CH_3)_x$ at 1167 cm^{-1} was very weak, and XPS revealed the formation of a Pd-Al alloy, suggesting that Al was completely demethylated. Given that the DFT-calculated dissociation barrier of MA on Pd steps is lower than on Pd(111) terraces by 1.16 eV (Figure 4.17), we conclude that most MA diffuses to steps and dissociates immediately upon adsorption, hence, MA was not detected experimentally as a major product (Figure 4.19b). Rejected $CH_{3,ads}$ groups form ethylidyne (CCH_3,ads) and dehydrogenate to other $CH_{x,ads}$ species (Figure 4.19f). These co-adsorbed hydrocarbons do not significantly increase the barrier for MA dissociation on steps relative to dissociation on clean steps. Furthermore, the major product ethylidyne is mobile at room temperature, [167] so it should not hinder MA surface diffusion.

Al atoms from MA dissociation on Pd steps either accumulate on the step via an exchange mechanism (Figure 4.18) resulting in a surface Pd-Al alloy along steps (Figure 4.19c) or diffuse across the surface until meeting another palladium or aluminum atom, creating a nucleus for a fractal island as observed in STM images (Figure 4.12).

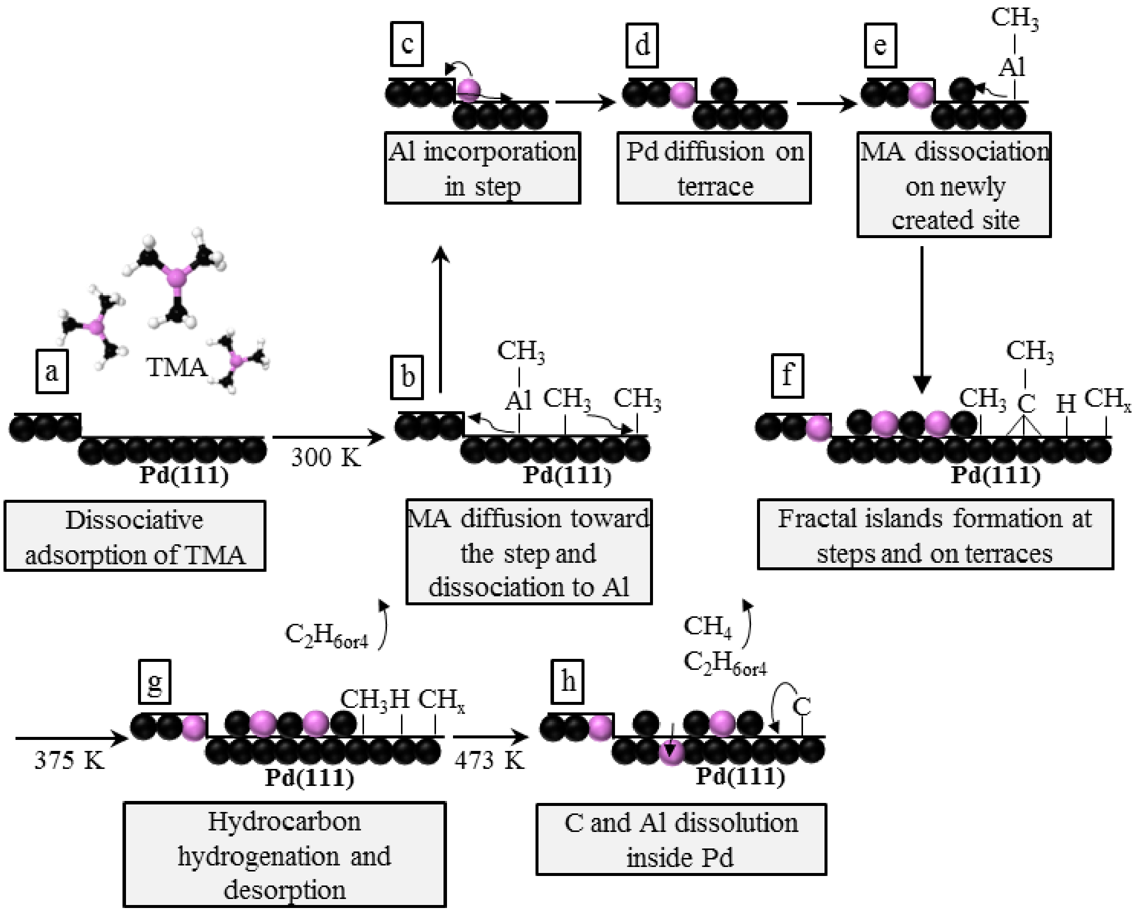

Figure 4.19. Schematic of TMA adsorption and dissociation on the Pd(111) surface.

Pd atoms displaced via the exchange mechanism also travel across the surface until agglomerating, forming irregularly shaped islands (Figure 4.19f). If the traveling atom (Pd or Al) collides with a step, then the Pd-Al alloy grows from the step. Newly created sites along the boundaries of fractal features serve as new dissociation sites for MA. The fractal dimension of 1.7 measured from STM images corresponds to a two-dimensional diffusion-limited-aggregation (DLA) growth mechanism [168, 169] in which atoms diffuse randomly on a two dimensional lattice and attach irreversibly to perimeters of growing aggregates forming irregular, branched fractal islands. The extended DLA mechanism allows atoms to relax locally after hitting an island by finding an energetically favorable site. Long-range diffusion along the island boundary is inhibited, and this results in the formation of highly fractal structures. This mechanism reasonably explains the fractal islands on terraces and fjord-like growths on the steps (Figure 4.12). Heating lifts the diffusion limitation along island boundaries, and the fractal islands compact. For a compact, two-dimensional object $d_p = 1$. The decrease of d_p with increasing temperature (Figure 4.13) signifies the diffusion of under-coordinated Pd and Al atoms along island boundaries, forming islands with a more compact shape at 623 K. A similar transition from fractal to compact island shape by annealing was observed for the Ag/Pt(111) system. [170] At room temperature, the Pd-Al alloy concentrates on the surface. Upon heating, aluminum dissolves in the palladium bulk. As a result, the surface concentration of aluminum decreases. The pinholes detected by STM are evidence of aluminum diffusion in the bulk. The main cause of stopping TMA adsorption and dissociation, either the accumulating carbonaceous species or the Pd-Al alloy, is unclear.

The fate of carbonaceous species on Pd deserves separate discussion. Adsorbed hydrogen atoms and ethylidyne were produced from dehydrogenation of $CH_{3,ads}$ species. Hydrogen hydrogenates carbonaceous species, resulting in product desorption (Figure 4.19g). This is consistent with very low carbon coverage that was observed during the early stages of TMA adsorption at 300 and 473 K (Figure 4.7) and literature reports of CH_4 (methane) and C_2H_6 (ethane) desorption during exposure of Pd nanoparticles to TMA. [123, 150, 171] Another route for carbon disappearance could be dissolution of carbon in palladium bulk (Figure 4.19h). [80, 139]

4.5.2 Pt(111)

Figure 4.20 shows the TMA adsorption and dissociation mechanisms on Pt(111). At 300 K, TMA dissociates to MA on Pt(111) terraces, as predicted by DFT. HREELS confirmed the presence of Al-$(CH_3)_x$ species. Further dissociation of MA on Pt step sties was predicted to be approximately as kinetically favorable as on Pd step sites

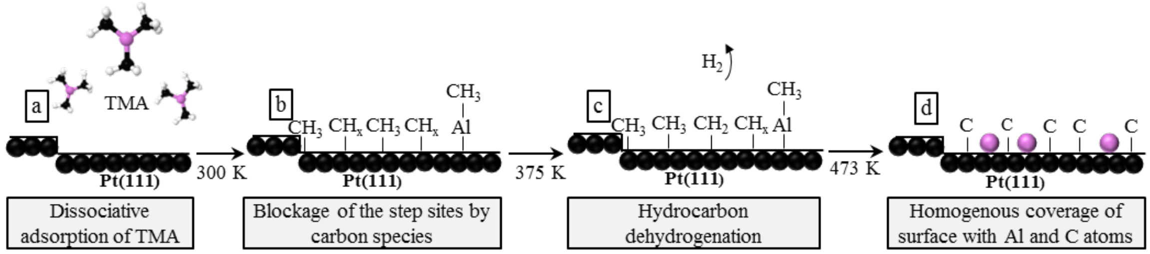

Figure 4.20. Schematic of TMA adsorption and dissociation on the Pt(111) surface.

(Figure 4.17), however MA dissociation at room temperature was not observed experimentally on Pt(111). We conclude that MA dissociation on Pd(111) proceeds due to the relatively low coverage of the carbonaceous species, enabling MA diffusion to steps. Carbon coverage on Pt(111) is high relative to Pd(111) (Figure 4.7), and we speculate that the absence of MA dissociation on Pt(111) is due to blockage of step sites and/or hindrance of MA diffusion across the surface toward the step. The diffusion limitation may explain the appearance of the isolated MA species on Pt(111) which were not observed on Pd(111). Indeed, carbon coverage was about 0.7 ML on Pt(111) after 2.5 L TMA exposure at 300 K, compared to 0.18 ML on the Pd(111) surface at the same dosing conditions (Figure 4.8). DFT calculations showed that the energy barrier for the formation of a platinum atom vacancy on Pt(211) is 0.46 eV higher than on Pd(211) (Figure 4.18). Therefore, it is less likely that a Pt atom would be released from a step site to form a nucleus for a fractal island.

Heating at 373 K resulted in MA dissociation, and most methyl ligands transferred from Al to the Pt(111) surface. The overall carbon coverage was relatively high and did not change on Pt(111) during annealing to 623 K (Figure 4.8). HREELS data showed that surface methyl groups dehydrogenated, forming methylene and methine groups at 375 K (Figure 4.20c). All carbonaceous species lost hydrogen at 473 K (Figure 4.20d). Hydrogen atoms recombined and desorbed. Carbon likely formed graphite-like patches and clusters (Figure 4.20d). No Pt-Al alloy formation was detected after MA decomposition, perhaps due to the presence of graphite-like carbon. The higher barrier for vacancy formation at steps on Pt(111) is another factor that might prevent Pt-Al alloy formation.

4.5.3 TMA Adsorption on Metal Surfaces

Hydrogenation, dehydrogenation, and removal of carbonaceous species are key factors determining TMA chemistry on Pt(111) and Pd(111). Saturation aluminum coverage is higher after TMA adsorption on Pd(111) than on Pt(111). Conversely, the carbon to aluminum ratio is two times higher on Pt(111), blocking the Pt(111) surface. At low TMA exposures (< 50 L) at 473 K, the Pd(111) surface is very efficient at hydrogenating and removing carbonaceous species. At the same conditions, the Pt(111) surface is covered with carbonaceous species which block adsorption/dissociation sites for TMA. The self-cleaning properties of the Pd(111) surface result in a nominal aluminum coverage that is higher than on Pt(111).

During an ideal ALD process, an organometallic precursor anchors to the surface through a ligand exchange reaction with surface functional groups. The amount of an organometallic precursor adsorbed on the surface is controlled by the amount of functional groups present. As demonstrated above, no functional groups were needed for TMA to react with Pt(111) and Pd(111) substrates, which are catalytically active. In general, the catalytic ability of a substrate determines adsorption chemistry of ALD precursors. Zhou et al. [165] found that TMA adsorbs as a monomer at 110 K on Ru(001). Upon heating, the monomer decomposes to dimethylaluminum (DMA) between 175-260 K. Above 420 K, H_2 and $Al(CH_3)_2H$ are evolved and DMA decomposes further to MA. On Ni(111), Al nucleates starting around 300 K, [172] and hydrogen and methane are gaseous products. Both Ru and Ni are able to hydrogenate/dehydrogenate TMA to some extent. The type of ALD precursor also plays a role. On Pt(111), Wenger et al. [173] found that for adsorption of dimethylmercury between 200-300 K, methylmercury was formed which persisted until 350 K. At 400

K, Hg-CH_3 dissociated and ethylidyne was observed, however, as we have shown, ethylidyne was not formed from TMA adsorption on Pt(111). Perhaps the second metal introduced by ALD also plays a role in hydrogenation or C-C chemistry. The catalytic abilities of the metals present, then, determine much of the surface chemistry during the first ALD half cycle, which likely impacts the quality of the interfacial ALD film. Carbon-containing ligands can be removed from surfaces such as Pt(111) and Pd(111), given the right choice of ALD processing conditions. [122]

4.6 Conclusion

The interaction of TMA with Pt(111) and Pd(111) surfaces was studied. Aluminum-containing species were observed. On Pd(111) at 300 K, TMA dissociates to Al, ethylidyne, and $CH_{x,ads}$ (x=1, 2, or 3) groups. DFT predicted that TMA dissociates on (111) terraces to form MA, and MA subsequently dissociates to aluminum and methyl groups on steps. Al atoms formed at a step or Pd atoms ejected from a step after exchanging with Al travel across the surface until encountering another Al or Pd atom, creating a nucleus for Pd-Al island formation. These irregularly shaped islands also act as steps for MA dissociation. Upon heating, fractal islands become more compact and aluminum diffuses into the palladium bulk. On Pt(111), TMA dissociates to MA. Unlike on Pd(111), Pt(111) is unable to efficiently hydrogenate and remove carbon species, which leads to higher carbon coverage at the same dosing conditions. Carbon atoms and clusters hinder surface diffusion of MA molecules and block MA dissociation sites at steps, resulting in more uniform coverage of Pt(111) by MA molecules. In contrast to Pd(111), Al does not alloy with the Pt(111) surface. On both surfaces, significant coverage of aluminum was achieved without any pre-adsorbed functional groups. Differences in the interaction of TMA with each surface arise due to the different hydrogenation and dehydrogenation properties of the Pt and Pd. In general, precursor-substrate interaction greatly affects morphology and chemical composition of the adlayer, ultimately affecting the chemistry and morphology of an ultra-thin ALD film.

4.7 Acknowledgment

DFT calculations were performed by Dr. Xiang-Kui Gu and Prof. Jeffrey Greeley. Adapted with permission from Gharachorlou, A.; Detwiler, M. D.; Mayr, L.; Gu, X.-K.; Greeley, J.; Reifenberger, R. G.; Delgass, W. N.; Ribeiro, F. H.; Zemlyanov, D. Y. The Surface Chemistry of Trimethylaluminum on Pd(111) and Pt(111). *J. Phys. Chem. C*, DOI: 10.1021/jp512915f. Copyright 2015 American Chemical Society.

Table 4.2.

Major HREELS peaks observed from the Pt(111) surface following 6 L TMA exposure at 300 K and subsequent annealing at 373 and 473 K in UHV. Abbreviations: w, weak; s, strong; sh, shoulder; br, broad. NA: not assigned.

Energy Loss / cm^{-1}	Vibrational Mode	Assignment
	TMA Adsorption at 300 K	
2950^{s}	$\nu_{as}(CH_3)$	$Al\text{-}(CH_3)_x/M\text{-}CH_3$
2906^{sh}	$\nu_{s}(CH_3)$	$Al\text{-}(CH_3)_x$
1460^{br}	$\delta_{as}(CH_3)$	$Al\text{-}(CH_3)_x$
1210^{s}	$\delta_{s}(CH_3)$	$M\text{-}CH_3$
1176^{s}	$\delta_{s}(CH_3)$	$Al\text{-}(CH_3)_x$
750^{sh}	$\rho(CH_3)$	$Al\text{-}(CH_3)_x$
540^{s}	$\delta(Al\text{-}CH_3)$	$Al\text{-}(CH_3)_x$
	Annealing in UHV at 373 K	
3030^{s}	$\nu(CH_2)$	$M\text{-}CH_2$
2950^{s}	$\nu_{as}(CH_3)$	$Al\text{-}(CH_3)_x/M\text{-}CH_3$
2906^{sh}	$\nu_{s}(CH_3/CH_2)$	$Al\text{-}(CH_3)_x/M\text{-}CH_3$
1980^{w}	$\nu(C\text{-}O)$	CO_{ads}
1460^{br}	$\delta_{as}(CH_3)$	$Al\text{-}(CH_3)_x$
1380^{w}	$\delta(CH_2)$	$M\text{-}CH_2$
1210^{s}	$\delta_{s}(CH_3)$	$M\text{-}CH_3$
1176^{s}	$\delta_{s}(CH_3)$	$Al\text{-}(CH_3)_x$
815^{sh}	$\rho(CH_3)$	$M\text{-}CH_3$
808^{sh}	$\delta(CH)$	$M\text{-}CH$
750^{sh}	$\rho(CH_3)$	$Al\text{-}(CH_3)_x$
	Annealing in UHV at 473 K	
1980^{w}	$\nu(C\text{-}O)$	CO_{ads}
660^{s}		NA
550^{sh}		NA

Table 4.3.
Major HREELS peaks observed from Pd(111) following 6 L TMA exposure at 300 K and subsequent annealing to 373 and 473 K in UHV. Abbreviations: vw, very weak; w, weak; s, strong; sh, shoulder; br, broad; NA, not assigned.

Energy Loss / cm^{-1}	Vibrational Mode	Assignment
	TMA Adsorption at 300 K	
2964^{br}	$\nu_s(CH_3)$	$M-CH_3/M\equiv CCH_3$
2890^{sh}	$\nu_{as}(CH_3)$	$M\equiv CCH_3$
1780^{br}	$\nu(C-O)$	CO_{ads}
1140^{br}	$\delta_{as}(CH_3)$	$M\equiv CCH_3$
1328^{s}	$\delta_s(CH_3)$	$M\equiv CCH_3$
1210^{s}	$\delta_s(CH_3)$	$M-CH_3$
1167^{vw}	$\delta_s(CH_3)$	$Al-(CH_3)_x$
1090^{w}	$\rho(CH_3)$	$M\equiv CCH_3$
1012^{br}	$\nu(C-C)$	$M\equiv CCH_3$
	Annealing in UHV at 373 K	
3015^{br}	$\nu_{as}(CH_3)$	$M-CH_3$
2906^{w}	$\nu_{as}(CH_3)$	$M-CH_2/M-CH$
1428^{vw}	$\delta_{as}(CH_3)$	$M-CH_3$
1210^{s}	$\delta_s(CH_3)$	$M-CH_3$
	Annealing in UHV at 473 K	
890^{s}		NA
636^{br}		NA
545^{sh}		NA

5. REACTION OF TRIMETHYLALUMINUM WITH WATER ON PT(111) AND PD(111) FROM 10^{-5} TO 10^{-1} MILLIBAR

5.1 Abstract

The reaction between adsorbed trimethylaluminum (TMA) and water was studied on Pt(111) and Pd(111) surfaces. Upon exposure to TMA at approximately 10^{-5} mbar, C and Al species appeared on both surfaces, as observed by X-ray photoelectron spectroscopy (XPS). On both surfaces, the adsorbed Al oxidation state observed by XPS was closest to metallic. Density functional theory (DFT) calculations suggest that decomposition to methyl aluminum (Al-CH_3; "MMA") or atomic Al is thermodynamically favorable. The formation of a Pd-Al alloy was observed on Pd(111), but Pt-Al alloy formation was not observed on Pt(111). Following TMA adsorption, each surface was exposed to water vapor at 400°C either at a pressure of 7×10^{-6} mbar (UHV-XPS) or at 0.1 mbar (*in situ* XPS). The substrate and water dosing conditions determined the ability of each surface to remove residual carbon on Pt(111), carbon from the TMA precursor was removed from Pt(111) during 0.1 mbar water exposure at 400°C, whereas carbon was not removed after the 7×10^{-6} mbar water exposure. On Pd(111), however, carbon-containing fragments of TMA were removed at both water pressures. X-ray photoelectron spectroscopy also revealed another effect of water dosing conditions: the as-deposited Al was only fully oxidized to Al_2O_3 during water exposure at 0.1 mbar, whereas mixed hydroxide-containing and metallic Al species persisted after exposure to water at 7×10^{-6} mbar on both surfaces.

5.2 Introduction

Atomic layer deposition (ALD) is a self-limiting technique for deposition of material onto solid substrates by sequential dosing cycles of gaseous precursors. [31, 174–176] ALD has been used for manufacturing of thin film electroluminescent flat-panel displays since the technology was developed in the 1970s. [174, 177] With growing demand for scaling down of microelectronic devices, ALD became a suitable technique for producing very thin, conformal films with thickness and film composition control at the atomic level. Recently, commercial ALD techniques have been developed for deposition of different high-k dielectric gate oxides, which form an insulating layer between the gate and channel in metal-oxide-semiconductor field-effect transistors (MOSFETs), minimizing leakage current. [34]

Applications of ALD have spread beyond microelectronics. Both oxides and metallic nanoparticles have been synthesized by ALD for heterogeneous catalysts. [36,41,84,178–180]. ALD Al_2O_3 overcoats grown on supported Pd and Cu nanoparticles by the trimethylaluminum (TMA) and water ALD system protect these nanoparticles from coking and sintering during methanol decomposition and oxidative dehydrogenation of ethane while preserving their catalytic activity. [36–38]

Fundamental mechanistic understanding of the first ALD cycle is crucial for both microelectronics and catalysis. To this end, our motivation for this study is two-fold: first, to understand the interaction of ALD precursors with transition metal surfaces during the first ALD cycle, and second, to develop knowledge that might ultimately be used to synthesize an inverse model catalyst on which oxide clusters are supported on the surface of a metal single crystal for use in future catalytic studies. Inverse catalysts allow for investigation of the influence of the metal-oxide interface on reaction kinetics, which is hypothesized to be the active site for several catalytic reactions. [181]

ALD is typically done at millibar pressure in flow reactors on the industrial and laboratory scale. [121] This pressure limits the number of applicable *in situ* surface characterization techniques which yield chemical information and are able to follow the initial growth steps. Though the TMA-water ALD system has been studied in-depth under realistic ALD conditions [148, 182–184] and in ultra-high vacuum (UHV) [148] conditions on various substrates, few *in situ* techniques have been used for characterization of Al_2O_3 films grown by this method. Studying the TMA-water deposition mechanism using surface sensitive characterization techniques carried out in UHV ($< 10^{-9}$ mbar), in turn, will result in better understanding of this process, and such studies are an important focus of the present work. However, because the results of experiments performed in UHV can differ substantially from experiments performed at higher pressures, as has been hypothesized for the TMA-water ALD system, [174, 185, 186] we have also complemented traditional UHV X-ray Photoelectron Spectroscopy (UHV-XPS) with synchrotron-based *in situ* X-ray photoelectron spectroscopy in 0.1 mbar H_2O, along with density functional theory modeling, in order to better understand the first cycle of the TMA-water ALD system on Pt(111) and Pd(111). UHV-XPS operates in vacuum at pressures $< 10^{-7}$ mbar, while *in situ* XPS can be operated at mbar pressures. The combination of the two techniques allows us both to obtain fundamental information about TMA and water deposition under UHV conditions and to follow the reaction of water with deposited TMA *in situ* under realistic ALD conditions. Below, we report on observed differences between the pressure regimes on both Pt(111) and Pd(111) substrates.

5.3 Experimental and Theoretical Methods

Samples used were Pt(111) and Pd(111) single crystals with orientation accuracy $< 0.1°$. (MaTecK GmbH and Princeton Scientific, respectively). Two experimental XPS apparatuses were used: the first uses synchrotron radiation and is capable of operating at pressures up to 1 mbar, and the second is a standard laboratory XPS operated in UHV ($< 10^{-9}$ mbar). The primary difference between the experiments carried out in each apparatus was the water pressure during the second half of the ALD cycle. In both experiments, the single crystals were prepared via multiple cycles of Ar^+ sputtering, annealing in 0.1 mbar O_2 at 650°C, and annealing in vacuum at 650°C. Sample cleanliness was checked with XPS.

5.3.1 Synchrotron-Based *in Situ* XPS Experiments

In situ XPS measurements were performed at the ISISS (Innovative Station for *In Situ* Spectroscopy) beamline at the BESSY II synchrotron in Berlin, Germany. The experimental apparatus consisted of a load lock and *in situ* cell connected to the XPS spectrometer via differential pumping stages. The experimental apparatus has been described in the literature extensively. [187] Samples were heated in the *in situ* cell via a near-infrared semiconductor laser (λ = 808 nm) from the rear. Temperature was measured by a K-type (chromel-alumel) thermocouple spot welded to the sides of the crystals.

TMA (Strem Chemicals, Inc., 98%) contained in a stainless steel Swagelok mini-cylinder was dosed to the samples in the load lock through a leak valve following several cycles of purification by freeze-pump-thaw. Dosing lines were purged by several cycles of TMA dosing followed by pumping prior to dosing to the samples. In order to avoid deposition of aluminum on the X-ray entrance window, TMA was dosed in a separate chamber while the samples were hot. Sample temperature was not controlled in this chamber, and the estimated TMA adsorption temperature was 100–200°C. For each sample, TMA was dosed at 2×10^{-5} mbar at a total exposure exceeding saturation (saturation exposure was determined to be 500-1000 L, measured by UHV-XPS). Samples were then transferred between the deposition chamber and the *in situ* cell by means of a transfer arm without exposure to air. The sample was exposed to deionized water vapor in the *in situ* cell at 0.1 mbar over the temperature range of 25°C to 400°C. The water was degassed and purified by multiple freeze-pump-thaw cycles.

Photoemission spectra were collected before and after TMA adsorption, and during water dosing in the *in situ* cell over the temperature range 25°C to 400°C. Photon energies were chosen so that the kinetic energy of ejected photoelectrons remained constant at approximately 120 eV for different core-level photoemission peaks in order to extract information from the same depth. The low kinetic energy of the photoelectrons also provides an analysis depth of 0.9 nm, less than the analysis depth for the UHV-XPS experiments described below. Photoelectrons were collected in the normal direction to the surface at constant pass energy of 10 eV. Binding energies were referenced to the Fermi edge, which was measured each time the monochromator moved to a new position (whenever the incident photon energy was changed). Photoemission peak intensities were corrected for the photon flux at a given photon energy. Since the BESSY II synchrotron operates in the top-off mode (constant ring current), no correction for the ring current was required. Since all photoemission peaks were collected approximately at the equal kinetic energy (120 eV) of photoelectrons, the attenuation through the gas phase was the same for all core levels and thus cancels out in coverage calculations.

5.3.2 Ultra-High Vacuum XPS Experiments

An Omicron Surface Analysis Cluster consisting of a UHV preparation chamber and μ-metal XPS chamber with base pressures of 1×10^{-9} mbar and 5×10^{-11} mbar, respectively, was used for the UHV ALD studies. The preparation chamber was equipped with a mass spectrometer, an Ar^{+} sputtering gun, a gas manifold system, and resistive sample heating. The XPS chamber was equipped with UHV-XPS, Low Energy Electron Diffraction (LEED), High Resolution Electron Energy Loss Spectroscopy (HREELS), Scanning Tunneling Microscopy (STM), and resistive sample heating.

Exposures to ALD precursors were performed in the preparation chamber. TMA (97%, Sigma Aldrich) was contained in a stainless steel mini cylinder and dosed to the preparation chamber via a leak valve. Prior to dosing TMA, several cycles of freeze-pump-thaw were performed for purification. Dosing lines were heated overnight at

150°C, and the lines were filled with TMA and pumped several times before dosing. TMA was dosed at 7×10^{-6} mbar at a sample temperature of 100°C for a total exposure of 2000 L. After dosing TMA, the sample was transferred to the analysis chamber for XPS analysis, during which time the empty preparation chamber was exposed to approximately 2000 L of water ("Birck Nanograde Water", as SEMI E1.2 with the Total Organic Carbon (TOC) reduced from 1 ppb to .25 ppb) in order to passivate residual TMA on chamber walls. Upon transferring the sample back to the preparation chamber, water was dosed under the same conditions as TMA through another leak valve. During TMA and water dosing, ionization gauges were left on for pressure measurement. It was verified by XPS that these gauges did not affect the state of the deposited material.

XPS data were acquired using a non-monochromatic Mg Kα X-ray source ($h\nu =$ 1253.6 eV) at 150 W. High resolution regions were recorded at the constant pass energy of 20 eV. The resolution of the instrument, which was measured as the full-width at half-maximum (fwhm) of the Pd $3d_{5/2}$ and Pt $4f_{7/2}$ peaks of clean Pd(111)/Pt(111) crystals, was approximately 1.2 eV. The energy scale calibration was carried out by setting the Au $4f_{7/2}$ peak to 84.0 eV. Photoelectrons were collected at a 45°photoemission angle with respect to the surface normal.

5.3.3 Analysis of XPS Data

All spectra were analyzed using the CasaXPS software program, version 2.3.16Prerel 1.4 (Casa Software Ltd.). A Shirley or linear background was subtracted from each region. Metallic Pt, Pd, and Al components, along with graphitic/carbidic C components, were fit using an asymmetric Gaussian/Lorentzian line shape with tail dampening (CasaXPS Lineshape = LF(1,1.8,30,90)). Nonmetallic species of C and Al (Al_2O_3 and Al oxyhydroxide) were fit with symmetric Gaussian/Lorentzian line shapes (CasaXPS Line shape = GL(x) or SGL(x), x = 10 to 30). Doublets arising from spin-orbit coupling in the Pt 4f ($4f_{7/2}$ and $4f_{5/2}$), Pd 3d ($3d_{5/2}$ and $3d_{3/2}$), and

Al 2p ($2p_{3/2}$ and $2p_{1/2}$) regions were subject to spacing constraints of 3.33, 5.26, and 0.43 eV, respectively. [68] Area ratios for doublets arising from spin-orbit coupling were constrained, and fwhms of these spin-orbit coupling doublets were constrained to be equal. Synthetic component curve fittings were propagated through all spectra in a series for consistency which sometimes resulted in curve fitting artefacts, e. g., the appearance of a small Pd-Al alloy component in the Pd 3d core level region for clean Pd(111).

High-resolution core-level Pt 4f/Al 2p, Al 2s, Pd 3d, and C 1s regions are shown in Figures 5.1–5.9. For the Pt 4f/Al 2p, Al 2s, and Pd 3d core-level regions, arbitrary intensity data on the y-axes have been plotted against binding energies such that the maximum peak intensities for each treatment are approximately the same. For the C 1s core-level regions, raw intensities are shown so that qualitative changes in carbon amount can be seen. For quantitative information, the reader should refer to reported adlayer coverage calculations, which were calculated assuming a non-attenuating overlayer on a semi-infinite substrate at fractional monolayer (ML) coverage. [62] Al_2O_3 and Pd-Al alloy overlayer thicknesses were calculated assuming a semi-infinite substrate of uniform thickness. Electron attenuation lengths (EAL) were calculated using NIST SRD 82 software. [188] Derivation of calculations are provided in Appendix A.

5.3.4 Density Functional Theory Calculations

DFT calculations were performed with the Vienna Ab-initio Simulation Package (VASP) [189, 190] using the project augmented wave method (PAW) [127] and the PW91 exchange-correlation functional. [126] A plane wave cutoff of 400 eV was used. The optimized lattice constants of bulk Pt and Pd were found to be 3.99 and 3.96 Å, respectively. The Pt(111) and Pd(111) surfaces were modeled by a (3×3) slab model with four layers, including nine atoms in each layer. To prevent artificial interaction between the repeated slabs along the z-direction, a 12 Å vacuum was introduced with correction of the dipole moment. A $(4 \times 4 \times 1)$ Monkhorst-Pack k-point mesh [191] was used to sample the Brillouin zone. During the optimization, the bottom two layers of metal atoms were fixed, while the remaining atoms and adsorbates were relaxed until the residual forces were less than 0.02 eV $Å^{-1}$.

5.4 Results

5.4.1 X-ray Photoelectron Spectroscopy

The reaction of TMA with Pt(111) and Pd(111) surfaces, and the subsequent reaction of water with the adsorbates, was studied using XPS. For UHV-XPS experiments, XP spectra were collected at $< 10^{-10}$ mbar following water exposure at 7×10^{-6} mbar pressure. *In situ* XP spectra were collected in 0.1 mbar water. In the first part of this section, the results observed on Pt(111) are discussed; the second part focuses on Pd(111).

High-resolution core-level Al 2p/Pt 4f, C 1s, and Al 2s core level regions shown in Figures 5.1 through 5.3 were collected following TMA adsorption on Pt(111) and subsequent heating in water. In both XPS experiments, only platinum was detected after cleaning. The Pt $4f_{7/2}$ peak of the clean Pt(111) crystal was fitted with a single asymmetric peak at 71.0 eV for the UHV-XPS spectrum (Figure 5.1), and fitted to 70.8 eV for the *in situ* XPS spectrum, which was referenced to the Fermi edge (Figure 5.1). These BE values are characteristic of metallic Pt. [68] The lower BE value for metallic Pt in the *in situ* experiment is likely due to the surface core-level shift for Pt 4f. [192]

Following dosing of TMA, carbon and aluminum appeared on the surface, as shown in the Al 2p, C 1s, and Al 2s regions (Figures 5.1–5.3). For the UHV experiment, despite the presence of aluminum on the Pt(111) surface following dosing of TMA, the Al 2p region makes no measurable contribution to the overall Pt 4f/Al 2p peak envelope, as shown in Figure 5.1. Unlike in the UHV experiment, the Al 2p contribution to the Pt 4f/Al 2p peak envelope was observed in the *in situ* XPS experiments, as shown in Figure 5.1. This effect was due to the increased surface

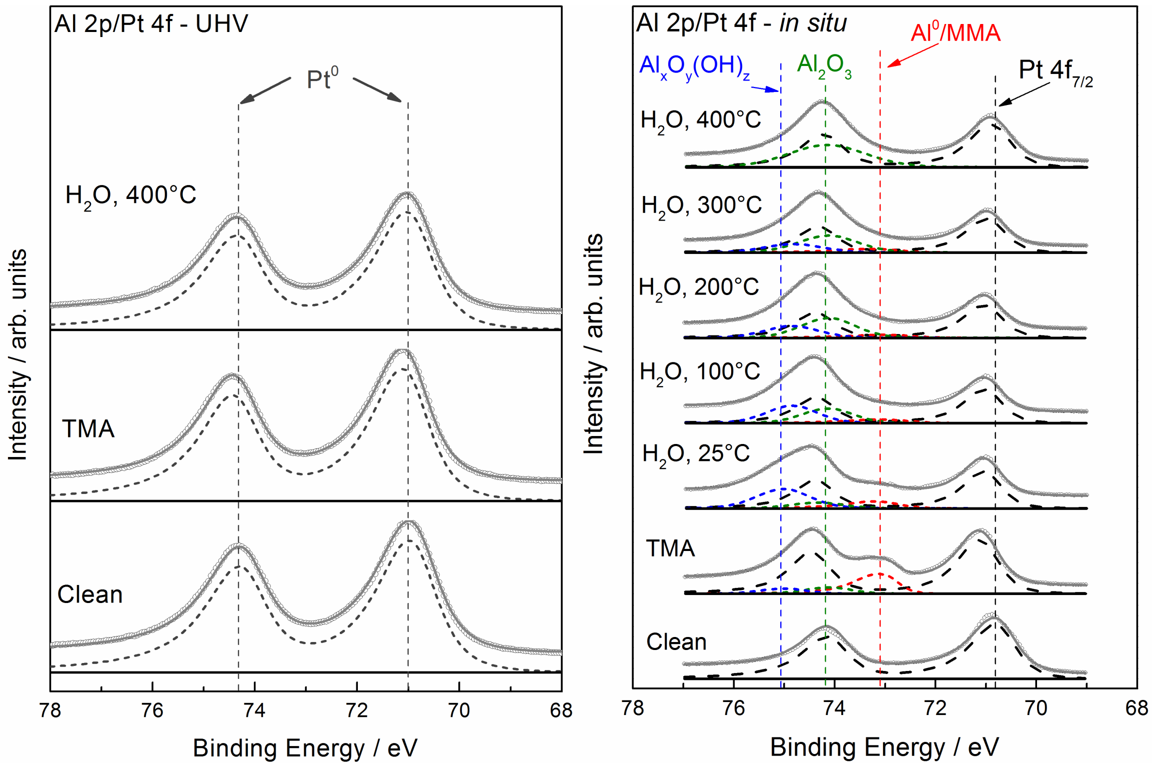

(a) UHV (b) *In situ*

Figure 5.1. Al 2p/Pt 4f regions. (a) UHV-XPS. From bottom to top: Pt(111) after repeated cleaning cycles, following dosing of TMA at 100°C, and after exposure to water at 400°C. (b) *In situ* XPS. From bottom to top: Pt(111) single crystal after cleaning cycles, following dosing of TMA between 100–200°C, and after exposure to water at 25°C and subsequently in steps to 400°C. Fitted components are shown as dashed lines and represent metallic Pt (dark grey), metallic Al or MMA (red), Al_2O_3 (green), and partially hydroxylated/oxyhydroxide aluminum (blue). The open circles are raw data points, and the light grey line is the sum of the deconvoluted peaks.

sensitivity related to the low kinetic energy of the ejected photoelectrons, and the increasing relative sensitivity factor (RSF) of Al 2p with decreasing photon energy. [193] In the UHV-XPS experiment, Mg Kα radiation was used ($h\nu = 1253.6$ eV). Electron attenuation lengths (EAL) of ejected electrons were estimated by NIST Standard Reference Database 82, [188] which uses IMFP data from Tanuma et al. [194] The

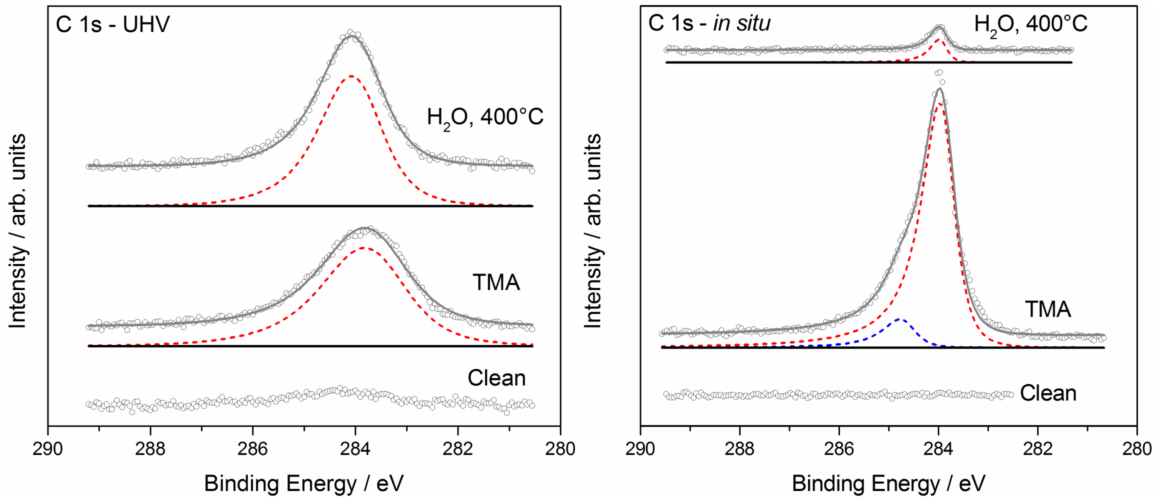

(a) UHV (b) *In situ*

Figure 5.2. C 1s regions for (a) UHV-XPS and (b) *in situ* XPS on Pt(111). From bottom to top: Pt(111) after cleaning cycles, after dosing of TMA (at 100°C for UHV-XPS and between 100–200°C for *in situ* XPS), and after exposure to water at 400°C. The fitted components are shown as red and blue dashed lines (assignments discussed in text). Open circles are raw data points, and the light grey line is the sum of the deconvoluted peaks.

kinetic energy of a Pt 4f photoelectron is approximately 1183 eV, and the EAL is approximately 1.1 nm. Because the 95% information depth is approximately equal to 3 times the EAL, [195] the information depth is approximately 3.3 nm. Therefore, the Pt substrate was the majority contributor to the Pt 4f/Al 2p photoemission peak. In the *in situ* XPS experiments, the kinetic energy of the photoelectrons was kept at approximately 120 eV, resulting in a Pt 4f photoelectron EAL of approximately 0.3 nm. Therefore, the information depth is estimated as 0.9 nm. Consequently, the chemical states of aluminum could be followed with the Al 2p peak by *in situ* XPS, whereas the Al 2s peak was used for UHV-XPS.

In order to determine the surface composition and the chemical states of platinum, aluminum, and carbon after each treatment, curve fitting was performed on the Pt 4f/Al 2p, Al 2s, and C 1s peaks. The component assignment and the peak posi-

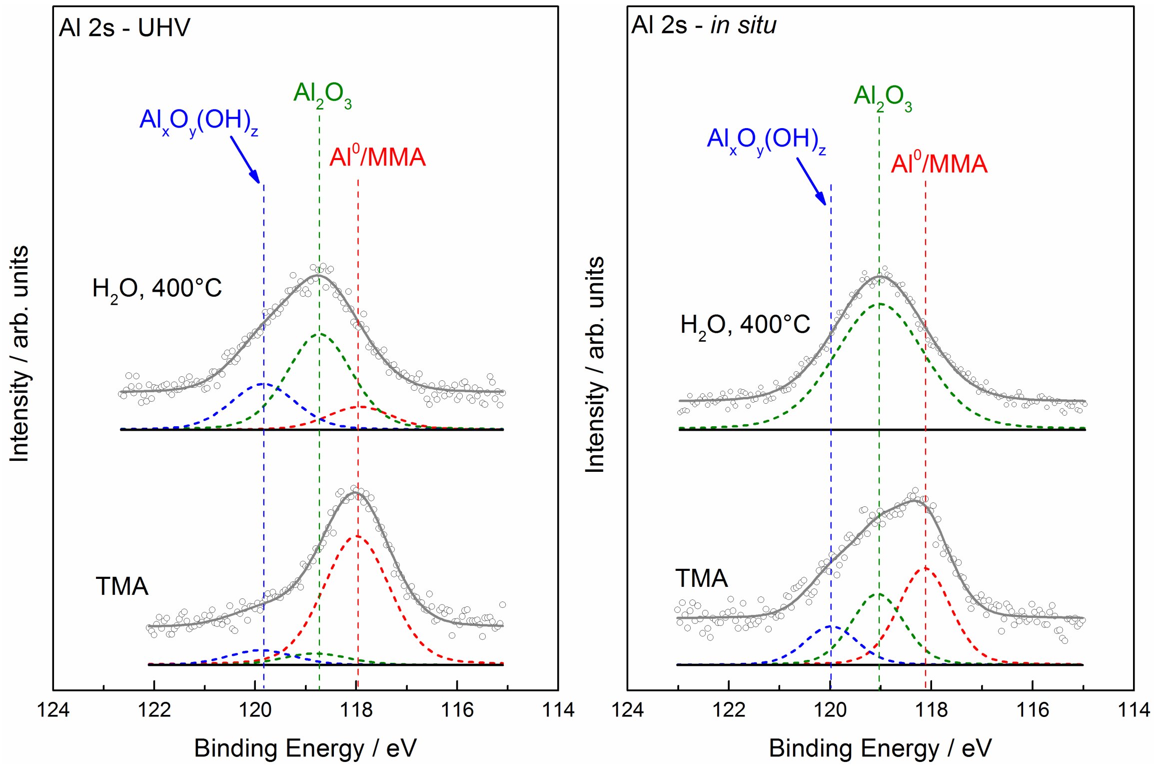

(a) UHV (b) *In situ*

Figure 5.3. Al 2s regions for (a) UHV-XPS and (b) *in situ* XPS (bottom) on Pt(111). From bottom to top: Pt(111) after dosing of TMA (at 100°C for the UHV experiment and between 100–200°C for the *in situ* experiment) and after water exposure at 400°C. Fitted components are shown as dashed lines and represent metallic Al or MMA (red), Al_2O_3 (green), and partially hydroxylated/oxyhydroxide aluminum (blue). The open circles are raw data points, and the light grey line is the sum of the deconvoluted peaks.

tions are listed in Tables 5.1 and 5.2. For deconvolution of the overlapping Pt 4f/Al 2p regions, the Pt $4f_{7/2}$ and $4f_{5/2}$ peaks were fit first subject to the constraints described in the experimental section, and then the remainder of the region was fit with peaks associated with aluminum (Figure 5.1).

In the UHV-XPS experiment, 83% of the Al 2s peak (Figure 5.3) was curve-fit with a component assigned to metallic Al or MMA species at 118.0 eV following TMA deposition. The reference for Al metal is 118 eV. [68] Two minority species,

Table 5.1.
Observed Al 2p and Al 2s component binding energies and envelope area % for Pt(111) samples after TMA exposure and water exposure at 400°C.

	UHV-XPS		*in situ* XPS			
	Al 2s		Al $2p_{3/2}$		Al 2s	
Component	BE / eV	% area	BE / eV	% area	BE / eV	% area
			TMA Exposure			
Al^0/MMA	118.0	83	73.0	63	118.1	47
Al_2O_3	118.8	7	74.0	20	119.1	34
$Al_xO_y(OH)_z$	119.9	10	74.9	17	120.0	19
			Water Exposure, 400°C			
Al^0/MMA	117.9	14	-	0	118.1	(< 1)
Al_2O_3	118.7	58	74.0	100	119.0	100
$Al_xO_y(OH)_z$	119.9	28	-	0	-	0

assigned to alumina and/or a partially hydroxylated Al species ($Al_xO_y(OH)_z$), appear at 118.8 and 119.9 eV. A detailed discussion of this assignment is given below. In the *in situ* XPS experiment, after dosing TMA, three aluminum-containing species could be detected in both the Al 2p and Al 2s regions. In the Al 2p region (Figure 5.1), the component at 73.0 eV was assigned to metallic or methylated Al and the components at 74.0 eV and 74.9 eV were assigned to oxidized and/or hydroxylated Al species. Similarly, 3 peaks in the Al 2s region were assigned to metallic Al or MMA (118.0 eV) and partially oxidized and/or hydroxylated Al species (119.1 and 120.0 eV). The oxidized and hydroxylated aluminum states that appeared in the *in situ* experiment following TMA dosing are likely due to residual water from the walls of the *in situ* cell, which began reacting with the deposited TMA. The presence of these species in the Al 2s spectrum after dosing TMA in the UHV-XPS experiment is due to the presence

Table 5.2.
Observed C 1s component binding energies and envelope area % for Pt(111) samples after TMA exposure and water exposure at 400°C.

	UHV-XPS		*in situ* XPS	
Component	BE / eV	% area	BE / eV	% area
		TMA Exposure		
1	283.8	100	284.0	90
2	-	0	284.8	0
		Water Exposure, 400°C		
1	284.0	100	284.0	100
2	-	0	-	0

of residual water or fitting artefacts. Al coverage was estimated for both experiments from XPS data assuming all Al was deposited as Al metal. Al coverage was estimated to be 0.8 ML and 0.5 ML for the *in situ* XPS and UHV-XPS experiments, respectively.

The C 1s core-level regions from the UHV- and *in situ* XPS experiments were fit differently following TMA dosing (Figure 5.2). For the UHV-XPS experiment, the BE of the majority species after TMA dosing was 283.8 eV. This peak likely includes contributions from carbon in several different environments. The BE value is close to reference binding energies for adsorbed methylidyne (CH) (283.61 eV) [196] and isolated C (283.8 eV). [69] DFT suggests the presence of monomethyl aluminum, but this could not be confirmed by XPS due to the lack of an appropriate reference.

For the *in situ* XPS experiment, the C 1s envelope was fit with two peaks at 284.0 (majority species) and 284.8 eV. The peak at 284.0 eV could be isolated C (283.8 eV) [69] or chain carbon (284.1 eV), [69] and the peak at 284.8 could be graphitic carbon (284.6 eV). [69] See Table 5.2 for a summary of C 1s component binding energies and component area percentages. The carbon coverage following

TMA adsorption was estimated from XPS data. For the *in situ* XPS experiment, C coverage was 1.7 ML. In the UHV-XPS experiment, the C coverage was 1.2 ML.

Water was dosed at 25°C and subsequently up to 400°C after analyzing the interaction of TMA with the bare surfaces. In 0.1 mbar of water at room temperature, changes were visible in the Al 2p spectrum of the *in situ* experiment. First, the Al $2p_{3/2}$ peak assigned to Al^0 or MMA at 73.0 eV decreases in intensity relative to the other peaks in the spectrum, resulting in a clear change to the resulting peak envelope at around 73 eV. Second, the higher binding energy peak assigned to $Al_xO_y(OH)_z$ at 74.9 eV increases in intensity relative to the other peaks. As the temperature of the single crystal is increased to 400°C in 0.1 mbar water, the peak at 74.9 eV shrinks. By 400°C, only the peak at 74.0 eV remains. In the Al 2s region, only the peak at 119.0 eV remains at 400°C (Figure 5.3). This is different from the observed Al 2s region in the UHV-XPS experiment, which consisted of all three Al species following water dosing at 400°C: metallic or methylated Al at 117.9 eV, Al_2O_3 at 118.7 eV, and $Al_xO_y(OH)_z$ at 119.9 eV (Figure 5.3).

From data presented in Figures 5.1 and 5.3, the state of deposited Al changes following water dosing, as evidenced by the growth of two higher BE Al 2p peaks. There is also a clear transition from the highest BE peak at 74.9 eV to the intermediate BE peak at 74.0 eV as the temperature is increased during water dosing for the *in situ* experiment. Interpretation of these spectral changes requires a careful review of the literature pertaining to XPS studies of different oxide- and hydroxide-containing aluminum species.

The first observed change, the disappearance of the peak resulting from adsorption of TMA at 73.0 eV, can be explained by the hydroxylation and/or oxidation of metallic aluminum or MMA following demethylation. As stated above, literature references of metallic Al place the Al 2p BE at 72.5-73.0 eV (Reference [68] and references therein), 72.77 and 73.18 eV ($2p_{3/2}$ and $2p_{1/2}$ lines, respectively), [197] 72.5 eV ($2p_{3/2}$), [198] 73.22 eV ($2p_{3/2}$ from clean NiAl(110)), [199] and 73.0 ± 0.1 (2p). [200] As discussed below, this peak includes contributions from both MMA and Al^0 given the DFT results (discussed below). We have included the MMA contribution in the metallic peak rather than the other two high BE species because methyl (CH_3) is generally considered to be a weak electron-donating functional group. Upon exposure to water, the peak assigned to Al^0/MMA nearly disappears, and the peaks at higher BEs grow. This indicates that Al is hydroxylated or oxidized, as hydroxylated/oxidized aluminum species are characterized by Al 2p BEs greater than those of metallic aluminum. [140, 197–200]

The second observed change is the shift from the higher to the lower BE hydroxylated/oxidized peak during heating in water between 25°C and 400°C. We attribute this shift to the dehydroxylation and subsequent oxidation of Al at temperatures approaching 400°C in water. Reaching this conclusion by only considering the shift of the Al 2p peak alone was not successful, as a range of BEs for various hydroxylated and oxidized Al-containing species have been presented in literature with no clear consensus. Kloprogge et al. [201] investigated the Al 2p region of various bulk Al-containing mineral powders with XPS. Following outgassing in vacuum, they reported BEs of 74.1, 74.4, 73.9, and 74.3 eV for corundum (Al_2O_3, α-alumina), gibbsite ($Al(OH)_3$), Boehmite ($AlO(OH)$), and Pseudoboehmite ($AlO(OH)$), respectively. They observed two peaks in the case of Bayerite ($Al(OH)_3$): one at 74.3 eV and a smaller peak at 75.0 eV. Following formation of an Al_2O_3 film through dehydration of $Al(OH)_3$ in vacuum, Nylund et al. [200] observed a single Al 2p peak at 75.8 eV which included contributions from both species. Alexander et al. [197] observed a shift of less than 1 eV to higher BE in the Al 2p peak centroid following heating of an $AlO(OH)$ sample to 300°C in vacuum. Lindsay et al. [202] measured Al 2p BEs of 76.3 ± 0.1, 74.8 ± 0.1, 75.7 ± 0.1, 74.9 ± 0.1, and 74.7 ± 0.2, for α-Al_2O_3, α-$AlO(OH)$, β-$AlO(OH)$, α-$Al(OH)_3$, and β-$Al(OH)_3$, respectively. The above references do not present a clear trend for aluminum oxides versus hydroxides, i. e., that oxide bound to aluminum results in a higher or lower Al 2p BE consistently versus hydroxide bound to aluminum. It should be noted that all of the above studies are for bulk aluminum oxide/hydroxide containing powders, and not for thin films of these species on transition metal substrates.

Several of the above authors also investigated the O 1s region during their experiments. Kloprogge et al. [201] fit the O 1s peaks of their bulk samples with 3 components: a low BE component between 530.5 and 530.8 eV assigned to aluminum oxide, a component between 531.8 and 532.2 eV, assigned to the oxygen in hydroxide, and a high BE component between 532.9 - 533.5 eV assigned to H_2O. For all phases, the H_2O peak was the smallest contributor to the overall peak envelope. The $Al(OH)_3$ phases were fit using only the OH and H_2O peaks. The AlO(OH) species were fit with all 3 peaks, and the area ratio of the oxide to OH peaks were nearly 1 to 1. α-Alumina was also fit with all 3 peaks, but the oxide peak dominated the spectrum. Alexander et al. [197] fit the O 1s peak for AlO(OH) with two main oxygen peaks at 530.95 and 532.35 eV, assigned to oxide and OH respectively. These peaks were constrained to be equal in area for 1:1 Al-O-Al to Al-O-H stoichiometry. Following annealing of the sample to 300°C, the separations between each O 1s peak and the Al 2p oxide peak were held constant, and the stoichiometry of the sample changed to 86% O, 13% OH, 1% H_2O. Nylund et al. [200] used a similar fitting strategy for Al_2O_3 and $Al(OH)_3$, using a higher BE peak for OH^- and a lower BE peak for O_2^-.

Our O 1s data on Pt(111) are consistent with the above 3 references that indicate the loss of hydroxyl species during heating. Following water treatment of as-dosed TMA at room temperature for the *in situ* experiment, the O 1s spectrum was fit with 2 peaks at 531.2 eV and 532.6 eV, assigned to O_2^- and OH^- respectively. The peaks comprised 37% and 63% of the total O 1s peak area, respectively. These O 1s core level regions are shown in Figure 5.4. As the temperature was increased during water treatment, the O_2^- peak increased in relative intensity while the OH^- component decreased in intensity. At 400°C, the OH^- peak comprised only 5% of the total peak area. A third peak for O in H_2O was not used, as no spectral features necessitated its use. A similar trend was observed in the UHV-XPS experiment where the higher

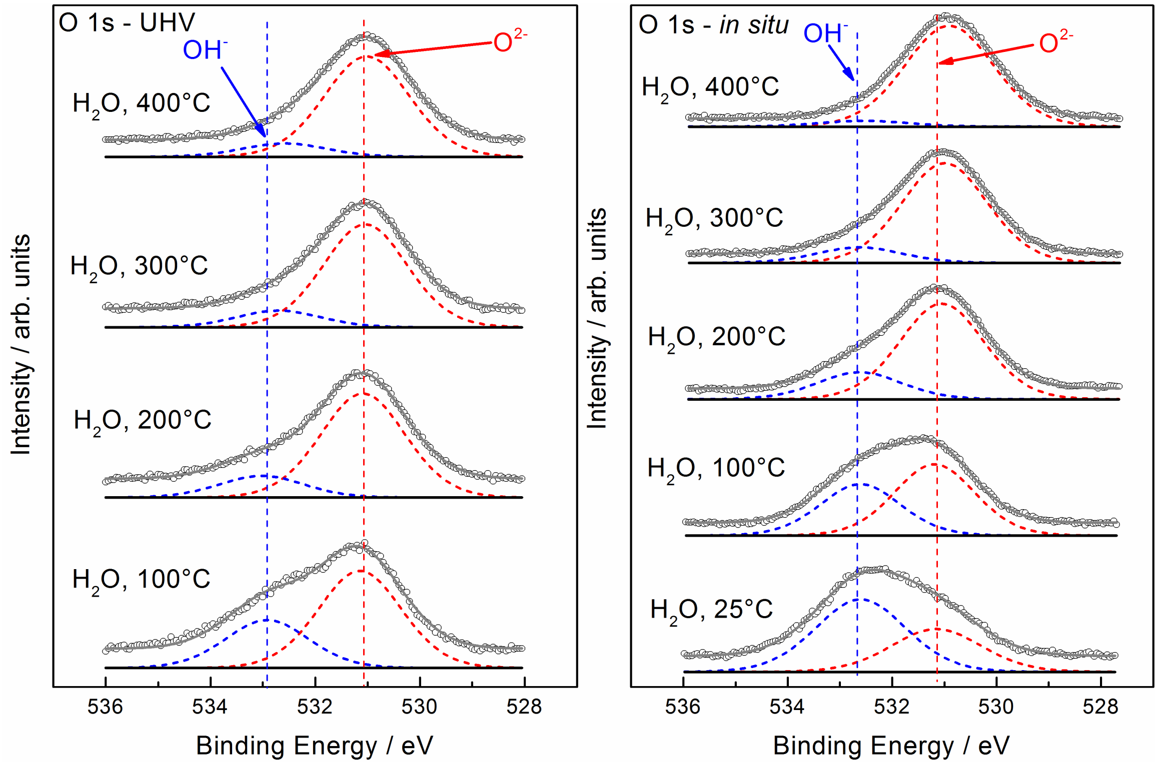

(a) UHV (b) *In situ*

Figure 5.4. (a) O 1s regions for UHV-XPS on Pt(111). From bottom to top: After water exposure at 100°C following TMA exposure and subsequently in steps to 400°C. (b) O 1s regions for *in situ* XPS on Pt(111). From bottom to top: Pt(111) after exposure to water at 25°C following dosing of TMA and subsequently in steps to 400°C. Dashed lines are fitted components and represent O_2^- bound to Al (red) and OH^- bound to Al (blue). Open circles are raw data and the grey line is the sum of deconvoluted peaks.

BE O 1s peak assigned to OH^- decreased as the sample temperature during water exposure was increased (shown in Figure 5.4).

Another piece of evidence suggesting that the higher BE Al 2p and O 1s components should be assigned to hydroxyl-containing species was a calcination experiment performed on Pd(111) using UHV-XPS. In this experiment 15 cycles of TMA-H_2O ALD were carried out (each cycle consists of TMA: 500 L at 7×10^{-6} mbar, 200°C; H_2O: 2000 L at 6.6×10^{-6} mbar, 200°C), followed by calcination in O_2 at 5×10^{-6}

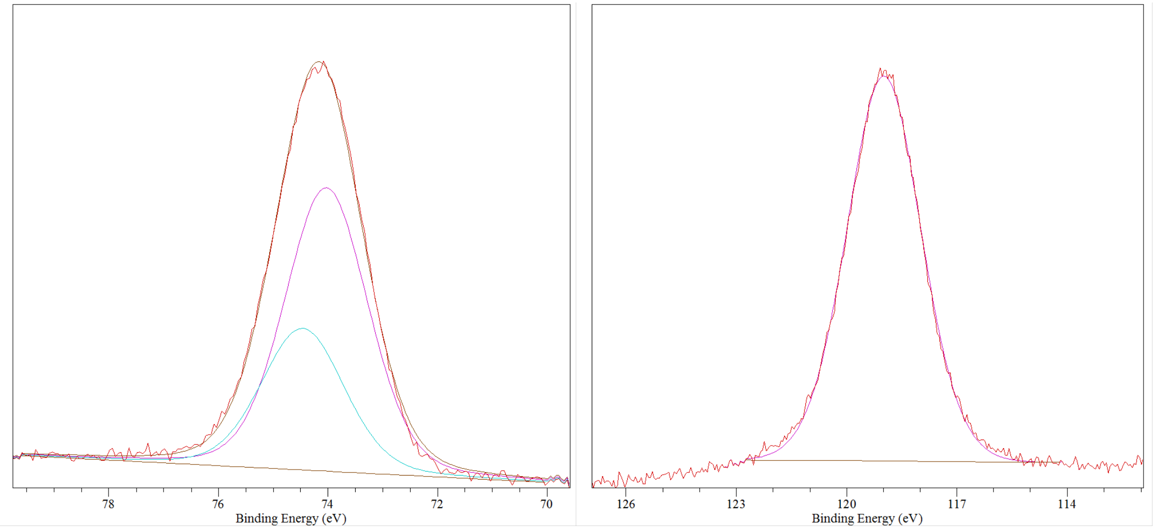

(a) Al 2p

(b) Al 2s

Figure 5.5. (a) Al 2p and (b) Al 2s regions following calcination of 10 cycles of TMA-H_2O ALD on Pd(111) at 600°C in 5×10^{-6} mbar O_2.

mbar at 600°C. Following calcination, Al 2p and Al 2s BEs were 74.0 and 119.0 eV, respectively (core level regions shown in Figure 5.5). Therefore, we attribute the shift from high to low BE peaks in the Al 2p/2s and O 1s regions to the dehydroxlation of the aluminum-containing film.

Another possible explanation for the shift to the lower BE oxide peak from the higher BE hydroxide peak is the transition from amorphous alumina to crystalline/semicrystalline alumina, but we have ruled that out on the basis that literature predicts such a change results in higher rather than lower BE. Several studies involving high resolution XPS have investigated various aluminum oxide/hydroxide phases and stoichiometries on surfaces. Mulligan et al. [199] studied aluminum oxide films formed on NiAl(110) following oxidation using synchrotron radiation XPS. Oxygen adsorption at 300 K resulted in 3 new states on a metallic surface: chemisorbed oxygen at 74.26–74.53 eV, tetrahedral amorphous-like alumina at 75.93, and octahedral Al^{3+} at 76.81 eV (only observed at exposures greater than 51 L). After 1200 L exposure of oxygen at 300 K, the resulting layer contains 90% tetrahedral aluminum.

The authors attribute this to amorphous alumina, which is the only bulk phase composed of mainly tetrahedral alumina. Absolute and relative amounts of octahedral aluminum increase after annealing at 573 and 1073 K. The authors attribute this to migration of subsurface Al to the oxidized layer. This increase in octahedral aluminum results in an increase in the highest BE peak at 76.81 eV. The layer formed at 1073 K is γ-alumina-like based on the relative amounts of octahedral and tetrahedral aluminum. The authors base their assignments on the works of Bianconi et al. [203] and McConville et al. [198] who used high resolution XPS to study the Al 2p core level. Bianconi et al. [203] combined Al 2p XPS with X-ray absorption near-edge spectroscopy (XANES) data and observed metallic Al at 73.0 eV, shifts of 1.4 eV for chemisorbed O and 2.8 and 3.3 eV for oxide states. The chemisorbed state at +1.4 eV was observed at room temperature along with the metallic state. The oxide state at +2.8 eV was observed after annealing to 200°C, and the state at +3.3 eV was observed after annealing to 400°C. McConville et al. [198] observed shifts of $+0.49 \pm 0.02$ (chemisorbed state 1), $+0.97 \pm 0.03$ (chemisorbed state 2), 1.46 (chemisorbed state 3), and 2.5–2.7 eV (oxide state). The shift to higher BE for more ordered alumina overlayers was confirmed also by Kovács et al. [204] who assigned Al 2p peaks at 74.2 and 74.9 eV to amorphous Al_2O_3 and γ- or α-alumina, respectively. All of the above references show a shift to higher binding energy for more crystalline alumina, but we observed a shift to lower BE while heating in water. Therefore, this binding energy shift is likely not caused by the transition from tetrahedral to octahedral Al_2O_3.

Thicknesses of the resultant Al_2O_3 films were estimated following exposure to water at 400°C. Details of this calculation are given in Appendix A. For the UHV- and *in situ* XPS experiments, films were estimated to be 3 Åand 9 Å, respectively. Note that this thickness calculation assumes that all Al was present as Al_2O_3 in both experiments. The lower thickness calculated for the UHV-XPS experiment was likely due to the lower initial Al coverage in the UHV-XPS experiment.

In the UHV experiment, the C 1s peak shifted to 284.0 eV after dosing water at 400°C. This is indicative of further dehydrogenation, leaving isolated (283.8 eV) [69] or chain (284.1 eV) [69] carbon. The coverage of carbon remained unchanged at approximately 1.3 ML after dosing 2000 L water at 7×10^{-6} mbar at 400°C. The 0.1 ML increase over the TMA-dosed surface is well within the error of the instrument. Carbon was also not removed following 16000 L H_2O exposure at the same water pressure at 400°C. The inability of water in the pressure range of 10^{-5} mbar to remove carbon is in contrast to the *in situ* XPS experiment, in which water was dosed at 0.1 mbar at 400°C. In this experiment, C coverage decreased from 1.7 ML to < 0.1 ML after dosing water at 400°C. As shown in Figure 5.2, the higher BE peak disappears after exposure to water at 400°C; the lower BE peak is still located at 284.0 eV, but was greatly decreased in intensity. C 1s XPS results are summarized in Table 5.2.

In both XPS experiments, only metallic palladium was detected by XPS after cleaning (Figure 5.6). The Pd^0 peak from the *in situ* experiment was located at 334.9 eV and the Pd^0 peak for the UHV experiment was located at 335.1 eV, the reference energy for metallic Pd. [68] The lower Pd 3d BE for the *in situ* experiment is likely due to the surface core-level shift for Pd(111), [205] similar to the observation for the Pt(111) system above. Contribution of the Pd-Al alloy peak (discussed in the experimental section) in the clean Pd 3d spectrum is due to fitting artefacts.

Upon dosing TMA, an additional peak in the Pd 3d region was observed in each experiment: For the *in situ* XPS experiment, the Pd $3d_{5/2}$ peak was fit with two components: the first at 335.2 eV corresponds to palladium metal and the second at 335.8 eV was assigned to a surface Pd-Al alloy. A similar result was observed in the UHV-XPS experiment with the two components located at 335.2 and 336.0 eV, respectively. The ratio between the metallic Pd and Pd-Al alloy components was used to estimate the alloy thickness (see Appendix A for calculation details). Alloy thicknesses were calculated to be 5 Å and 6 Å for the *in situ* XPS and UHV-XPS experiments, respectively. Assuming that all Al assigned to Al metal or MMA is alloyed with Pd following TMA dosing, quantified XPS data estimate the average Pd-Al alloy composition to be Pd_2Al (UHV-XPS) or Pd_4Al (*in situ* XPS). The higher BE Pd 3d peak that appears after dosing TMA could also be assigned to a PdC_x phase

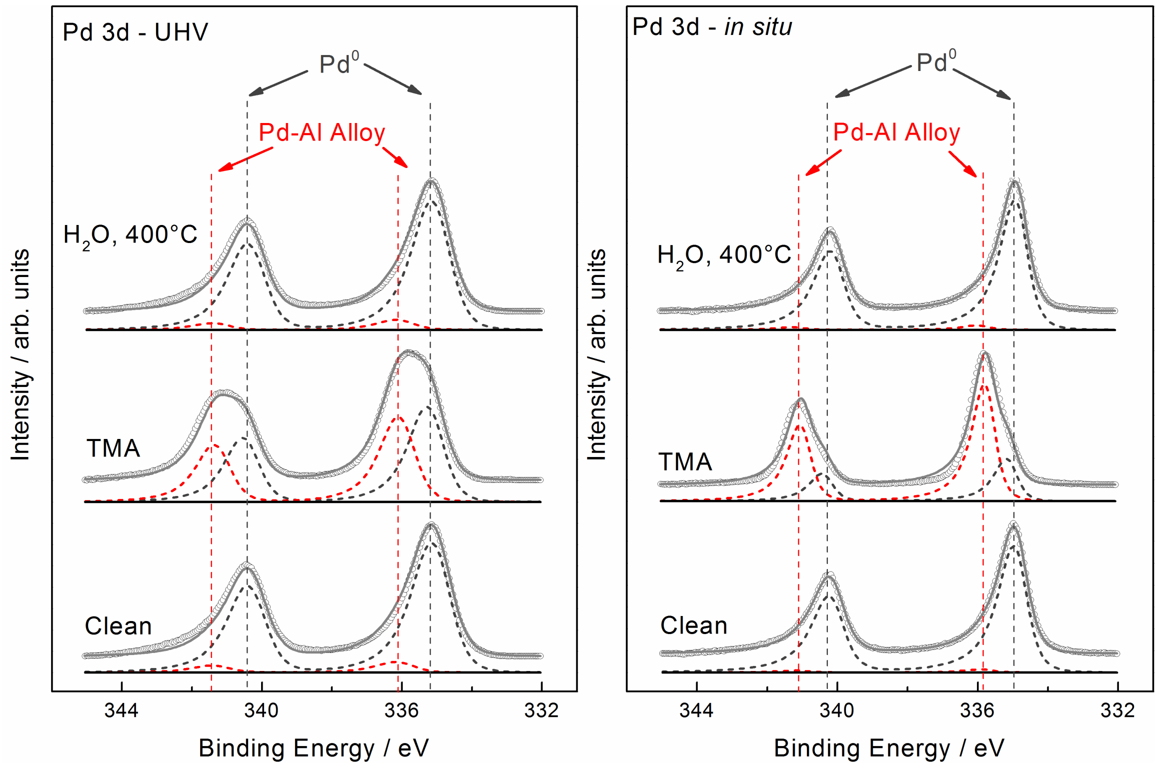

(a) UHV (b) *In situ*

Figure 5.6. Pd 3d regions for (a) UHV-XPS and (b) *in situ* XPS on Pd(111). From bottom to top: Pd(111) after cleaning, following dosing of TMA (at 100°C for UHV-XPS and between 100–200°C for *in situ* XPS), and after water exposure at 400°C. Fitted components are dashed lines and represent metallic Pd (dark grey) and Pd-Al alloy phase(s) (red). Open circles are raw data, and the grey line is the sum of the deconvoluted peaks.

resulting from carbon incorporation into Pd(111). Teschner et al. [139] and Gabasch et al. [80] observed the formation of this phase during pentyne hydrogenation and ethylene oxidation, respectively. Teschner et al. assigned Pd $3d_{5/2}$ and C 1s peaks to this phase located at 335.7 eV and 283.4 eV, respectively. Gabasch et al. observed peaks associated with the Pd $3d_{5/2}$ and C 1s components at 335.34 eV and 284.5 eV, respectively. While contribution to the higher BE Pd 3d peak from a PdC_x phase was not disproved, a corresponding C 1s peak consistent with either of the above references was not observed for the *in situ* experiment.

After dosing TMA, carbon (Figure 5.7) and aluminum (Figures 5.8–5.9) also appear on the surface. For the UHV-XPS experiment, the Al 2p envelope is composed primarily of a peak at 72.7 eV, assigned to either metallic Al or MMA. For the *in situ* XPS experiment, the majority of Al was deposited as Al metal or MMA at 72.7 eV, but some of the oxide (74.1 eV) species is present. As in the case of Pt(111), the oxidation was likely due to the reaction of oxygen-containing molecules from the walls of the *in situ* cell with the as-deposited TMA. The Al 2s results after dosing TMA mirror the Al 2p results (see Table 5.3). The coverage of total Al as Al metal was calculated for Pd(111) in the same manner as for Pt(111); nominal coverages were 0.5 ML and 0.9 ML for the *in situ* and UHV-XPS experiments, respectively. However, one should not think of coverage in a typical fractional monolayer fashion for Al on Pd(111) due to the formation of the Pd-Al alloy.

The C 1s region in the UHV-XPS experiment was fit with 2 peaks at 283.3 and 284.3 eV. For the *in situ* XPS experiment, only one asymmetric peak was needed to fit the envelope at 284.1 eV. The peaks at 284.1-284.2 eV are assigned to dehydrogenated species such as CH, isolated C, or “chain” C (see discussion in Pt(111) section). The low BE peak at 283.3 eV could be assigned to a PdC_x phase, in agreement with the value of 283.4 eV observed by Teschner et al. [139] DFT predicted the presence of MMA, but due to the lack of an appropriate binding energy reference this could not be confirmed by XPS.

C coverage for the *in situ* XPS experiment was approximately 0.5 ML, whereas coverage was 1.1 ML for the UHV-XPS experiment. The differences in the C 1s region could be due to the uncertainty of the TMA adsorption temperatures in the *in situ* XPS experiment, which might be higher than those in UHV-XPS experiment (see Experimental Section).

The relative amount of Al deposited as metallic Al or MMA decreased after dosing water at room temperature in the *in situ* experiment, and the higher binding energy Al

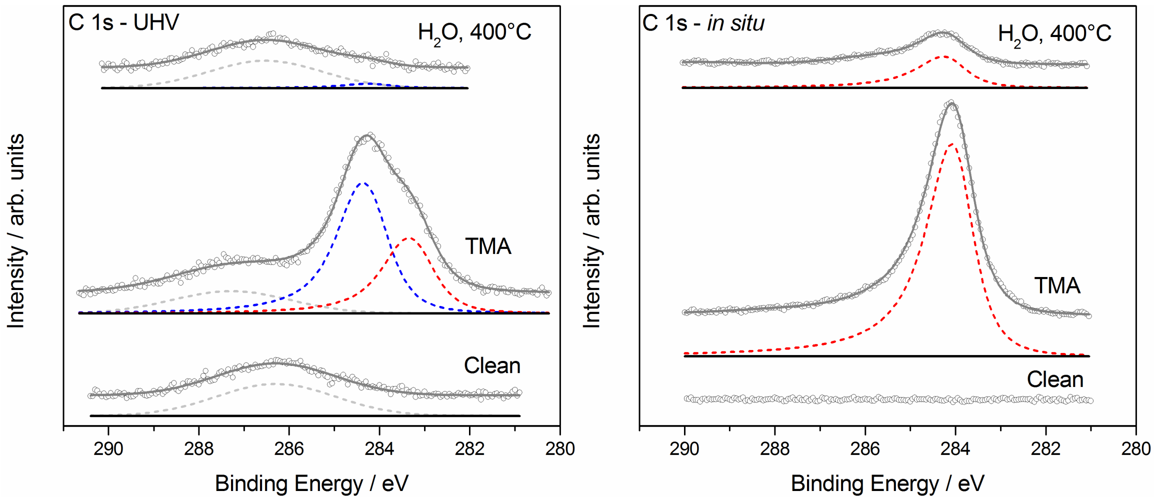

(a) UHV (b) *In situ*

Figure 5.7. C 1s regions for (a) UHV-XPS and (b) *in situ* XPS on Pd(111). From bottom to top: Pd(111) after repeated cleaning cycles, following dosing of TMA (at 100°C for the UHV experiment and between 100-200°C for the *in situ* experiment), and after exposure to water at 400°C. Fitted components originating from carbon-containing components are shown as red and blue dashed lines (assignments discussed in text). Also present is a Pd 3d ghost peak (light grey). The open circles are raw data points, and the light grey line is the sum of the deconvoluted peaks.

2p peak at 74.8 eV appeared and is assigned to $Al_xO_y(OH)_z$. As shown in Figure 5.8, as the temperature was increased during water dosing, the higher BE oxide/hydroxide peak decreased in intensity, as did the peak assigned to metallic aluminum or MMA, while the other oxide/hydroxide peak at 74.1 eV increased in relative intensity. At 400°C, 91% of the Al was present as Al_2O_3 on Pd(111) for the *in situ* XPS experiment. However, both the aluminum oxide and hydroxide/oxyhydroxide phases were present after dosing water at 400°C in the UHV-XPS experiment (66% of Al 2p peak area assigned to Al_2O_3). Component percentages of total envelope areas are listed in Table 5.3 as a percentage of total envelope area. Upon dosing water at 400°C, the Pd-Al alloy component nearly disappeared. Calculated thicknesses were < 1 Å (this

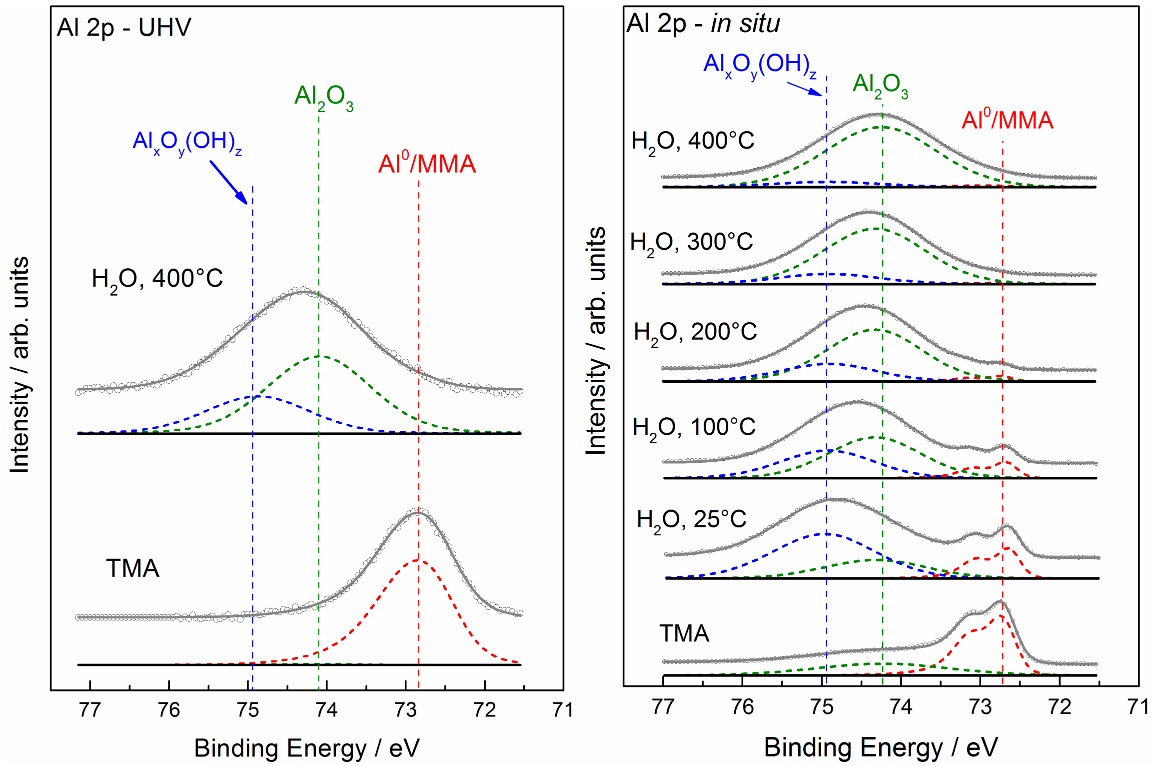

(a) UHV (b) *In situ*

Figure 5.8. (a) Al 2p regions for UHV-XPS experiment on Pd(111). From bottom to top: Pd(111) following dosing of TMA at 100°C, and after exposure to water at 400°C. (b) Al 2p high resolution core level regions for *in situ* XPS experiment on Pd(111). From bottom to top: Pt(111) single crystal after repeated cleaning cycles, following dosing of TMA between 100–200°C, and after exposure to water at 25°C and subsequently in steps to 400°C. Fitted components are shown as dashed lines and represent metallic Al or MMA (red), Al_2O_3 (green), and partially hydroxylated/oxyhydroxide aluminum (blue). The open circles are raw data points, and the light grey line is the sum of the deconvoluted peaks.

small thickness value was likely due to an XPS curve-fitting artifact since the apparent alloy thickness from fitting artefacts for the clean surface was similar).

Overall carbon coverage decreases from 1.1 to < 0.1 ML after dosing water on the UHV prepared sample at 400°C, and from 0.5 to 0.2 ML on the *in situ* sample after dosing water at 400°C compared to after dosing TMA. The decrease in C 1s intensity

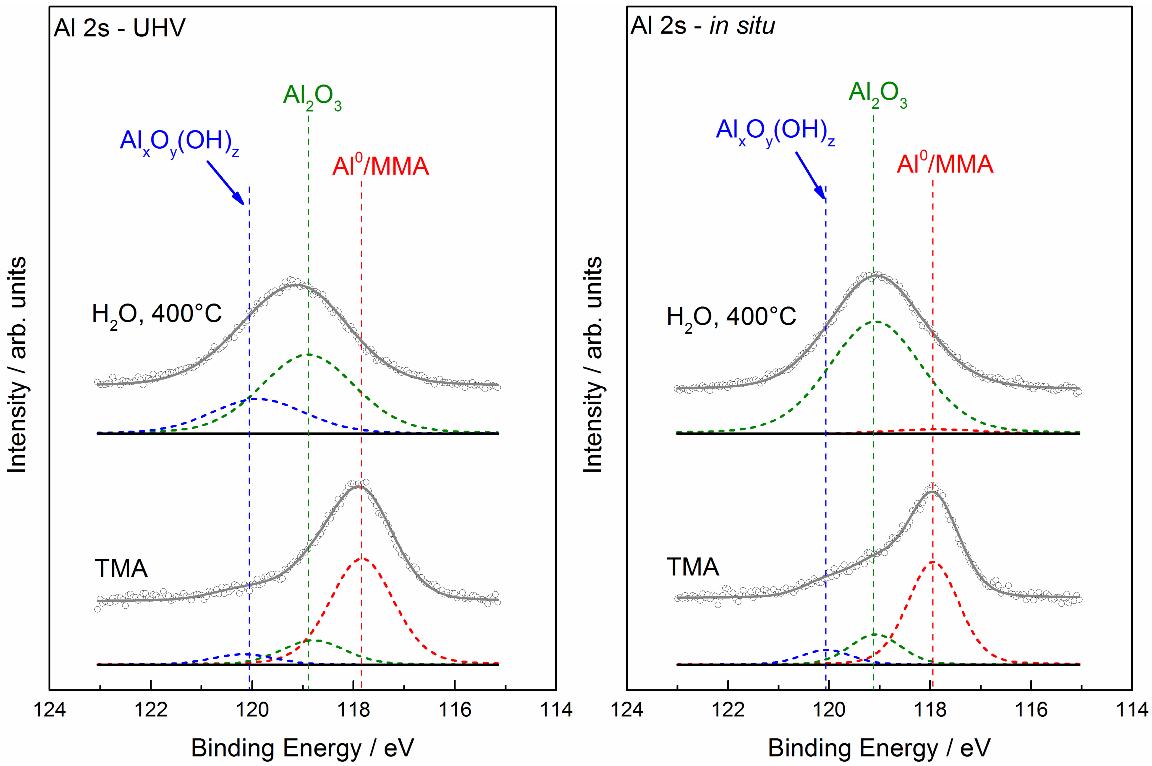

(a) UHV

(b) *In situ*

Figure 5.9. Al 2s core level regions for (a) UHV-XPS and (b) *in situ* XPS (bottom) on Pd(111). From bottom to top: Pd(111) following dosing of TMA (at 100°C for the UHV experiment and between 100–200°C for the *in situ* experiment), and after exposure to water at 400°C. Fitted components are shown as dashed lines and represent metallic Al or MMA (red), Al_2O_3 (green), and partially hydroxylated/oxyhydroxide aluminum (blue). The open circles are raw data points, and the light grey line is the sum of the deconvoluted peaks.

for both experiments can be seen in Figure 5.7. For the UHV-XPS experiment, only the peak at 284.2 eV remains after dosing water at 400°C. The peak at 284.2 eV in the *in situ* XPS experiment decreases in intensity, and two small peaks appear at 285.9 and 289.8 eV (cannot be seen in Figure 5.7 because they are too small). These peaks are assigned to adsorbed CO [206] and carboxyl species, [69] respectively. A scaled version of this core level region showing the CO and carboxyl species contribution

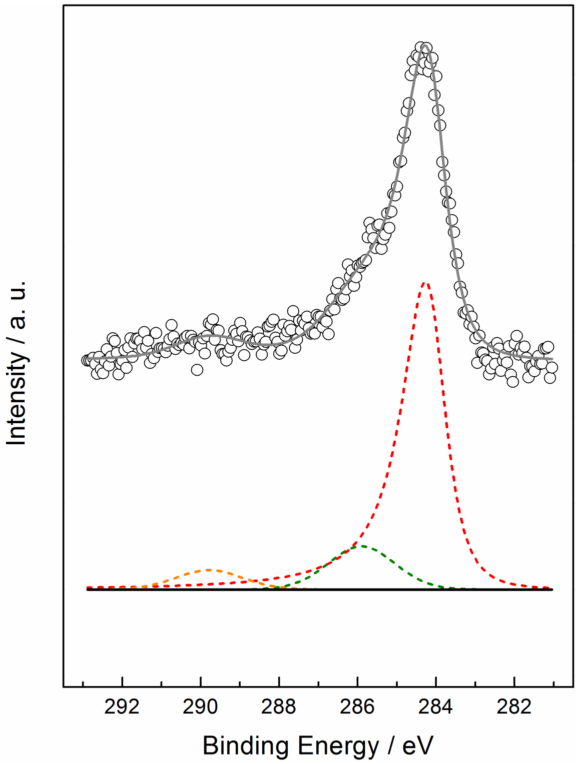

Figure 5.10. C 1s core level region for *in situ* XPS on Pd(111) during exposure to 0.1 mbar water at 400°C. Fitted components originating from carbon-containing components are shown as orange (adsorbed carboxyl), dark green (adsorbed CO), and red (assignment discussed in text) dashed lines. The open circles are raw data points, and the light grey line is the sum of the deconvoluted peaks.

to the overall peak envelope are shown in Figure 5.10. C 1s BEs and percentages of total area are summarized in Table 5.4.

Thicknesses of the resultant Al_2O_3 films were estimated following exposure to water at 400°C. Details of this calculation are given in the SI. For the *in situ* XPS experiment, the Al_2O_3 film thickness was estimated to be 5 Å, and for the UHV experiment, 7 Å. Note that this thickness calculation assumes that all Al is present as Al_2O_3 in both experiments.

Table 5.3.
Observed Al 2p and Al 2s component binding energies envelope area % for Pd(111) samples after TMA exposure and water exposure at 400°C.

	UHV-XPS				*in situ* XPS			
	Al 2s		Al $2p_{3/2}$		Al 2s		Al $2p_{3/2}$	
Component	BE / eV	% area	BE / eV	% area	BE / eV	% area	BE / eV	% area
				TMA Exposure				
Al^0/MMA	117.8	75	72.7	99	117.9	69	72.7	65
Al_2O_3	118.8	17	74.0	1	119.1	21	74.1	35
$Al_xO_y(OH)_z$	120.2	8	-	0	120.0	10	-	0
				Water Exposure, 400°C				
Al^0/MMA	-	0	72.7	2	117.9	4	72.8	1
Al_2O_3	118.9	69	74.0	66	119.1	96	74.1	91
$Al_xO_y(OH)_z$	119.9	31	74.7	32	-	0	74.8	8

Table 5.4.
Observed C 1s component binding energies and envelope area % for Pd(111) samples after TMA exposure and water exposure at 400°C.

	UHV-XPS		*in situ* XPS	
Component	BE / eV	% area	BE / eV	% area
		TMA Exposure		
1	283.3	30	-	0
2	284.3	53	284.1	100
		Water Exposure, 400°C		
1	-	0	-	0
2	284.2	100	284.2	81

5.4.2 Density Functional Theory

The mechanism of TMA dissociation is analyzed with DFT calculations on Pt(111) and Pd(111) surfaces, as shown in Figure 5.11. All energies are referenced to gas phase TMA and the clean metal slabs, and it is assumed that dissociated methyl groups spontaneously form methane gas with preadsorbed hydrogen atoms that are initially far removed from the adsorbing TMA. The entropy loss (TΔS) associated with TMA adsorption, 0.74 eV, is assumed to be equal to the translational entropy of gaseous TMA at 150°C, and the corresponding entropy gain for desorbing methane is calculated to be 0.66 eV. The entropy change of purely surface reactions, in turn, is assumed to be zero. TMA decomposition on both surfaces is highly exothermic although the process is slightly more exothermic on Pt(111) than on Pd(111). Both TMA and dimethyl aluminum (DMA) are most favorably adsorbed in a partially dissociated configuration at the considered coverage of $^1/_9$ ML. Nondissociated configurations (not shown) are much less stable and can only be identified, in select circumstances, with a very careful choice of force optimizer, suggesting that barriers to break Al-C bonds in TMA and DMA are very small. The lowest energy points

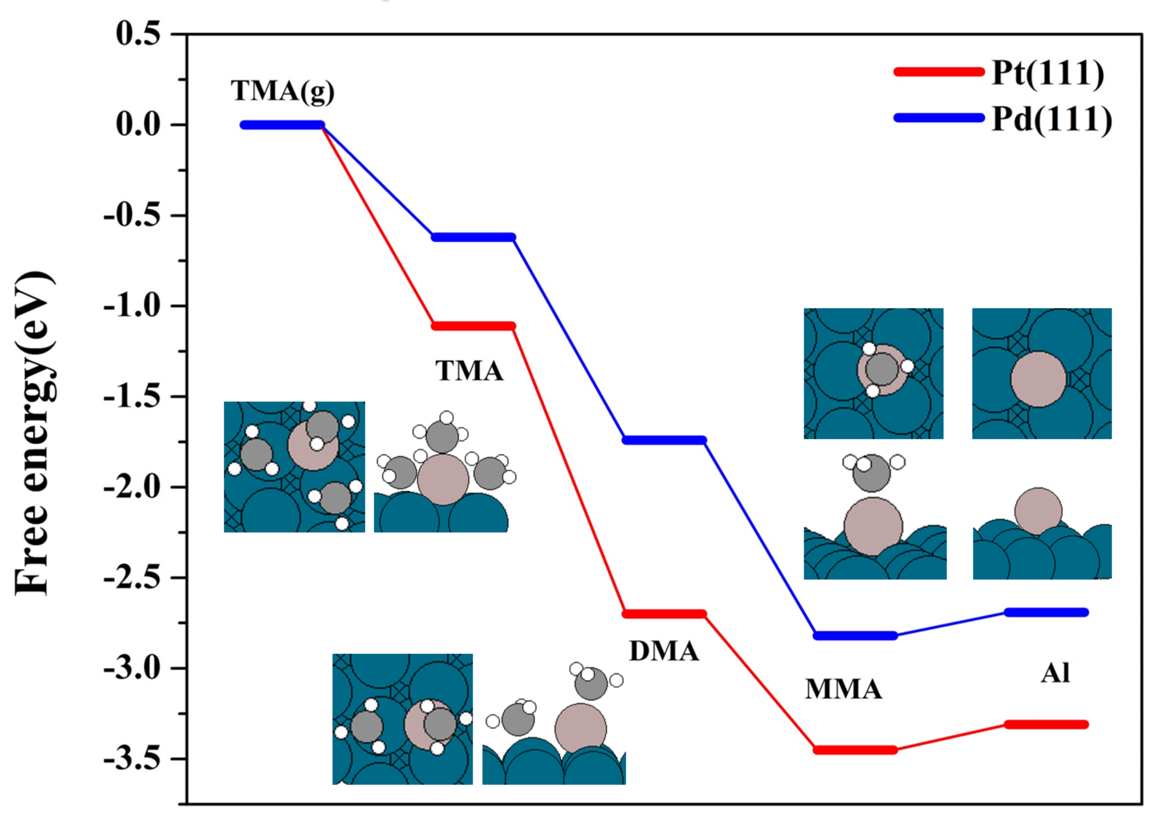

Figure 5.11. Free energy vs. reaction coordinate for TMA decomposition on Pt(111) and Pd(111). Entropies are calculated at a temperature of 150°C at standard pressures of 1 bar.

in the free energy diagram correspond to monomethyl aluminum (Al-CH_3, "MMA"), while atomic aluminum is slightly less stable on both metals. The results suggest that the XPS signatures at 118.1 eV likely correspond to a mixture of adsorbed MMA and Al, with MMA formation being modestly favored on terraces and Al formation being perhaps more favorable at defect sites. [85]

5.5 Discussion

After dosing TMA at 10^{-5} mbar, formation of a surface Pd-Al alloy phase was observed, as evidenced by the appearance of a higher BE peak in the Pd 3d core level. A similar phenomenon was not observed in the Pt 4f core level. It should be noted that the Pd-Al alloy formed during TMA exposure between 100-200°C (shown in Figure 5.6). TMA adsorption on Pd(111) even at room temperature resulted in the surface Pd-Al alloy (data not shown). Previous XPS studies of Pd-Al alloys have observed BE shifts of the Pd $3d_{5/2}$ peak between +0.8 to +2.1 eV relative to the Pd^0 peak. [131, 132, 132, 134] Shifts observed in the current study are in the range of +0.6 to +0.8 eV relative to the Pd^0 peak. The Pt $4f_{7/2}$ peak undergoes a shift of +0.3 eV in the *in situ* XPS study and +0.1 eV in the UHV study, however, this is unlikely due to the formation of a surface Pt-Al alloy. The fwhms of the Pt^0 4f peaks decrease from 0.96 to 0.91 eV and from 1.23 to 1.19 eV after deposition of TMA for the *in situ* and UHV experiments, respectively, whereas the formation of an alloy associated with a slightly higher binding energy would likely cause a broadening of Pt 4f region due to the new type of Pt chemical environment. Wilson et al. [135] observed an alloy shift of 1.4 eV for the Pt-Al alloy Pt $4f_{7/2}$ component relative to the metal following deconvolution of the Pt 4f region. The alloy formation was accompanied by a broadening of the overall envelope. However, any contribution of the Al 2p signal in this deconvolution was not included. Finally, this small shift cold be due to the influence of adsorbates. Adsorbed CO was found to shift the Pt 4f peak by +1.3 eV in synchrotron radiation XPS experiments. [138] The extent, then, to which Al alloys with Pt in this study was not detectable by XPS.

Dosing water at 400°C to the Pd(111) surface removes the Pd-Al alloy phase, restoring all Pd to the metallic state. Johańek et al. [133] observed the formation of aluminum oxide following exposure of a Pd-Al alloy to CO, indicating that CO partially dissociated on the alloy surface, and the oxygen reacted with Al. Furthermore, they observed an increase in the relative surface concentration of Al following CO dosing, indicating that dissociated O was reacting with subsurface Al to form aluminum oxide on the surface. This behavior is similar to that observed in this study, where the formation of an oxidized aluminum overlayer occurs simultaneously with the removal of the Pd-Al alloy phase.

By following the first cycle of TMA-water ALD with XPS, the fate of the carbon species can be elucidated. Carbon was observed by XPS on both Pd(111) and Pt(111) surfaces following TMA deposition. The C:Al coverage ratios were approximately 1:1 and 2:1 on Pd(111) and Pt(111) surfaces, respectively. Two components of the C 1s peak were observed on Pd(111) in the UHV experiment and on Pt(111) in the *in situ* experiment. While DFT calculations showed that the most stable Al-containing decomposition product on both surfaces was MMA, differences in the C 1s regions between the two experiments indicate that the resulting carbon overlayer is dependent on both substrate and TMA dosing temperature, which was likely higher for the *in situ* experiment (see Experimental section). Peaks in the XPS C 1s deconvolutions likely represent several carbon species in different environments. The presence of the Pd-Al alloy phase indicates that at least some TMA molecules lose all attached methyl ligands in order for Al to alloy with Pd. Lu et al. [85] followed desorption of products during dosing of TMA and water on Pd nanoparticles *in situ* with quadrupole mass spectrometry used in an ALD reactor. They observed the evolution of methane (97.9 mol %) and ethane (2.1 mol %) after dosing TMA on the Pd nanoparticles. They attribute the ability of Pd to form ethane to a high coverage of CH_3 groups on the Pd, which can combine to form ethane (see Reference [85] and references therein). In order to form methane, TMA methyl groups must be hydrogenated by other methyl groups, which dehydrogenate to form CH_x species ($x < 3$) on the surface. CH_3 adsorbed on Pt(111) is known to exhibit similar chemistry, where methane is produced along with dehydrogenated C1 species, and at high CH_3 coverages adsorbed methyl groups can combine to form ethylidyne. [145] However, the lack of evidence for Pt-Al alloy formation on Pt(111) might indicate a lower probability for all methyl ligands to desorb from an Al atom on that surface.

Another observed difference in the behavior of Pt(111) and Pd(111) with TMA and water related to the carbon chemistry is the ease with which carbon can be removed from both surfaces. Dosing 0.1 mbar water at 400°C results in the removal of carbon from both Pd(111) and Pt(111), whereas at 7×10^{-6} mbar water, carbon disappears only from Pd(111), and the carbon coverage remains constant on Pt(111). Carbon removal, then, appears to be substrate dependent. To increase our understanding of the carbon removal mechanism, Pt(111) and Pd(111) surfaces were annealed in UHV following TMA adsorption at 100°C (spectra not shown). On Pd(111), metallic aluminum was present at 400°C and carbon was fully removed. On Pt(111), heating in UHV at 400°C did not result in carbon removal. Therefore, though water plays a role in carbon removal as evidenced by the appearance of oxygenated C compounds in the C 1s spectrum of the *in situ* experiment for Pd(111) in Figure 5.10 and the removal of carbon from Pt(111) in 0.1 mbar water vapor, the substrate effects the carbon chemistry. The driving force behind the different carbon removal behavior at 7×10^{-6} mbar and 0.1 mbar water pressure on Pt(111) could be a thermodynamic limitation, where water coverage is negligible at a background pressure of 7×10^{-6} mbar, or it could be a kinetic limitation related to the slow oxidation of carbon with water. The observed effect could also be a combination of thermodynamic and kinetic limitations. The formation of a Pd-Al alloy on Pd(111) suggests that all methyl groups from Al atoms alloyed with Pd must be rejected to the Pd surface, which can then react even in the absence of water. For Pt, an alloy was not observed, suggesting that complete removal of methyl groups from Al on Pt(111) is more difficult than from Al on Pd(111). At 10^{-5} mbar, water cannot react with these methyl groups attached to Al on Pt(111). The carbon chemistry on Pt and Pd is not straightforward and shows dependence on the metal substrate; therefore this chemistry will be the focus of a future publication. [207]

A final interesting phenomenon is aluminum oxidation by H_2O. In the case of Pd(111), the Al-Pd alloy is reversed and all Pd was reverted to the monometallic phase. Water caused Al to oxidize to Al^{3+} on both surfaces following dosing at 0.1 mbar and 400°C, but Al is only partially hydroxylated on both surfaces following water dosing at 7×10^{-6} mbar and 400°C. In addition to the inability of water vapor at 7×10^{-6} mbar to remove adsorbed carbon on Pt(111), Al was not completely oxidized to Al_2O_3 after dosing water at the same pressure. The state of adsorbates on the surface, then, affects the reaction pathway of TMA with oxidized or hydroxylated aluminum in subsequent ALD cycles: TMA can react through ligand exchange with two hydroxyl groups, or dissociatively with aluminum oxide Al-O pairs (see Reference [31] and references therein).

5.6 Conclusions

The findings of this investigation of the reaction between TMA and water on Pt(111) and Pd(111) are summarized as follows:

Surface Pd-Al alloy. After dosing TMA between 100–200°C to Pd(111), a Pd-Al surface alloy forms. No alloy of Pt and Al was observed under the same conditions.

Carbon removal. Carbon was removed from both Pt(111) and Pd(111) in 0.1 mbar H_2O at 400°C. At 7×10^{-6} mbar H_2O and 400°C, carbon was removed from Pd(111), whereas the carbon coverage does not change on Pt(111).

Aluminum oxidation. In 0.1 mbar H_2O at 400°C, aluminum was oxidized to Al_2O_3 on both surfaces. On the other hand, at 7×10^{-6} mbar H_2O and 400°C, the majority species was Al_2O_3, but other Al oxidized and hydroxylated species were present.

On both surfaces, DFT calculations suggested that rapid TMA decomposition to methyl aluminum (MMA) or atomic Al is thermodynamically favorable, which agrees with the experimental observations. However, Pd(111) and Pt(111) act differently during TMA adsorption and then during the reaction with H_2O. Therefore, future studies are required to understand this difference, specifically regarding the differences in carbon chemistry on each surface. Many mechanistic details of the interactions of the precursors with Pd(111) and Pt(111) were not ascertained during this study, and will be the subject of future work. However, two observations, the formation of the Pd-Al alloy and the difference in carbon chemistries between Pt(111) and Pd(111), highlight the chemical sensitivity of the first ALD cycle. The results of this study should also cause caution for those planning to study ALD reactions in UHV.

Therefore, we conclude that the results obtained from studying ALD systems in UHV may not be fully applicable to other industrial or laboratory studies performed in the millibar pressure range. However, UHV experiments can screen substrates for specific properties, such as the ability to desorb carbon-containing ligands. UHV experiments can also be useful for determining dosing parameters for ALD precursors for experiments carried out at facilities with *in situ* capabilities, where user time may be limited.

The findings presented here demonstrate that the effect the metal substrate must be considered when choosing process conditions for ALD applications, especially for those involving a low number of ALD cycles. In order to minimize carbon incorporation into the ALD film, the temperature of water dosing must be sufficient to remove carbon. These conditions must be carefully chosen depending on the substrate, especially for ultra-thin films. Furthermore, since the water dosing temperature determines the extent to which Al is oxidized, this could impact mass gain per ALD cycle and affect the film quality.

5.7 Acknowledgments

DFT calculations were performed by Dr. Xiang-Kui Gu, Prof. Bin Liu, and Prof. Jeffrey Greeley. Adapted with permission from Detwiler, M. D.; Gharachorlou, A.; Mayr, L.; Gu, X.-K.; Liu, B.; Greeley, J.; Delgass, W. N.; Ribeiro, F. H.; Zemlyanov, D. Y. Reaction of Trimethylaluminum with Water on Pt(111) and Pd(111) from 10^{-5} to 10^{-1} Millibar. *J. Phys. Chem. C*, 2015, 119, 2399-2411. Copyright 2015 American Chemical Society.

6. TRIMETHYLALUMINUM AND OXYGEN ATOMIC LAYER DEPOSITION ON HYDROXYL-FREE CU(111)

6.1 Abstract

Atomic layer deposition (ALD) of alumina using trimethylaluminium (TMA) has technological importance in microelectronics. This process has demonstrated a high potential in applications of protective coatings on Cu surfaces for control of diffusion of Cu in $Cu2_S$ films in photovoltaic devices and sintering of Cu nanoparticles in liquid phase, catalytic hydrogenation reactions. With this motivation in mind, the reaction between TMA and oxygen was investigated on Cu(111) and Cu_2O/Cu(111) surfaces. TMA did not adsorb on the Cu(111) surface, a result consistent with density functional theory (DFT) calculations predicting that TMA adsorption and decomposition are thermodynamically unfavorable on pure Cu(111). On the other hand, TMA readily adsorbed on the Cu_2O/Cu(111) surface at 473 K resulting in the reduction of some surface Cu^+ to metallic copper (Cu^0) and the formation of a copper aluminate, most likely $CuAlO_2$. The reaction is limited by the amount of the surface oxygen. After the first TMA half-cycle on Cu_2O/Cu(111), two-dimensional (2D) islands of the aluminate were observed on the surface by scanning tunneling microscopy (STM). According to DFT calculations, TMA decomposed completely on Cu_2O/Cu(111). High-resolution electron energy loss spectroscopy (HREELS) was used to distinguish between tetrahedrally (Al_{tet}) and octahedrally coordinated (Al_{oct}) Al^{3+} in surface adlayers. TMA half-cycles produced an aluminum oxide film which contained more octahedral coordinated Al^{3+} (Al_{tet}/Al_{oct} HREELS peak area ratio ≈ 0.3) than was observed after O_2 half-cycles (Al_{tet}/Al_{oct} HREELS peak area ratio ≈ 0.5). After the first ALD cycle, TMA reacted with both Cu_2O and aluminum oxide surfaces in the

absence of hydroxyl groups until film closure by the 4th ALD cycle. Then, TMA continued to react with surface Al-O, forming stoichiometric Al_2O_3. O_2 half-cycles at 623 K were more effective for carbon removal than O_2 half cycles at 473 K or water half cycles at 623 K.

6.2 Introduction

Copper is widely used for a variety of applications including water heat exchangers, [35] interconnect and gate electrodes for microelectronics, [208,209] and heterogeneous catalysts for reactions including low temperature water-gas shift (WGS) [210] and methanol steam reforming. [39,211] However, the use of copper in these applications is limited by corrosion in oxidative environments, [35,212] diffusion into adjacent layers in microelectronics, [208,213] and particle sintering and leaching in Cu-based catalysts. [39] Recently, atomic layer deposition (ALD) of alumina using trimethylaluminium (TMA) has been introduced to form protective coatings on Cu surfaces which prevent corrosion in oxidative environments, [35,212] diffusion of Cu in Cu_2S films in photovoltaic (PV) devices, [213] and sintering of Cu-based nanoparticles in liquid phase hydrogenation reactions. [39,124]

ALD is a variation of chemical vapor deposition (CVD) based on self-limiting reactions of gaseous precursors with a solid surface. [121] ALD is performed in a cyclic manner. For binary ALD reactions, each ALD cycle consists of two half-cycles during which the surface is consecutively exposed to a precursor and a co-reactant. Between each cycle, the reaction chamber is purged with an inert gas or vacuum. TMA is the most widely used ALD precursor for growth of aluminum oxide films, and water is the most common co-reactant (see, for instance, reference [31] and references therein).

Though the interaction of TMA with adsorbed hydroxyl functional groups on Al has been studied in depth, [31] the reaction of TMA with air-exposed copper surfaces complicates this ideal ALD picture due to the formation of a surface oxide at room temperature. [214] Furthermore, this oxide persists and rearranges to form the ordered

44-structure on Cu(111), [214] a structured Cu_2O overlayer with unit cell size 44 times larger than the Cu(111) unit cell, at 473-623 K, a temperature range encompassing processing temperatures for TMA-H_2O ALD with a maximum growth rate. [215] This and other adsorbed oxygen reconstructions persist on the surface until at least 773 K. Hydroxyl formation via water dissociation on copper surfaces is difficult. On Cu(111), thermally induced water dissociation was not observed in UHV. [216] No adsorbed hydroxyl species formed following exposure of clean Cu(111) to 1 Torr of water up to 333 K, however, a pre-oxidized Cu surface readily forms hydroxyls during water exposure at the same conditions. [217] In UHV, exposure of a pre-oxidized Cu(111) surface to 200 L H_2O at 1×10^{-6} Torr at 473 K resulted in a surface with both oxide (Cu_2O) patches and patches with hydroxyls. [123]

TMA-H_2O ALD performed on oxidized Cu surfaces results in low growth per cycle during the first several cycles. An *in situ* copper-plated quartz crystal microbalance (QCM) was used by Abdulagatov et al. [35] to study the ALD alumina growth on copper oxide. They observed a nucleation delay at 450 K using TMA and water. The nucleation delay was caused by blockage of the copper oxide surface by carbonaceous species and/or lack of initial hydroxyl groups, however, the cause was not determined due to the lack of chemical information. Lu et al. [123] demonstrated that alumina grows preferentially on step edges of a partially hydroxylated oxidized Cu(111) surface for TMA-H_2O ALD. They speculate from STM images that TMA reacts with OH^- but not copper oxide.

The goal of this work was to better understand the reactivity of TMA with copper oxide surfaces. More broadly, we sought to study the reactivity of TMA with copper oxide and alumina in the absence of a source of hydroxyl groups and to examine the resulting surface chemistry and morphology. The reaction of TMA with alumina has received some attention in the literature, [182, 215, 218] however, here we used O_2 as the ALD co-reactant rather than H_2O to isolate the interaction with the oxide. In order to obtain direct chemical information and elucidate the reaction pathways of TMA with copper oxide and alumina, we coupled surface-sensitive techniques including X-ray photoelectron spectroscopy (XPS) and high-resolution electron energy loss spectroscopy (HREELS) with scanning tunneling microscopy (STM) and density functional theory (DFT) modeling. We found that TMA reacts with oxygen in both alumina and copper oxide.

6.3 Experimental Methods

Experiments were performed in an Omicron Surface Analysis Cluster at the Birck Nanotechnology Center (BNC) at Purdue University and at the ISISS beamline at the BESSY II synchrotron in Berlin, Germany. The Omicron Surface Analysis Cluster consists of an ultra-high vacuum (UHV) preparation chamber and a μ-metal analysis chamber with base pressures of 1×10^{-9} mbar and 5×10^{-11} mbar, respectively. The preparation chamber was equipped with a residual gas analyzer, an Ar^+ sputtering gun, resistive sample heating, and ALD precursor manifolds for precursor dosing, which are connected to the system via leak valves. The analysis chamber was equipped with XPS, HREELS, STM, low energy electron diffraction (LEED), and resistive sample heating. The sample temperature was measured by a K-type thermocouple attached to the sample holder.

STM images were obtained at room temperature in constant current (topographic) mode with electrochemically etched W tips. Etched W tips were conditioned in UHV by electron bombardment. STM images were analyzed using WSxM software. [96] STM height measurement was calibrated by setting the step height of a monatomic step on clean Cu(111) equal to the calculated or observed step height on clean Cu(111) (0.208 nm).

HREELS spectra were acquired using an ELS5000 instrument (LK Technologies) in the specular direction with a primary beam energy of 5 eV. The resolution, measured as the full width at half maximum (FWHM) of the elastic peak, was < 3 meV (< 24 cm^{-1}). All HREELS spectra have been normalized to the elastic peak intensity.

XPS data were acquired using a non-monochromatic Mg Kα X-ray source (hν = 1253.6 eV) with gun power of 150 W. High resolution spectra were recorded at a constant pass energy of 20 eV. The resolution, measured as the FWHM of the Cu 2p$_{3/2}$ peak, was approximately 1.2 eV. Photoelectrons were collected at a photoemission angle of 45° with respect to the surface normal.

The experimental apparatus at BESSY II has been described in detail previously. [187] It contained a load lock and *in situ* cell connected to the XPS spectrometer via differential pumping stages. The experimental procedures for sample preparation, TMA dosing, and data collection have been described in detail. [122]

XPS data were analyzed with CasaXPS (version 2313Dev64) software. Cu 3s peaks were fitted using an asymmetric Gaussian/Lorentzian line shape with tail dampening (CasaXPS Line shape=LF(1.2,1.3,15,60)). Nonmetallic species of oxygen (O 1s) and aluminum (Al 2s) were fitted with symmetric Gaussian/Lorentzian line shapes (CasaXPS Line shape=GL(30)). The two most intense core level Al peaks, Al 2p and Al 2s, overlap with the Cu 3p and Cu 3s peaks, respectively, associated with the Cu(111) substrate. However, Al 2s formed a distinct shoulder on the Cu 3s peak, whereas the Al 2p peak was fully masked by the Cu 3p peak and could not be deconvoluted even after several ALD deposition cycles. Therefore, the Cu 3s/Al 2s region was chosen for quantitative and qualitative analysis of the Al overlayer.

To calculate coverage from XPS data, we followed Fadleys approach, [62] which assumes a non-attenuating adlayer at fractional coverage. Details of this calculation are given in Appendix A. Overlayer thicknesses were also calculated using the approach outlined in Appendix A.

A Cu(111) single crystal disk with 10.0 mm diameter, 1.0 mm thickness (Princeton Scientific Corp.), and crystallographic orientation accuracy $< 0.5°$ was used. The copper single crystal was routinely cleaned by repeated cycles of Ar$^+$ sputtering and vacuum annealing at 1000 K. During the initial cleaning cycles, the crystals were treated in 5×10^{-6} mbar of O$_2$ at 623–673 K for 20 minutes to remove adventitious carbon. Crystal cleanliness was monitored by XPS, STM, and LEED.

The Cu(111) crystal was exposed to TMA (Aldrich, 97%) in the preparation chamber via a leak valve at reported exposure values and temperatures. Prior to dosing TMA, several cycles of freeze-pump-thaw were performed for purification. Dosing lines were heated overnight at 423 K, and the lines were filled with TMA and pumped several times before dosing. Exposure values are reported in Langmuir (1 Langmuir = 1 L = 1×10^{-6} Torr·s). During TMA dosing, ionization gauges were left on for pressure measurement. Similar cycles of freeze-pump-thaw were performed on water (Birck Nanograde Water, as SEMI E1.2 with the total organic carbon (TOC) reduced from 1 ppb to 0.25 ppb). The water mini-cylinder was kept at room temperature during the dosing. A separate dosing line and leak valve were used for water to avoid cross contamination and accidental exposure of TMA to water in the dosing manifold.

6.4 Computational methods

DFT calculations were performed by Vienna ab initio simulation package (VASP) [189] using projected augmented wave (PAW) [127] potential and PW91 exchange-correlation functional. [126] The plane wave cutoff of 400 eV was used. To model Cu(111), A three-layer slab model with (3×3) unit cell was used. The long-range ordered Cu_2O layer grown on Cu(111) has a well-defined structure in the literature. [214, 219, 220] The Cu_2O layer on Cu(111) consists of Cu-O rings with an isolated O located inside the ring. The appearance of this structure is further confirmed by our STM images. To model this structure, a ring including 12 Cu and 13 O atoms on two-layer Cu(111) with (5×5) unit cell was used (Figure 6.1). The $(4 \times 4 \times 1)$ and $(2 \times 2 \times 1)$ k-point meshes were used to sample the Brillouin zone for Cu(111) and Cu_2O, respectively. The bottom-layer Cu atoms were fixed and the remained atoms and adsorbates were relaxed until the residual forces less than 0.02 eV/Å. To prevent the artificial interaction between the repeated slabs along z-direction, 12 Å vacuum was introduced with correction of the dipole moment.

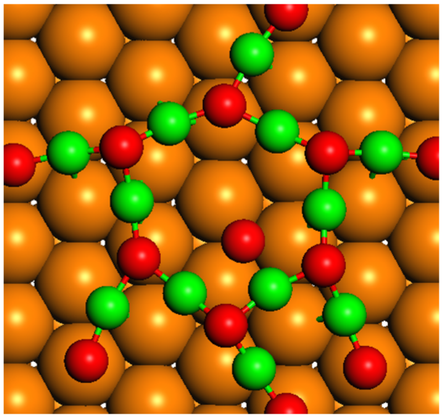

Figure 6.1. The optimized Cu_2O/Cu(111) structure. The orange, green, and red spheres present Cu in Cu(111) lattice, Cu in Cu_2O layer and O atoms, respectively. Adlayer atoms are not drawn to scale for visibility.

6.5 Results and Discussion

6.5.1 Interaction of TMA and H_2O on Cu Foil

The interaction of TMA with H_2O on Cu foil was studied using synchrotron-based XPS. It was found that the Al 2p BE shifted from ca. 75.1 eV after dosing TMA to 74.7 eV after dosing water at 473 K (Figure 6.2). It was unclear if this shift was due to the restructuring of an aluminum oxide film, such as the transition of Al^{3+} from octahedral to tetrahedral coordinated sites, or the dehydroxylation of an oxyhydroxide film (a detailed discussion is given in Chapter 5 of this dissertation). This was a major motivation for studying TMA-O_2 ALD in the absence of hydroxyl groups.

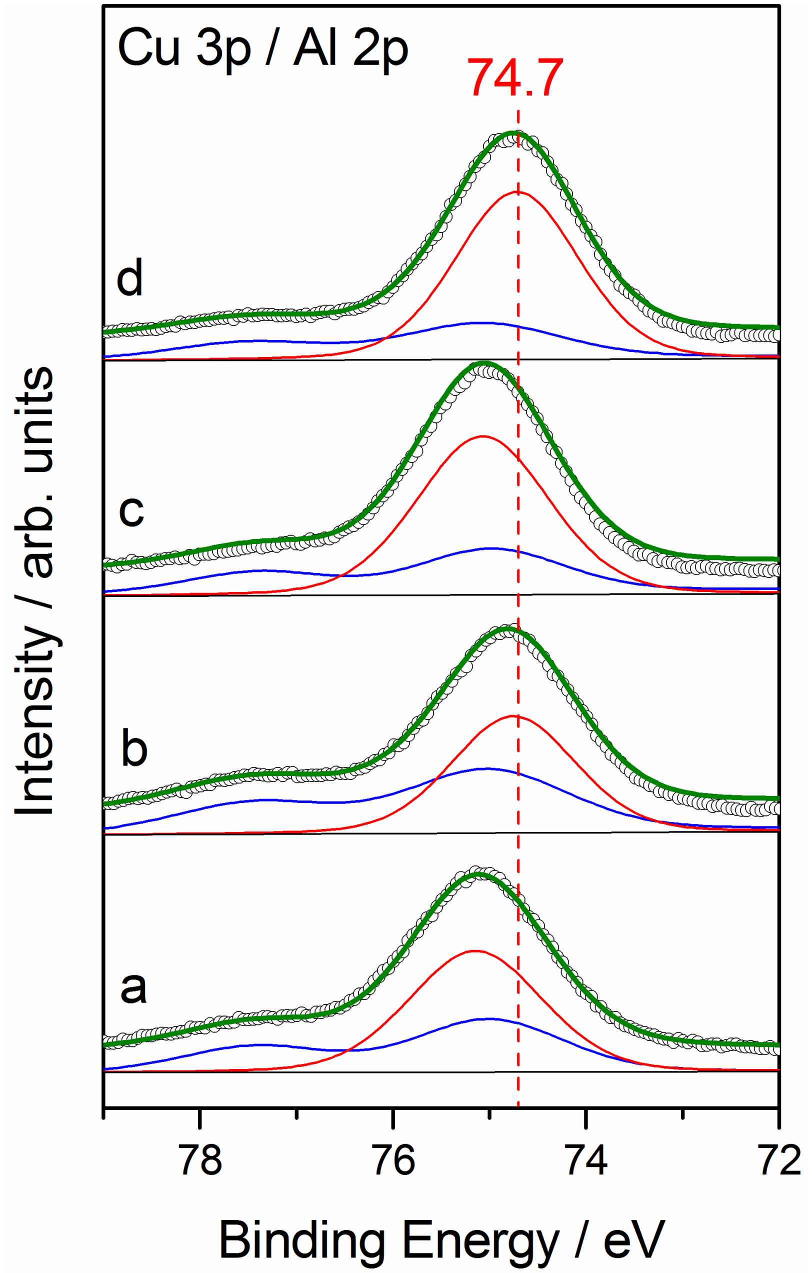

Figure 6.2. Cu 3p/Al 2p core-level regions obtained from TMA-H_2O ALD cycles on Cu foil by in situ XPS. (a) 2nd TMA half cycle, (b) 2nd H_2O half cycle, (c) 3rd TMA half cycle, (d) 3rd H_2O half-cycle. TMA was exposed for 2000 L at ca. 373–473 K for all TMA half-cycles, and H_2O was dosed *in situ* at 473 K at 0.1 mbar for all H_2O half-cycles.

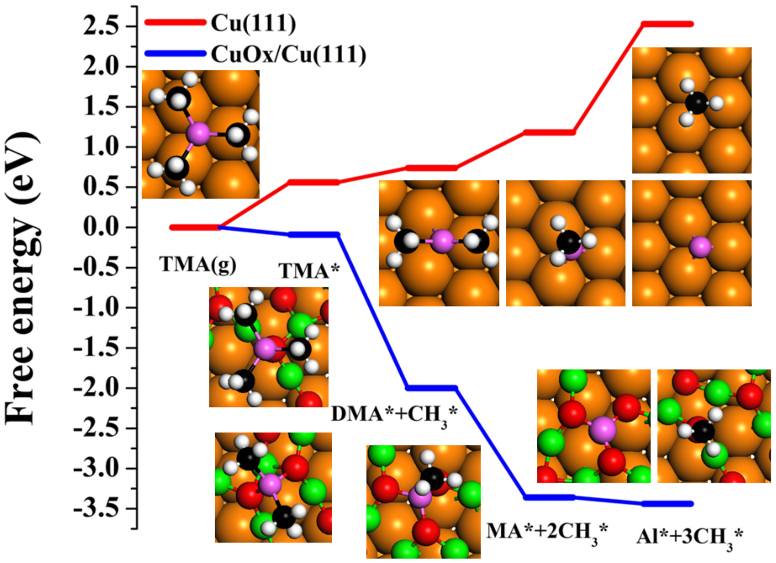

Figure 6.3. Free energy diagrams of TMA dissociation on Cu(111) and Cu_2O/Cu(111). Insets are the optimized most stable structures of adsorbed TMA, dimethylaluminum (DMA), methylaluminum (MA), Al, and CH_3, respectively. Orange, green, pink, black, red, and white spheres represent Cu of Cu(111), Cu of Cu_2O, Al, C, O, and H atoms, respectively.

6.5.2 Interaction of TMA with Clean Cu(111)

The interaction of TMA with the clean Cu(111) surface was investigated after TMA exposure by XPS and HREELS. The Cu $2p_{3/2}$ and Cu 3s peaks obtained from clean, oxygen-free Cu(111) were located at 932.8 and 122.3 eV, respectively, both within 0.1 eV of literature-reported values for metallic Cu. [68] Figure 6.6 shows the Cu 3s/Al 2s XPS region obtained from the clean Cu(111) surface and following 2000 L TMA exposure at 473 K. The range of BEs where a contribution from the Al 2s core level would be expected is marked by a red bar and is shown in the inset. After TMA adsorption on Cu(111) no aluminum was observed by XPS or HREELS. This is in agreement with the findings of Lu et al. for clean Cu(111). [123]

DFT calculations are also consistent with the lack of TMA adsorption on clean Cu(111). Figure 6.3 shows the free energy diagram for dissociative TMA adsorption on Cu(111) at 473 K. The energy loss from the entropy of the gas-phase TMA (g) at 473 K was 0.84 eV and the binding energy of TMA adsorbed on Cu(111) was -0.28 eV. Therefore, the difference between the free energy level of TMA (g) and TMA* was +0.56 eV. This means that the TMA adsorption on Cu(111) is endothermic. Moreover, TMA dissociation on clean Cu(111) was also found to be endothermic: the calculated energies for dissociative reactions of TMA to dimethylaluminum (DMA), DMA to methylaluminum (MA), and MA to Al and CH_3 were 0.17, 0.45, and 1.35 eV, respectively.

6.5.3 Preparation of Cu_2O/Cu(111)

Oxygen was adsorbed on Cu(111) by exposing the Cu(111) surface to 4500 L O_2 at 623 K. O 1s, Al 2s, and C 1s XPS core-level regions obtained from the Cu_2O/Cu(111) surface are shown in Figure 6.6, and STM images are presented in Figure 6.7. The O 1s peak was fitted with one component at 529.8 eV, which was assigned to oxygen in the Cu_2O layer (assignment made by STM below). Reported Cu_2O BEs range from 529.9 to 531.0 eV (see Reference [221] and references therein). A slight high BE shoulder at ca. 936.0 eV was observed in the Cu $2p_{3/2}$ core-level region following oxygen exposure indicating that some CuO was likely also present (data shown in Figure 6.4). The Cu 3s / Al 2s region was unaffected by the first O_2 exposure. Neither XPS nor HREELS of this surface revealed any hydroxyl species (HREELS spectrum shown in supplementary information Figure 6.5).

Figure 6.7a shows STM images of clean Cu(111), and Figure 6.7b-e show Cu(111) following oxygen exposure. The step edges of the clean Cu(111) surface are smooth with step height of 0.21 nm. After oxygen exposure at 623 K, a saw-tooth pattern is observed on the steps (Figure 6.7b), and a well-ordered oxide structure is observed on terraces (Figure 6.7c-e). After annealing O_{ads}/Cu(111) surfaces at 473–623 K, Matsumoto et al. [214] observed the well-ordered “44”-structure, which consists of 7 hexagonal O-Cu-O rings in a unit cell 44 times larger than the (1×1) unit cell of

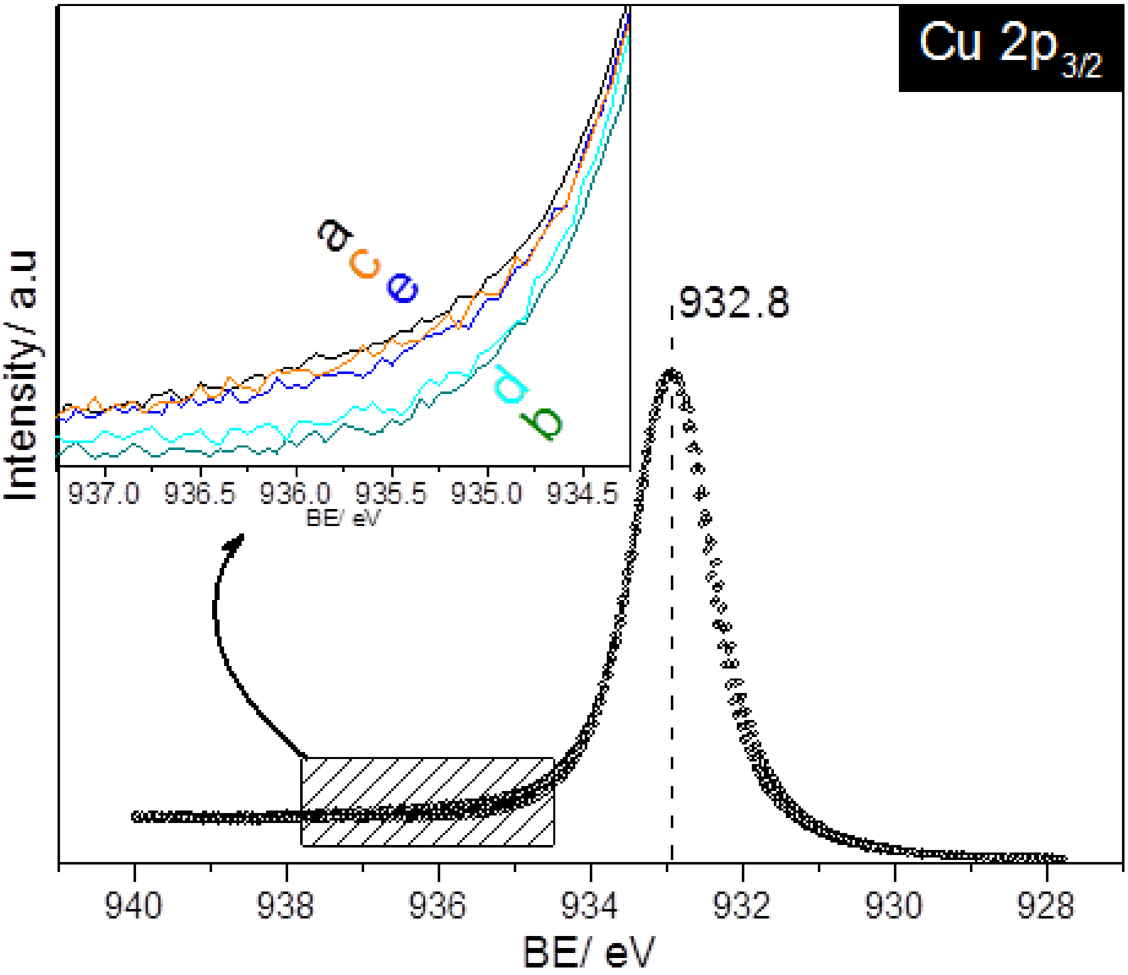

Figure 6.4. Cu $2p_{3/2}$ core-level region obtained from (a) Cu_2O/Cu(111) (4500 L O_2 at 623 K), (b) 1st TMA half-cycle, (c) 1st O_2 half-cycle, (d) 2nd TMA half-cycle, (e) 2nd O_2 half-cycle. Inset: close of up high-BE shoulder.

Cu(111). This superficial oxide has stoichiometry Cu_2O. A scheme of the 7 rings is shown overlaying our STM image in Figure 6.7e.

The assignment to Cu_2O is based on the STM images showing the “44” structure and lack of pronounced XPS shake-up in the Cu 2p region. We cannot rule out the presence of small amounts of Cu^{2+} given the surface sensitivity of our instrument.

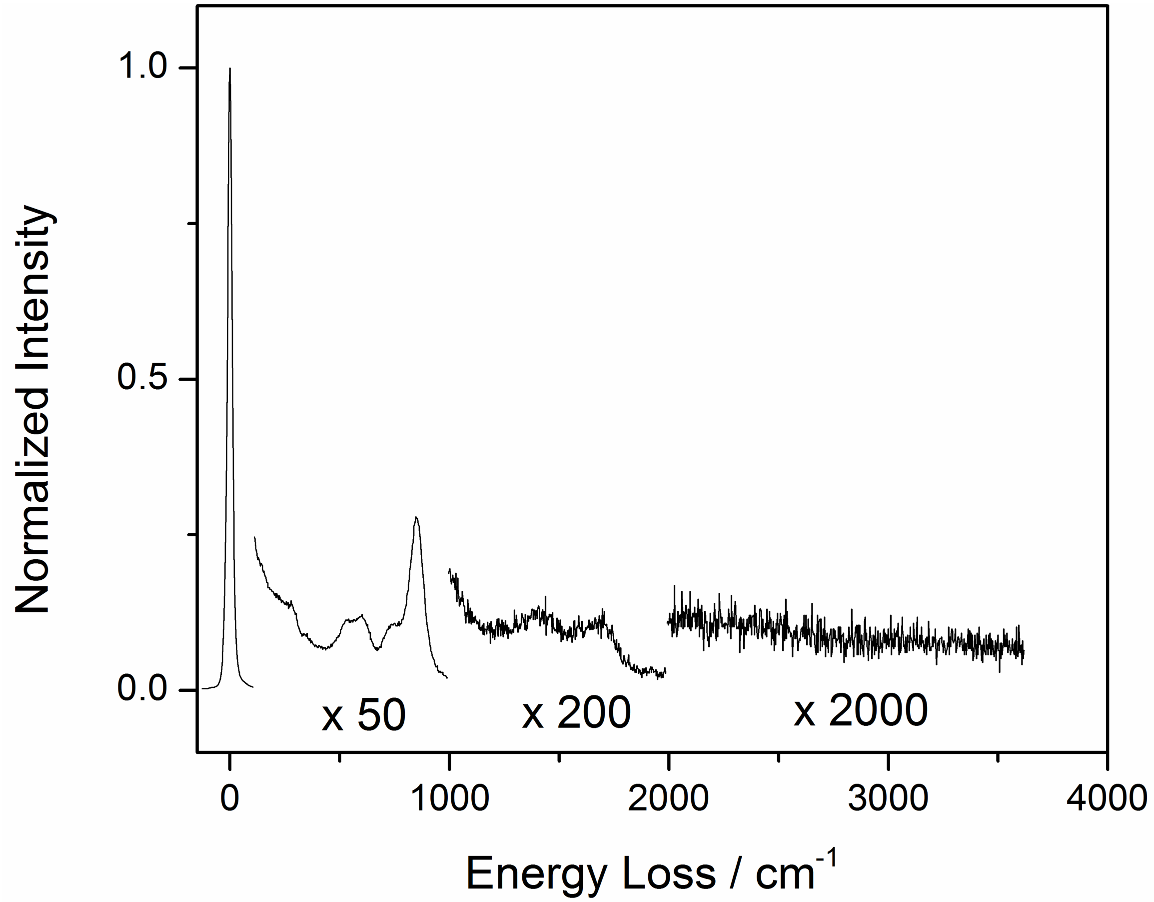

Figure 6.5. HREELS spectrum of Cu_2O/Cu(111) surface prepared by exposure of Cu(111) to 4500 L O_2 at 623 K.

After O_2 half cycles, we do see slight broadening of the Cu 2p peak high BE side (shown in Figure 6.4), which might be indicative of the formation of some Cu^{2+}. Cu^{+} and Cu^{0} are difficult to separate from the Cu 2p core-level as their range of reported binding energies overlap. [68]

6.5.4 First TMA Half-Cycle

Figure 6.8 shows the HREELS spectrum obtained after Cu_2O/Cu(111) was exposed to 2000 L TMA at 473 K. Major peaks were detected at 608, 747 and 882

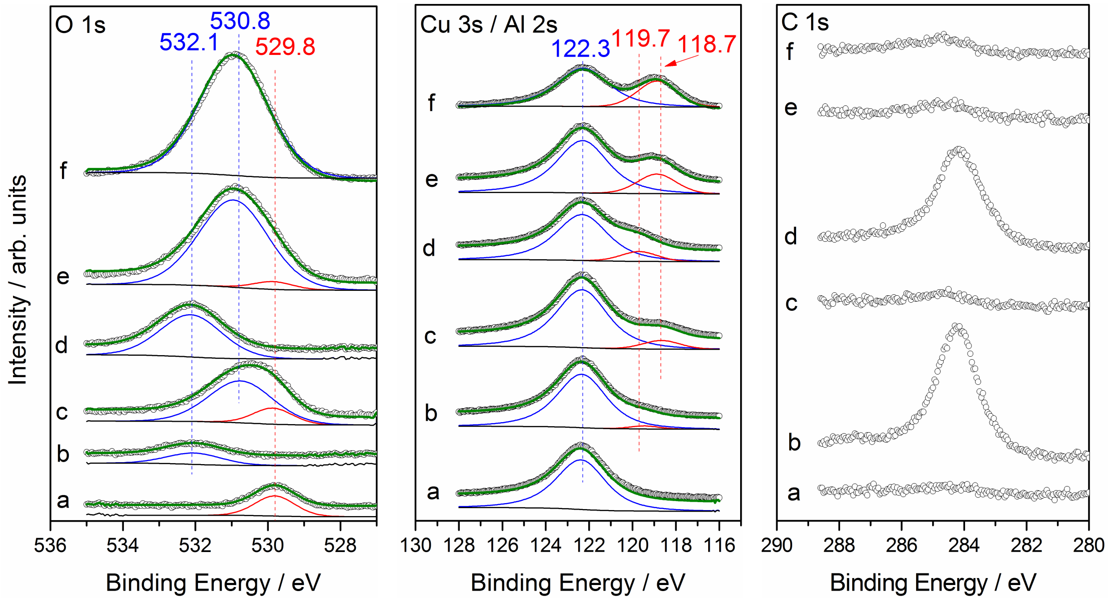

(a) O 1s (b) Cu 3s/Al 2s (c) C 1s

Figure 6.6. O 1s, Cu 3s/Al 2s, and C 1s XPS core-level regions obtained from (a) Cu_2O/Cu(111) (4500 L O_2 at 623 K), (b) 1st TMA half-cycle, (c) 1st O_2 half-cycle, (d) 2nd TMA half-cycle, (e) 2nd O_2 half-cycle, (f) after 4 complete ALD cycles. TMA was exposed for 2000 L at 473 K for all TMA half-cycles, and O_2 was exposed for 4500 L O_2 at 623 K for all O_2 half-cycles.

cm^{-1}, and weaker peaks were detected at ca. 1480, 1645, and 1750 cm^{-1}. The peak at 608 cm^{-1} (ν_1) was assigned to the group of stretching vibrations between tetrahedrally coordinated Al^{3+} cations (Al_{tet}) and their four nearest O_2^- neighbors, the peak at 880 cm^{-1} (ν_3) was due to the group of stretching vibrations between octahedrally coordinated Al^{3+} cations (Al_{oct}) and their six nearest O_2^- neighbors (ν_3), and the peaks at 1480 and 1750 cm^{-1} correspond to $\nu_1 + \nu_3$ and $2\nu_3$ multiple loss events, respectively. [222, 223]

The ratio of the peak areas of tetrahedral to octahedral alumina, Al_{tet}/Al_{oct}, (Figure 6.8) was 0.27. The peak at 740-770 cm^{-1} (ν_2) (and the multiple loss event peak $\nu_2+\nu_3$ at 1645 cm^{-1}) was not assigned. Other weak peaks that appeared at 1215 and 2920 cm^{-1} likely were $\delta_s(CH_3)$ and $\nu_s(CH_3)/\nu_{as}(CH_3)$ signatures, respectively, of

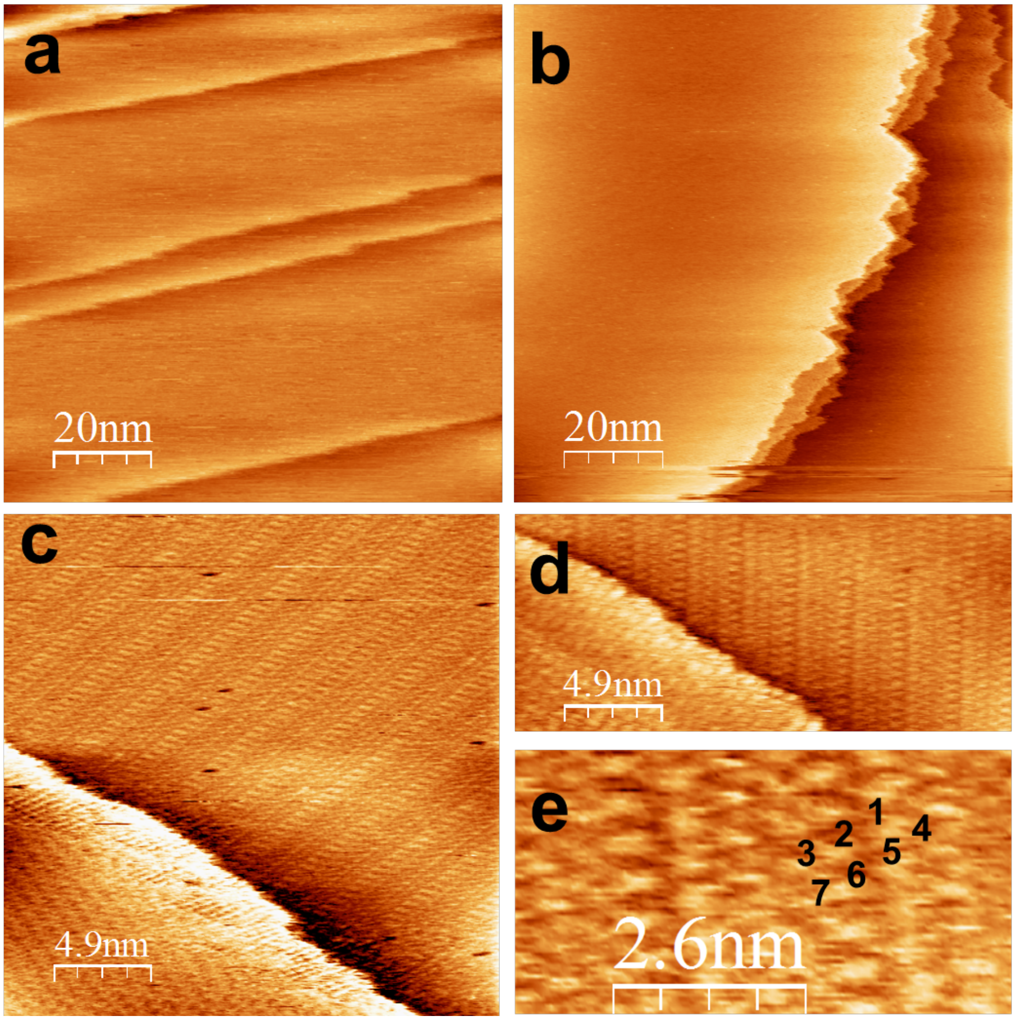

Figure 6.7. STM images of (a) clean Cu(111) and (b-e) Cu(111) exposed to 4500 L O_2 at 623 K. The seven rings of the Cu_2O with the "44"-structure [214] are numbered inside image (e). Bias voltages were −0.5 V for all images, and tunneling currents were 0.5 nA (images a, b) and 1.0 nA (images c–e).

methyl groups attached to the copper surface. [224, 225] We did not observe a loss peak at ca. 400 cm^{-1} that has been assigned previously to vertical Al-O vibrations between in-phase alumina layers on different metal surfaces. [222] This supports the assignment of monolayer growth during the first cycle. As shown in Figure 6.7, the ratio of ν_1 to ν_3 (tetrahedral to octahedral) peak areas was 0.27.

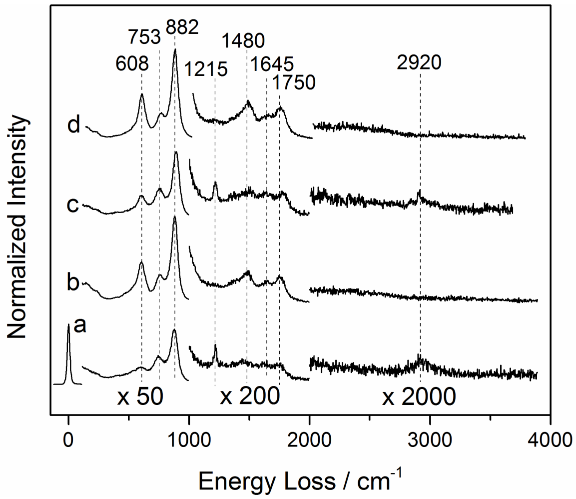

(a)

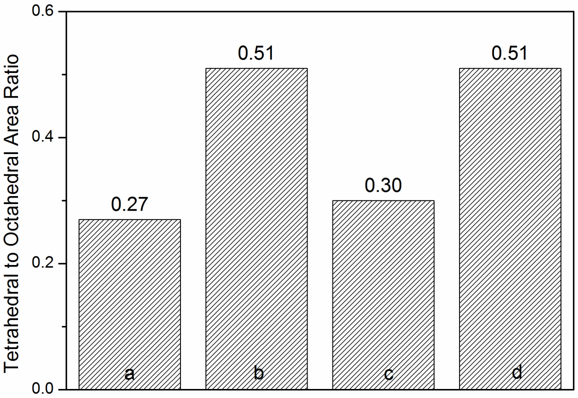

(b)

Figure 6.8. (a) HREELS spectra obtained after (a) 1st TMA half-cycle, (b) 1st O_2 half-cycle, (c) 2nd TMA half-cycle (d) 2nd O_2 half-cycle. (b) Area ratio between ν_1 and ν_3 peaks (Al_{tet}/Al_{oct}) for each TMA and O_2 half-cycle. TMA was exposed for 2000 L at 473 K for all TMA half-cycles, and O_2 was exposed for 4500 L O_2 at 623 K for all O_2 half-cycles.

After dosing TMA to the Cu_2O/Cu(111) surface, the XPS O 1s peak shifted from 529.7 eV to 532.1 eV (Figure 6.6) and the shoulder of Cu $2p_{3/2}$ at 936.0 eV disappeared, revealing that oxygen adsorbed on Cu was incorporated into the adlayer structure. Similarly, surface oxides have been reduced on GaAs and Ge(100) substrates during TMA exposure. [226, 227] The Al 2s contribution to the Al 2s/Cu 3s

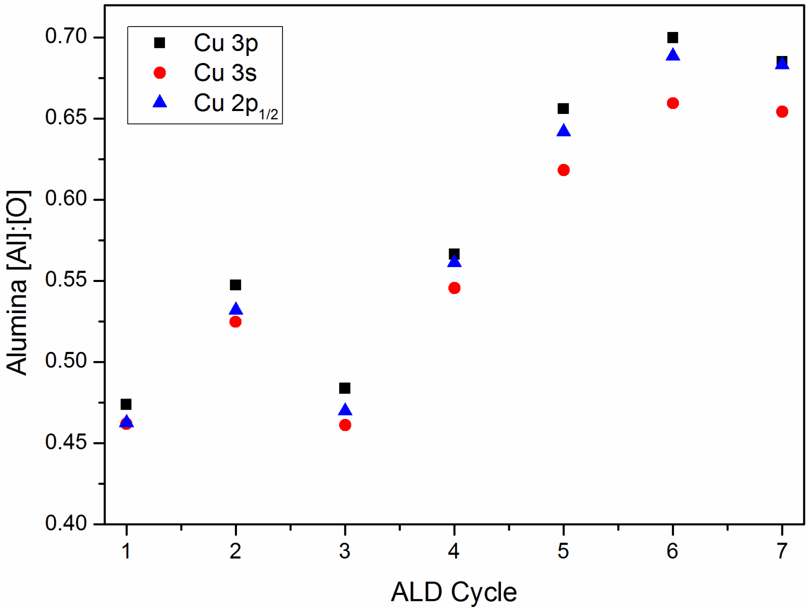

Figure 6.9. Alumina Al:O atomic percentage ratio versus ALD cycle number. TMA was exposed for 2000 L at 473 K for all TMA half-cycles, and O_2 was exposed for 4500 L O_2 at 623 K for all O_2 half-cycles. Atomic percentages were calculated using Cu 3p (black square), Cu 3s (red circle), and Cu $2p_{1/2}$ (blue triangle) peaks. In all cases the Al 2s peak and Al-O component of the O 1s peak were used for atomic percentage calculations.

peak envelope was observed at ca. 119.5 eV (Figure 6.6b). The O 1s (Al-O contribution) and Al 2s peak areas were used to calculate O and Al atomic percentages. The resulting Al:O atomic percentage ratios are plotted for each O_2 half cycle in Figure 6.9. For the first TMA half-cycle, the Al:O ratio was approximately 0.46. Stoichiometric Al_2O_3 would yield an Al:O ratio of 0.66. This Al:O ratio of approximately 0.5 suggests the presence of a copper aluminate, for example $CuAlO_2$.

STM images of the TMA-exposed surface (Figure 6.10) reveal two-dimensional (2D) islands on the surface with an average height of approximately 0.19 nm. No long range order of the copper surface oxide was observed. The bimodal peak distribution in the height histogram confirmed that the islands are flat with uniform height on

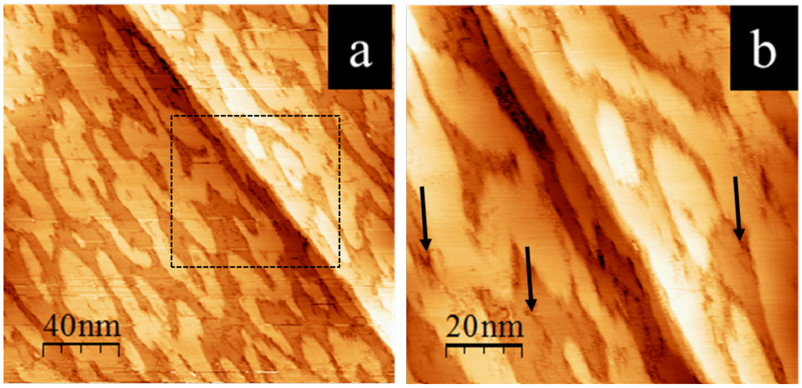

Figure 6.10. STM images of the $Cu_2O/Cu(111)$ surface exposed to 2000 L TMA at 473 K (a) 200 nm × 200 nm and (b) 100 nm × 100 nm. The tunneling current was 1.0 nA; the bias voltage was -0.75 V.

Cu(111). Some vacancies (shown by black arrows in Figure 6.10b) were also observed on the copper surface.

TMA adsorption and dissociation on the $Cu_2O/Cu(111)$ surface was found to be exothermic (Figure 6.3). TMA tends to adsorb at the top position on O in the Cu-O ring via an Al atom with a binding energy of -0.93 eV, which is stronger by 0.65 eV compared to adsorption on clean Cu(111). The free energy for TMA dissociation to DMA is -1.91 eV, and the formed DMA is bound to the bridge site of two adjacent O atoms in the Cu-O ring. DMA dissociation to MA is exothermic by -1.36 eV, and the Al atom of MA is coordinates with three O atoms including the isolated O inside the ring. The final step considered, MA dissociation to Al and CH_3, is exothermic by -0.09 eV, and the formed an Al atom is bound to three O atoms. This is the precursor for alumina. The exothermicity of dissociative TMA adsorption on the $Cu_2O/Cu(111)$ surface is the result of high binding energies of the intermediates on this surface. Compared with clean Cu(111), the binding energies of DMA, MA, Al, and CH_3 are stronger on $Cu_2O/Cu(111)$ by 2.19, 3.45, 4.35, and 0.54 eV, respectively. In conclusion, DFT calculations predicted no TMA adsorption on Cu(111) but TMA adsorption and dissociation on $Cu_2O/Cu(111)$, consistent with experimental data.

Both experiments and first principles calculations demonstrate that TMA is capable of reacting with a copper oxide surface in the absence of hydroxyl species. The reaction of TMA with the $Cu_2O/Cu(111)$ layer is limited by the initial amount of oxygen present in the Cu_2O lattice. TMA consumes oxygen from the surface oxide and reduces Cu^+ to the metallic state, as evidenced by no long range order following the TMA half cycle in STM on bare patches and the shift in the O 1s XPS peak. Once the substrate is reduced to Cu^0, the surface is inactive for further TMA adsorption and decomposition. As evidenced by the partial monolayer film growth, oxygen must migrate across the surface, forming islands of the overlayer. Based on the Al:O ratio of 0.46, these islands are most likely $CuAlO_2$. The island height of 0.19 nm is close to the reported Cu-O and Al-O bond lengths of 1.861 and 1.912 Å, respectively, in crystalline $CuAlO_2$. [228] During TMA adsorption on $Cu_2O/Cu(111)$, HREELS showed that TMA decomposed on $Cu_2O/Cu(111)$, and DFT predicted that methyl ligands were transferred from Al center to the copper surface (Figure 6.3). C coverage was approximately 1.0 ML.

6.5.5 First O_2 half-cycle

Following TMA exposure to the $Cu_2O/Cu(111)$ surface, O_2 was exposed to the resulting surface for 4500 L at 623 K. The HREELS spectrum obtained from this surface is shown in Figure 6.8b. Compared to the first TMA half-cycle, the intensity of the peak at 608 cm^{-1} related to Al_{tet} increased, and the Al_{tet}/Al_{oct} intensity ratio was equal to 0.51 (Figure 6.8). The $\delta_s(CH_3)$ and $\nu_s(CH_3)/\nu_{as}(CH_3)$ vibrations of the $CH_{3,ads}$ groups on Cu(111) disappeared, but a weak C 1s peak was detected by XPS (Figure 6.6). The fact that there was more octahedral Al^{3+} present after the TMA cycle than after the O_2 half cycle could be due to the formation of $CuAlO_2$ after the TMA half cycle, in which Al^{3+} cations are octahedrally coordinated. [228]

Curve-fitting of the O 1s peak showed two components: the component at 529.9 eV represents Cu_2O (19% of the total O 1s area) and the second component at 530.8

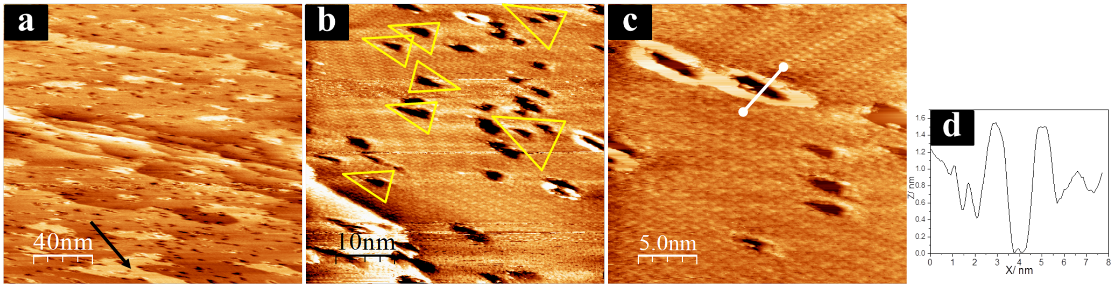

Figure 6.11. STM images after first O_2 half-cycle (4500 L O_2 at 623 K) (a) 200 nm × 200 nm and (b) 50 nm × 50 nm (c) 25 nm × 25 nm. (d) Line profile along the solid white line indicated in image (c). $I_t = 1.0$ nA, $U_t = -0.75$ V.

eV is from oxygen in the copper aluminate (81% of the total O 1s area) (Figure 6.6). For thin film alumina on transition metals, an O 1s BE of 531.2 eV has been reported previously for thin film alumina on Pt(111). [122] The slight Cu $2p_{3/2}$ peak shoulder reappeared at ca. 936.0 eV, consistent with the formation of some CuO (see Figure 6.4). Cu_2O was also formed as evidenced by long range order observed in STM images (Figure 6.11c). The Al 2s peak is distinguishable from the shoulder of Cu 3s at 118.7 eV (Figure 6.6). This Al 2s peak shifted by -0.8 to 118.7 eV following O_2 exposure. Lower Al 2p binding energies for aluminum oxides have been attributed to the presence of Al^{3+} coordinated tetrahedrally [198, 199, 203, 204] (see discussion in Chapter 5). In this case, the Al 2p and Cu 3p peaks overlap, but the Al 2s and Al 2p peaks should exhibit a similar chemical shift in XPS. Here, the shift to lower BE is consistent with the formation of alumina with an increased Al_{tet}/Al_{oct} ratio following the O_2 half-cycle. A hydroxide-containing species can cause a similar shift of the O 1s and Al 2p (Al 2s) peaks, [140,197,201] however, no O-H stretching vibrations were detected by HREELS after TMA or O_2 half-cycles at ca. 3300 cm^{-1}. The Al:O ratio after the 1st O_2 half cycle was approximately 0.53, nearly unchanged from after the first TMA cycle. The resulting Al:O atomic percentage ratios after each O_2 half cycle are plotted in Figure 6.9.

Figure 6.11 shows STM images of the copper surface after the first O_2 half-cycle. As evidenced by the well-ordered Cu_2O structure that can be seen in atomic-resolution images (Figure 6.11b and c), O_2 exposure re-oxidizes the copper surface. Two other features are observed: Aluminum oxide islands that appeared after the first TMA half-cycle with an average height of 0.17 nm (marked by black arrow in Figure 6.11a), and dark spots appeared on the Cu terrace. Obtaining STM images over regions with a high density of aluminum oxide islands was problematic due to the low density of states for achieving a stable tunneling current and therefore was avoided. Dark spots with a triangular shape are marked inside yellow lines in Figure 6.11b. As shown by Matsumoto et al., [214] oxygen is capable of abstracting Cu from terraces and leaves behind triangular holes with the three-fold symmetry. Some of these pits are decorated with bright features (apparent height of ca. 1.5 nm, Figure 6.11c and d). These features could be Cu adatoms from the oxide structure that became mobile and diffused across the surface until reaching a low-coordination site such as a hole on the surface. The holes detected by STM are likely “mines” delivering copper to the surface, as has been observed for Ag in the Cu/Ag(111) system. [229]

6.5.6 Second ALD Cycle

Figure 6.12 shows STM images obtained after the second TMA half-cycle. Numerous holes were seen on terraces and islands. Terraces were covered with islands having sharp boundaries and a ridge-like structure (marked by a rectangle in Figure 6.12b and c). These morphological changes reflected the transition from monolayer alumina islands after the first TMA half-cycle (Figure 6.10) to multilayer islands, as the ridge structure is likely the second alumina layer or methyl groups. The ridges have an apparent height of about 0.17 nm (Figure 6.12b), close to the average height for the alumina islands (0.19 nm) after the first TMA half-cycle observed in Figure 6.10.

Similar to the first TMA half-cycle, TMA consumed oxygen from the Cu_2O structure and reduced Cu oxide to Cu^0 as evident from the disappearance of long range

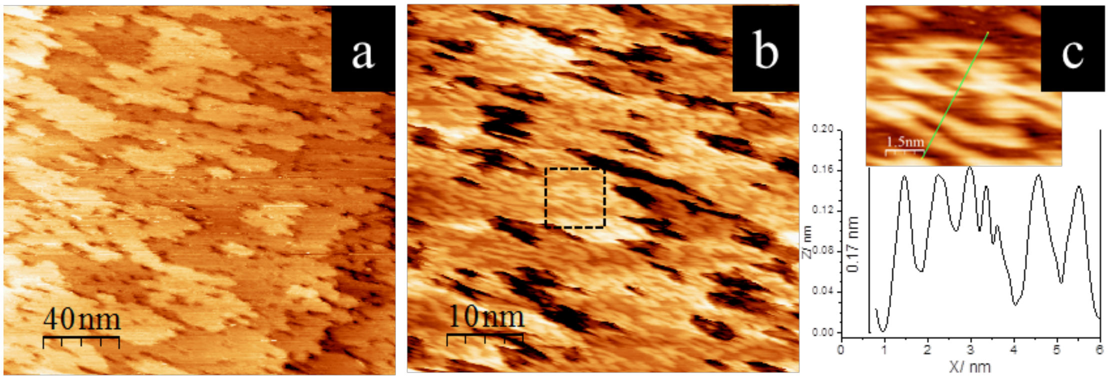

Figure 6.12. STM images (a) 200 nm × 200 nm and (b) 50 nm × 50 nm obtained after the second TMA half-cycle (2000 L TMA at 473 K). (c) The zoomed-in region of the highlighted section in image (b) and the line profile along the solid line indicated in the image. The tunneling current was 0.5 nA; the bias voltage was −0.9 V.

ordered structures of Cu_2O in STM images. Unlike the first TMA half cycle, growth is not limited to the copper oxide surface as existing alumina islands can serve as the oxygen source. TMA reduces the aluminum oxide layer wherever the two are in direct contact.

After the second O_2 half-cycle, the Al 2s and O 1s peaks were shifted towards lower BEs at 118.9 and 531.0 eV, respectively (Figure 6.6). As discussed above, these peaks are characteristic of the alumina structure with the Al_{tet}/Al_{oct} HREELS peak area ratio of about 0.5 (Figure 6.8 inset). The Cu_2O contribution in the O 1s peak was one quarter the size (5% of the O 1s area) of the corresponding value observed after the first O_2 half-cycle, which reflected the decrease in the copper surface available for oxygen adsorption. Most carbon was removed after the second O_2 half-cycle (Figure 6.6), consistent with HREELS (Figure 6.8).

6.5.7 Subsequent ALD half cycles and film growth behavior

7 ALD cycles (14 half-cycles of O_2 and TMA) were performed on the Cu_2O/Cu(111) surface (Figure 6.13). Each TMA half-cycle consisted of 2000 L TMA at 473 K and each O_2 half-cycle consisted of 4500 L O_2 at 623 K. Alumina thicknesses calculated from the Al 2s and O 1s peaks are plotted in Figure 6.13. Roughly linear alumina growth is observed during the first 7 ALD cycles. The calculated thickness gain per cycle using the Al 2s and O 1s peaks, respectively, were 3.4 and 2.8 Å. From STM images, we conclude that Al deposition occurred on the surface with Cu_2O available and then the process proceeded on porous alumina once all Cu was covered. At the oxygen conditions used (623 K, 4500 L, 5×10^{-6} mbar), the carbon atomic percentage (calculated using the C 1s and Cu 3s regions) was equal to or less than 2% for all ALD cycles. DFT calculations demonstrated that O_2 dissociates on Cu(111) to atomic oxygen. [230] This reactive atomic oxygen reacts with carbon clusters or methyl groups.

Figure 6.14 plots O 1s and Al 2s BEs after each TMA and O_2 half-cycle. The common behavior of the O 1s and Al 2s peaks was the shift to higher BE after TMA half-cycles and the shift to lower BE after O_2 half-cycles. Based on the HREELS data from the first two cycles, these changes were concluded to be from the transition between the octahedral and tetrahedral coordination of aluminum cations. The Al_{oct} contribution increased during TMA half-cycles, and the Al_{tet} contribution increased during O_2 half cycles.

Figure 6.13 also shows alumina thicknesses and carbon atomic percentages after each ALD cycle for a variety of co-reactant dosing conditions. In all cases, the first TMA half-cycle was performed over Cu(111) exposed to O_2 for 4500 L at 623 K to form Cu_2O. For TMA-O_2 ALD when the O_2 half-cycle was done at 473 K rather than 623 K, oxygen was not as effective in carbon removal as at 623 K. The carbon atomic percentage increased after each ALD cycle. After four ALD cycles at 473 K, carbon coverage was about 10 times higher than for the O_2 half-cycle at 623 K. Alumina growth observed for the O_2 half-cycles at 473 K was much slower at these

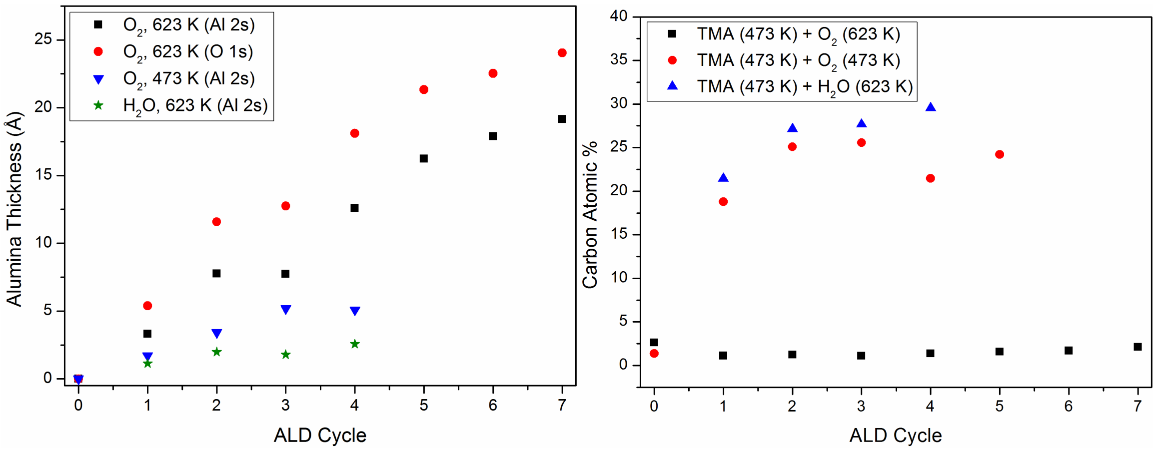

(a) (b)

Figure 6.13. (a) Alumina thickness versus ALD cycle for various co-reactant dosing conditions. Dosing conditions were O_2, 623 K (Black squares, calculated using Al 2s; red circles, calculated using O 1s), O_2, 473 K (red triangles, calculated using Al 2s), and H_2O, 623 K (green stars, calculated using Al 2s). (b) Carbon atomic % for various co-reactant dosing conditions.

conditions, with a measured thickness of ca. 5 Å after 4 ALD cycles, compared to ca. 15 Å after 4 cycles with O_2 dosing performed at 623 K. This slower growth is likely due to poisoning of the surface with carbon species.

To evaluate the effectiveness of the second reactant in carbon removal and alumina growth, O_2 was replaced with water dosed at 623 K as shown in Figure 6.13. The water half-cycles were also ineffective for carbon removal. After four ALD cycles the carbon atomic percentage was 30%. After one H_2O ALD cycle at 473 K, the alumina thickness was about 3 Å, and the thickness did not increase for subsequent cycles. It must be noted that carbon removal behavior at the dosing pressures of O_2 and H_2O used in this study (approximately 10^{-6} mbar) may not be representative of the same ALD process carried out in a typical ALD reactor at pressures of a few millibar. [122]

For ideal alumina ALD using H_2O as the co-reactant, methyl ligands from TMA are partially exchanged with surface hydroxyl groups and the precursor becomes anchored to the surface during the first TMA half-cycle. The detection of the CH_4 group

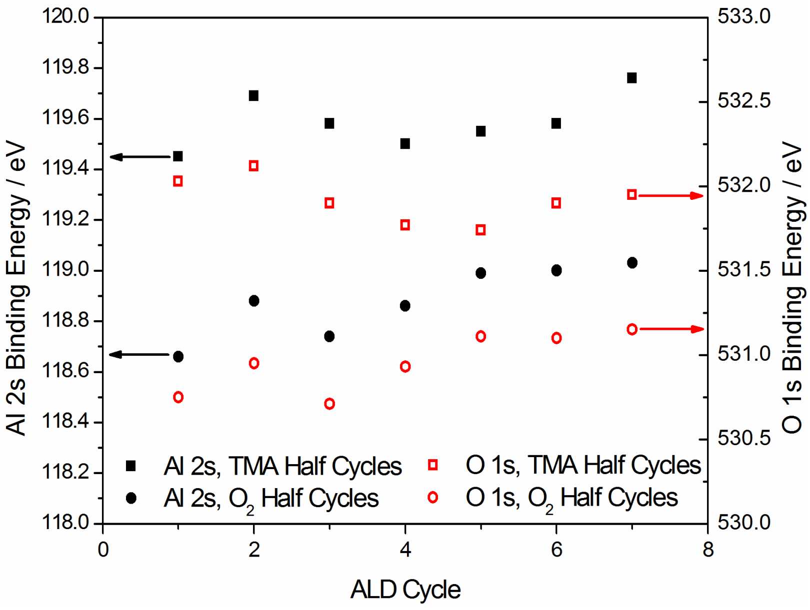

Figure 6.14. BEs of O 1s (red outlines) and Al 2s (solid black) peaks after each half-cycle of TMA or O_2. Squares were data points taken after TMA half cycles, and circles were data points taken after O_2 half cycles. 7 cycles total were performed. The starting surface was the Cu_2O/Cu(111) surface.

by *in situ* quadrupole mass spectrometry (QMS) is used to confirm this mechanism. Ideally, the co-reactant provides the missing element (oxygen), removes the carbon groups via hydrogen transfer to CH_3, and functionalizes the surface for the upcoming TMA half-cycle. However, as demonstrated, this ideal picture is not always fulfilled, as TMA fully decomposes and forms an aluminate by losing all its methyl ligands upon deposition on a hydroxide-free Cu_2O surface at 473 K. TMA decomposition leaves behind carbon atoms and clusters, and methyl groups attached to the copper surface. Once the copper surface is completely covered, TMA continues to react with hydroxide-free alumina.

Others have studied the reaction of TMA with oxide-terminated alumina. Dillon et al. [182] observed the appearance of IR features assigned to CH_3 stretching following a saturation exposure of TMA to a porous alumina membrane previously annealed to 1000 K. These IR features had an integrated absorbance equal to 72% of the same features following exposure of an alumina surface with a saturation amount of hydroxyl. These CH_3 stretching features attenuated upon annealing between 300 to 860 K. [182] Puurunen et al. [218] found that TMA reacted between 353 to 573 K with alumina pretreated between 473–1073 K. TMA decomposed above 600 K. Assuming that all TMA reacts with hydroxyl groups, releases methane, and forms OAlMe species, the amount of carbon observed on the alumina with the highest pretreatment temperatures was higher than expected based on this assumption, suggesting that TMA adsorbs dissociatively on coordinatively unsaturated Al. They found that the amount of methyl groups present on alumina pretreated at 1073 K was 15% less than on alumina treated at 473 K. Elliott et al. [215] showed with first principles calculations that TMA will chemisorb on both bare alumina and hydroxylated surfaces, that hydroxyl coverage does not affect site density, and that adsorbed TMA dissociates to form $AlMe_2$, AlMe, and Me on both surfaces. However, the hydrogen in OH^- reacts with methyl groups and CH_4 is evolved, so the ALD rate, which is affected by steric hindrance of CH_3 groups, is greater on hydroxylated surfaces.

Oxygen exposure temperature plays an important role in carbon removal and alumina growth behavior. Incorporation of impurities including carbon is a major concern in oxide dielectrics where an ultra-thin film (< 10 nm) is deposited by ALD. A carbon-free oxide film is required to achieve high-quality microelectronic devices. [231]

As shown in Figure 6.9, the Al:O ratio is about 0.5 for the first 3-4 ALD cycles before increasing and stabilizing at about 0.66. This transition in stoichiometry corresponds to film closure. As shown in the O 1s region in Figure 6.6, the Cu-O peak from the Cu_2O surface oxide is not present after 4 ALD cycles. In the first several ALD cycles, the Al:O stoichiometry of 1:2 is due to the presence of $CuAlO_2$. There is more octahedral alumina after the early TMA cycles, since Al occupies the octahedral sites in $CuAlO_2$. [228] The presence of copper in the first few cycles forces Al into octahedral positions. As the film closes and Cu is covered, the stoichiometry shifts to that of alumina, Al_2O_3. Alumina interacts with Cu at the interface. Though there is no HREELS data for cycles beyond the second cycle, amorphous alumina is likely formed by ALD at these conditions.

6.6 Conclusion

TMA does not react with or adsorb on metallic Cu(111), but TMA adsorption and decomposition to Al is thermodynamically favorable on Cu_2O. During the first half cycle, TMA reacts with O adsorbed on Cu(111), depositing Al in the form of single layered aluminate islands. This reduces surface copper not bound to the aluminate to the metallic state, which does not interact with TMA. Therefore, the amount of adsorbed O limits the growth of Al during the first half cycle.

From XPS and HREELS, TMA half cycles favor production of octahedrally coordinated alumina, while O_2 half cycles at higher temperature favor tetrahedrally coordinated alumina. During the first 3 cycles while Cu is still exposed, XPS can differentiate between O in Cu_2O and $CuAlO_2$, and TMA interacts with both Cu_2O and the aluminate. TMA continues to interact with the aluminate/alumina once Cu is completely covered.

The choice of processing conditions in high vacuum determines the extent of carbon incorporation in the ALD film. Dosing TMA at 473 K and O_2 at 673 K results in a film with less carbon than when H_2O is used instead of O_2 at the same temperature, and for O_2 at 473 K. These alternative processing conditions result in increasing C deposition with each ALD cycle and little or no Al adsorption after about the 3rd ALD cycle. It was demonstrated that TMA readily reacts with oxide surfaces even in the absence of co-adsorbed hydroxyls. For ALD applications on an air-exposed Cu surfaces, large domains of oxides might still exist. This is of importance to thin film applications like microelectronics and catalysis where a small number of ALD cycles is desirable.

6.7 Acknowledgments

DFT calculations were performed by Dr. Xiang-Kui Gu and Prof. Jeffrey Greeley.

7. CHARACTERIZATION AND THEORY OF RE FILMS ON PT(111) GROWN BY UHV-CVD

7.1 Abstract

Changes in surface chemistry and morphology of Re/Pt(111) surfaces synthesized by ultra-high vacuum chemical vapor deposition (UHV-CVD) of Re on Pt(111) were studied by a combination of experiment and density functional theory (DFT) modeling. A Re oxide formed following exposure of the as-deposited Re to 1×10^{-6} mbar oxygen at 600–673 K. Subsequent annealing at 973 K resulted in oxygen desorption and a decrease in Re coverage, as calculated by XPS and as observed by STM. This observation was explained by DFT calculations which showed that a clean Pt surface slab with subsurface Re is thermodynamically more favorable than Pt(111) with Re on the surface. DFT calculations also predicted weaker O and CO binding on this surface compared to both monometallic Pt and Re, and HREELS and temperature desorption measurements suggested that O binds weakly to the Pt skin surface, with oxygen on the Pt skin desorbing from this surface following annealing at 373 K. Trends in adsorption energies were consistent with DFT calculated d-band centers of surface atoms for model Pt-Re structures. Comparison of HREELS data and STM images with DFT calculated vibrational frequencies have been used to understand the structure of rhenium oxide on Pt(111).

7.2 Introduction

Pt-Re catalysts have been used for hydrocarbon reforming since their invention in the 1960s. [232] Recently, Pt-Re and other Pt-containing bimetallic catalysts have been used for aqueous phase reforming (APR) of model polyol compounds. [233–239] Investigators have discovered many benefits of using bimetallic over monometallic catalyst systems, specifically Pt-Re. Improved turnover rates for glycerol conversion to syngas for Pt-Re/C catalysts were reported by Simonetti et al., [239] and Kunkes et al. [238] discovered that the addition of Re to a Pt/C catalyst promoted the overall rates of glycerol APR and the water-gas shift reactions by weakening CO binding to the surface. They also found that Re prevents sintering of Pt nanoparticles. Daniel et al. [237] similarly found that the addition of Re to Pt increased glycerol hydrogenolysis rates and leads to measured selectivity toward 1,3-propanediol as high as 34%. Multiple groups have found that the addition of Re to Pt catalysts promotes the reduction of Pt. [236, 237]

Understanding the nature of the active sites responsible for improvements in APR reaction rates and selectivities on Pt-Re bimetallic catalysts remains a challenge given the complexity of this bimetallic system. Surface sensitive studies in controlled ultra-high vacuum (UHV) environments have been used to better understand the interaction between Pt and Re using model systems on single crystal and foil surfaces. [240–249] Bimetallic systems have been prepared on flat samples by evaporation of Pt on Re(0001), [243, 245, 246] by evaporation of Pt on Re foil, [242, 250, 251] by evaporation of Re on Pt foil, [248] and by evaporation of Re on Pt(111) [240, 241, 244–247, 249] and Pt(100). [244] The resulting surfaces have been subjected to a variety of treatments including heating, oxidation, and exposure to small probe molecules. Of special interest to many of these studies are the properties of Re films on Pt and alloyed Pt-Re systems, formed by annealing a surface containing Re and Pt to temperatures $\geq$ 900 K. [240–242, 244, 248, 249] In one study, CO was found to bind more weakly to this alloy surface than monometallic Pt or Re, and O interaction with this surface was not detected by XPS. [240] Similarly, Duke et al. [249] found that Pt-Re alloy surfaces on Pt(111) produced more CO_2 from CO oxidation than monometallic Pt(111) and that the alloy surface was more resistant to oxidation. The unique properties of Pt-Re alloy surfaces have been attributed to electronic effects associated with this bimetallic system. [241]

In this study, bimetallic Pt-Re surfaces were synthesized by UHV chemical vapor deposition (UHV-CVD) of Re onto Pt(111) and followed chemical and morphological changes to the surfaces after annealing and oxidative treatments using surface sensitive experiments. DFT modeling aided interpretation of the experimental results. Briefly, we found that as-deposited Re formed an oxide upon exposure to 1×10^{-6} mbar O_2 at temperatures ≥ 673 K. Oxygen desorbed at about 1000 K. This annealing resulted in Re diffusion into the Pt subsurface and increased alloying with Pt, resulting in a surface with a Pt skin. O bound more weakly to this surface than to monometallic Pt(111). We found that O and CO binding energies on Pt-skin surfaces were much weaker than on a monometallic Pt or a Re film. This type of adsorption behavior, predicted in the past based on relative metal-metal bond strengths for bimetallic systems, [252] can also be explained on the basis of calculated d-band centers of Pt-Re systems. This work shows the power of coupling surface sensitive characterization experiments with DFT modeling, which together can predict thermodynamics of adsorption processes and surface structures for the complicated Pt-Re bimetallic system.

7.3 Experimental Materials and Methods

Experiments were performed in an Omicron Surface Analysis Cluster at the Birck Nanotechnology Center, Purdue University. This system has been described in detail elsewhere [22]. Briefly, it consists of a preparation chamber and μ-metal analysis chamber with base pressures of 1×10^{-9} and 5×10^{-11} mbar, respectively. The preparation chamber contains an Ar^+ sputter gun, resistive sample heating, and leak valves connected to gas dosing manifolds for precursor and gas dosing. The analysis chamber is equipped with instrumentation for X-ray photoelectron spectroscopy

(XPS), scanning tunneling microscopy (STM), high resolution electron energy loss (HREELS), and low energy electron diffraction (LEED).

A Pt(111) single crystal (MaTecK) with 9.0 mm diameter, 1.0 mm thickness, and orientation accuracy $< 0.5°$ was used. Repeated cycles of Ar^+ sputtering and annealing at 1000 K were used to clean the crystal, as monitored by XPS, LEED, HREELS, and STM. Re was deposited on Pt(111) by UHV-CVD using $Re_2(CO)_{10}$ as the precursor (98%, Strem Chemicals Inc.). $Re_2(CO)_{10}$ was pumped through the dosing manifold for several minutes prior to sample dosing in the preparation chamber through a leak valve at a pressure of approximately 5×10^{-6} mbar. To have sufficient and stable pressure during precursor exposure, a mini-cylinder with $Re_2(CO)_{10}$ was heated in a hot water bath. Crystal temperatures, controlled by resistive heating, precursor temperatures, controlled by a hot water bath, and exposure times are reported in Table 7.1. For annealing treatments in oxygen, the crystal was cooled in oxygen following heating. Oxygen was pumped from the system once the crystal was cooled for transfer from the preparation to the analysis chamber, which took approximately 5 minutes. At this time, the pressures of each chamber were close to the base pressures reported above.

HREELS data were acquired with an ELS5000 (LK Technologies). Electrons were collected in the specular direction with primary beam energies of 5 or 7 eV. The fwhm of the elastic peak was roughly 2.8 meV (23 cm^{-1}) and the peak had intensity above 105 cps. All HREELS spectra have been normalized to the elastic peak intensity.

XPS data were collected using non-monochromatic Mg Kα X-rays (1253.6 eV) at a X-ray gun power of 150 W. High-resolution core level spectra were obtained at a constant pass energy of 20 eV with an energy spacing of 0.05 eV. XPS resolution, expressed as the fwhm of the Pt $4f_{7/2}$ peak, was approximately 1.2 eV. Electrons were collected at a 45° photoemission angle with respect to the surface normal. No energy scale correction was foreseen by the analyzer manufacturer (the electron energy analyzer - Omicron EAC 125 and the analyzer controller - Omicron EAC 2000);

therefore, it was possible only to set the Au $4f_{7/2}$ peak at 84.0 eV by changing the spectrometer work function.

XPS data were analyzed using CasaXPS (version 2313Dev64) software. Metallic Re 4f and Pt 4f components were fit with an asymmetric line-shape with both Gaussian (10%) and Lorentzian (90%) components and tail dampening (CasaXPS Line-shape = LF(1, x, y, 90); x = 2 for Pt 4f and x = 1.5 for Re 4f; y = 50 for Pt 4f and y = 10 for Re 4f.) The superficial Re oxide and O 1s peaks were fit using a symmetric line-shape with both Gaussian (70%) and Lorentzian (30%) components (CasaXPS Line-shape = GL(30)). Spin orbit doublets for the Pt 4f and Re 4f regions were subject to spacing constraints of 3.33 and 2.43 eV, respectively. Areas of spin orbit doublets were also constrained to their expected ratios. Coverages for Re, C, and O reported in this work have been calculated using Fadleys approach, [62] which assumes fractional coverage of a non-attenuating overlayer on a semi-infinite substrate. Coverage is in expressed monolayers (ML), and is the ratio of the number of adsorbed species per surface Pt atom on Pt(111). This model is described in detail in Appendix A.

STM images were collected with an Omicron ambient temperature UHV STM/AFM in constant current mode. W tips were made via electrochemical etching followed by electron bombardment in UHV. Images were analyzed using WSxM software. [96] LEED patterns were acquired using an Omicron rear-view LEED optics with primary electron energies between 63-261 eV.

7.4 Computational Details

DFT calculations were performed using plane wave-based VASP (Vienna Ab initio Simulation Package) code. Exchange correlation energies were described using GGA-PW91 treatment. Ionic cores were represented using the PAW (Projector Augmented Wave) method. The as-deposited Re on Pt was modeled using a Re film of 1 ML coverage on the Pt(111) surface. We also looked at subsurface Re at different coverages to model the Pt-Re structure after annealing. (111) surfaces were modeled using 2 × 2 unit cells with 5 layers, with the bottom two layers fixed at bulk atomic distances. The vacuum layer between the slabs was fixed at 13–14 Å. The surface Brillouin zone was sampled using Monkhorst scheme with a $4 \times 4 \times 1$ k point grid. The energy cutoff was fixed at 400 eV. Self-consistent electronic iteration steps were converged to 1.0×10^{-4} and ionic forces were converged to 0.02 eVÅ^{-1}. Gas phase calculations were performed in $13 \times 14 \times 15$ Å unit cells. Methfessel Paxton smearing of 0.1 eV for surface slabs and Gaussian smearing of 0.01 eV for gas phase molecules was applied in the calculations. The binding energy of atomic oxygen was referenced to gas phase molecular oxygen. The DFT calculated lattice constant for Pt was 3.99 Å. This is close to the experimentally reported value of 3.92 Å. [253]

7.5 Results and Discussion

The experimental results that follow three stages of the preparation and characterization of the Re-Pt bimetallic system on Pt(111): (1) preparation via UHV-CVD, (2) oxygen exposure for carbon removal and Re oxidation, and (3) subsequent annealing to increase Pt-Re alloying. The use of theory for interpretation of these results follows.

7.5.1 Deposition of Re using UHV-CVD

The as-synthesized Re/Pt(111) surface was characterized by XPS and STM. $Re_2(CO)_{10}$ was dosed on clean Pt(111) surfaces, as well as on Pt(111) surfaces with residual subsurface Re (calculated $\Theta_{Re} < 0.1$ ML) several times. CVD has been used previously for deposition of Re onto a variety of substrates, [254–257] but not for deposition of Re onto Pt in UHV for surface sensitive studies.

The Re coverage calculated from XPS data varied between 0.4 and 1.0 ML using a variety of dosing conditions. The Pt(111) sample temperature varied between 393 and 573 K, and precursor temperatures varied between 313 and 363 K. Immediately

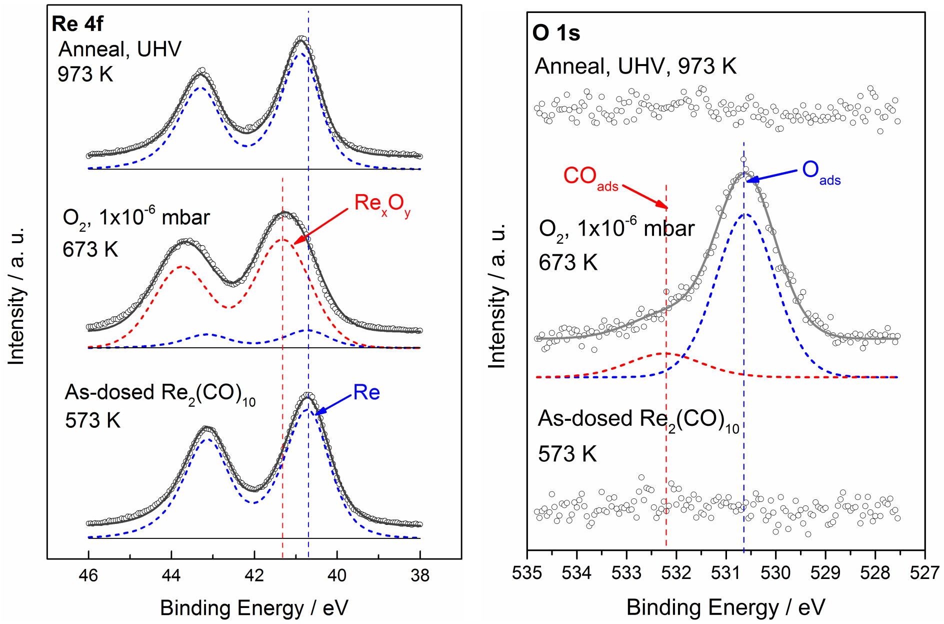

(a) Re 4f (b) O 1s

Figure 7.1. Re 4f and O 1s core level regions. Bottom spectra: after dosing $Re_2(CO)_{10}$ on Pt(111) at ca. 5×10^{-6} mbar, $T_{sample} = 573$ K, $T_{precursor} = 353$ K. Middle: after heating at 673 K in 1×10^{-6} mbar O_2 for 20 min. Top: after subsequent stepwise heating to 973 K. Open circles: raw data after background subtraction, grey line: peak envelope. In Re 4f region, blue line: Re^0 component, red line: Re_xO_y component. In the O 1s region, blue dashed line: O_{ads} component, red dashed line: CO_{ads} component.

after all precursor exposures carbon contamination with coverage ranging between 1.9 to 5.3 ML was detected. $\Theta_O < 0.1$ ML in all cases, however, indicating that adsorbed carbon was not in the form of CO. Dosing conditions and XPS results for the four separate experiments are summarized in Table 7.1.

The Re $4f_{7/2}$ binding energy (BE) varied between 40.5 and 40.8 eV on the as-dosed surface. A typical Re $4f_{7/2}$ region after dosing $Re_2(CO)_{10}$ is shown in Figure 7.1. The measured Re $4f_{7/2}$ BEs are 0.2-0.5 eV higher than the bulk metallic reference BE of 40.3 eV. [68] This range of BEs is similar to that observed by Ramstad et al. [241] for sub-monolayer coverages of Re islands deposited on Pt(111) by evaporation. They fit the Re 4f region with two components: one at 40.6 eV, assigned to Re surrounded by

Re in a Re 2D island, and another at 40.8 eV assigned to Re on the edge of an island. Duke et al. observed a Re $4f_{7/2}$ BE of 40.9 eV following evaporation of 2.9 ML of Re onto Pt(111). [249]

The as-dosed surface was imaged with STM. An image of this surface is shown in Figure 7.2. Imaging of this surface was difficult because it was very rough, and the tip was most likely dragging carbon. Bright features cover the majority of the surface and are assigned to Re or C clusters. The presence of carbon likely affects the morphology of the as-deposited Re. This carbon might be responsible for the 3D particle growth observed in STM by blocking adsorption sites on Pt. The carbon might also poison the surface, limiting the amount of Re deposited by this technique.

7.5.2 Rhenium Oxide Formation

Oxygen treatments were used to remove carbon from the as-deposited surface. Oxygen was dosed at 1×10^{-6} mbar for a total of 20 minutes while a sample with $\Theta_{Re} = 0.8$ ML was held at 673 K. The resulting Re 4f and O 1s core level regions are shown in Figure 7.1. Following this treatment, 87% of the Re 4f envelope was fit with a Re $4f_{7/2}$ component at 41.3 eV assigned to a rhenium surface oxide, Re_xO_y. The reminder of the $4f_{7/2}$ region was fit with the metallic/alloy Re component at 40.7 eV. Following the oxygen treatment, the Re coverage decreased from 0.8 to 0.6 ML, carbon coverage decreased from 3.4 to 0.1 ML, and oxygen appeared on the surface with coverage of 0.4 ML. The O 1s region was fitted with two components: a dominant feature at 530.6 eV and a weak feature at 532.2 eV assigned to O adsorbed on Re and CO adsorbed on Pt, respectively. Literature reports have assigned peaks at about 530.0 eV to O on both Pt and Re, and peaks around 532 eV to CO on both Pt and Re. The justification for our assignment is discussed below in the presentation of HREELS results. From XPS, the coverage ratio of the oxygen (from the total area of O 1s) to oxidized Re (from the area of Re_xO_y component) was 0.7. In a separate experiment, when Pt(111) with $\Theta_{Re} = 1.0$ ML was exposed to O_2 at 1×10^{-6} mbar at

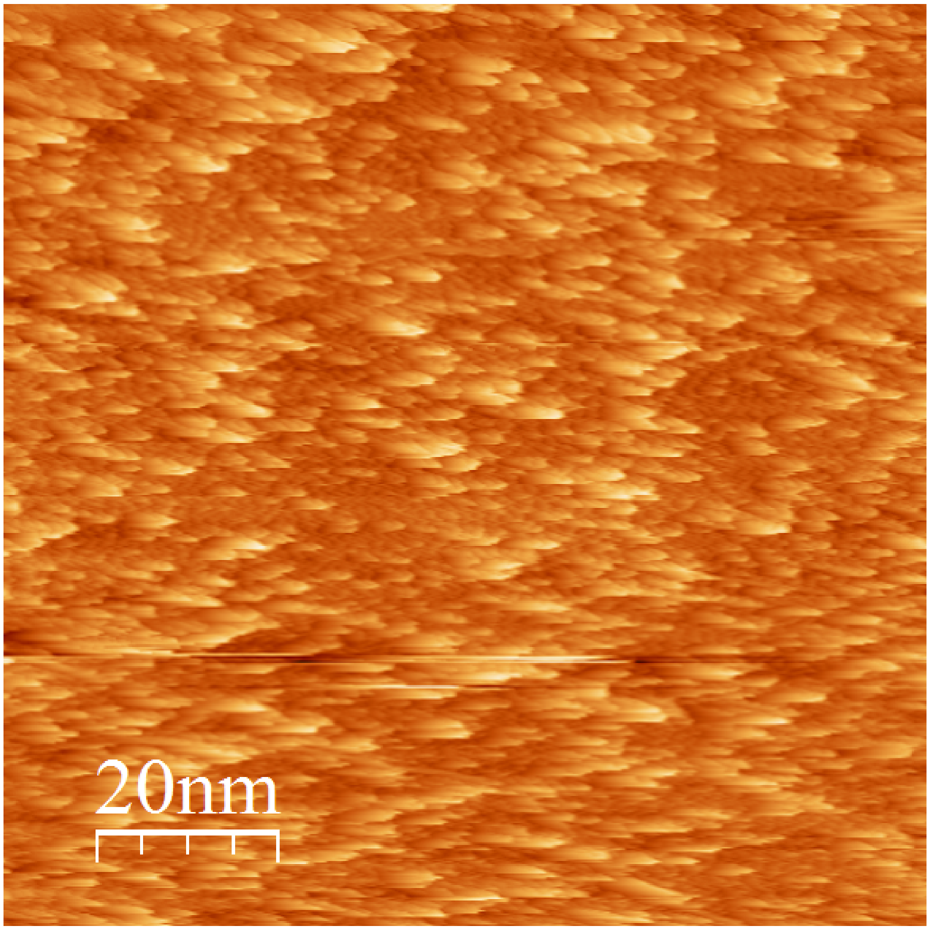

Figure 7.2. STM image of as-dosed surface (Dosing 4 in Table 7.1). 100 nm × 100 nm, $I_t = 0.3$ nA, $U_t = 600$ mV. From XPS, $\Theta_{Re} = 0.4$ ML, $\Theta_C = 4.5$ ML.

598 K, the oxygen/oxidized rhenium ratio was 0.9. The oxidized Re $4f_{7/2}$ component, Re_xO_y, was still located at 41.3 eV.

Based on comparison to literature, the Re $4f_{7/2}$ component attributed to Re_xO_y likely did not arise from a rhenium oxide with bulk stoichiometry. Tysoe et al. [248] measured the Re $4f_{7/2}$ BEs of various Re oxides prepared by evaporating approximately 10 ML of Re on a Pt ribbon and then oxidizing these surfaces in 1 atm of oxygen at various temperatures. They reported Re $4f_{7/2}$ BEs of 42.5, 44.9, and 46.7 eV for ReO_2, ReO_3, and Re_2O_7, respectively. Binding energies of 41.3 to 41.4 eV have been attributed previously to a superficial rhenium oxide with stoichiometry

ReO. [249,258–261] The Re $4f_{7/2}$ peaks with similar BEs were assigned by other groups to ReO_x, $0.5 \leq x \leq 1$ [35], (BE = 41.2 eV) and to superficial oxide stoichiometries of $ReO_{1/3}$ (BE = 41.1 eV) and $ReO_{2/3}$ (BE = 41.5 eV). [240] Based on these BE assignments and the ReO_x stoichiometry of $0.7 \leq x \leq 0.9$ calculated using XPS data, the superficial Re oxide stoichiometry was between $ReO_{1/2}$ and ReO in our experiments. We also note that adsorption of oxygen on other Pt-bimetallic systems has resulted in surface segregation of the second metal, as has been observed for Pt-Ni [262, 263] and Pt-Co. [262] Given the trend in O binding energies calculated below (see DFT section), this seems likely for Pt with Re in the subsurface, given the observed correlation of surface segregation of 3d metals with O binding energies. [262] While we cannot eliminate the possibility of this happening with Re, we did not see any direct evidence to suggest Re is segregating on the surface. The drop in Re coverage during the first oxidation treatment supports the lack of Re surface segregation.

The superficial oxide surface was also investigated by HREELS (Figure 7.3). In one experiment (Figure 7.3, left panel), the Re/Pt(111) surface was treated in 1×10^{-6} mbar oxygen at 673 K and cooled to 373 K in oxygen until being transferred to the analysis chamber under UHV conditions. Initial coverage of Re on this surface was 0.6 ML. HREELS revealed a feature at 670 cm^{-1} which was assigned to a Re-O loss in the rhenium superficial oxide. A summary of HREELS literature with assignments for adsorbed CO, O, and C is given in Table 7.2. Ducros et al. [264] observed an Re-O vibration at 580 cm^{-1} after oxygen adsorption on Re(0001),and Asscher et al. [265] observed a band at 585 ± 20 cm^{-1} assigned to the Re-O bond on Re(0001) for co-adsorbed CO and O. The frequency of the vibration here is higher than references for O adsorbed on various Re surfaces in the literature. This is likely caused by clusters of ReO_x on Pt(111), which are predicted to have higher frequencies than O adsorbed on monometallic Re (see DFT calculations below). The identity of the weak loss peak at ca. 970 likely also results from O adsorbed on Re single atoms or very small clusters, as per the DFT section below. The assignment of the broad, weak loss peak at approximately 1100 cm^{-1} is unclear, but similar frequencies have been reported for

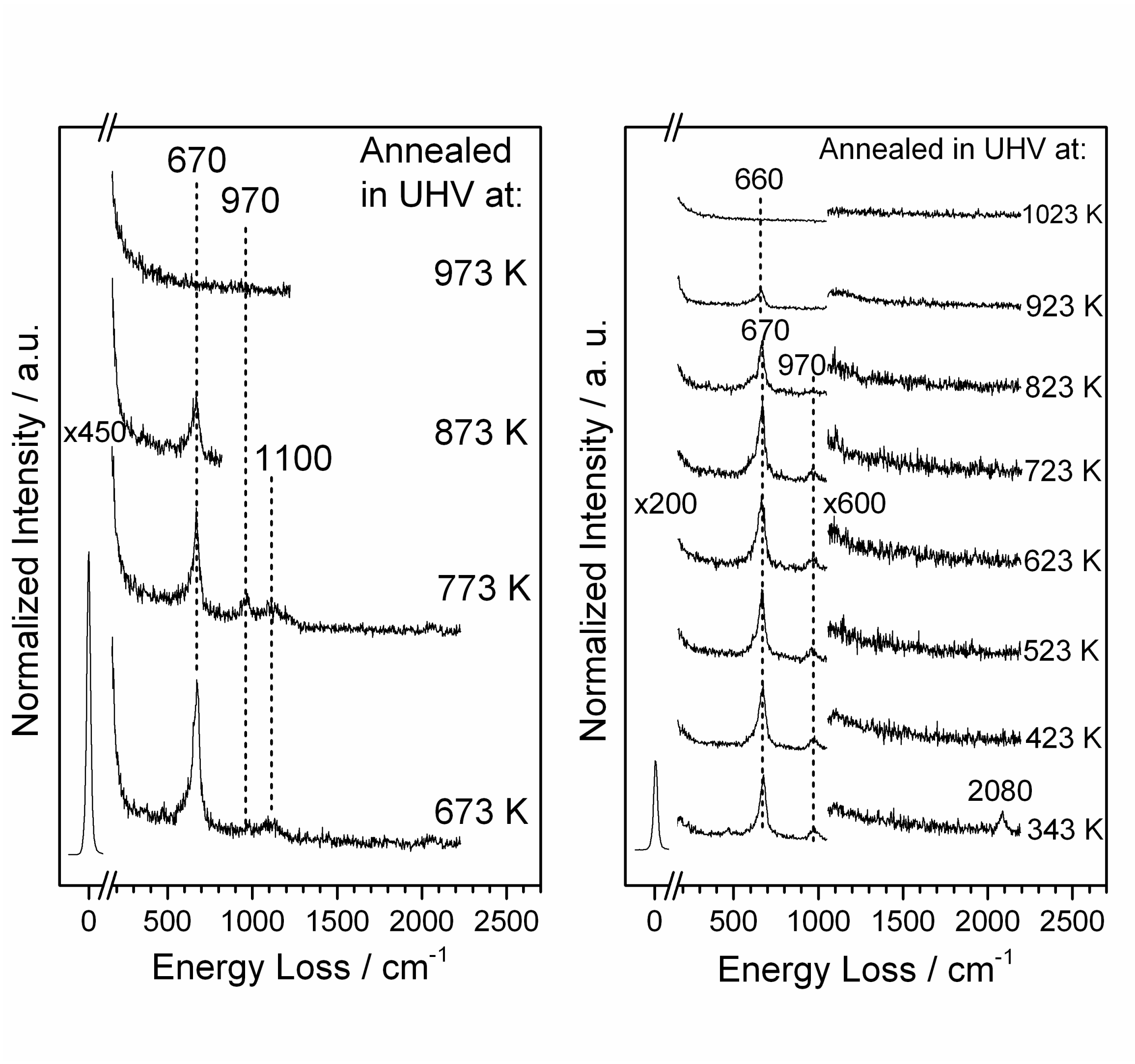

(a) (b)

Figure 7.3. HREELS spectra of superficial oxide surface and subsequent annealing in UHV at specified temperature for 5 min. Superficial oxide surface was prepared by exposing Re/Pt(111) to 1×10^{-6} mbar O_2 for 20 min. at 673 K (a) and for 10 min. at 723 K (b) followed by cooling in O_2 to 373 K and 343 K, respectively.

graphitic or carbidic carbon on Pt(111). [48] This surface was subsequently annealed to 973 K in 100 K steps for 5 min. at each temperature. The Re-O peak attenuated at each temperature, and all vibrations involving O disappeared by 973 K.

In a second similar experiment (Figure 7.3, right panel), the Re/Pt(111) surface was treated in 1×10^{-6} mbar oxygen at 723 K and cooled to 343 K in oxygen before being transferred to the analysis chamber under UHV conditions. Initial coverage of Re on this surface was 0.9 ML. HREELS again showed a loss peak at about 670 cm^{-1}, again assigned to O adsorbed on Re clusters, and a peak at 970 cm^{-1} due to O adsorbed on Re single atoms or very small clusters. Linear CO stretching was present at 2080 cm^{-1} as a result of CO adsorption on Pt from vacuum residual gas at 343 K. No loss peak at 1100 cm^{-1} was detected confirming that at 723 K, graphitic and/or carbidic carbon can be efficiently removed. Following O_2 exposure, the surface was annealed to 1023 K in 100 K steps. The Re-O peak at 970 cm^{-1} attenuated with increasing temperature, and this oxygen vibration disappeared between 923-1023 K. The oxygen atoms coordinated single Re atom/small cluster characterized by the loss peak at 970 cm^{-1} showed slightly lower thermal stability and this species was present until heated above 723 K. No Pt-O vibrations at ca. 490 cm^{-1} were detected.

7.5.3 Pt Skin Surface with Subsurface Pt-Re Alloy

Annealing the superficial Re oxide surfaces to 973 K or greater resulted in a decrease in the Re coverage calculated from XPS data regardless of sample history or initial Re coverage (see plot of Re 4f BE versus coverage in Figure 7.4). For the experiments above, the sample with initial $\Theta_{Re} = 0.8$ ML had a drop in Re coverage to 0.6 ML following annealing to 973 K. The Re coverage for Re/Pt(111) with initial $\Theta_{Re} = 0.9$ ML dropped to 0.6 ML after annealing to 1023 K. In fact, through the course of characterizing Re films in this paper, calculated Re coverage dropped continuously as the result of annealing and oxidative treatments. The amount by which Re coverage dropped was not easy to correlate with the specific annealing or oxidative procedure. However, the Re $4f_{7/2}$ BE increased linearly with the decrease in Re coverage as plotted in Figure 3 for all treatments. The Re $4f_{7/2}$ BE as a function of Re concentration has been reported previously, and these Re coverages

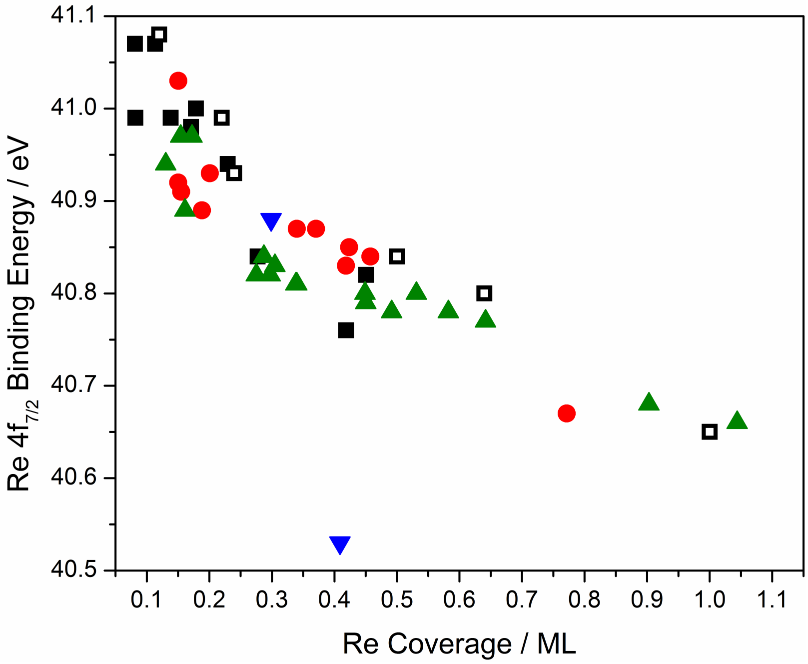

Figure 7.4. Re $4f_{7/2}$ BE plotted as a function of Re coverage calculated from the XPS data. Filled shapes (green and blue triangles, black squares, and red circles) are from this work, with each shape representing a different experimental series. Open black squares are coverages calculated from linear interpolations of Re concentrations taken from Reference [241].

interpolated from concentration values in reference [241] are also plotted in Figure 7.4 for comparison.

The drop in Re coverage, which is calculated using a non-attenuating fractional overlayer model (see Experimental Materials and Methods section), could be due to two factors: 1) evaporation of Re, or 2) diffusion of Re into the Pt bulk. Though we could not eliminate the possibility of Re evaporation, it is unlikely occurring under the experimental conditions used here. Tysoe et al. [248] observed depletion of surface Re on a Pt foil following oxidation in 700 Torr O_2 at 625 K. They attributed this loss of Re to the formation of the volatile Re_2O_7 species. Following this treatment, some Re_2O_7 remained on the surface, which was detected by XPS. However, we observed no evidence of the formation of Re_2O_7 from XPS, and our oxygen pressure was 8 orders of magnitude lower. Oxygen also desorbs from Re(0001) as ReO_2 or ReO_3 above 1700 K, [270] but temperatures used in the present study did not exceed 1100 K. Likely, diffusion of Re into the Pt bulk resulted in the attenuation of the Re 4f XPS signal by platinum and increasing of the Re 4f BE was indicative of Re alloying with Pt. [241, 244]

An STM image taken of the Pt-skin surface is shown in Figure 7.5. The amount of bright features on the surface in these images is much less than on the as-dosed surface shown in Figure 7.2. Some surface features are one atomic Pt or Re step high and others are approximately two atomic steps high. Though measuring the exact lateral dimensions of the features was not possible due to thermal drift, the image revealed that the bright features, likely Re that has not diffused into the Pt subsurface, are of two sizes: small clusters and much larger agglomerates.

The Re-Pt surface alloy interacted with oxygen very differently than the as-dosed Re surface. Figure 7.6 shows the HREELS spectra obtained following O_2 dosing and subsequent annealing to 373 K in UHV for 5 min for two similar Re-Pt surface alloys, which were prepared by the oxidative treatment of $Re_2(CO)_{10}$ exposed Pt(111) followed annealing to 973 K or higher in UHV. For all experiments, the Re-Pt surface alloy was exposed to 1×10^{-6} mbar O_2 while heating the sample to temperatures between 373-723 K and while cooling to 273 K. Regardless of dosing conditions, all HREELS spectra following O_2 dosing revealed energy loss features at approximately 460–465 cm^{-1} and 2080–2085 cm^{-1}, were assigned to the Pt-CO and C-O stretching vibrations of CO adsorbed in the on-top configuration on Pt(111). Literature values for these assignments are given in Table 7.2. This CO originated from vacuum residual gas and, judging from the ν(C-O) intensity and frequency, the CO coverage was very similar in these experiments and did not exceed 0.05 ML. Only the Pt-O vibration appeared at 455 cm^{-1} when a clean Pt(111) surface (no rhenium) was exposed to O_2 under similar conditions (Figure 7.7); no C-O stretching vibration was detected. This led to the conclusion that the feature at 465 cm^{-1} observed after O_2 exposure to the Re-Pt surface alloy (Figure 7.6) contained the contribution of the Pt-O vibration.

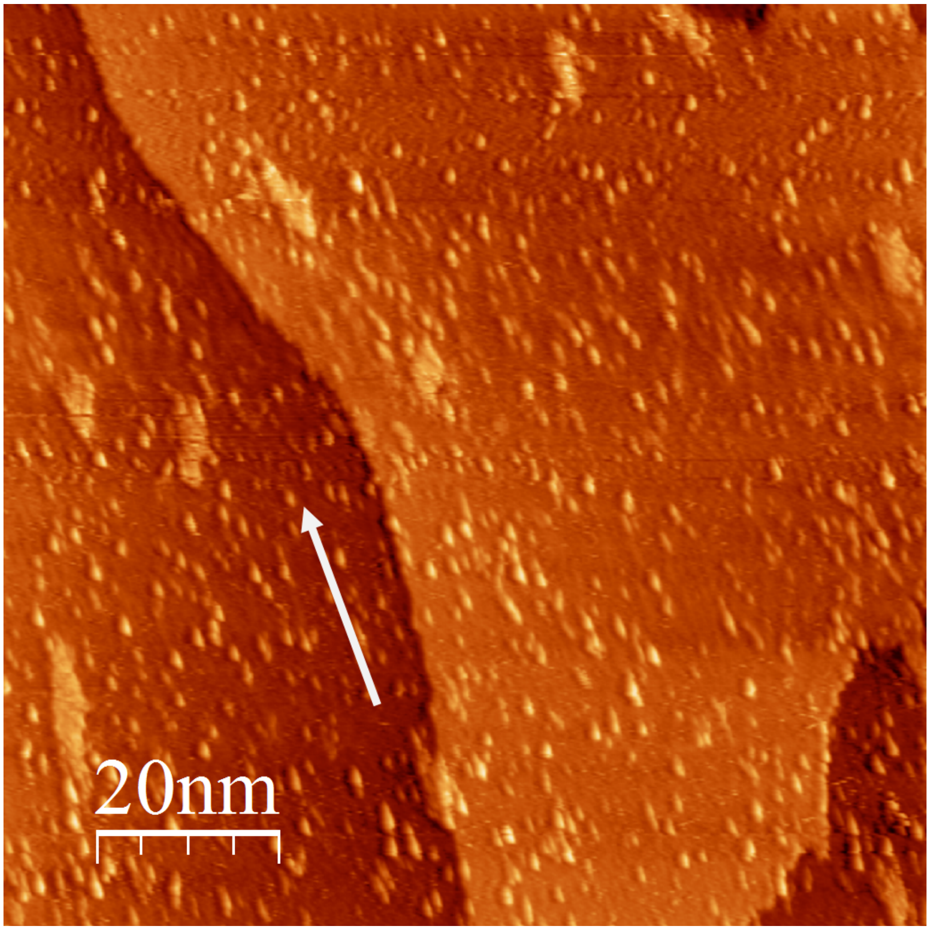

Figure 7.5. STM image of Pt-Re surface after annealing to 973 K. 100 nm × 100 nm, $I_t = 0.3$ nA, $U_t = 1000$ mV. From XPS, calculated $\Theta_{Re} = 0.3$ ML. Features are elongated in the direction of the white arrow due to drift.

Indeed, in a control experiment, when the Pt(111) surface was exposed to CO up to saturation, the ratio between the intensities of ν(C-O) and ν(Pt-CO) was 1.6. For the Re-Pt surface alloy (Figure 7.6), the ratio between the intensities of the peak at approximately 465 cm^{-1} and ν(C-O) at 2085 cm^{-1} was 1.1 and 0.5 for O_2 adsorption temperature of 373 and 723 K, respectively. This trend was confirmed in the other experiments and it demonstrated that the amount of oxygen adsorbed on the platinum surface increased with O_2 adsorption temperature. On the other hand, estimating from the relative intensity of ν(Pt-O), the oxygen coverage was more than 5 times

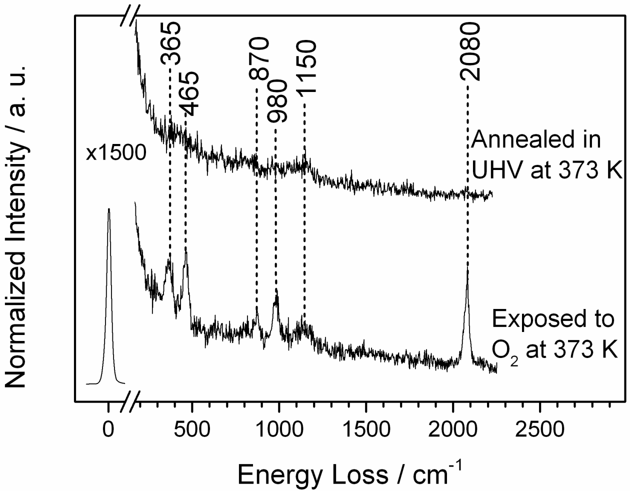

(a)

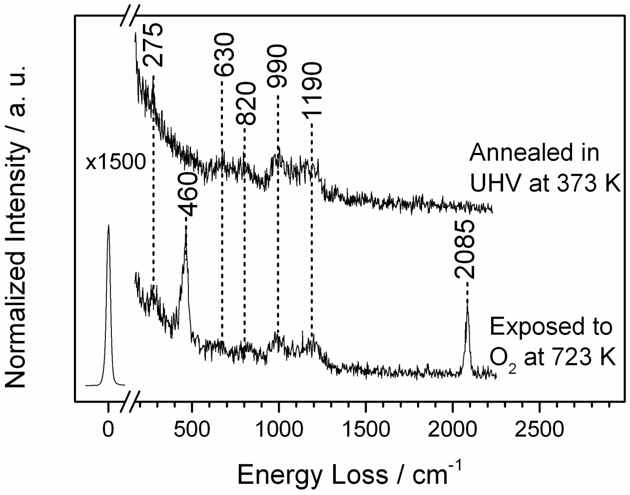

(b)

Figure 7.6. HREELS spectra obtained from the Re-Pt surface alloy exposed to 1×10^{-6} mbar O_2 at 373 K for 5 min (a), and at 723 K for 10 min. (b) In both experiments, the sample was cooled in O_2 to 273 K. Following O_2 dosing, each sample was heated in UHV at 373 K for 5 min.

less following O_2 adsorption on the Re-Pt surface alloy at 723 K (maximum amount of O_{ads}) compared to Pt(111). It is clear that HREELS is an inferior technique

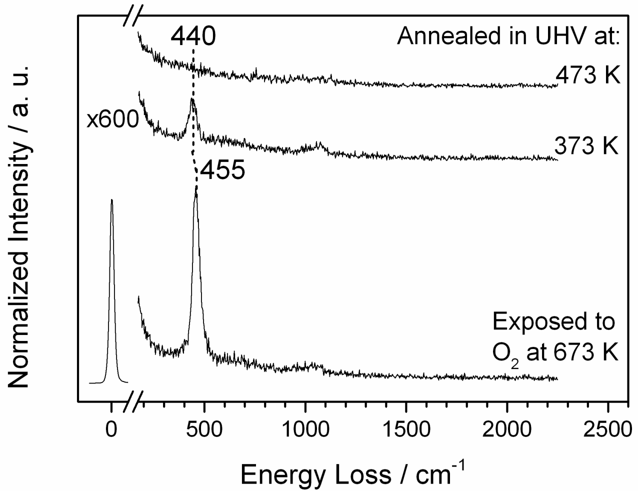

Figure 7.7. HREELS spectra obtained Pt(111) exposed to 1×10^{-6} mbar O_2 at 673 K followed by annealing at 373 K and 473 K in UHV for 5 min.

for quantification of adsorbates compared to temperature programmed desorption (TPD). Unfortunately, the STM sample holder is not compatible with TPD, and TPD was not done. In conclusion, very little O adsorbed on the Re-Pt surface alloy during O_2 exposure or CO reacted very quickly with adsorbed oxygen during transfer to the HREELS stage and data acquisition (total time was approx. 1 hour). This is in agreement with the XPS study by Alnot et al. [243] which showed that CO partially reacted with adsorbed O on a Pt-Re alloy surface.

Several other vibrations not discussed above appeared on alloy surfaces and were difficult to assign. It is interesting that after annealing of the Re-Pt alloy surfaces at 373 K in UHV, all vibrations assigned to CO_{ads}, ν(C-O) at 2085 cm^{-1} and ν(Pt-CO) at 465 cm^{-1}, and to O_{ads}/Pt(111), Pt-O at 460 cm^{-1}, disappeared completely (Figure 7.6), while the other vibrations were still detectable. The DFT calculation helped to understand the nature of these vibrations. The peaks between 630–990 cm^{-1} could be due to Re-O stretching vibrations for varying Re coverages and Re cluster sizes (see DFT section below). The assignment of low frequency features at 275 and

365 cm^{-1} and high frequency feature at 1190 cm^{-1} are unclear, but may be related to vibrational modes of oxygen atoms coordinated with platinum and rhenium atoms. It should be noted that the Re 4f peaks were unaffected by O adsorption on the Re-Pt surface alloys.

Once again, we would like to underline that O$_{\mathrm{ads}}$ thermal stability changed on the Re-Pt surface alloys compared with Pt(111) and Re monometallic surfaces. On Pt(111), oxygen desorbs between 600–1100 K (see reference [271] and references therein). O desorbs from Re(0001) [272] and from polycrystalline Re [273] at about 1700 K. In our case, ReO$_x$/Pt(111) decomposed between 923 and 973 K as shown by HREELS (Figure 7.3). However, it is not very fair to compare the decomposition/desorption temperatures obtained in TPD and HREELS experiments. In our case, cooling in UHV was slow and O$_{\mathrm{ads}}$ could react on a warm surface with residual gases, resulting in an apparent lowering of the desorption temperature. In a control experiment, O desorbed from the clean Pt(111) surface at 473 K as shown in Figure 7.7. This desorption temperature is lower than those reported in the literature (reference [271] and references therein) due to reaction with residual gas, however, this temperature is higher than what was observed on the Re-Pt surface alloy where O$_{\mathrm{ads}}$ desorbed at 373 K. This confirmed that O$_{\mathrm{ads}}$ was destabilized by the presence of rhenium.

7.5.4 DFT Calculations

O binding energies were computed on different surfaces as shown in Figure 7.8. The as-dosed Re on Pt(111) was modeled using a pseudomorphic film of Re on Pt(111) (Figure 7.8b). Segregation of Re into the bulk of Pt was modeled by assuming a Re sublayer in Pt with different coverages of Re (Figures 7.8c to 7.8f). The structure shown in Figure 7.8f, with a full monolayer of Re in the subsurface, was found to be more stable than that in Figure 7.8b by 3.39 eV per unit cell. This result indicates that Re strongly prefers to segregate into the Pt substrate. This is in agreement with

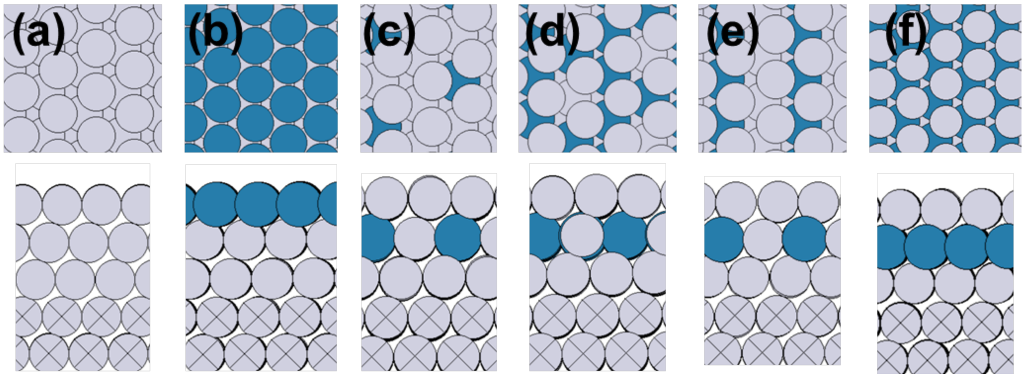

Figure 7.8. Close packed surface structures used in DFT calculations: (a) Monometallic Pt(111) (b) Re film on Pt (c):(f) Re sub layer of coverage (c) 0.25 (d) 0.5 (e) 0.75 and (f) 1.0 ML. Blue spheres = Re, Grey spheres = Pt.

other theoretical results where Pt segregation was found to be favorable in Pt-Re bimetallic systems. [274, 275]

The results of the calculations of O adsorption on these structures have been summarized in Table 7.3. The Re-film-on-Pt binds O more strongly than does monometallic Pt. However, the structures with Re present in the subsurface are found to bind O much more weakly than monometallic Pt. Increased Re coverage in the subsurface increases the degree of weakening. The DFT calculated trend in O adsorption energy is consistent with experimental measurements where as-dosed Re on Pt was found to bind O more strongly than pure Pt, but Pt-Re alloys formed after annealing and desorption of oxygen bound O more weakly than pure Pt. These results indicate that one possible reason for the alloy weakly adsorbing oxygen may be due to segregation of Pt to the top layer with concomitant Re segregation into the bulk of Pt. Structures having sub surface Re also adsorb CO more weakly than monometallic Pt.

Since the lattice constant of all the structures in the calculations were kept constant at the optimum lattice constant of monometallic Pt, the change in O binding energy in the different structures can be attributed to electronic effects. To understand the effect of electronic structure on the adsorption energies, we calculated the d-band centers of the surface atoms of the structures shown in Figure 7.8. The results are shown in Table 7.4. We find that the presence of subsurface Re in Pt (structures c through f) lowers the d-band center of surface Pt atoms, resulting in weaker binding of O as compared to monometallic Pt (structure a). The structure with a Re film on Pt (structure b), however, has a much higher d-band center than pure Pt and adsorbs O very strongly.

DFT-calculated vibrational frequencies for adsorbed O and CO on monometallic Pt, Re film on Pt, and the Re sublayer in Pt with a monolayer of Re coverage are shown in Table 7.5. The calculated frequencies agree with literature values reported in Table 7.2. The trend in the M-adsorbate frequency is consistent with the trend in binding energies of the adsorbates. This is not surprising as an increased stretching frequency could be associated with stronger binding. Quite different from these results, however, HREELS performed on the superficial rhenium oxide was seen to exhibit peaks at much higher frequencies of 670 cm^{-1} and 970 cm^{-1}, which are assigned to Re-O bonds of rhenium oxide. The exact structure of the oxide surface is difficult to ascertain, however, and in order to gain some insight into the effect of oxide structure into the stretching frequency of oxygen, we performed DFT calculations on some model oxide structures, as shown in Figure 7.9. The stretching frequencies of oxygen in these structures are reported in Table 7.6. The stretching frequencies of oxygen in the oxide are, in general, higher than that of an oxygen adsorbed on Re, as reported in Table 7.5. For a uniform rhenium oxide film on Pt(111), the frequency is 570 cm^{-1} for ReO and 563 cm^{-1} for ReO_2. However, the frequency is much higher if the oxide is present in the form of a cluster, even if it has same oxidation state as an oxide film. The calculated stretching frequency for a single ReO cluster is 982 cm^{-1} while for ReO_2 it is 909 cm^{-1}. These trends indicate that the superficial oxide experimentally observed, with a peak at 670 cm^{-1}, is possibly a cluster bigger than the single Re atom clusters considered in the calculations, but it is not quite a uniform oxide film. The HREELS peaks observed at 970 cm^{-1}, however, can be due to the presence of

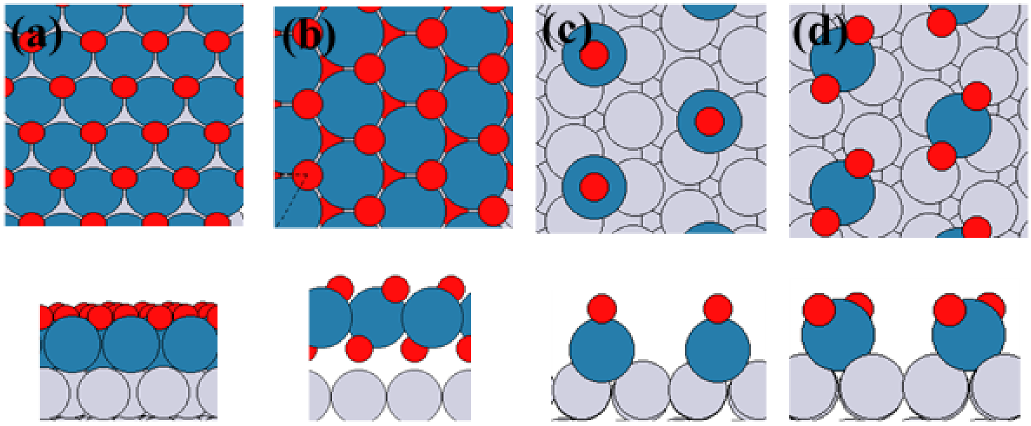

Figure 7.9. Rhenium oxide structures on Pt(111) (a) ReO film (b) ReO_2 film (c) single ReO islands, and (d) single ReO_2 islands. Grey spheres = Pt, blue spheres = Re, red spheres = O.

additional Re-O clusters on the Pt surface. This analysis is consistent with the STM image shown in Figure 7.5, which reveals a distribution of Re cluster sizes.

The lack of evidence of oxygen adsorption on the Pt-Re alloy surface, predicted to contain a Pt skin by DFT, as observed by experiment and confirmed by DFT calculations, is in agreement with observations in Reference [240], where dosing O_2 on a Re/Pt(111) surface following annealing did not result in formation of a superficial oxide as detected by XPS. Pt-Re alloy systems are also known to bond CO more weakly than either monometallic Pt or Re. [238, 240] Furthermore, CO oxidation activity is enhanced on Pt-Re alloy surfaces, resulting in more CO_2 produced compared to monometallic Pt(111). [249] Therefore, even if O did adsorb on the Pt-skin surface, it may have reacted with residual CO in the vacuum chamber at room temperature during the 5 minute transfer to the HREELS stage. Further, Pt skin formation is consistent with experiments which show Re coverage dropping following annealing. The results for O/CO binding are consistent with our HREELS data, showing no evidence of O or CO binding on Re sites on the annealed surface. Our analysis of the d-band centers further shows that the lower adsorption energies on Pt skin surfaces can be correlated to a decrease in the d-band center of the surface Pt atoms. Finally, vibrational frequency calculations were found to be consistent with both literature and experimental observations and indicate that the superficial rhenium oxide on the Pt(111) surface could be present in the form of rhenium oxide islands on Pt, in agreement with STM images.

7.6 Conclusions

Studying changes to the Re/Pt(111) system using surface sensitive experiments in UHV and DFT modeling provided detailed information on the morphology of this system and how it interacts with adsorbates.

- UHV-CVD is able to deposit sub-monolayer amounts of Re on Pt(111) using $Re_2(CO)_{10}$ as a precursor.

- The as-deposited Re film readily forms a superficial oxide in 1×10^{-6} mbar oxygen at temperatures greater than 573 K. The stoichiometry of this surface oxide is between $ReO_{0.5}$ and ReO. ReO_x/Pt(111) decomposes at approximately 973 K.

- Annealing the superficial oxide surface to 973 K in UHV results in the decrease of the calculated surface coverage of Re from XPS. Subsequent annealing treatments reduce the Re coverage further and increase the Re 4f BE relative to the as-dosed surface, indicating greater alloying of Re with Pt.

- STM indicates that the Re surface coverage decreases during these conditions.

- The annealed Pt-Re alloy surface likely forms at least a partial Pt skin. Oxygen adsorption on Re sites is hindered, and oxygen binding to Pt sites is weaker compared to Pt(111). CO from vacuum residual gas can adsorb the Pt-Re surface alloy exposed to O_2, which does not happen on O_{ads}/Pt(111).

- DFT predicts that a Pt substrate with a monolayer of subsurface Re is more stable than one with a monolayer of Re on top of Pt.

- DFT predicted O/CO binding on Pt skin surfaces are much weaker than that on monometallic Pt or on a monolayer of Re deposited on Pt.
- The trends in binding energy can be explained on the basis of d-band centers of Pt-Re systems. The DFT calculated trend in vibrational frequencies for adsorbed oxygen is consistent with binding energies. Vibrational frequency calculations for rhenium oxide indicate the oxide could be present in the form of islands on the Pt, some of which might be ReO clusters.

7.7 Acknowledgments

DFT calculations were performed by Paulami Majumdar, Dr. Xiang-Kui Gu, and Prof. Jeffrey Greeley. Text in this chapter adapted from Detwiler, M. D.; Majumdar, P.; Gu, X.-K.; Delgass, W. N.; Ribeiro, F. H.; Greeley, J.; Zemlyanov, D. Y. Characterization and Theory of Re films on Pt(111) Grown by UHV-CVD. *Surf. Sci.*, 2015, accepted. Copyright 2015 Elsevier.

Table 7.1.
Summary of dosing experiments. * = not controlled.

		Temperatures / K				Coverage / ML			
Dosing No.	Dosing Time / min.	Sample	Precursor	Pressure / mbar	Re $4f_{7/2}$ BE / eV	Re	C	O	Status
1	*	410	313	$< 5 \times 10^{-6}$	40.8	0.5	1.9	0.1	Clean
2	20	573	353	5×10^{-6}	40.7	0.8	3.4	0.0	Resid. Re
3	30	573	340	5×10^{-6}	40.7	1.0	5.3	0.0	Resid. Re
4	30	573	358	5×10^{-6}	40.5	0.4	4.5	0.0	Clean

Table 7.2.
Summary of vibration frequencies for O and CO adsorbed on Pt(111) and Re(0001). * = This work, DFT calculation.

Vibrational Mode	Frequency / cm^{-1}	
Catalyst	Re(0001)	Pt(111)
ν(M-CO) (on top)	415, [264] 405 $\pm$ 15, [265] 428 [266]	470, [267] 466*
ν(C=O) (on top)	1990-2050, [264] 2010 $\pm$ 15, [265] 2054 [266]	2100, [267] 2059*
ν(M-CO) (bridge)		380 [267]
ν(C=O) (bridge)		1850 [267]
ν(M-O)	560-585, [264] 550, [265] 540, [266]	490, [268] 480, [269] 466*
ν(M-O) (oxide)		760 [268]
ν(M-C)	495, [264] 709 (hcp) [266]	

Table 7.3.
DFT calculation results. Oxygen adsorption energies are referenced to a gas phase oxygen molecule.

Structure	O Adsorption		CO Adsorption	
	Adsorption Site	Adsorption Energy	Adsorption Site	Adsorption Energy
A	FCC	-1.28	FCC	-1.72
B	HCP	-3.73	Top	-2.15
C	FCC	-1.07	FCC	-1.57
D	FCC	-0.99	Top	-1.51
E	FCC	-0.90	Top	-1.48
F	FCC	-0.89	Top	-1.51

Table 7.4.
Comparison of O adsorption energies with d-band center.

Structure	O Adsorption Energy / eV	d-band Center / eV
A	-1.28	-1.94
B	-3.73	-1.18
C	-1.07	-2.12
D	-0.99	-2.34
E	-0.90	-2.56
F	-0.89	-2.67

Table 7.5.
DFT calculated vibrational frequencies for adsorbed oxygen.

Structure	ν(M-O) / cm^{-1}	ν(M-CO) / cm^{-1}	ν(C-O) / cm^{-1}
A	436	466	2059
B	486	460	1983
F	425	431	2040

Table 7.6.
DFT calculated vibrational frequencies for oxygen in rhenium oxide on Pt(111).

Structure	ν(Re-O) / cm^{-1}
A	570
B	563 (Upper O) ; 493 (Lower O)
C	982
D	909

8. XPS CHARACTERIZATION OF PT-MO/MWCNT BIMETALLIC CATALYSTS FOR HIGH PRESSURE VAPOR PHASE HYDRODEOXYGENATION OF LIGNIN-DERIVED MODEL COMPOUNDS

8.1 Abstract

A series of Pt-Mo bimetallic catalysts have been synthesized, characterized, and tested for their ability to remove oxygen from lignin model compounds. Lignin comprises up to 40% of the total energy content of biomass, [276] and is a promising feedstock for the production of renewable fuels and chemicals. This chapter focuses on the XPS characterization of these Pt-Mo bimetallic catalysts, which were able to completely deoxygenate several lignin-derived model compounds in yields greater than 98% in the vapor phase. XPS characterization as it relates to the other characterization techniques is discussed, and an overall picture of catalyst structure is presented. For information on catalyst performance and details on the other characterization methods, refer to reference [277].

8.2 Experimental Methods

X-ray Photoelectron Spectroscopy (XPS) measurements were performed using a Kratos Axis Ultra DLD with monochromatic Al Kα radiation ($h\nu$ =1486.6 eV) at constant pass energies of 20 eV for high resolution region scans and 160 eV for survey scans. Spectra were collected with an anode power of 75 W. Fresh catalysts were loaded into a stainless-steel sample holder capable of holding 5 different samples. Prior to analysis, samples were reduced under 35 sccm H_2 and 50 sccm Ar flow at atmospheric pressure for 2 hours at 450°C. Samples were reduced in a standard

Kratos catalytic cell connected to the XPS chamber via a transfer arm so that reduced samples could be transferred between the two chambers without air exposure.

The binding energy scale was calibrated to the Au $4f_{7/2}$, Cu $2p_{3/2}$, and Ag $3d_{5/2}$ signals at 84.0, 932.7, and 368.3 eV, respectively, using a sputter-cleaned sample consisting of each type of foil. All spectra were analyzed using the CasaXPS software program, version 2.3.16 PR 1.6 (Casa Software Ltd.). Binding energies were charge corrected to the graphitic C 1s component associated with the MWCNT support at 284.6 eV. A linear or Shirley type background was subtracted from each region before curve fitting and quantification. Metallic Mo 3d species (Mo^0, molybdenum carbide-like phase) and the Pt 4f region were fit with an asymmetric Gaussian-Lorentzian peak with tail dampening (CasaXPS Lineshape = LF) and non-metallic molybdenum species ($Mo4^+$, $Mo6^+$) were fit with symmetric Gaussian-Lorentzian peaks (CasaXPS Lineshape = GL). Positions, fwhms, lineshapes, and lineshape parameters for the Mo 3d and Pt 4f region deconvolutions are listed in Tables 8.1 through 8.5.

Doublets arising from spin orbit coupling in the Pt 4f ($4f_{7/2}$ and $4f_{5/2}$) and Mo 3d ($3d_{5/2}$ and $3d_{3/2}$) regions were subject to spacing constraints of 3.33 eV and 3.13 eV, respectively [25]. The Pt $4f_{5/2}$ peak area was set to 0.75 times the area of the Pt $4f_{7/2}$ peak, and the Mo $3d_{3/2}$ area was constrained to 0.67 times the area of the Mo $3d_{5/2}$ peak. fwhms of all spin orbit coupling doublets in the Pt 4f and Mo 3d regions were constrained to be equal with the exception of the Mo $3d_{5/2}$ and Mo $3d_{3/2}$ lines assigned to Mo metal as alloy or isolated nanoparticles. This exception was made based on a reference Mo foil for which the Mo $3d_{3/2}$ peak was wider than the Mo $3d_{5/2}$ peak.

Quantification of relative region areas was performed following background subtraction, yielding atomic % values for each element present assuming a homogeneously mixed sample. Each area was divided by the spectrometer transmission function, relevant Scofield relative sensitivity factor, and electron inelastic mean free path.

Table 8.1.
XPS Binding Energies and Component Area Percents for Pt, Mo and Pt-Mo Catalysts.

Component	BE / eV					Component Area %			
	Mo^{6+}	Mo^{4+}	Mo^0 Carbide-like	Mo^0 Alloy	Pt $4f_{7/2}$	Mo^{6+}	Mo^{4+}	Mo^0 Carbide-like	Mo^0 Alloy
5% Pt	-	-	-	-	71.4	-	-	-	-
5% Pt-Mo(1:0.05)	n/a	n/a	n/a	n/a	71.5	-	-	-	-
5% Pt-Mo(1:0.5)	232.5	230.2	228.9	228.3	71.7	20	24	27	29
5% Pt-Mo(1:1)	232.6	230.6	229.0	228.3	71.8	18	18	38	26
5% Pt-Mo(1:2)	232.6	230.6	228.8	228.2	71.8	16	15	45	24
5% Pt-Mo(1:5)	232.3	230.0	228.9	228.2	71.8	25	17	41	17
2.46% Mo	232.4	230.0	229.0	228.2	-	26	26	43	5

Table 8.2.
XPS spectra fwhm values for the Mo 3d region for the Pt-Mo/MWCNT series, 5%Pt/MWCNT, and 2.46%Mo/MWCNT catalysts.

	Mo^0		Mo carbide-like		Mo^{4+}		Mo^{6+}	
Catalyst	$3d_{5/2}$	$3d_{3/2}$	$3d_{5/2}$	$3d_{3/2}$	$3d_{5/2}$	$3d_{3/2}$	$3d_{5/2}$	$3d_{3/2}$
5% Pt-Mo(1:0.05)	n/a	n/a	n/a	n/a	n/a	n/a	n/a	n/a
5% Pt-Mo(1:0.5)	0.800	1.033	0.925	0.925	2.321	2.321	2.313	2.313
5% Pt-Mo(1:1)	0.766	0.872	1.095	1.095	2.208	2.208	2.208	2.208
5% Pt-Mo(1:2)	0.667	0.815	1.208	1.208	2.175	2.175	2.283	2.283
5% Pt-Mo(1:5)	0.692	0.824	1.205	1.205	2.582	2.582	2.573	2.573
2.46% Mo	0.619	0.619	1.333	1.333	1.768	1.768	2.947	2.947

Table 8.3.
XPS fwhm values for the Pt 4f region for the Pt-Mo series, 5%Pt, and 2.46%Mo MWCNT-supported catalysts.

Catalyst	$4f_{7/2}$	$4f_{5/2}$
5% Pt-Mo(1:0.05)	1.249	1.249
5% Pt-Mo(1:0.5)	1.180	1.180
5% Pt-Mo(1:1)	1.174	1.174
5% Pt-Mo(1:2)	1.117	1.117
5% Pt-Mo(1:5)	1.116	1.116
5% Pt	1.024	1.024

8.3 Results

This section is presented in two parts: in the first, the base case 5% Pt-Mo/MWCNT (Pt:Mo = 1:1) catalyst is compared with monometallic Pt and Mo catalysts, and the

Table 8.4.
XPS lineshapes for the Mo 3d region for the Pt-Mo bimetallic series, 5%Pt, and 2.46%Mo MWCNT-supported catalysts.

Catalyst	Mo^0	Mo carbide-like	Mo^{4+}	Mo^{6+}
5% Pt-Mo(1:0.05)	n/a	n/a	n/a	n/a
5% Pt-Mo(1:0.5)	LF(1,2.5,50,90)	LF(1,2.5,50,90)	GL(60)	GL(60)
5% Pt-Mo(1:1)	LF(1,2.5,50,90)	LF(1,2.5,50,90)	GL(80)	GL(80)
5% Pt-Mo(1:2)	LF(1,2.5,50,90)	LF(1,2.5,50,90)	GL(60)	GL(60)
5% Pt-Mo(1:5)	LF(1,2.5,50,90)	LF(1,2.5,50,90)	GL(60)	GL(60)
2.46% Mo	LF(1,2.5,50,90)	LF(1,2.5,50,90)	GL(80)	GL(0)

Table 8.5.
XPS lineshapes for the Pt 4f region for the Pt-Mo bimetallic series, 5%Pt, and 2.46%Mo MWCNT-supported catalysts.

Catalyst	Pt 4f
5% Pt-Mo(1:0.05)	LF(1,3,80,90)
5% Pt-Mo(1:0.5)	LF(1,2.3,70,90)
5% Pt-Mo(1:1)	LF(1,2,50,90)
5% Pt-Mo(1:2)	LF(1,2,50,90)
5% Pt-Mo(1:5)	LF(1,2,50,90)
5% Pt	LF(1,2.5,50,30)

justification for peak assignments and deconvolutions are presented. In the second section, the deconvolutions are applied to a series of Pt-Mo bimetallic catalysts of varying Mo:Pt ratios.

8.3.1 Comparison of Pt-Mo Catalyst to Pt and Mo Catalysts

X-ray Photoelectron Spectroscopy (XPS) measurements were conducted to determine catalyst chemical information and to quantify overall atomic ratios on the fresh, reduced catalysts. The Pt $4f_{7/2}$ regions on the 5%Pt/MWCNT and 5%Pt-Mo/MWCNT catalysts were fit in each case with a single asymmetric peak at binding energies (BE) of 71.4 and 71.8 eV, respectively. The Pt $4f_{7/2}$ peak on the 5%Pt/MWCNT monometallic catalyst was assigned to metallic Pt; a BE value of 71.2 eV has been reported for metallic Pt. [68] The shift to higher BE on the bimetallic catalyst relative to the monometallic catalyst indicated the presence of Pt_xMo_y alloy phase(s) based on previous XPS studies on Pt-Mo systems; [233, 278–280] the corresponding alloy Mo $3d_{5/2}$ line at 228.3 eV is discussed below. The Pt 4f regions for the 5%Pt/MWCNT and 5%Pt-Mo/MWCNT catalysts are shown in Figure 8.1a.

The Mo 3d envelope for the bimetallic 5%Pt-Mo/MWCNT catalyst was fit with four species: Mo^0 (26% of total envelope area), a molybdenum carbide-like species (38%), Mo^{4+} (18%), and Mo^{6+} (18%), as shown in Figure 8.1B. The $3d_{5/2}$ peak of the Mo^0 species appeared at a BE of 228.3 eV. This peak was assigned primarily to a Pt_xMo_y alloy phase(s) based on the Pt 4f chemical shift to higher BE for the 5%Pt-Mo/MWCNT bimetallic catalyst relative to the 2.46%Mo/MWCNT monometallic catalyst, and the difference in BE between the Mo 3d and Pt 4f peaks, which is indicative of a Pt-rich Pt-Mo alloy. [279] Speculation on the possible alloy composition(s) is presented in the discussion section. This peak also incorporates some reduced monometallic Mo^0, but this is likely a minority species given its reduced contribution to the overall Mo 3d peak envelope in the monometallic 2.46%Mo/MWCNT catalyst relative to the 5%Pt-Mo/MWCNT bimetallic catalyst (5% and 26%, respectively).

The Mo $3d_{5/2}$ component at 229.0 eV was assigned to a molybdenum carbide-like species. Barthos et al. [280] observed the appearance of a shoulder at 228.9 eV after treatment of MoO_3/MWCNT in H_2 between 400°C and 500°C. This shoulder dominated the XP spectrum, shifted to 227.8 eV after H_2 treatment at 700°C, and was attributed to molybdenum carbide. The H_2 reduction temperature of 450°C and

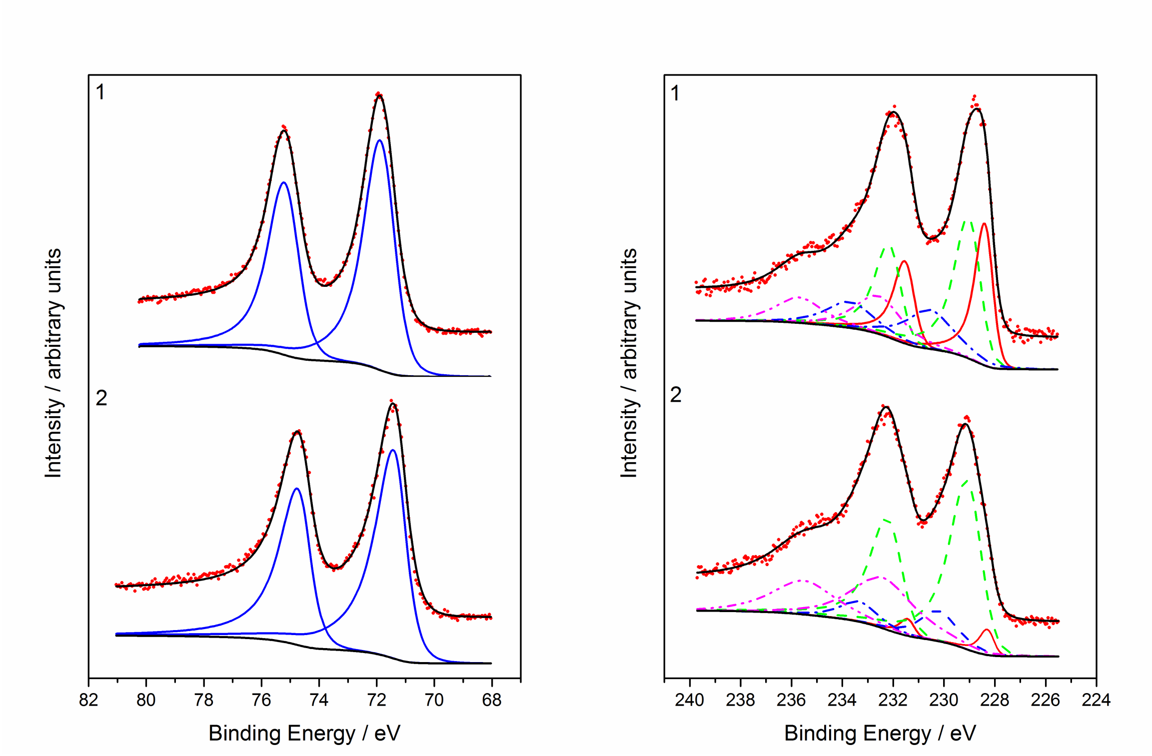

(a) Pt 4f

(b) Mo 3d

Figure 8.1. (a) Pt 4f region for 1) 5%Pt-Mo and 2) 5%Pt MWCNT-supported catalysts (Pt^0, solid blue; Pt fit components, solid black; data, red dots) and (b) the Mo 3d region for 1) the 5%Pt-Mo and 2) 2.46%Mo MWCNT-supported catalysts (Mo^{6+}, magenta dash/dot/dot; Mo^{4+}, blue dash/dot; Mo carbide-like species, green dash; Mo^0, solid red; all Mo fit components, solid black; data, red dots).

observation of a Mo $3d_{5/2}$ peak at 229.0 eV in the present work are in agreement with the intermediate state observed by Barthos et al. [280], suggesting that the carbide formed was not stoichiometric Mo_2C. This assignment was supported by the Mo-Mo bond distance of 2.88 Å from XAS reported above, which fell between that reported for a metallic foil (2.76 Å) and a stoichiometric Mo_2C (2.96-2.97 Å) [281]. Determination of the stoichiometry of this carbide-like species by XPS was not successful due domination of the C 1s region by the MWCNT support signal.

The balance of the Mo 3d peak envelope was composed of Mo^{4+} as MoO_2 ($3d_{5/2}$ BE = 230.6 eV) and Mo^{6+} as MoO_3 ($3d_{3/2}$ BE = 232.6 eV). Numerous references report binding energies for these Mo species with reported Mo^{4+} $3d_{5/2}$ BEs ranging between 229.1–231.0 eV [282–287] and reported Mo^{6+} $3d_{5/2}$ BEs ranging between 232.3 - 232.8 eV [282–285, 287]. No internal Mo oxide standards were used to determine XPS binding energies on the MWCNT supports, therefore the assignments of Mo^{4+} and Mo^{6+} (the most stable oxidation states of Mo) may include some Mo in defect states like Mo^{5+}.

The monometallic 2.46%Mo/MWCNT catalyst Mo 3d region was fit with the same four Mo species. The region was composed of Mo^0 (228.2 eV, 5% of total region area), a carbide-like species (229.0 eV, 43%), Mo^{4+} (230.0 eV, 26%), and Mo^{6+} (232.5 eV, 26%).

Platinum and molybdenum binding energies and percentages of each Mo component relative to the total Mo 3d region areas for the Mo:Pt = 1:1 5%Pt/MWCNT, 5%Pt-Mo/MWCNT, and 2.46%Mo/MWCNT catalysts are given in Table 8.1. Fwhm fitting values are given in Tables 8.2 and 8.3. Detailed region scans of the C 1s and O 1s regions were also performed for all catalysts and the as-received MWCNT support.

Quantification yielding the Pt:Mo atomic ratio was performed via integration of the XPS total Pt and Mo regions. For the fresh nominal 5% Pt-Mo/MWCNT catalyst (Pt:Mo = 1:1), the Pt:Mo ratio calculated by this method was $1 : 1.22 \pm 0.06$.

8.3.2 Pt:Mo Bimetallic Catalyst Series

Catalyst chemical information from deconvolution of the Mo 3d and Pt 4f regions and overall quantification of Mo:Pt atomic ratios for bimetallic catalysts of varying Mo:Pt ratios was also obtained by XPS. Binding energies and percentages of each Mo component relative to the total Mo 3d region areas for the Pt-Mo catalysts are given in Table 8.1. The deconvolution of the Mo 3d region on the nominal Mo:Pt 0.05:1 catalyst was omitted due to the poor signal-to-noise ratio as a result of the low Mo

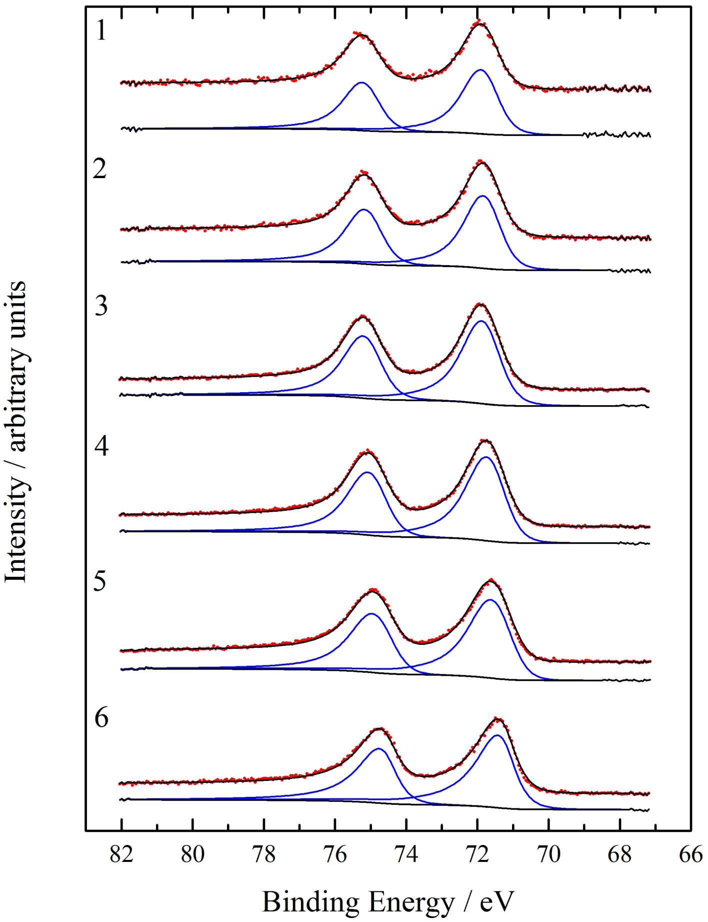

Figure 8.2. Pt 4f region for (1) 2%Pt-Mo(1:5), (2) 2.5%Pt-Mo(1:2), (3) 5%Pt-Mo(1:1), (4) 5%Pt-Mo(1:0.5), (5) 5%Pt-Mo(1:0.05), and (6) 5%Pt MWCNT-supported catalysts (Pt^0, solid blue; Pt fit components, solid black; data, red dots)

loading. Binding energies for the Pt 4f region for each Pt-containing catalyst are also given in Table 8.1. Region scans (Pt 4f, Mo 3d) for the Pt-Mo catalyst series are shown in Figures 8.2 and 8.3, and fwhm values and other XPS fitting information are given in Tables 8.1 through 8.5.

The Pt $4f_{7/2}$ BEs for the bimetallic catalysts were higher than for the monometallic Pt catalyst in all cases, as seen in Table 8.1 and Figure 8.2. As the Mo loading

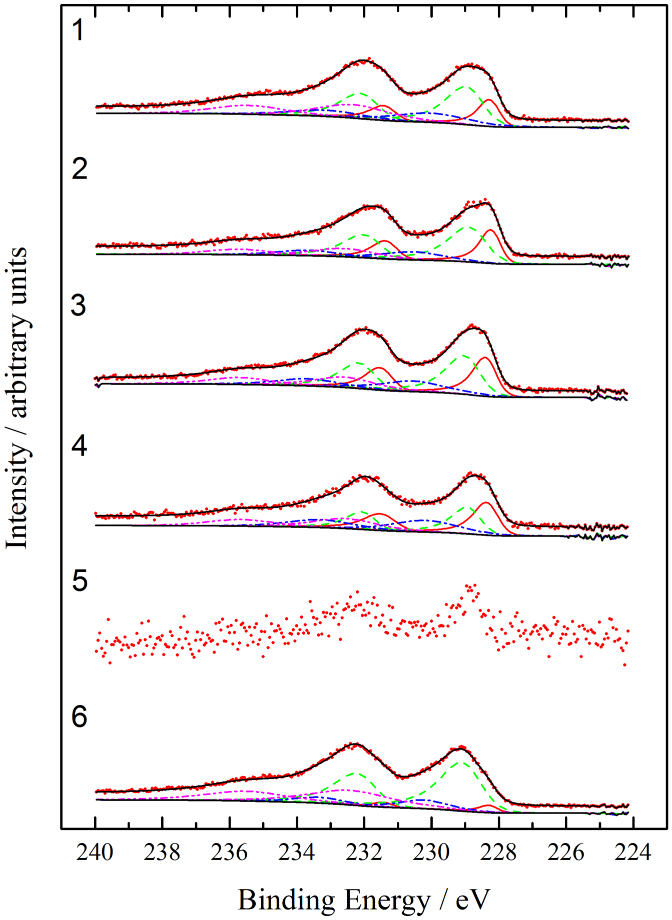

Figure 8.3. Mo 3d region for (1) 2%Pt-Mo(1:5), (2) 2.5%Pt-Mo(1:2), (3) 5%Pt-Mo(1:1), (4) 5%Pt-Mo(1:0.5), (5) 5%Pt-Mo(1:0.05), and (6) 2.46%Mo MWCNT-supported catalysts (Mo^{6+}, magenta dash/dot/dot; Mo^{4+}, blue dash/dot; Mo carbide-like species, green dash; Mo^0, solid red; all Mo fit components, solid black; data, red dots).

increased, the Pt BE increased by ca. 0.3 eV for the Mo:Pt = 0.5:1 sample and then increased and stabilized at ca. 71.8 eV for the 3 higher Mo loading samples (Mo:Pt = 1:1, 2:1, and 5:1). As described above, this shift was attributed to the existence of a Pt_xMo_y alloy phase(s).

The Mo 3d envelopes were fit with 4 species: Mo^0 (as a Pt_xMo_y alloy phase(s) or isolated Mo monometallic nanoparticles), a molybdenum carbide-like phase, Mo^{4+} as MoO_2, and Mo^{6+} as MoO_3. Justification for these assignments is given above. As reported in Table 8.1, binding energies for each species changed across the series of catalysts. The BE ranges for Mo^{6+} (232.3 to 232.6 eV), Mo^{4+} (230.0 to 230.6 eV), and the carbide species (228.8 to 229.0 eV) did not follow any trend, and the changes in BE from one catalyst to another were likely due to slight differences the chemical environments of these species perhaps arising from differences in preparation, or due to artifacts of the XPS curve fitting. The BE for the Mo^0 peak associated with a Pt-Mo alloy changed from 228.3 to 228.2 eV with increasing Mo loading relative to Pt loading.

The percentage of each Mo component in the Mo 3d region as a function of increasing Mo loading relative to Pt is shown in Figure 8.4. The clearest observed trend for the change in % of total Mo 3d envelope with increasing Mo loading was that the fraction of Mo^0 decreased from 29% to 5%, while the carbide-like species increased from 28% up to 43% for the nominal Mo:Pt = 2:1 catalyst, and then remained about constant. The Mo^{6+} and Mo^{4+} species contribution to the overall envelope ranged across the series from 15% to 25%, but did not follow an apparent trend.

Overall Mo 3d and Pt 4f region quantification yielded an Mo:Pt ratio for each catalyst. In Figure 8.5, the nominal Mo:Pt ratios are compared to Mo:Pt ratios calculated by XPS.

8.4 Discussion

A brief summary of the discussion presented in reference [277] follows, with a focus on the results obtained by XPS.

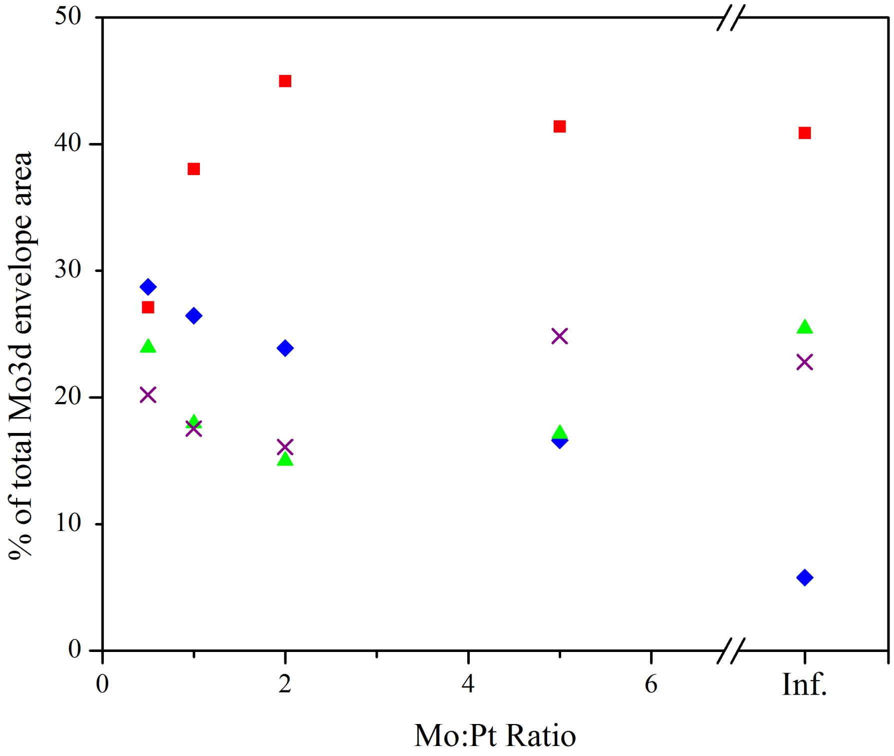

Figure 8.4. % area of Mo 3d peak envelope as determined by XPS for Mo oxidation states as a function of increasing Mo loading: Mo^0 (black squares), Mo carbide-like species (red circles), Mo^{4+} (blue triangles), Mo^{6+} (green X). Infinity on the x-axis represents the 2.46%Mo/MWCNT catalyst

8.4.1 Monometallic Platinum Particles and Alloying of Platinum and Molybdenum

Although both monometallic Pt and Pt_xMo_y nanoparticles were observed on the fresh, reduced catalysts by STEM, the XPS Pt 4f region was fit using only one species, as no spectral features existed to justify fitting the Pt 4f region with more than one species. However, the FWHMs for the Pt 4f lines of the bimetallic catalysts are larger than for the monometallic Pt catalyst, indicating a broader range of Pt chemistries for the bimetallic catalyst, explaining this discrepancy between STEM and XPS results.

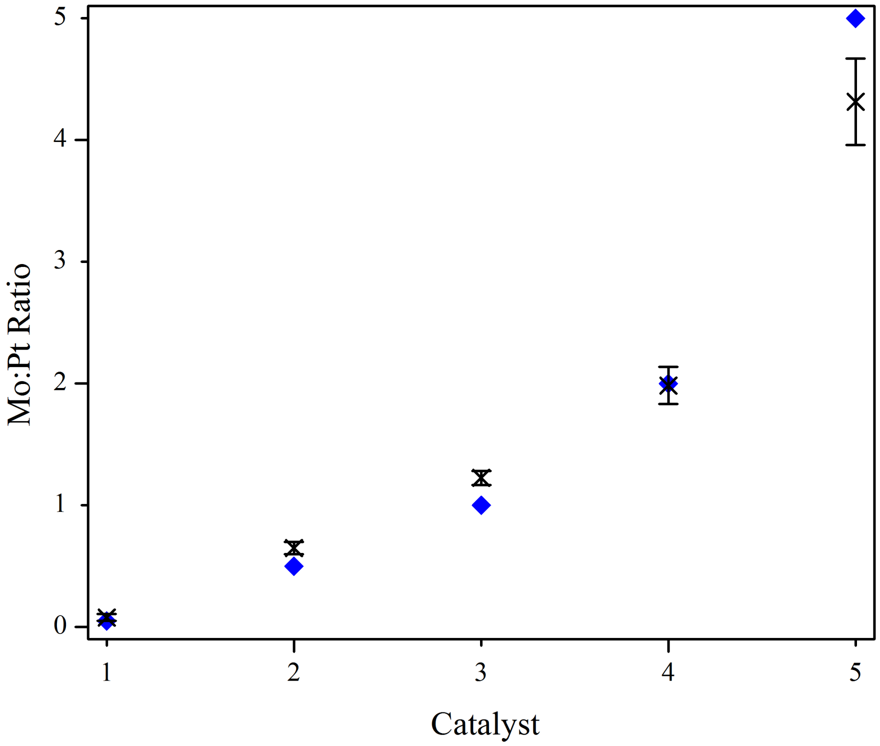

Figure 8.5. Mo:Pt ratio as a function of increasing Mo loading for the peak envelopes determined from XPS (black X) and the nominal catalyst synthesis loading (blue diamond).

Alloying of Pt with Mo was supported by XPS due to the shift of the Pt 4f peaks to higher binding energy and the decrease in normalized intensity of the Mo^0 peak for the pure Mo catalyst. STEM and EXAFS results support the assertion that the extent of alloying increased with additional Mo loading. The Pt $4f_{7/2}$ XPS peak BE increased with increasing Mo loading up to the Mo:Pt=1:1 bimetallic catalyst, then remained about constant around 71.8 eV. The change in the Pt $4f_{7/2}$ BE for the Pt-Mo catalysts relative to the monometallic 5%Pt/MWCNT catalyst BE of 71.4 eV is shown in Figure 8.6. This BE shift was due to increased alloying of the Pt with Mo as

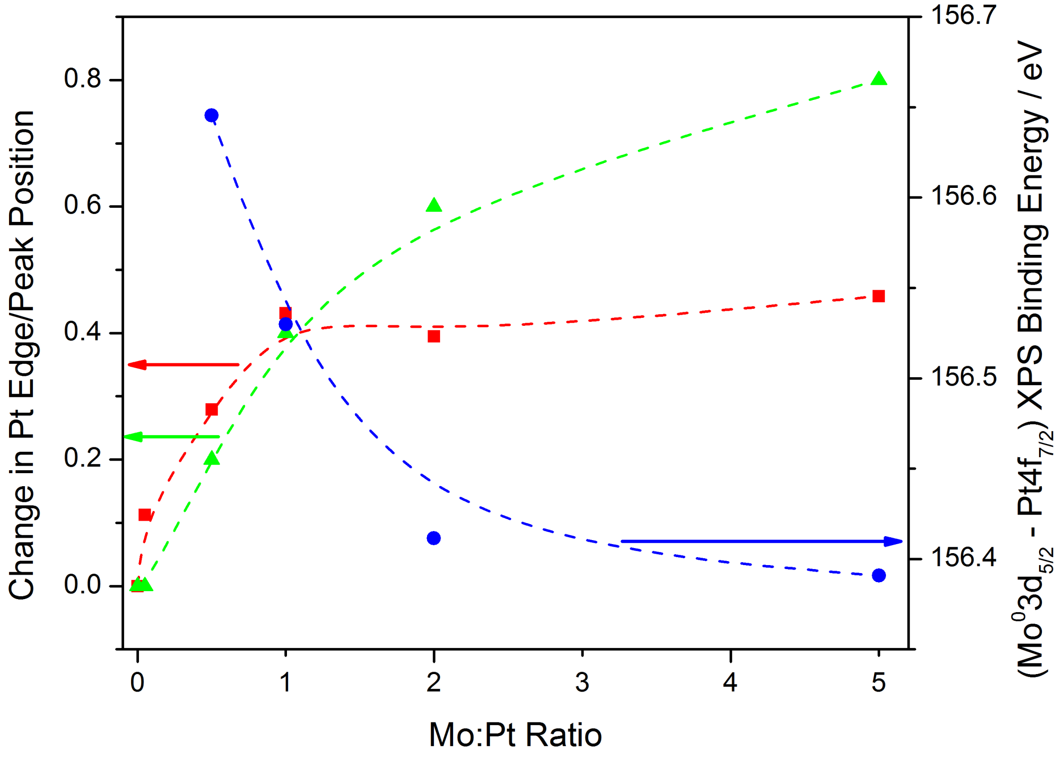

Figure 8.6. The difference in the XPS Pt $4f_{7/2}$ and $Mo^03d_{5/2}$ BE as a function Pt:Mo ratio (right axis, blue circles), difference in XPS Pt $4f_{7/2}$ BE of the Pt-Mo/MWCNT catalysts relative to the 5%Pt/MWCNT catalyst as a function of Pt:Mo ratio (left axis, red squares), and difference in XAS Pt E_0 of the Pt-Mo/MWCNT catalysts relative to the 5%Pt/MWCNT catalyst as a function of Pt:Mo ratio (left axis, green triangles).

the Mo loading increased. A similar trend was observed with XAS, and the difference in the XAS Pt E_0 of the Pt-Mo/MWCNT catalysts relative to the 5%Pt/MWCNT catalyst E_0 of 11.5640 keV is also shown in Figure 8.6. The increasing shift seen with XAS tracks with the shift observed by XPS for Mo loadings up to the Mo:Pt = 1:1 catalyst. On the higher Mo-loaded catalysts (Mo:Pt=2:1 and Mo:Pt=5:1), a shift was observed with XAS whereas the shift measured with XPS stabilized for these higher Mo loading catalysts. The shift in Pt 4f BE from XPS implies that the alloy composition reaches saturation, but the edge shift in XAS implies that alloying does not reach a saturation composition, even at the highest Mo loading (Mo:Pt = 5:1). This is likely because the signal from the Mo-rich alloy in the higher Mo loading catalysts is attenuated by other Mo phases. XAS, which is a bulk averaging technique, is not affected, whereas XPS is a surface averaging technique. Support for this idea comes from STEM and the XPS quantification: more large patches attributed to MoO_x or Mo_xC phases were visible in STEM, and only for the Mo:Pt=5:1 catalyst is the XPS-calculated Mo:Pt ratio is below the nominal value (nominal is 5:1, XPS calculates 4.3:1 Mo:Pt, see Figure 8.5). Therefore, the alloy composition does not reach saturation, and continues to become Mo rich as Mo loading is increased across the whole series.

Determination of the average Pt_xMo_y alloy stoichiometry from XPS was attempted, but was complicated by the appearance of both mono- and bimetallic Pt-containing nanoparticles in STEM images, indicating that the total Pt 4f region area represented both of these phases. Furthermore, the existence of monometallic Mo^0 phase could not be eliminated by XPS. However, the assigned Mo^0 XPS peak almost disappeared on the monometallic 2.46%Mo/MWCNT catalyst. This supports the assignment of the Mo^0 observed on the bimetallic catalysts to Mo^0 present in a Pt-Mo alloy, agreeing with the Pt XPS BE shift suggesting alloying and the observation of alloy particles via STEM/EELS. Additionally, alloy nanoparticles dispersed on MWCNTs may have different electronic properties than bulk alloys. Despite these issues, comparison of the XPS alloy results for the 5%Pt-Mo/MWCNT catalyst to literature values is presented below. For these comparisons, the differences in binding energies between the Pt $4f_{7/2}$ and $Mo^0 3d_{5/2}$ (BE = 228.2 eV) lines was used to avoid complications arising from differences in charge correction or binding energy reference.

The difference in Pt $4f_{7/2}$ and Mo^0 $3d_{5/2}$ BEs can be calculated from Table 8.1. Grgur et al. [278] reported a +0.3 eV shift to 71.4 eV of the Pt $4f_{7/2}$ line on a bulk $Pt_{77}Mo_{23}$ alloy relative to the metallic Pt BE. This was accompanied by a -0.5 eV shift in the Mo 3d alloy line to 227.3 eV compared to a metallic sample. The difference in BE between these two lines was 155.9 eV, about 0.6 eV smaller than the difference between the two peaks for the bimetallic catalyst in this work. Neophytides et al. [279] varied the Pt:Mo atomic ratio of Pt-Mo alloys over the range 0 to 80 atomic % Pt and found that the Pt $4f_{7/2}$ BE ranged from 70.9 eV at low Mo loadings to 71.5 eV at higher loadings, and the Mo $3d_{5/2}$ BE ranged from 227.4 eV for pure Mo metal to 228.2 eV for lower Mo loadings. Interpolation of this data implies that the average alloy composition of the bimetallic catalysts in this study was roughly between a Pt_2Mo and Pt_3Mo alloy, and as Mo loading increases, the alloy composition approaches Pt_2Mo. Interpolation of the binding energy difference in Neophytides et al. [279] is the same approached used by Dietrich et al. [233] for a Pt-Mo alloy catalyst supported on Norit activated carbon, and the authors reported binding energy difference matched exactly with that reported for a Pt_3Mo alloy. EXAFS coordination numbers presented in reference [277] also suggest the presence of a Pt-rich alloy.

8.4.2 Molybdenum Oxide and Carbide Phases

The phase consisting of monometallic Mo observed via STEM showed well-distributed patches that appeared to wet the MWCNT surface. STEM line-scans also showed that the molybdenum patches were located in regions surrounding or underneath monometallic Pt or bimetallic Pt-Mo particles. Based on the XPS results, these Mo only patches were attributed to molybdenum carbide-like and molybdenum oxide phases.

Assignment of a molybdenum carbide-like phase was made based the observed Mo-Mo bond distance of 2.87 Å from XAS and deconvolution of a Mo $3d_{5/2}$ peak at 229.0 eV in the XPS spectrum. The molybdenum carbide BE of 229.0 eV from XPS would suggest the carbide was not a stoichiometric Mo_2C, but an intermediate carbide-like state that could potentially be: a Mo_xC phase, an oxycarbide phase, or a thin Mo_2C phase with a passivating oxide layer on the surface. This assignment was

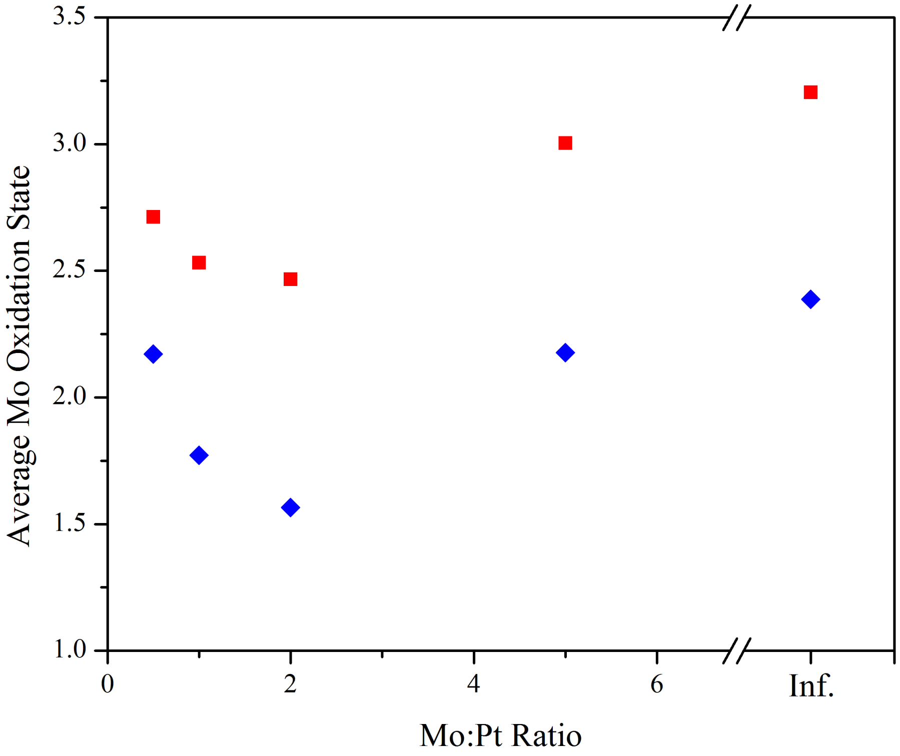

Figure 8.7. Average calculated Mo oxidation state versus increasing Mo loading for the Pt/MWCNT, Pt-Mo/MWNCT series, and Mo/MWCNT catalysts. Molybdenum in carbide-like species as 2+ is shown as red squares; molybdenum in carbide-like species as Mo^0 is shown as blue diamonds. Infinity on the x-axis represents the 2.46%Mo/MWCNT catalyst.

consistent with the fit bond distance of 2.87 Å from the EXAFS, which was consistent with an intermediate carbide-like phase as opposed to a fully formed stoichiometric Mo_2C phase (R = 2.97 Å). [281, 288]

The presence of a molybdenum oxide was also consistent with the EXAFS results, which showed Mo-O coordination representative of an oxide phase. The amount of molybdenum oxide and molybdenum carbide-like phases relative to the total Mo amount increased on the higher loading Mo catalysts. The STEM images visually show Mo patches with increasing area and frequency on the higher Mo loading samples. The Mo-Mo (Mo carbide) and Mo-O (Mo oxide) CNs from EXAFS increased with Mo loading, as the amount of molybdenum carbide and molybdenum oxide phases increased. XPS analysis trends for the change in % of the total Mo 3d envelope with increasing Mo loading showed a higher fraction of molybdenum carbide-like species (up to nominal Mo:Pt=2:1, after which it remained constant) and a lower fraction of alloyed Mo^0 (Figure 8.4). This supports the earlier discussion where as more Mo was loaded, some alloyed with Pt, and the additional Mo formed more molybdenum oxide and molybdenum carbide-like phases. The average Mo oxidation state was calculated for each catalyst based on the XPS Mo 3d region. Since the average formal charge of the molybdenum carbide-like state was unknown, the average Mo state was calculated assuming the formal charge was either 0 or 2^+. In all cases, and for either formal charge, the average oxidation state for all catalysts was between 0 and 4^+, in agreement the average oxidation states predicted by XAS. Average oxidation states are plotted in Figure 8.7.

8.5 Summary

Combined analysis of all the catalyst characterization techniques showed changes in the structures and phases present on the Pt-Mo catalysts as the Mo loading increased. The catalysts can be grouped into three categories of structure. The first category was a Pt-rich structure as seen on the Pt monometallic catalyst and the lowest Mo loading Mo-Pt = 1:0.05 catalyst. In general, as the Mo loading increased, the amount of monometallic Pt particles decreased as more Pt-Mo bimetallic particles were formed, relative to the total number of metal nanoparticles on each sample. The alloy particles were estimated to be between Pt_2Mo and Pt_3Mo in stoichiometry at the lowest Mo loadings, and approached Pt_2Mo at the higher Mo loadings.

The additional Mo at higher Mo catalyst loadings resulted in formation of more of the molybdenum oxide and molybdenum carbide-like phases. The second catalyst category, as seen on the intermediate Mo loading catalysts (Mo:Pt = 0.5:1, 1:1, and 2:1), contained a mix of Pt particles, Pt-Mo particles, molybdenum carbide-like, and molybdenum oxide phases. The third category, as seen on the highest Mo loading Mo:Pt = 5:1 catalyst, was dominated by the molybdenum carbide and molybdenum oxide phases.

9. SUMMARY AND RECOMMENDATIONS

The goal of this section is primarily to offer recommendations for future work, since each dissertation chapter already has a conclusion section. To briefly summarize the ALD alumina work, the idea that ALD is a neat, layer-by-layer synthesis method for alumina on different transition metal surfaces should be discarded. As shown by work in this dissertation, the identity of the substrate ultimately decides the chemistry and morphology of alumina films for the first few ALD cycles. The notion that initial co-reactant functional groups are absolutely necessary (in this case, -OH on Pd and Pt) should also be thrown out. Real ALD processes are much more complicated and, as is the case on transition metal surfaces, the substrate itself should be thought of as one of the precursors, as its catalytic ability determines film structure. I sincerely hope that the use of ALD to synthesize model catalyst systems continues in the Purdue catalysis center, especially as many of our labs approach state-of-the-art technology. Coupled with theoretical contributions from Prof. Jeff Greeley's research group and others, this type of research has the potential to be very powerful.

The missing piece of this dissertation, and perhaps ultimate goal of this research, is to couple the ALD-synthesized model systems with ambient pressure batch reactions, as was performed here on bare Pt catalysts for formic acid decomposition, which was shown to be a structure insensitive reaction. To complete a project of this scale in the duration of a Ph. D. is daunting, as kinetic measurements on monometallic single crystal systems are difficult as is. In this author's opinion, the best way forward is to first build upon the work done during the past several years by myself and the others that are acknowledged in this thesis by focusing on improving our ability to understand the interaction of molecules with surfaces in UHV before making the leap to ambient pressure. Immediately, I recommend that attention is focused on the Omicron cluster in the Surface Analysis Laboratory in Birck. The installation of a cooling system in the analytic chamber, new STM electronics, and an evaporation source are underway. The next technique which would add the most capability would be a fast mass spectrometer capable of measuring multiple masses simultaneously for temperature programmed experiments. Given our ability to synthesize alloys and metal oxides with ALD and soon evaporation, the combination of available techniques to probe the resulting surfaces will be very powerful. Though the specific system studied depends of course on the funding situation, we have found that ALD specifically is great for depositing sub-monolayer amounts of a material, which is often difficult by evaporation. This is an area that could differentiate our lab from the rest. Work is already underway on Pd-Zn alloys synthesized using diethyl zinc as a Zn source on Pd(111).

REFERENCES

REFERENCES

[1] A. J. Ragauskas, C. K. Williams, B. H. Davison, G. Britovsek, J. Cairney, C. A. Eckert, W. J. Frederick, J. P. Hallett, D. J. Leak, and C. L. Liotta. The path forward for biofuels and biomaterials. *Science*, 311(5760):484–489, 2006.

[2] E. L. Kunkes, D. A. Simonetti, R. M. West, J. C. Serrano-Ruiz, C. A. Grtner, and J. A. Dumesic. Catalytic conversion of biomass to monofunctional hydrocarbons and targeted liquid fuel classes. *Science*, 322(5900):417–421, 2008.

[3] S. Chu and A. Majumdar. Opportunities and challenges for a sustainable energy future. *Nature*, 488(7411):294–303, 2012.

[4] G. W. Huber, S. Iborra, and A. Corma. Synthesis of transportation fuels from biomass: Chemistry, catalysts, and engineering. *Chemical reviews*, 106(9):4044–4098, 2006.

[5] R. Agrawal and N. R. Singh. Synergistic routes to liquid fuel for a petroleum-deprived future. *AIChE Journal*, 55(7):1898–1905, 2009.

[6] D. Pimentel. Ethanol fuels: energy balance, economics, and environmental impacts are negative. *Natural resources research*, 12(2):127–134, 2003.

[7] J. Q. Bond, D. M. Alonso, D. Wang, R. M. West, and J. A. Dumesic. Integrated catalytic conversion of γ-valerolactone to liquid alkenes for transportation fuels. *Science*, 327(5969):1110–1114, 2010.

[8] C. Adams. Applied catalysis: A predictive socioeconomic history. *Topics in Catalysis*, 52(8):924–934, 2009.

[9] P. L. J. Gunter, J. W. Niemantsverdriet, F. H. Ribeiro, and G. A Somorjai. Surface science approach to modeling supported catalysts. *Catalysis Reviews*, 39(1-2):77–168, 1997.

[10] D. M. Alonso, J. Q. Bond, and J. A. Dumesic. Catalytic conversion of biomass to biofuels. *Green Chemistry*, 12(9):1493–1513, 2010.

[11] H. Mehdi, V. Fbos, R. Tuba, A. Bodor, L. T. Mika, and I. T. Horvth. Integration of homogeneous and heterogeneous catalytic processes for a multi-step conversion of biomass: From sucrose to levulinic acid, γ-valerolactone, 1,4-pentanediol, 2-methyl-tetrahydrofuran, and alkanes. *Topics in Catalysis*, 48(1-4):49–54, 2008.

[12] H. Heeres, R. Handana, D. Chunai, C. B. Rasrendra, B. Girisuta, and H. J. Heeres. Combined dehydration/(transfer)-hydrogenation of C6-sugars (D-glucose and D-fructose) to γ-valerolactone using ruthenium catalysts. *Green Chemistry*, 11(8):1247–1255, 2009.

[13] M. Ojeda and E. Iglesia. Formic acid dehydrogenation on Au-based catalysts at near-ambient temperatures. *Angewandte Chemie*, 121(26):4894–4897, 2009.

[14] F. Solymosi, Á. Koós, N. Liliom, and I. Ugrai. Production of CO-free h_2 from formic acid. a comparative study of the catalytic behavior of Pt metals on a carbon support. *Journal of Catalysis*, 279(1):213–219, 2011.

[15] N. V. Rees and R. G. Compton. Sustainable energy: A review of formic acid electrochemical fuel cells. *Journal of Solid State Electrochemistry*, 15(10):2095–2100, 2011.

[16] P. Mars, J. J. F. Scholten, and P. Zwietering. The catalytic decomposition of formic acid. *Adv. Catal*, 14:35–113, 1963.

[17] W. M. H. Sachtler and J. Fahrenfort. The catalytic decomposition of formic acid vapour on metals. In *Actes Du Deuxieme Congres International De Catalyse*, pages 831–852, 1960.

[18] P. Sabatier. Hydrognations et deshydrognations par catalyse. *Berichte der deutschen chemischen Gesellschaft*, 44(3):1984–2001, 1911.

[19] J. K. Nrskov, T. Bligaard, J. Rossmeisl, and C. H. Christensen. Towards the computational design of solid catalysts. *Nature chemistry*, 1(1):37–46, 2009.

[20] D. E. Fein and I. E. Wachs. Quantitative determination of the catalytic activity of bulk metal oxides for formic acid oxidation. *Journal of Catalysis*, 210(2):241–254, 2002.

[21] Y. Tang, C. A. Roberts, R. Perkins, and I. E. Wachs. Revisiting formic acid decomposition on bulk metallic catalysts. In *23rd North American Catalysis Society Meeting*. NAM, 2013.

[22] J. S. Yoo, F. Abild-Pedersen, J. K. Nrskov, and F. Studt. A theoretical analysis of transition metal catalysts for formic acid decomposition. *ACS Catalysis*, 2014.

[23] S. Singh, S. Li, R. Carrasquillo-Flores, A. C. Alba-Rubio, J. A. Dumesic, and M. Mavrikakis. Formic acid decomposition on au catalysts: DFT, microkinetic modeling, and reaction kinetics experiments. *AIChE Journal*, 60(4):1303–1319, 2014.

[24] N. Tian, Z.-Y. Zhou, and S.-G. Sun. Platinum metal catalysts of high-index surfaces: From single-crystal planes to electrochemically shape-controlled nanoparticles. *The Journal of Physical Chemistry C*, 112(50):19801–19817, 2008.

[25] C. Wang, H. Daimon, Y. Lee, J. Kim, and S. Sun. Synthesis of monodisperse pt nanocubes and their enhanced catalysis for oxygen reduction. *Journal of the American Chemical Society*, 129(22):6974–6975, 2007.

[26] R. D. Cortright, R. R. Davda, and J. A. Dumesic. Hydrogen from catalytic reforming of biomass-derived hydrocarbons in liquid water. *Nature*, 418(6901):964–967, 2002.

[27] R. R. Davda and J. A. Dumesic. Renewable hydrogen by aqueous-phase reforming of glucose. *Chemical Communications*, pages 36–37, 2004.

[28] J. W. Shabaker, G. W. Huber, and J. A. Dumesic. Aqueous-phase reforming of oxygenated hydrocarbons over sn-modified ni catalysts. *Journal of Catalysis*, 222(1):180–191, 2004.

[29] E. L. Kunkes, R. R. Soares, D. A. Simonetti, and J. A. Dumesic. An integrated catalytic approach for the production of hydrogen by glycerol reforming coupled with water-gas shift. *Applied Catalysis B-Environmental*, 90(3-4):693–698, 2009.

[30] P. J. Dietrich, F. G. Sollberger, M. C. Akatay, E. A. Stach, W. N. Delgass, J. T. Miller, and F. H. Ribeiro. Structural and catalytic differences in the effect of co and mo as promoters for pt-based aqueous phase reforming catalysts. *Applied Catalysis B-Environmental*, 156:236–248, 2014.

[31] R. L. Puurunen. Surface chemistry of atomic layer deposition: A case study for the trimethylaluminum/water process. *Journal of Applied Physics*, 97(12), 2005.

[32] G. N. Parsons, J. W. Elam, S. M. George, S. Haukka, H. Jeon, W. M. M. Kessels, M. Leskela, P. Poodt, M. Ritala, and S. M. Rossnagel. History of atomic layer deposition and its relationship with the american vacuum society. *Journal of Vacuum Science & Technology A*, 31(5), 2013.

[33] B. J. O'Neill, D. H. K. Jackson, J. Lee, C. Canlas, P. C. Stair, C. L. Marshall, J. W. Elam, T. F. Kuech, J. A. Dumesic, and G. W. Huber. Catalyst design with atomic layer deposition. *ACS Catalysis*, 5(3):1804–1825, 2015.

[34] M. T. Bohr, R. S. Chau, T. Ghani, and K. Mistry. The high-k solution. *IEEE Spectrum*, 44(10):29–35, 2007.

[35] A. I. Abdulagatov, Y. Yan, J. R. Cooper, Y. Zhang, Z. M. Gibbs, A. S. Cavanagh, R. G. Yang, Y. C. Lee, and S. M. George. Al_2O_3 and tio_2 atomic layer deposition on copper for water corrosion resistance. *ACS Appl. Mater. Interfaces*, 3(12):4593–4601, 2011.

[36] J. Lu, B. Fu, M. C. Kung, G. Xiao, J. W. Elam, H. H. Kung, and P. C. Stair. Coking- and sintering-resistant palladium catalysts achieved through atomic layer deposition. *Science*, 335(6073):1205–1208, 2012.

[37] N. A. Ray, R. P. Van Duyne, and P. C. Stair. Synthesis strategy for protected metal nanoparticles. *Journal of Physical Chemistry C*, 116(14):7748–7756, 2012.

[38] J. Lu, J. W. Elam, and P. C. Stair. Synthesis and stabilization of supported metal catalysts by atomic layer deposition. *Accounts of Chemical Research*, 46(8):1806–1815, 2013.

[39] B. J. O'Neill, D. H. K. Jackson, A. J. Crisci, C. A. Farberow, F. Shi, A. C. Alba-Rubio, J. Lu, P. J. Dietrich, X. Gu, C. L. Marshall, P. C. Stair, J. W. Elam, J. T. Miller, F. H. Ribeiro, P. M. Voyles, J. Greeley, M. Mavrikakis, S. L. Scott, T. F. Kuech, and J. A. Dumesic. Stabilization of copper catalysts for liquid-phase reactions by atomic layer deposition. *Angewandte Chemie International Edition*, 52(51):13808–13812, 2013.

[40] J. Rebelli, M. Detwiler, S. Ma, C. T. Williams, and J. R. Monnier. Synthesis and characterization of Au–Pd/SiO_2 bimetallic catalysts prepared by electroless deposition. *Journal of Catalysis*, 270(2):224–233, 2010.

[41] J. Lu, K.-B. Low, Y. Lei, J. A. Libera, A. Nicholls, P. C. Stair, and J. W. Elam. Toward atomically-precise synthesis of supported bimetallic nanoparticles using atomic layer deposition. *Nature Communications*, 5, 2014.

[42] H. Wang, C. Wang, H. Yan, H. Yi, and J. Lu. Precisely-controlled synthesis of Au@Pd core–shell bimetallic catalyst via atomic layer deposition for selective oxidation of benzyl alcohol. *Journal of Catalysis*, 324:59–68, 2015.

[43] F. Zaera. The surface chemistry of atomic layer depositions of solid thin films. *Journal of Physical Chemistry Letters*, 3(10):1301–1309, 2012.

[44] W.-J. Chun, K. Tomishige, M. Hamakado, Y. Iwasawa, and K. Asakura. Surface structure change of a $[Pt_4(\mu\text{-}CH_3COO)_8]/SiO_2$ catalyst active for the decomposition of formic acid. *J. Chem. Soc., Faraday Trans.*, 91(22):4161–4170, 1995.

[45] J. Block and J. Vogl. Scheinbare und wahre aktivierungswrmen beim katalytischen zerfall der ameisensure an platin. *Zeitschrift fr Elektrochemie, Berichte der Bunsengesellschaft fr physikalische Chemie*, 63(1):3–6, 1959.

[46] N. R. Avery. Adsorption of formic acid on clean and oxygen covered Pt(111). *Applications of Surface Science*, 11:774–783, 1982.

[47] M. R. Columbia, A. M. Crabtree, and P. A. Thiel. The temperature and coverage dependences of adsorbed formic acid and its conversion to formate on platinum (111). *Journal of the American Chemical Society*, 114(4):1231–1237, 1992.

[48] M. R. Columbia, A. M. Crabtree, and P. A. Thiel. Effect of CO on Pt-catalyzed decomposition of formic acid in ultrahigh vacuum. *Journal of Electroanalytical Chemistry*, 345(1):93–105, 1993.

[49] N. Abbas and R. J. Madix. Surface reaction modification: The effect of structured overlayers of sulfur on the kinetics and mechanism of the decomposition of formic acid on Pt(111). *Applications of surface science*, 16(3):424–440, 1983.

[50] M. B. Jensen, U. Myler, and P. A. Thiel. Local and collective structure of formate on Pt(111). *Surface Science Letters*, 290(1):L655–L661, 1993.

[51] P. Hofmann, S. R. Bare, N. V. Richardson, and D. A. King. Orientation of chemisorbed species from electron impact and dipole selection rules: The formate on Pt(110). *Surface Science Letters*, 133(1):L459–L464, 1983.

[52] R. J. Madix. Reaction kinetics and mechanism on metal single crystal surfaces. *Advances in Catalysis*, 29:1–53, 1980.

[53] N. Kizhakevariam and E. M. Stuve. Coadsorption of bismuth with electrocatalytic molecules: A study of formic acid oxidation on Pt(100). *Journal of Vacuum Science and Technology A*, 8(3):2557–2562, 1990.

[54] N. R. Avery. Reaction of HCOOH with a Pt(111)-O surface; identification of adsorbed monodentate formate. *Applications of Surface Science*, 14(2):149–156, 1983.

[55] M. R. Columbia, A. M. Crabtree, and P. A. Thiel. Chemical reactions between atomic oxygen and formic acid on Pt(111). *Journal of Electroanalytical Chemistry*, 351(1):207–226, 1993.

[56] W. Gao, J. A. Keith, J. Anton, and T. Jacob. Oxidation of formic acid on the pt (111) surface in the gas phase. *Dalton Transactions*, 39(36):8450–8456, 2010.

[57] R. S. Monteiro, D. Zemlyanov, J. M. Storey, and F. H. Ribeiro. Turnover rate and reaction orders for the complete oxidation of methane on a palladium foil in excess dioxygen. *Journal of Catalysis*, 199(2):291–301, 2001.

[58] A. D. Smeltz, R. B. Getman, W. F. Schneider, and F. H. Ribeiro. Coupled theoretical and experimental analysis of surface coverage effects in Pt-catalyzed NO and O $_2$ reaction to NO_2 on Pt(111). *Catalysis Today*, 136(1):84–92, 2008.

[59] S. Hagstrom, H. B. Lyon, and G. A. Somorjai. Surface structures on clean platinum (100) surface. *Physical Review Letters*, 15(11):491–493, 1965.

[60] G. R. Schoofs and J. B. Benziger. Decomposition of acetic acid monomer, acetic acid dimer, and acetic anhydride on Ni(111). *Surface science*, 143(2):359–368, 1984.

[61] A. S. Coolidge. The vapor density and some other properties of formic acid. *Journal of the American Chemical Society*, 50(8):2166–2178, 1928.

[62] C. S. Fadley. *Basic concepts of X-ray photoelectron spectroscopy*, volume 2, pages 1–156. Academic Press, New York, 1978.

[63] R. C. Millikan and K. S. Pitzer. Infrared spectra and vibrational assignment of monomeric formic acid. *The Journal of Chemical Physics*, 27(6):1305–1308, 1957.

[64] R. L. Redington. Vibrational spectra and normal coordinate analysis of isotopically labeled formic acid monomers. *Journal of Molecular Spectroscopy*, 65(2):171–189, 1977.

[65] J. E. Bertie and K. H Michaelian. The Raman spectra of gaseous formic acid -h_2 and -d_2. *The Journal of Chemical Physics*, 76(2):886–894, 1982.

[66] R. C. Millikan and K. S. Pitzer. The infrared spectra of dimeric and crystalline formic acid. *Journal of the American Chemical Society*, 80(14):3515–3521, 1958.

[67] H. Wolff, H. Mller, and E. Wolff. Structure of the OH stretching vibrational band of formic acid. *The Journal of Chemical Physics*, 64(5):2192–2196, 2008.

[68] J. F. Moulder, J. Chastain, and R. C. King. *Handbook of X-ray photoelectron spectroscopy: a reference book of standard spectra for identification and interpretation of XPS data.* Physical Electronics Eden Prairie, MN, 1995.

[69] N. M. Rodriguez, P. E. Anderson, A. Wootsch, U. Wild, R. Schlogl, and Z. Paal. XPS, EM, and catalytic studies of the accumulation of carbon on Pt black. *Journal of Catalysis*, 197(2):365–377, 2001.

[70] M. Temkin. Relation between the apparent and the true activation energy of heterogeneous reactions. *Acta physicochim. URSS*, 2:313–316, 1935.

[71] G. Ertl, M. Neumann, and K. M. Streit. Chemisorption of CO on Pt(111) surface. *Surface Science*, 64(2):393–410, 1977.

[72] P. A. Thiel, R. J. Behm, P. R. Norton, and G. Ertl. The interaction of CO and Pt(100). II. energetic and kinetic parameters. *The Journal of Chemical Physics*, 78(12):7448–7458, 1983.

[73] T. L. Silbaugh, E. M. Karp, and C. T. Campbell. Energetics of formic acid conversion to adsorbed formates on Pt(111) by transient calorimetry. *Journal of the American Chemical Society*, 136(10):3964–3971, 2014.

[74] W. D. Williams, M. Shekhar, W.-S. Lee, V. Kispersky, W. N. Delgass, F. H. Ribeiro, S. M. Kim, E. A. Stach, J. T. Miller, and L. F. Allard. Metallic corner atoms in gold clusters supported on rutile are the dominant active site during watergas shift catalysis. *Journal of the American Chemical Society*, 132(40):14018–14020, 2010.

[75] B. Hammer, O. H. Nielsen, and J. K. Norskov. Structure sensitivity in adsorption: CO interaction with stepped and reconstructed Pt surfaces. *Catalysis Letters*, 46(1-2):31–35, 1997.

[76] A. Biffis, M. Zecca, and M. Basato. Palladium metal catalysts in Heck C-C coupling reactions. *Journal of Molecular Catalysis A: Chemical*, 173(12):249–274, 2001.

[77] Á. Molnár, A. Sárkány, and M. Varga. Hydrogenation of carboncarbon multiple bonds: chemo-, regio- and stereo-selectivity. *Journal of Molecular Catalysis A: Chemical*, 173(12):185–221, 2001.

[78] H.-U. Blaser, A. Indolese, A. Schnyder, H. Steiner, and M. Studer. Supported palladium catalysts for fine chemicals synthesis. *Journal of Molecular Catalysis A: Chemical*, 173(12):3–18, 2001.

[79] G. Zhu, J. Han, D. Y. Zemlyanov, and F. H. Ribeiro. Temperature dependence of the kinetics for the complete oxidation of methane on palladium and palladium oxide. *Journal of Physical Chemistry B*, 109(6):2331–2337, 2004.

[80] H. Gabasch, E. Kleimenov, D. Teschner, S. Zafeiratos, M. Hvecker, A. Knop-Gericke, R. Schlgl, D. Zemlyanov, B. Aszalos-Kiss, K. Hayek, and B. Kltzer. Carbon incorporation during ethene oxidation on Pd(111) studied by *In Situ* X-ray photoelectron spectroscopy at 2x10^{-3} mbar. *Journal of Catalysis*, 242(2):340–348, 2006.

[81] M. A. Newton, C. Belver-Coldeira, A. Martinez-Arias, and M. Fernandez-Garcia. Dynamic *In Situ* observation of rapid size and shape change of supported Pd nanoparticles during CO/NO cycling. *Nature Materials*, 6(7):528–532, 2007.

[82] H. Feng, J. A. Libera, P. C. Stair, J. T. Miller, and J. W. Elam. Subnanometer palladium particles synthesized by atomic layer deposition. *ACS Catalysis*, 1(6):665–673, 2011.

[83] J. W. Elam, A. Zinovev, C. Y. Han, H. H. Wang, U. Welp, J. N. Hryn, and M. J. Pellin. Atomic layer deposition of palladium films on Al_2O_3 surfaces. *Thin Solid Films*, 515(4):1664–1673, 2006.

[84] H. Feng, J. W. Elam, J. A. Libera, W. Setthapun, and P. C. Stair. Palladium catalysts synthesized by atomic layer deposition for methanol decomposition. *Chemistry of Materials*, 22(10):3133–3142, 2010.

[85] J. Lu, B. Liu, J. P. Greeley, Z. Feng, J. A. Libera, Y. Lei, M. J. Bedzyk, P. C. Stair, and J. W. Elam. Porous alumina protective coatings on palladium nanoparticles by self-poisoned atomic layer deposition. *Chemistry of Materials*, 24(11):2047–2055, 2012.

[86] H. Feng, J. Lu, P. C. Stair, and J. W. Elam. Alumina over-coating on Pd nanoparticle catalysts by atomic layer deposition: Enhanced stability and reactivity. *Catalysis Letters*, 141(4):512–517, 2011.

[87] E. Rikkinen, A. Santasalo-Aarnio, S. Airaksinen, M. Borghei, V. Viitanen, J. Sainio, E. I. Kauppinen, T. Kallio, and A. O. I. Krause. Atomic layer deposition preparation of Pd nanoparticles on a porous carbon support for alcohol oxidation. *Journal of Physical Chemistry C*, 115(46):23067–23073, 2011.

[88] J. Hmlinen, M. Ritala, and M. Leskel. Atomic layer deposition of noble metals and their oxides. *Chemistry of Materials*, 26(1):786–801, 2013.

[89] D. N. Goldstein and S. M. George. Surface poisoning in the nucleation and growth of palladium atomic layer deposition with Pd(hfac)$_2$ and formalin. *Thin Solid Films*, 519(16):5339–5347, 2011.

[90] J. Lu and P. C. Stair. Nano/subnanometer pd nanoparticles on oxide supports synthesized by AB-type and low-temperature ABC-type atomic layer deposition: Growth and morphology. *Langmuir*, 26(21):16486–16495, 2010.

[91] M. J. Weber, A. J. M. Mackus, M. A. Verheijen, V. Longo, A. A. Bol, and W. M. M. Kessels. Atomic layer deposition of high-purity palladium films from Pd(hfac)$_2$ and H_2 and O_2 Plasmas. *Journal of Physical Chemistry C*, 118(16):8702–8711, 2014.

[92] V. R. Anderson, N. Leick, J. W. Clancey, K. E. Hurst, K. M. Jones, A. C. Dillon, and S. M. George. Atomic layer deposition of platinum nanoparticles on titanium oxide and tungsten oxide using platinum(II) hexafluoroacetylacetonate and formalin as the reactants. *Journal of Physical Chemistry C*, 118(17):8960–8970, 2014.

[93] J. E. Parmeter. Copper CVD chemistry on a reactive substrate: Cu(hfac)$_2$ and hfacH on Pt(111). *Journal of Physical Chemistry*, 97(44):11530–11541, 1993.

[94] J. S. Mulley, R. A. Bennett, and V. R. Dhanak. Adsorption, orientation and thermal decomposition of copper(II) hexafluoroacetylacetonate on rutile TiO_2(110). *Surface Science*, 602(18):2967–2974, 2008.

[95] Y. Lei, J. Lu, H. Zhao, B. Liu, K.-B. Low, T. Wu, J. A. Libera, J. P. Greeley, P. J. Chupas, J. T. Miller, and J. W. Elam. Resolving precursor deligation, surface species evolution, and nanoparticle nucleation during palladium atomic layer deposition. *Journal of Physical Chemistry C*, 117(21):11141–11148, 2013.

[96] I. Horcas, R. Fernandez, J. M. Gomez-Rodriguez, J. Colchero, J. Gomez-Herrero, and A. M. Baro. WSXM: A software for scanning probe microscopy and a tool for nanotechnology. *Review of Scientific Instruments*, 78(1):013705 1–8, 2007.

[97] U. Diebold, M. Li, O. Dulub, E. L. D. Hebenstreit, and W. Hebenstreit. The relationship between bulk and surface properties of rutile TiO_2(110). *Surface Review and Letters*, 7(5-6):613–617, 2000.

[98] J. C. Yu, J. Yu, W. Ho, Z. Jiang, and L. Zhang. Effects of F^- doping on the photocatalytic activity and microstructures of nanocrystalline TiO_2 powders. *Chemistry of Materials*, 14(9):3808–3816, 2002.

[99] H. Gabasch, W. Unterberger, K. Hayek, B. Kloetzer, E. Kleimenov, D. Teschner, S. Zafeiratos, M. Haevecker, A. Knop-Gericke, R. Schloegl, J. Han, F. H. Ribeiro, B. Aszalos-Kiss, T. Curtin, and D. Zemlyanov. *In situ* XPS study of Pd(111) oxidation at elevated pressure, part 2: Palladium oxidation in the 10^{-1} mbar range. *Surface Science*, 600(15):2980–2989, 2006.

[100] W. B. Lin, R. G. Nuzzo, and G. S. Girolami. Mechanistic studies of palladium thin film growth from palladium(II) beta-diketonates. 2. Kinetic analysis of the transmetalation reaction of bis(hexafluoroacetylacetonato)palladium(II) on copper surfaces. *Journal of the American Chemical Society*, 118(25):5988–5996, 1996.

[101] G. Beamson and D. Briggs. *High Resolution XPS of Organic Polymers: The Scienta ESCA300 Database.* Wiley, New York, NY, 1992.

[102] S. L. Cohen, M. Liehr, and S. Kasi. Mechanisms of copper chemical vapor deposition. *Applied Physics Letters*, 60(1):50–52, 1992.

[103] S. L. Cohen, M. Liehr, and S. Kasi. Selectivity in copper chemical vapor deposition. *Applied Physics Letters*, 60(13):1585–1587, 1992.

[104] V. M. Donnelly and M. E. Gross. Copper metalorganic chemical vapor deposition reactions of hexafluoroacetylacetonate Cu(I) vinyltrimethylsilane and bis (hexafluoroacetylacetonate) Cu(II) adsorbed on titanium nitride. *Journal of Vacuum Science and Technology A*, 11(1):66–77, 1993.

[105] W. B. Lin, B. C. Wiegand, R. G. Nuzzo, and G. S. Girolami. Mechanistic studies of palladium thin film growth from palladium(II) beta-diketonates. 1. Spectroscopic studies of the reactions of bis(hexafluoroacetylacetonato)palladium(II) on copper surfaces. *Journal of the American Chemical Society*, 118(25):5977–5987, 1996.

[106] T. T. P. Cheung. Lineshape studies of the X-ray photoemission of small metal clusters. *Surface Science*, 127(2):L129–L134, 1983.

[107] U. Diebold. The surface science of titanium dioxide. *Surface Science Reports*, 48(5-8):53–229, 2003.

[108] J. H. Horton, J. G. Shapter, T. Cheng, W. N. Lennard, and P. R. Norton. STM investigation of a Cu organometallic complex adsorbed on Si(111)-(7 7). *Surface Science*, 375(23):171–182, 1997.

[109] D. G. Rayner, J. S. Mulley, and R. A. Bennett. Copper deposition on TiO_2 from copper(II) hexafluoroacetylacetonate. *Journal of Vacuum Science and Technology A*, 31(1):01A121 1–5, 2012.

[110] A. R. Siedle, R. A. Newmark, and L. H. Pignolet. Structure of palladium bis(hexafluoroacetylacetonate) and the systematics of its acid-base chemistry. *Inorganic Chemistry*, 22(16):2281–2286, 1983.

[111] R. A. Bennett, P. Stone, and M. Bowker. Pd nanoparticle enhanced re-oxidation of non-stoichiometric TiO_2: STM imaging of spillover and a new form of SMSI. *Catalysis Letters*, 59(2-4):99–105, 1999.

[112] V. Cal, A. Nacci, A. Monopoli, and P. Cotugno. Heck reactions with palladium nanoparticles in ionic liquids: Coupling of aryl chlorides with deactivated olefins. *Angewandte Chemie International Edition*, 48(33):6101–6103, 2009.

[113] W. D. Williams, L. Bollmann, J. T. Miller, W. N. Delgass, and F. H. Ribeiro. Effect of molybdenum addition on supported platinum catalysts for the water-gas shift reaction. *Applied Catalysis B*, 125(0):206–214, 2012.

[114] S. S. Mulla, N. Chen, L. Cumaranatunge, G. E. Blau, D. Y. Zemlyanov, W. N. Delgass, W. S. Epling, and F. H. Ribeiro. Reaction of NO and O_2 to N_2 on Pt: Kinetics and catalyst deactivation. *Journal of Catalysis*, 241(2):389–399, 2006.

[115] P. J. Berlowitz, C. H. F. Peden, and D. W. Goodman. Kinetics of carbon monoxide oxidation on single-crystal palladium, platinum, and iridium. *Journal of Physical Chemistry*, 92(18):5213–5221, 1988.

[116] T. Hbert, L. Boon-Brett, G. Black, and U. Banach. Hydrogen sensors a review. *Sensors and Actuators, B*, 157(2):329–352, 2011.

[117] L. K. Randeniya, P. J. Martin, and A. Bendavid. Detection of hydrogen using multi-walled carbon-nanotube yarns coated with nanocrystalline Pd and Pd/Pt layered structures. *Carbon*, 50(5):1786–1792, 2012.

[118] W. Li, C. Liang, W. Zhou, J. Qiu, Z. Zhou, G. Sun, and Q. Xin. Preparation and characterization of multiwalled carbon nanotube-supported platinum for cathode catalysts of direct methanol fuel cells. *Journal of Physical Chemistry B*, 107(26):6292–6299, 2003.

[119] X. Liang, J. Li, M. Yu, C. N. McMurray, J. L. Falconer, and A. W. Weimer. Stabilization of supported metal nanoparticles using an ultrathin porous shell. *ACS Catalysis*, 1(10):1162–1165, 2011.

[120] B. Fu, J. Lu, P. C. Stair, G. Xiao, M. C. Kung, and H. H. Kung. Oxidative dehydrogenation of ethane over alumina-supported Pd catalysts. Effect of alumina overlayer. *Journal of Catalysis*, 297(0):289–295, 2013.

[121] M. Leskel and M. Ritala. Atomic layer deposition (ALD): From precursors to thin film structures. *Thin Solid Films*, 409(1):138–146, 2002.

[122] M. D. Detwiler, A. Gharachorlou, L. Mayr, X.-K. Gu, B. Liu, J. P. Greeley, W. N. Delgass, F. H. Ribeiro, and D. Zemlyanov. Reaction of trimethylaluminum with water on Pt(111) and Pd(111) from 10^{-5} to 10^{-1} millibar. *Journal of Physical Chemistry C*, 119(5):2399–2411, 2014.

[123] J. Lu, B. Liu, N. P. Guisinger, P. C. Stair, J. P. Greeley, and J. W. Elam. First-principles predictions and *in Situ* experimental validation of alumina atomic layer deposition on metal surfaces. *Chemistry of Materials*, 26:6752–6761, 2014.

[124] A. C. Alba-Rubio, B. J. ONeill, F. Shi, C. Akatay, C. Canlas, T. Li, R. Winans, J. W. Elam, E. A. Stach, P. M. Voyles, and J. A. Dumesic. Pore structure and bifunctional catalyst activity of overlayers applied by atomic layer deposition on copper nanoparticles. *ACS Catalysis*, pages 1554–1557, 2014.

[125] J. M. Gomez-Rodriguez, A. M. Baro, L. Vazquez, R. C. Salvarezza, J. M. Vara, and A. J. Arvia. Fractal surfaces of gold and platinum electrodeposits: Dimensionality determination by scanning tunneling microscopy. *Journal of Physical Chemistry*, 96(1):347–350, 1992.

[126] J. P. Perdew and Y. Wang. Accurate and simple analytic representation of the electron-gas correlation energy. *Physical Review B: Condensed Matter*, 45(23):13244–13249, 1992.

[127] P. E. Blchl. Projector augmented-wave method. *Physical Review B: Condensed Matter*, 50(24):17953–17979, 1994.

[128] G. Henkelman, B. P. Uberuaga, and H. Jnsson. A climbing image nudged elastic band method for finding saddle points and minimum energy paths. *Journal of Chemical Physics*, 113(22):9901–9904, 2000.

[129] L. Ley, F. R. Mcfeely, S. P. Kowalczyk, J. G. Jenkin, and D. A. Shirley. Many-body effects in X-Ray photoemission from magnesium. *Physical Review B*, 11(2):600–612, 1975.

[130] I. Olefjord, H. J. Mathieu, and P. Marcus. Intercomparison of surface analysis of thin aluminium oxide films. *Surface and Interface Analysis*, 15(11):681–692, 1990.

[131] V. Matoln, I. Stará, N. Tsud, and V. Johánek. XPS and TDS study of CO interaction with PdAlO$_x$ systems. *Progress in Surface Science*, 67(1):167–181, 2001.

[132] V. Johánek, N. Tsud, V. Matoln, and I. Stará. TPD and XPS study of the CO adsorption on transition-SP metal systems: Pd and Al. *Vacuum*, 63(1):15–22, 2001.

[133] V. Johánek, I. Stara, and V. Matoln. Role of PdAl bimetallic interaction in CO adsorption and catalytic properties of bulk PdAl alloy: XPS, ISS, TDS, and SIMS study. *Surface science*, 507:92–98, 2002.

[134] V. Shutthanandan, A. A. Saleh, N. R. Shivaparan, and R. J. Smith. Growth of ultrathin pd films on Al(001) surfaces. *Surface science*, 350(1):11–20, 1996.

[135] K. Wilson, J. Brake, A. F. Lee, and R. M. Lambert. Growth morphology and electronic properties of ultrathin Al films on Pt(111). *Surface Science*, 387(13):257–268, 1997.

[136] E. G. Colgan. Phase formation and dissociation in the thin-film Pt/Al system. *Journal of Applied Physics*, 62(4):1224–1231, 1987.

[137] A. F. Lee, K. Wilson, and R. M. Lambert. Structure and stability of the platinum/aluminium interface: Alloying and substrate vacancy formation on Pt111/Al. *Surface Science*, 446(12):145–152, 2000.

[138] R. C. Baetzold, G. Apai, E. Shustorovich, and R. Jaeger. Surface core-level shifts for Pt single-crystal surfaces. *Physical Review B*, 26(8):4022–4027, 1982.

[139] D. Teschner, E. Vass, M. Havecker, S. Zafeiratos, P. Schnorch, H. Sauer, A. Knop-Gericke, R. Schloegl, M. Chamam, A. Wootsch, A. S. Canning, J. J. Gamman, S. D. Jackson, J. McGregor, and L. F. Gladden. Alkyne hydrogenation over pd catalysts: A new paradigm. *Journal of Catalysis*, 242(1):26–37, 2006.

[140] P. M. A. Sherwood. Introduction to studies of aluminum and its compounds by XPS. *Surface Science Spectra*, 5(1):1–3, 1998.

[141] I. Matolinova, V. Johanek, T. Skala, K. Veltruska, and V. Matolin. XPS, TDS and static SIMS studies of binary Pd/Al system properties: Correlation between Pd-Al bimetallic interaction and CO adsorption. *Applied Surface Science*, 245(1-4):87–93, 2005.

[142] J. J. Hill, A. A. Aquino, C. P. A. Mulcahy, N. Harwood, A. C. Jones, and T. S. Jones. The adsorption and thermal decomposition of trimethylaluminium and dimethylaluminium hydride on GaAs(100). *Surface Science*, 340(12):49–56, 1995.

[143] A. A. Aquino, C. P. A. Mulcahy, and T. S. Jones. Spectroscopic identification of the reaction intermediates in the thermal decomposition of trimethylindium at GaAs(100) surfaces. *Surface Science*, 344(3):L1231–L1238, 1995.

[144] M. Y. Smirnov, V. V. Gorodetskii, A. R. Cholach, and D. Y. Zemlyanov. Hydrogenation of isolated atoms and small clusters of carbon on Pt(111) surface: HREELS/TDS studies. *Surface Science*, 311(3):308–321, 1994.

[145] D. H. Fairbrother, X. D. Peng, R. Viswanathan, P. C. Stair, M. Trenary, and J. Fan. Carbon-carbon coupling of methyl groups on Pt(111). *Surface Science Letters*, 285(12):L455–L460, 1993.

[146] S. Kvisle and E. Rytter. Infrared matrix isolation spectroscopy of trimethylgallium, trimethylaluminium and triethylaluminium. *Spectrochimica Acta, Part A*, 40(10):939–951, 1984.

[147] C. Soto, R. Wu, D. W. Bennett, and W. T. Tysoe. Infrared spectroscopy of trimethylaluminum and dimethylaluminum chloride adsorbed on alumina. *Chemistry of Materials*, 6(10):1705–1711, 1994.

[148] C. Soto and W. T. Tysoe. The reaction pathway for the growth of alumina on high surface area alumina and in ultrahigh vacuum by a reaction between trimethyl aluminum and water. *Journal of Vacuum Science and Technology A*, 9(5):2686–2695, 1991.

[149] W. Cabrera, M. D. Halls, I. M. Povey, and Y. J. Chabal. Surface oxide characterization and interface evolution in atomic layer deposition of Al_2O_3 on InP(100) studied by *in Situ* infrared spectroscopy. *Journal of Physical Chemistry C*, 118(11):5862–5871, 2014.

[150] L. L. Kesmodel and J. A. Gates. Ethylene adsorption and reaction on Pd(111): An angle-dependent EELS analysis. *Surface Science Letters*, 111(3):L747–L754, 1981.

[151] M. Sock, A. Eichler, S. Surnev, J. N. Andersen, B. Kltzer, K. Hayek, M. G. Ramsey, and F. P. Netzer. High-resolution electron spectroscopy of different adsorption states of ethylene on Pd(111). *Surface Science*, 545(12):122–136, 2003.

[152] A. M. Bar and H. Ibach. Thermal evolution and decomposition of ethylene on Pt(111). *Journal of Chemical Physics*, 74(7):4194–4199, 1981.

[153] H. Ibach and S. Lehwald. Identification of surface radicals by vibration spectroscopy: Reactions of C_2H_2, C_2H_4, and H_2 on Pt (111). *Journal of Vacuum Science and Technology*, 15(2):407–415, 1978.

[154] Y. Zhou, W. M. Feng, M. A. Henderson, B. Roop, and J. M. White. Surface photochemistry: Products retained on platinum (111) during photolysis of adsorbed methyl bromide. *Journal of the American Chemical Society*, 110(13):4447–4448, 1988.

[155] M. A. Henderson, G. E. Mitchell, and J. M. White. The chemisorption of methyl halides (Cl, Br and I) on Pt(111). *Surface Science*, 184(12):L325–L331, 1987.

[156] F. Solymosi and G. Klivnyi. HREELS study of CH_3I and CH_3 adsorbed on Rh(111) surface. *Journal of Electron Spectroscopy and Related Phenomena*, 6465(0):499–506, 1993.

[157] H. S. Kato, J. Noh, M. Hara, and M. Kawai. An HREELS study of alkanethiol self-assembled monolayers on Au(111). *Journal of Physical Chemistry B*, 106(37):9655–9658, 2002.

[158] M. Y. Smirnov, N. R. Gall, A. R. Cholach, V. V. Gorodetskii, A. Y. Tontegode, E. V. Rut'kov, and D. Y. Zemlyanov. HREELS study and catalytic significance of low-temperature interaction of isolated carbon atoms with hydrogen on Pt(111). *Catalysis Letters*, 8(1):101–106, 1991.

[159] D. N. Goldstein, J. A. McCormick, and S. M. George. Al_2O_3 atomic layer deposition with trimethylaluminum and ozone studied by *In Situ* transmission FTIR spectroscopy and quadrupole mass spectrometry. *Journal of Physical Chemistry C*, 112(49):19530–19539, 2008.

[160] J. L. Eilertsen, E. Rytter, and M. Ystenes. *In situ* FTIR spectroscopy during addition of trimethylaluminium (TMA) to methylaluminoxane (MAO) shows no formation of MAO-TMA compounds. *Vibrational Spectroscopy*, 24(2):257–264, 2000.

[161] M. Kaltchev, A. W. Thompson, and W. T. Tysoe. Reflection-absorption infrared spectroscopy of ethylene on palladium (111) at high pressure. *Surface Science*, 391(13):145–149, 1997.

[162] J. A. Gates and L. L. Kesmodel. Thermal evolution of acetylene and ethylene on Pd(111). *Surface Science*, 124(1):68–86, 1983.

[163] M. Gajdo, A. Eichler, and J. Hafner. CO adsorption on close-packed transition and noble metal surfaces: trends from ab initio calculations. *Journal of Physics: Condensed Matter*, 16(8):1141, 2004.

[164] L. L. Kesmodel, L. H. Dubois, and G. A. Somorjai. Dynamical LEED study of C_2H_2 and C_2H_4 chemisorption on Pt(111): Evidence for the ethylidyne group. *Chemical Physics Letters*, 56(2):267–271, 1978.

[165] Y. Zhou, M. A. Henderson, and J. M. White. Interaction of trimethylaluminum with Ru(001). *Surface Science*, 221(1-2):160–182, 1989.

[166] R. Batabyal, J. C. Mahato, D. Das, A. Roy, and B. N. Dev. Self-organized one-atom thick fractal nanoclusters via field-induced atomic transport. *Journal of Applied Physics*, 114(6):064304, 2013.

[167] T. A. Land, T. Michely, R. J. Behm, J. C. Hemminger, and G. Comsa. Direct observation of surface reactions by scanning tunneling microscopy: Ethyleneethylidynecarbon particlesgraphite on Pt(111). *Journal of Chemical Physics*, 97(9):6774–6783, 1992.

[168] T. A. Witten and L. M. Sander. Diffusion-limited aggregation. *Physical Review B: Condensed Matter*, 27(9):5686–5697, 1983.

[169] Z. Zhang and M. G. Lagally. Atomistic processes in the early stages of thin-film growth. *Science*, 276(5311):377–383, 1997.

[170] H. Brune, H. Rder, C. Boragno, and K. Kern. Microscopic view of nucleation on surfaces. *Physical Review Letters*, 73(14):1955–1958, 1994.

[171] D. Stacchiola and W. T. Tysoe. The kinetics of ethylidyne formation from ethylene on Pd(111). *Journal of Physical Chemistry C*, 113(19), 2009.

[172] X. L. Zhou and J. M. White. Interactions of trimethyl gallium and trimethyl aluminum with Ni(111) - a TPD, SIMS and AES study. *Surface Science*, 273(3):322–340, 1992.

[173] J. C. Wenger, M. R. S. McCoustra, and M. A. Chesters. An infrared study of the chemistry of methyl species on Pt(111) formed by the decomposition of dimethylmercury. *Surface Science*, 360(1-3):93–103, 1996.

[174] M. Ritala and M. Leskel. *Atomic layer deposition*, volume 1, book section 4, pages 103–159. Academic Press: San Diego, CA, 2002.

[175] B. S. Lim, A. Rahtu, and R. G Gordon. Atomic layer deposition of transition metals. *Nature Materials*, 2(11):749–754, 2003.

[176] S. M. George. Atomic layer deposition: An overview. *Chemical Reviews*, 110(1):111–131, 2009.

[177] T. Suntola. Atomic layer epitaxy. *Thin Solid Films*, 216(1):84–89, 1992.

[178] J. Kernen, A. Auroux, S. Ek, and L. Niinist. Preparation, characterization and activity testing of vanadia catalysts deposited onto silica and alumina supports by atomic layer deposition. *Applied Catalysis A*, 228(1):213–225, 2002.

[179] S. T. Christensen, H. Feng, J. L. Libera, N. Guo, J. T. Miller, P. C. Stair, and J. W Elam. Supported RuPt bimetallic nanoparticle catalysts prepared by atomic layer deposition. *Nano letters*, 10(8):3047–3051, 2010.

[180] J. Lu, K. M. Kosuda, R. P. Van Duyne, and P. C. Stair. Surface acidity and properties of TiO_2/SiO_2 catalysts prepared by atomic layer deposition: UVvisible diffuse reflectance, DRIFTS, and visible Raman spectroscopy studies. *Journal of Physical Chemistry C*, 113(28):12412–12418, 2009.

[181] J. A. Rodrguez and J. Hrbek. Inverse oxide/metal catalysts: A versatile approach for activity tests and mechanistic studies. *Surface Science*, 604(3):241–244, 2010.

[182] A. C. Dillon, A. W. Ott, J. D. Way, and S. M. George. Surface chemistry of Al_2O_3 deposition using $Al(CH_3)_3$ and H_2O in a binary reaction sequence. *Surface Science*, 322(1):230–242, 1995.

[183] M. D. Groner, F. H. Fabreguette, J. W. Elam, and S. M. George. Low-temperature Al_2O_3 atomic layer deposition. *Chemistry of Materials*, 16(4):639–645, 2004.

[184] J. W. Elam, M. D. Groner, and S. M. George. Viscous flow reactor with quartz crystal microbalance for thin film growth by atomic layer deposition. *Review of Scientific Instruments*, 73(8):2981–2987, 2002.

[185] M. Juppo, A. Rahtu, M. Ritala, and M. Leskel. *In situ* mass spectrometry study on surface reactions in atomic layer deposition of Al_2O_3 thin films from trimethylaluminum and water. *Langmuir*, 16(8):4034–4039, 2000.

[186] M. Tallarida and D. Schmeisser. *In situ* ALD experiments with synchrotron radiation photoelectron spectroscopy. *Semiconductor Science and Technology*, 27(7):074010, 2012.

[187] M. Salmeron and R. Schlgl. Ambient pressure photoelectron spectroscopy: A new tool for surface science and nanotechnology. *Surface Science Reports*, 63(4):169–199, 2008.

[188] C. J. Powell and A. Jablonski. *NIST Electron Effective-Attenuation-Length Database - Version 1.3.* National Institute of Standards and Technology, Gaithersburg, MD, 2011.

[189] G. Kresse and J. Furthmller. Efficiency of ab-initio total energy calculations for metals and semiconductors using a plane-wave basis set. *Computational Materials Science*, 6(1):15–50, 1996.

[190] G. Kresse and J. Furthmller. Efficient iterative schemes for ab initio total-energy calculations using a plane-wave basis set. *Physical Review B: Condensed Matter*, 54(16):11169–11186, 1996.

[191] H. J. Monkhorst and J. D. Pack. Special points for Brillouin-zone integrations. *Physical Review B: Condensed Matter*, 13(12):5188–5192, 1976.

[192] H. Ogasawara, B. Brena, D. Nordlund, M. Nyberg, A. Pelmenschikov, L. G. M. Pettersson, and A. Nilsson. Structure and bonding of water on Pt(111). *Physical Review Letters*, 89(27):276102, 2002.

[193] J. J. Yeh and I. Lindau. Atomic subshell photoionization cross sections and asymmetry parameters: $1 \leq Z \leq 103$. *Atomic Data and Nuclear Data Tables*, 32(1):1–155, 1985.

[194] S. Tanuma, C. J. Powell, and D. R. Penn. Calculations of electron inelastic mean free paths. 2. Data for 27 elements over the 50-2000 eV range. *Surface and Interface Analysis*, 17(13):911–926, 1991.

[195] D. Briggs and John T. Grant. *Surface analysis by Auger and X-ray photoelectron spectroscopy.* IM Publications and SurfaceSpectra Limited, Chichester, 2003.

[196] T. Fuhrmann, M. Kinne, C. M. Whelan, J. F. Zhu, R. Denecke, and H. P. Steinruck. Vibrationally resolved *in situ* XPS study of activated adsorption of methane on Pt(111). *Chemical Physics Letters*, 390(1-3):208–213, 2004.

[197] M. R. Alexander, G. E. Thompson, and G. Beamson. Characterization of the oxide/hydroxide surface of aluminium using X-ray photoelectron spectroscopy: A procedure for curve fitting the O 1s core level. *Surface and Interface Analysis*, 29(7):468–477, 2000.

[198] C. F. Mcconville, D. L. Seymour, D. P. Woodruff, and S. Bao. Synchrotron radiation core level photoemission investigation of the initial-stages of oxidation of Al(111). *Surface Science*, 188(1-2):1–14, 1987.

[199] A. Mulligan, V. Dhanak, and M. Kadodwala. A high-resolution photoemission study of nanoscale aluminum oxide films on NiAl(110). *Langmuir*, 21(18):8312–8318, 2005.

[200] A. Nylund and I. Olefjord. Surface-analysis of oxidized aluminum. 1. Hydration of Al_2O_3 and decomposition of $Al(OH)_3$ in a vacuum as studied by ESCA. *Surface and Interface Analysis*, 21(5):283–289, 1994.

[201] J. T. Kloprogge, L. V. Duong, B. J. Wood, and R. L. Frost. XPS study of the major minerals in bauxite: Gibbsite, bayerite and (pseudo-)boehmite. *Journal of Colloid and Interface Science*, 296(2):572–576, 2006.

[202] J. R. Lindsay, H. J. Rose, W. E. Swartz, P. H. Watts, and K. A. Rayburn. X-Ray photoelectron spectra of aluminum oxides - structural effects on chemical-shift. *Applied Spectroscopy*, 27(1):1–5, 1973.

[203] A. Bianconi, R. Z. Bachrach, S. B. M. Hagstrom, and S. A. Flodstrom. Al-Al_2O_3 interface study using surface soft X-Ray absorption and photoemission spectroscopy. *Physical Review B: Condensed Matter*, 19(6):2837–2843, 1979.

[204] K. Kovacs, I. V. Perczel, V. K. Josepovits, G. Kiss, F. Reti, and P. Deak. *In situ* surface analytical investigation of the thermal oxidation of Ti-Al intermetallics up to 1000C. *Applied Surface Science*, 200(1-4):185–195, 2002.

[205] D. Zemlyanov, B. Aszalos-Kiss, E. Kleimenov, D. Teschner, S. Zafeiratos, M. Havecker, A. Knop-Gericke, R. Schlogl, H. Gabasch, W. Unterberger, K. Hayek, and B. Koltzer. *In situ* XPS study of Pd(111) oxidation. Part 1: 2D oxide formation in 10^{-3} mbar o_2. *Surface Science*, 600(5):983–994, 2006.

[206] M. Morkel, V. V. Kaichev, G. Rupprechter, H. J. Freund, I. P. Prosvirin, and V. I. Bukhtiyarov. Methanol dehydrogenation and formation of carbonaceous overlayers on Pd(111) studied by high-pressure SFG and XPS spectroscopy. *Journal of Physical Chemistry B*, 108(34):12955–12961, 2004.

[207] A. Gharachorlou, M. D. Detwiler, L. Mayr, X.-K. Gu, J. P. Greeley, R. G. Reifenberger, W. N. Delgass, F. H. Ribeiro, and D. Y. Zemlyanov. The surface chemistry of trimethylaluminum on pd(111) and pt(111). Submitted.

[208] J. Kelly, C. Parks, J. Demarest, J. Li, and C. Penny. *Microstructure Evolution of Copper in Nanoscale Interconnect Features*, book section 6, pages 115–130. Nanostructure Science and Technology. Springer New York, 2014.

[209] Y. Ma, D. R. Evans, T. Nguyen, Y. Ono, and S. T. Hsu. Fabrication and characterization of sub-quarter-micron MOSFETs with a copper gate electrode. *Electron Device Letters, IEEE*, 20(5):254–255, 1999.

[210] A. A. Gokhale, J. A. Dumesic, and M. Mavrikakis. On the mechanism of low temperature water gas shift reaction on copper. *Journal of the American Chemical Society*, 130(4):1402–1414, 2008.

[211] X.-K. Gu and W.-X. Li. First-principles study on the origin of the different selectivities for methanol steam reforming on Cu(111) and Pd(111). *The Journal of Physical Chemistry C*, 114(49):21539–21547, 2010.

[212] M. L. Chang, T. C. Cheng, M. C. Lin, H. C. Lin, and M. J. Chen. Improvement of oxidation resistance of copper by atomic layer deposition. *Applied Surface Science*, 258(24):10128–10134, 2012.

[213] S. C. Riha, S. Jin, S. V. Baryshev, E. Thimsen, G. P. Wiederrecht, and A. B. F. Martinson. Stabilizing Cu_2S for photovoltaics one atomic layer at a time. *ACS Applied Materials and Interfaces*, 5(20):10302–10309, 2013.

[214] T. Matsumoto, R. A. Bennett, P. Stone, T. Yamada, K. Domen, and M. Bowker. Scanning tunneling microscopy studies of oxygen adsorption on Cu(111). *Surface Science*, 471(13):225–245, 2001.

[215] S. D. Elliott and J. C. Greer. Simulating the atomic layer deposition of alumina from first principles. *Journal of Materials Chemistry*, 14(21):3246–3250, 2004.

[216] B. J. Hinch and L. H. Dubois. Stable and metastable phases of water adsorbed on Cu(111). *Journal of Chemical Physics*, 96(4):3262–3268, 1992.

[217] S. Yamamoto, K. Andersson, H. Bluhm, G. Ketteler, D. E. Starr, T. Schiros, H. Ogasawara, L. G. M. Pettersson, M. Salmeron, and A. Nilsson. Hydroxyl-induced wetting of metals by water at near-ambient conditions. *Journal of Physical Chemistry C*, 111(22):7848–7850, 2007.

[218] R. L. Puurunen, M. Lindblad, A. Root, and A. O. I. Krause. Successive reactions of gaseous trimethylaluminium and ammonia on porous alumina. *Physical Chemistry Chemical Physics*, 3(6):1093–1102, 2001.

[219] F. Jensen, F. Besenbacher, E. Lgsgaard, and I. Stensgaard. Oxidation of Cu(111): Two new oxygen induced reconstructions. *Surface Science*, 259(3):L774–L780, 1991.

[220] F. Jensen, F. Besenbacher, and I. Stensgaard. Two new oxygen induced reconstructions on Cu(111). *Surface Science*, 269270(0):400–404, 1992.

[221] J. Ghijsen, L. H. Tjeng, J. Vanelp, H. Eskes, J. Westerink, G. A. Sawatzky, and M. T. Czyzyk. Electronic structure of Cu_2O and CuO. *Physical Review B*, 38(16):11322–11330, 1988.

[222] M. B. Lee, J. H. Lee, B. G. Frederick, and N. V. Richardson. Surface structure of ultra-thin Al_2O_3 films on metal substrates. *Surface Science*, 448(23):L207–L212, 2000.

[223] M. Frank, K. Wolter, N. Magg, M. Heemeier, R. Khnemuth, M. Bumer, and H.-J. Freund. Phonons of clean and metal-modified oxide films: An infrared and HREELS study. *Surface Science*, 492(3):270–284, 2001.

[224] J.-L. Lin and B. E. Bent. Iodomethane dissociation on Cu(111): Bonding and chemistry of adsorbed methyl groups. *Journal of Vacuum Science and Technology A*, 10(4):2202–2209, 1992.

[225] C. Chao-Ming and B. E. Bent. Methyl radical adsorption on Cu(111): Bonding, reactivity, and the effect of coadsorbed iodine. *Surface Science*, 279(12):79–88, 1992.

[226] M. Milojevic, R. Contreras-Guerrero, M. Lopez-Lopez, J. Kim, and R. M. Wallace. Characterization of the ”clean-up” of the oxidized Ge(100) surface by atomic layer deposition. *Appl. Phys. Lett.*, 95(21):212902/1–212902/3, 2009.

[227] C. L. Hinkle, A. M. Sonnet, E. M. Vogel, S. McDonnell, G. J. Hughes, M. Milojevic, B. Lee, F. S. Aguirre-Tostado, K. J. Choi, H. C. Kim, J. Kim, and R. M. Wallace. GaAs interfacial self-cleaning by atomic layer deposition. *Appl. Phys. Lett.*, 92(7):071901/1–071901/3, 2008.

[228] T. Ishiguro, A. Kitazawa, N. Mizutani, and M. Kato. Single crystal growth and crystal structure refinement of $CuAlO_2$. *Journal of Solid State Chemistry*, 40(2):170–174, 1981.

[229] C. Maurel, M. Abel, M. Koudia, F. Bocquet, and L. Porte. Pit formation and segregation effects during Cu thin-film growth on Ag(111). *Surface Science*, 596(1-3):45–52, 2005.

[230] Y. Xu and M. Mavrikakis. Adsorption and dissociation of o_2 on Cu(111). Thermochemistry, reaction barrier and the effect of strain. *Surf. Sci.*, 494(2):131–144, 2001.

[231] M. Choi, J. L. Lyons, A. Janotti, and C. G. Van de Walle. Impact of carbon and nitrogen impurities in high-κ dielectrics on metal-oxide-semiconductor devices. *Appl. Phys. Lett.*, 102(14):142902/1–142902/4, 2013.

[232] H. E. Kluksdahl. United States Patent 3,415,737 A. Reforming a sulfur-free naphtha with a platinum-rhenium catalyst, 1968.

[233] P. J. Dietrich, R. J. Lobo-Lapidus, T. Wu, A. Sumer, M. C. Akatay, B. R. Fingland, N. Guo, J. A. Dumesic, C. L. Marshall, E. Stach, J. Jellinek, W. N. Delgass, F. H. Ribeiro, and J. T. Miller. Aqueous phase glycerol reforming by PtMo bimetallic nano-particle catalyst: Product selectivity and structural characterization. *Topics in Catalysis*, 55(1-2):53–69, 2012.

[234] L. Zhang, A. M. Karim, M. H. Engelhard, Z. H. Wei, D. L. King, and Y. Wang. Correlation of Pt-Re surface properties with reaction pathways for the aqueous-phase reforming of glycerol. *Journal of Catalysis*, 287:37–43, 2012.

[235] D. M. Alonso, S. G. Wettstein, and J. A. Dumesic. Bimetallic catalysts for upgrading of biomass to fuels and chemicals. *Chemical Society Reviews*, 41(24):8075–8098, 2012.

[236] C. H. Deng, X. Z. Duan, J. H. Zhou, D. Chen, X. G. Zhou, and W. K. Yuan. Size effects of Pt-Re bimetallic catalysts for glycerol hydrogenolysis. *Catalysis Today*, 234:208–214, 2014.

[237] O. M. Daniel, A. DeLaRiva, E. L. Kunkes, A. K. Datye, J. A. Dumesic, and R. J. Davis. X-ray absorption spectroscopy of bimetallic Pt-Re catalysts for hydrogenolysis of glycerol to propanediols. *ChemCatChem*, 2(9):1107–1114, 2010.

[238] E. L. Kunkes, D. A. Simonetti, J. A. Dumesic, W. D. Pyrz, L. E. Murillo, J. G. G. Chen, and D. J. Buttrey. The role of rhenium in the conversion of glycerol to synthesis gas over carbon supported platinum-rhenium catalysts. *Journal of Catalysis*, 260(1):164–177, 2008.

[239] D. A. Simonetti, E. L. Kunkes, and J. A. Dumesic. Gas-phase conversion of glycerol to synthesis gas over carbon-supported platinum and platinum-rhenium catalysts. *Journal of Catalysis*, 247(2):298–306, 2007.

[240] A. Ramstad, F. Strisland, S. Raaen, A. Borg, and C. Berg. CO and o_2 adsorption on the Re/Pt(111) surface studied by photoemission and thermal desorption. *Surface Science*, 440(1-2):290–300, 1999.

[241] A. Ramstad, F. Strisland, S. Raaen, T. Worren, A. Borg, and C. Berg. Growth and alloy formation studied by photoelectron spectroscopy and STM. *Surface Science*, 425(1):57–67, 1999.

[242] M. Alnot, A. Cassuto, R. Ducros, J. J. Ehrhardt, and B. Weber. XPS and UPS study of the reaction of carbon monoxide with oxygen and nitrogen monoxide on platinum-rhenium alloy. *Surface Science*, 114(2-3):L48–L56, 1982.

[243] M. Alnot, V. Gorodetskii, A. Cassuto, and J. J. Ehrhardt. Auger-electron spectroscopy, X-ray photoelectron-spectroscopy, work function measurements and photoemission of adsorbed xenon on thin-films of Pt-Re(111) alloys. *Thin Solid Films*, 151(2):251–262, 1987.

[244] D. J. Godbey and G. A. Somorjai. The adsorption and desorption of hydrogen and carbon monoxide on bimetallic Re-Pt(111) surfaces. *Surface Science*, 204(3):301–318, 1988.

[245] D. J. Godbey, F. Garin, and G. A. Somorjai. The hydrogenolysis of ethane over Re-Pt(111) and Pt-Re(0001) bimetallic crystal surfaces. *Journal of Catalysis*, 117(1):144–154, 1989.

[246] D. J. Godbey and G. A. Somorjai. The preparation and characterization of rhenium modified Pt(111) and Pt(100), and platinum modified Re(0001) single-crystal surfaces. *Surface Science*, 202(1-2):204–226, 1988.

[247] C. M. Kim and G. A. Somorjai. The effects of rhenium and sulfur on the reactivity and selectivity of Pt single crystal catalysts. *Journal of Catalysis*, 134(1):179–185, 1992.

[248] W. T. Tysoe, F. Zaera, and G. A. Somorjai. An XPS study of the oxidation and reduction of the rhenium platinum system under atmospheric conditions. *Surface Science*, 200(1):1–14, 1988.

[249] A. S. Duke, R. P. Galhenage, S. A. Tenney, P. Sutter, and D. A. Chen. In situ studies of carbon monoxide oxidation on platinum and platinum-rhenium alloy surfaces. *Journal of Physical Chemistry C*, 119(1):381–391, 2014.

[250] M. Alnot, A. Cassuto, J. J. Ehrhardt, A. Slavin, and B. Weber. Growth of platinum on rhenium and evolution of the interface under thermal-treatment. *Applied Surface Science*, 10(1):85–99, 1982.

[251] N. Mesboua, B. Weber, and A. Cassuto. The stationary oxidation of rhenium in the presence of platinum atoms - a mass spectrometry study under low oxygen pressures. *Surface Science*, 231(3):356–360, 1990.

[252] C. T. Campbell. Bimetallic surface-chemistry. *Annual Review of Physical Chemistry*, 41:775–837, 1990.

[253] C. Kittel. *Introduction to Solid State Physics*. John Wiley & Sons, Hoboken, NJ, 8th edition, 2005.

[254] N. V. Gelfond, N. B. Morozova, E. S. Filatov, S. A. Gromilov, and I. K. Igumenov. Structure of rhenium coatings obtained by CVD. *Journal of Structural Chemistry*, 50(6):1126–1133, 2009.

[255] Y. Isobe, M. Tanaka, S. Yamanaka, and M. Miyake. Chemical vapor deposition of rhenium on graphite. *Journal of the Less-Common Metals*, 152(1):177–184, 1989.

[256] K. T. Kim, J. J. Wang, and G. Welsch. Chemical vapor-deposition (CVD) of rhenium. *Materials Letters*, 12(1-2):43–46, 1991.

[257] Y. G. Tong, S. X. Bai, H. Zhang, and Y. C. Ye. Rhenium coating prepared on carbon substrate by chemical vapor deposition. *Applied Surface Science*, 261:390–395, 2012.

[258] M. Alnot and J. J. Ehrhardt. A study of oxygen-rhenium interactions in various pressure and temperature conditions. *Journal De Chimie Physique Et De Physico-Chimie Biologique*, 79(10):735–739, 1982.

[259] R. Ducros and J. Fusy. Core level binding-energy shifts of rhenium surface atoms for a clean and oxygenated surface. *Journal of Electron Spectroscopy and Related Phenomena*, 42(4):305–312, 1987.

[260] A. S. Y. Chan, W. H. Chen, H. Wang, J. E. Rowe, and T. E. Madey. Methanol reactions over oxygen-modified re surfaces: Influence of surface structure and oxidation. *Journal of Physical Chemistry B*, 108(38):14643–14651, 2004.

[261] C. Morant, L. Galan, and J. M. Sanz. X-ray photoelectron spectroscopic study of the oxidation of polycrystalline rhenium by exposure to O_2 and low energy ${O_2}^+$ ions. *Analytica Chimica Acta*, 297(1-2):179–186, 1994.

[262] C. A. Menning, H. H. Hwu, and J. G. G. Chen. Experimental and theoretical investigation of the stability of Pt-3d-Pt(111) bimetallic surfaces under oxygen environment. *Journal of Physical Chemistry B*, 110(31):15471–15477, 2006.

[263] P. Weigand, P. Novacek, G. Vanhusen, T. Neidhart, and P. Varga. Surface analysis of Pt_xNi_{1-x} single crystals. *Surface Science*, 269:1129–1134, 1992.

[264] R. Ducros, B. Tardy, and J. C. Bertolini. Carbon monoxide adsorption on Re(0001) between 120 k and 600 k studied by vibrational electron energy loss spectroscopy. *Surface Science*, 128(2-3):L219–L223, 1983.

[265] M. Asscher, C. T. Kao, and G. A. Somorjai. High-resolution electron-energy loss spectroscopic study of CO_2 adsorbed on Re(0001). *Journal of Physical Chemistry*, 92(10):2711–2714, 1988.

[266] K. Hahn and M. Mavrikakis. Atomic and molecular adsorption on Re(0001). *Topics in Catalysis*, 57(1-4):54–68, 2014.

[267] H. Steininger, S. Lehwald, and H. Ibach. Adsorption of oxygen on Pt(111). *Surface Science*, 123(1):1–17, 1982.

[268] J. L. Gland, B. A. Sexton, and G. B. Fisher. Oxygen interactions with the Pt(111) surface. *Surface Science*, 95(2-3):587–602, 1980.

[269] H. Steininger, S. Lehwald, and H. Ibach. On the adsorption of CO on Pt(111). *Surface Science*, 123(2-3):264–282, 1982.

[270] R. Ducros, M. Housley, and G. Piquard. Influence of structural defects, steps and kinks, on oxygen-adsorption on rhenium single-crystals. *Physica Status Solidi A: Applied Research*, 56(1):187–193, 1979.

[271] C. T. Campbell, G. Ertl, H. Kuipers, and J. Segner. A molecular-beam study of the adsorption and desorption of oxygen from a Pt(111) surface. *Surface Science*, 107(1):220–236, 1981.

[272] G. J. Dooley and T. W. Haas. Some properties of rhenium (0001) surface. *Surface Science*, 19(1):1–8, 1970.

[273] B. Weber and A. Cassuto. States of adsorption, rate of adsorption, desorption of oxygen on rhenium and atomization and oxidation mechanisms at high temperature and low pressure. *Surface Science*, 36(1):81–108, 1973.

[274] Y. G. Ma and P. B. Balbuena. Pt surface segregation in bimetallic Pt_3M alloys: A density functional theory study. *Surface Science*, 602(1):107–113, 2008.

[275] G. F. Wang, M. A. Van Hove, P. N. Ross, and M. I. Baskes. Monte carlo simulations of segregation in Pt-Re catalyst nanoparticles. *Journal of Chemical Physics*, 121(11):5410–5422, 2004.

[276] J. E. Holladay, J. J. Bozell, J. F. White, and D. Johnson. Top value-added chemicals from biomass. *DOE Report PNNL*, 16983, 2007.

[277] Sara L. Yohe. *High-pressure vapor-phase catalytic hydrodeoxygenation of lignin-derived compounds to hydrocarbons on bimetallic catalysts in the range of 0.2-2.4 MPa.* PhD thesis, Purdue University, 2013.

[278] B. N. Grgur, N. M. Markovic, and P. N. Ross. Electrooxidation of H_2, CO, and H_2/CO mixtures on a well-characterized $Pt_{70}M_{30}$ bulk alloy electrode. *The Journal of Physical Chemistry B*, 102(14):2494–2501, 1998.

[279] S. G. Neophytides, S. H. Zafeiratos, and M. M. Jaksic. Selective interactive grafting of composite bifunctional electrocatalysts for simultaneous anodic hydrogen and CO oxidation I. Concepts and embodiment of novel-type composite catalysts. *Journal of the Electrochemical Society*, 150(10):E512–E526, 2003.

[280] R. Barthos, A. Széchenyi, and F. Solymosi. Efficient H_2 production from ethanol over Mo_2C/C nanotube catalyst. *Catalysis Letters*, 120(3-4):161–165, 2008.

[281] W. Ding, S. Li, G. D. Meitzner, and E. Iglesia. Methane conversion to aromatics on Mo/H-ZSM5: Structure of molybdenum species in working catalysts. *The Journal of Physical Chemistry B*, 105(2):506–513, 2001.

[282] J. E. deVries, H. C. Yao, R. J. Baird, and H. S. Gandhi. Characterization of molybdenum-platinum catalysts supported on γ-alumina by X-ray photoelectron spectroscopy. *Journal of Catalysis*, 84(1):8–14, 1983.

[283] J. Goldwasser, S. M. Fang, M. Houalla, and W. K. Hall. On the surface chemistry of molybdena-alumina catalysts prepared from $Mo(CO)_6$. *Journal of Catalysis*, 115(1):34–51, 1989.

[284] J.-G. Choi and L. T. Thompson. XPS study of as-prepared and reduced molybdenum oxides. *Applied Surface Science*, 93(2):143–149, 1996.

[285] B. Brox and I. Olefjord. ESCA studies of MoO_2 and MoO_3. *Surface and interface analysis*, 13(1):3–6, 1988.

[286] S. O. Grim and L. J. Matienzo. X-ray photoelectron spectroscopy of inorganic and organometallic compounds of molybdenum. *Inorganic Chemistry*, 14(5):1014–1018, 1975.

[287] P. A. Spevack and N. S. McIntyre. Thermal reduction of molybdenum trioxide. *The Journal of Physical Chemistry*, 96(22):9029–9035, 1992.

[288] J. S. Lee, S. Locatelli, S. T. Oyama, and M. Boudart. Molybdenum carbide catalysts 3. Turnover rates for the hydrogenolysis of n-butane. *Journal of catalysis*, 125(1):157–170, 1990.

[289] J. H. Scofield. Hartree-Slater subshell photoionization cross-sections at 1254 and 1487 eV. *Journal of Electron Spectroscopy and Related Phenomena*, 8(2):129–137, 1976.

APPENDICES

A. XPS MODELS

Differential photoelectron peak intensity as a function of photoemission angle, $\mathrm{d}N(\theta)$, from a bounded, uniform density material can be written as:

$$\mathrm{d}N(\theta) = I \times \rho \times \frac{d\sigma}{\mathrm{d}\Omega} \times \Omega(E_{kin}, x, y, z) \times D \times \exp\left(\frac{-z}{\Lambda(E_{kin}) \times \cos\theta}\right) \mathrm{d}x\mathrm{d}y\mathrm{d}z \quad \text{(A.1)}$$

where I is the X-ray flux, constant in most spectrometer systems at constant $h\nu$; Ω is the acceptance solid angle of the electron analyzer which is a function of photoelectron kinetic energy, E_{kin}, and the position; D is the instrument detection efficiency, which is the probability that an escaped electron encompassed by the acceptance solid angle will yield a single count; ρ is the number of atoms or molecules per unit volume, $\frac{\mathrm{d}\sigma}{\mathrm{d}\Omega}$ is the differential cross section for the photoemission peak, which can be calculated from Scofield cross sections [289] and the Reilman asymmetry parameter, [193] Λ is the electron attenuation length calculated using NIST SRD-82; [188] and θ is the electron takeoff angle relative to the surface normal. The exponential term is the probability for no-loss escape from the specimen where $\frac{z}{\cos\theta}$ is the path length.

Integrating over x and y and from the surface to a depth of thickness t,

$$\begin{aligned} \int \mathrm{d}N(\theta) = \int_{-\infty}^{\infty}\int_{-\infty}^{\infty}\int_{0}^{t} I \times \rho \times \frac{\mathrm{d}\sigma}{\mathrm{d}\Omega} \times \Omega(E_{kin}, x, y, z) \times D \\ \times \exp\left(\frac{-z}{\Lambda(E_{kin}) \times \cos\theta}\right) \mathrm{d}x\mathrm{d}y\mathrm{d}z \end{aligned} \quad \text{(A.2)}$$

Solving for $N(\theta)$,

$$\begin{aligned} N(\theta) = I \times \Omega(E_{kin}) \times A(E_{kin}) \times D(E_{kin}) \times \rho \times \frac{\mathrm{d}\sigma}{\mathrm{d}\Omega} \times \Lambda(E_{kin}) \times \cos\theta \\ \times \left(1 - \exp\left(\frac{-t}{\Lambda_e(E_s) \times \cos\theta}\right)\right) \end{aligned} \quad \text{(A.3)}$$

where A is the effective sample area.

A.1 Non-attenuating Overlayer at Fractional Monolayer Coverage

This derivation follows Fadley's approach. [62] Substrate peak intensity for a semi-infinite substrate, represented by subscript s, is calculated by taking the limit of Equation A.3 as t tends to infinity:

$$N_s(\theta) = I_s \times \Omega_s(E_s) \times A_s(E_s) \times D_s \times \rho_s \times \frac{\mathrm{d}\sigma_s}{\mathrm{d}\Omega} \times \Lambda_e^{subst}(E_s) \times \cos\theta \tag{A.4}$$

Peak intensity from the overlayer, represented by subscript l, is given by:

$$N_l(\theta) = I_l \times \Omega_l(E_l) \times A_l(E_l) \times D_l \times s_l \times \frac{\mathrm{d}\sigma_l}{\mathrm{d}\Omega} \tag{A.5}$$

where s_l is the average surface density of atoms in the overlayer. The ratio of overlayer to substrate peak intensity is:

$$\frac{N_l(\theta)}{N_s(\theta)} = \frac{I_l \times \Omega_l(E_l) \times A_l(E_l) \times D_l \times s_l \times \frac{\mathrm{d}\sigma_l}{\mathrm{d}\Omega}}{I_s \times \Omega_s(E_s) \times A_s(E_s) \times D_s \times \frac{s_s}{d_s} \times \frac{\mathrm{d}\sigma_s}{\mathrm{d}\Omega} \times \Lambda_e^{subst}(E_s) \times \cos\theta} \tag{A.6}$$

where $\rho_s = \frac{s_s}{d_s}$, and d_s is the average separation of layers of density s_s in the substrate. Solving for $\frac{s_l}{s_s}$ yields the coverage, Θ:

$$\Theta = \frac{s_l}{s_s} = \frac{N_l(\theta) \times I_s \times \Omega_s(E_s) \times A_s(E_s) \times D_s \times \frac{\mathrm{d}\sigma_s}{\mathrm{d}\Omega} \times \Lambda_e^{subst}(E_s) \times \cos\theta}{N_s(\theta) \times I_l \times \Omega_l(E_l) \times A_l(E_l) \times D_l \times \frac{\mathrm{d}\sigma_l}{\mathrm{d}\Omega} \times d_s} \tag{A.7}$$

For XPS done with a typical laboratory source, $I_s = I_l$ and $D_s = D_l$ for constant pass energies. Assuming that Ω and A are equal for the overlayer and substrate, Equation A.7 simplifies to:

$$\frac{s_l}{s_s} = \frac{N_l(\theta) \times \Omega_s(E_s) \times A_s(E_s) \times \frac{\mathrm{d}\sigma_s}{\mathrm{d}\Omega} \times \Lambda_e^{subst}(E_s) \times \cos\theta}{N_s(\theta) \times \Omega_l(E_l) \times A_l(E_l) \times \frac{\mathrm{d}\sigma_l}{\mathrm{d}\Omega} \times d_s} \tag{A.8}$$

For XPS done at the BESSY II synchrotron, where $h\nu$ is usually adjusted so that E_{kin} is constant, $E_s = E_l$, $D_s = D_l$ for constant pass energies, and $\theta = 0\,\mathrm{deg}$. Assuming that Ω and A are equal for the overlayer and substrate, Equation A.7 simplifies to:

$$\frac{s_l}{s_s} = \frac{N_l(\theta) \times I_s \times \frac{\mathrm{d}\sigma_s}{\mathrm{d}\Omega} \times \Lambda_e^{subst}(E_s)}{N_s(\theta) \times I_l \times \frac{\mathrm{d}\sigma_l}{\mathrm{d}\Omega} \times d_s} \tag{A.9}$$

A.2 Thickness of a Uniform Overlayer

Peak intensity from an overlayer $N_l(\theta)$ follows from integrating Equation A.6 over z from 0 to t:

$$\begin{aligned} N_l(\theta) = {} & I_l \times \Omega_l(E_l) \times A_l(E_l) \times D_l \times \rho_l \times \frac{\mathrm{d}\sigma_l}{\mathrm{d}\Omega} \times \Lambda_l(E_l) \times \cos\theta \\ & \times \left(1 - \exp\left(\frac{-t}{\Lambda_l(E_l) \times \cos\theta}\right)\right) \end{aligned} \tag{A.10}$$

where $\Lambda_l(E_l)$ is the electron attenuation length of an electron originating from the overlayer with kinetic energy E_l. For the substrate, Equation A.6 is integrated over z from t to ∞, yielding:

$$N_s(\theta) = I_s \times \rho \times \frac{\mathrm{d}\sigma_s}{\mathrm{d}\Omega} \times \Lambda_e(E_s) \times \cos\theta \times \left(1 - \exp\left(\frac{-t}{\Lambda_e(E_s) \times \cos\theta}\right)\right) \tag{A.11}$$

where $\Lambda_l(E_s)$ is the electron attenuation length of an electron originating from the substrate with kinetic energy E_s passing through the overlayer. The intensity ratio for the overlayer to the substrate signal takes the form of the following equation, assuming constant pass energy ($D_s = D_l$) and that Ω and A are constant for the overlayer and substrate:

$$\frac{N_l(\theta)}{N_s(\theta)} = \frac{I_l \times \rho_l \times \frac{\mathrm{d}\sigma_l}{\mathrm{d}\Omega} \times \Lambda_l(E_l) \times \cos\theta}{I_s \times \rho_s \times \frac{\mathrm{d}\sigma_s}{\mathrm{d}\Omega} \times \Lambda_s(E_s) \times \cos\theta} \times \frac{\left(1 - \exp\left(\frac{-t}{\Lambda_l(E_l) \times \cos\theta}\right)\right)}{\exp\left(\frac{-t}{\Lambda_l(E_s) \times \cos\theta}\right)} \tag{A.12}$$

For *in situ* XPS experiments performed at the BESSY II synchrotron, $E_l = E_s$, so $\Lambda_l(E_s) \approx \Lambda_l(E_l)$. Also, $\cos\theta = 1$. In this case, thickness can be explicitly solved:

$$t = \Lambda_l(E_l) \times \ln\left(\frac{N_l(\theta) \times I_s \times \rho_s \times \frac{\mathrm{d}\sigma_s}{\mathrm{d}\Omega} \times \Lambda_s(E_s)}{N_s(\theta) \times I_l \times \rho_l \times \frac{\mathrm{d}\sigma_l}{\mathrm{d}\Omega} \times \Lambda_l(E_l)} + 1\right) \tag{A.13}$$

A.3 *In situ* Carbon Coverage Calculation

Due to adsorption of X-rays by the *in situ* cell window, quantification of the C 1s signal was not successful following the above procedures for experiments performed at BESSY II. Instead, this coverage was estimated by dosing CO in saturation (assumed to be 0.5 ML on Pt(111) [71]), and using atomic concentration ratios as outlined below to calculate carbon coverages on Pt(111) and Pd(111).

Carbon coverage on surface i, Θ_i was estimated by comparison of atomic concentration $\frac{C}{Pt}$ ratios between CO saturated Pt(111) and the surface $\frac{C}{Pt}$ ratio for surface i on Pt(111):

$$\frac{\mathrm{C}}{\mathrm{Pt}}_{\mathrm{CO,sat'd}} = \frac{0.5\mathrm{ML}}{\Theta_i} \tag{A.14}$$

$$\Theta_i = 0.5\mathrm{ML} \times \frac{\frac{\mathrm{C}}{\mathrm{Pt}}_i}{\frac{\mathrm{C}}{\mathrm{Pt}}_{\mathrm{CO,sat'd}}} \tag{A.15}$$

B. FORMIC ACID DECOMPOSITION MECHANISMS

B.1 Single Site Formate Decomposition Mechanism

The overall rate of the reaction, assuming that formate decomposition (Equation 2.3 in the main text) is the rate determining step, is written as:

$$r = k_2[HCOO \cdot S] \tag{B.1}$$

Assuming quasi-equilibrium for the other elementary steps, equations can be written for each step. For formic acid adsorption (Equation 2.2):

$$K_1[HCOOH][S]^2 = [HCOO \cdot S][H \cdot S] \tag{B.2}$$

For hydrogen recombination (Equation 2.4):

$$K_3[H \cdot S]^2 = [H_2][S]^2 \tag{B.3}$$

Finally, for CO adsorption (Equation 2.5 in the main text):

$$K_4[CO][S] = [CO \cdot S] \tag{B.4}$$

Substituting Equation B.3 into Equation B.2 and solving for $[HCOO \cdot S]$ yields the following:

$$[HCOO \cdot S] = \frac{K_1 K_3^{1/2}[HCOOH][S]}{[H_2]^{1/2}} \tag{B.5}$$

Solving Equation B.3 for $[H \cdot S]$ yields:

$$[H \cdot S] = \frac{[H_2]^{1/2}[S]}{K_3^{1/2}} \tag{B.6}$$

And solving Equation B.4 for $[CO \cdot S]$ yields:

$$[CO \cdot S] = K_4[CO][S] \tag{B.7}$$

A site balance can now be written where L is the total number of sites.

$$\begin{aligned} L &= [S] + [HCOO \cdot S] + [H \cdot S] + [CO \cdot S] \\ &= [S] + \frac{K_1 K_3^{1/2}[HCOOH][S]}{[H_2]^{1/2}} + \frac{[H_2]^{1/2}[S]}{K_3^{1/2}} + K_4[CO][S] \\ &= [S]\left(1 + \frac{K_1 K_3^{1/2}[HCOOH]}{[H_2]^{1/2}} + \frac{[H_2]^{1/2}}{K_3^{1/2}} + K_4[CO]\right) \end{aligned} \tag{B.8}$$

Solving the site balance for $[S]$ and combining Equations B.1, B.5, and B.8 yields the rate expression.

$$r = \frac{L K_1 k_2 K_3^{1/2}[HCOOH]}{[H_2]^{1/2}\left(1 + \frac{K_1 K_3^{1/2}[HCOOH]}{[H_2]^{1/2}} + \frac{[H_2]^{1/2}}{K_3^{1/2}} + K_4[CO]\right)} \tag{B.9}$$

The reaction order with respect to formic acid, n_{HCOOH}, is determined by taking the log derivative of the log formic acid concentration:

$$\begin{aligned} n_{HCOOH} &= \frac{\partial \ln r}{\partial ln[HCOOH]} \\ &= [HCOOH]\frac{\partial \ln r}{\partial [HCOOH]} \\ &= \frac{K_1 K_3^{1/2}[HCOOH]}{[H_2]^{1/2}\left(1 + \frac{K_1 K_3^{1/2}[HCOOH]}{[H_2]^{1/2}} + \frac{[H_2]^{1/2}}{K_3^{1/2}} + K_4[CO]\right)} \end{aligned} \tag{B.10}$$

Dividing both sides of Equation B.5 by L yields the formate coverage, θ_{HCOO}:

$$\theta_{HCOO} = \frac{[HCOO \cdot S]}{L} = \frac{K_1 K_3^{1/2}[HCOOH][S]}{[H_2]^{1/2} L} \tag{B.11}$$

Combining Equation B.11 with the site balance (Equation B.8) allows for the formic acid reaction order to be expressed as a function of formic acid coverage as follows:

$$n_{HCOOH} = 1 - \theta_{HCOO} \tag{B.12}$$

Similar expressions can be derived for the hydrogen and CO orders using the same approach:

$$n_{H2} = -\frac{1}{2} + \frac{\theta_{HCOO}}{2} - \frac{\theta_{H2}}{2} \tag{B.13}$$

$$n_{CO} = -\theta_{CO} \tag{B.14}$$

The measured $n_{HCOOH} = 0.4$ and $n_{CO} = -0.4$ yield formate and CO coverages equal to 0.6 and 0.4 ML, respectively. For $\theta_{H2} = 0$, $n_{H2} = -0.2$.

B.2 Dual Site Formate Decomposition Mechanism

A rate equation and reaction orders in terms of adsorbate coverages can be calculated similarly for a dual site formate decomposition mechanism. In this mechanism, Equation 2.3 in the main text is replaced by Equation 2.7 in the main text, with all other steps remaining the same. The derived rate expression is as follows:

$$r = \frac{zk_2[HCOO \cdot S][S]}{L} \tag{B.15}$$

where z is the coordination number. The rate expression as well as reaction orders expressed in terms of coverages, expressed in terms of gas phase concentrations, are obtained in the same manner as for the single site mechanism above.

$$r = \frac{zLK_1k_2K_3^{1/2}[HCOOH]}{[H_2]^{1/2}\left(1 + \frac{K_1K_3^{1/2}[HCOOH]}{[H_2]^{1/2}} + \frac{[H_2]^{1/2}}{K_3^{1/2}} + K_4[CO]\right)^2} \tag{B.16}$$

$$n_{HCOOH} = 1 - 2\theta_{HCOO} \tag{B.17}$$

$$n_{H2} = -\frac{1}{2} + \theta_{HCOO} - \theta_{H2} \tag{B.18}$$

$$n_{CO} = -2\theta_{CO} \tag{B.19}$$

The measured $n_{HCOOH} = 0.4$ and $n_{CO} = -0.4$ yield formate and CO coverages equal to 0.3 and 0.2 ML, respectively. As above, for $\theta_{H2} = 0$, $n_{H2} = -0.2$.

VITA

VITA

Michael Donald Detwiler was born on December 29, 1987 to Donald and JoAntonia Detwiler in Youngstown, Ohio. He has one sister, Rachel. Mike grew up in nearby Austintown, Ohio. He graduated from Austintown-Fitch High School in 2006 as Valedictorian. During high school, Mike participated on the varsity tennis and debate teams. After high school, he studied chemical engineering with math and chemistry minors at Youngstown State University, graduating *summa cum laude* with his B. Eng. in 2010. Mike was part of the University Scholars program at YSU. As part of this program, he volunteered as a judge at local high school debate competitions and other area events while living on campus. Mike was first exposed to academic research and the catalysis field during summer 2008, when he worked as an undergraduate researcher in labs of Dr. Chris Williams and Dr. John Monnier at the University of South Carolina. He worked as an engineering intern during the summers of 2009 and 2010 at Bechtel Marine Propulsion Corporation, Bettis Atomic Power Laboratory, in West Mifflin, Pennsylvania. He began his graduate studies at Purdue in August 2010 working in the labs of Dr. Fabio H. Ribeiro and Dr. W. Nicholas Delgass, studying model catalytic systems in ultra-high vacuum. He graduated with a Ph. D. in chemical engineering in 2015. During his time as an undergraduate and graduate student, Mike won several awards including an NSF Graduate Research Fellowship Program honorable mention (2010), YSU's Engineering Man of the Year (2010), AIChE Professional Promise Award (2010), Magoon Award for Excellence in Teaching (2011-2012), and an Outstanding Poster Presentation Award from the Catalysis Club of Chicago (2013). Upon graduation, Mike will join BASF Corporation's Ph. D. Professional Development Program in Iselin, New Jersey.